Fundamentals of Discharge Initiation by ICRF Antennas in Fusion Devices

Beginselen van ontladingsinitiatie door ICRF-antennes in fusiemachines

Matěj Tripský

Promotoren: prof. dr. ir. J.-M. Noterdaeme, prof. dr. ir. M. Van Schoor
Proefschrift ingediend tot het behalen van de graden van
Doctor in de ingenieurswetenschappen: toegepaste natuurkunde (Universiteit Gent)
en Doctor in de ingenieurswetenschappen (Koninklijke Militaire School)

UNIVERSITEIT
GENT

Vakgroep Toegepaste Fysica
Voorzitter: prof. dr. ir. C. Leys
Faculteit Ingenieurswetenschappen en Architectuur

Departement Fysica
Departementshoofd: prof. dr. ir. M. Van Schoor
Faculteit Polytechniek

Academiejaar 2017 - 2018

ISBN 978-94-6355-099-4
NUR 926, 928
Wettelijk depot: D/2018/10.500/17

Members of the examination committee

prof. dr. ir. Jean-Marie Noterdaeme *Promotor*
Ghent University, Department of Applied physics
prof. dr. ir. Michael Van Schoor *Promotor*
Royal Military Academy of Belgium, Head Department of Physics
dr. ir. Tom Wauters *Supervisor*
Royal Military Academy of Belgium
dr. ir. Anatoli Lyssoivan *Supervisor*
Royal Military Academy of Belgium

prof. dr. ir. Patrick De Baets *Chairman*
Ghent University, Dean of the Faculty of Engineering and Architecture
prof. dr. ir. Kristel Crombé *Secretary*
Ghent University, Department of Applied physics
prof. dr. ir. Hendrik Rogier
Ghent University, Department of Information technology
dr. ir. Raymond Koch
Royal Military Academy of Belgium
dr. David Douai
CEA, Institute for Magnetic Fusion Research
dr. Vladimir Moiseenko
National Science Center ”Kharkiv Institute of Physics and Technology”

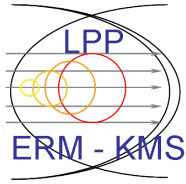

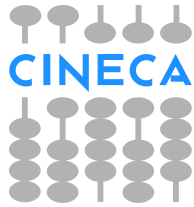

This work was carried out using the HELIOS supercomputer system at Computational Simulation Centre of International Fusion Energy Research Centre (IFERC-CSC), Aomori, Japan, under the Broader Approach collaboration between Euratom and Japan, implemented by Fusion for Energy and JAEA. We acknowledge the CINECA award under the ISCRA initiative, for the availability of high performance computing resources and support. This work has been carried out within the framework of the EUROfusion Consortium and has received funding from the Euratom research and training program 2014-2018 under grant agreement No 633053. The views and opinions expressed herein do not necessarily reflect those of the European Commission.

Acknowledgments

Firstly, I would like to express my sincere gratitude to my supervisor Dr. Tom Wauters for the continuous support of my Ph.D study and related research, for his patience, motivation, and immense knowledge. I would also like to thank my supervisor Dr. Anatoli Lyssoivan for its insightful comments and encouragement, but also for the hard questions which urge me to widen my research from various perspectives. I could not have imagined having better supervisors and mentors for my Ph.D study. Besides my supervisors, I would like to thank Prof. Noterdaeme and Prof. Van Schoor for accepting the co-tutorship of this Ph.D and for creating conditions to work on my research in the Laboratory for Plasma Physics at Royal Military Academy of Belgium in Brussels.

My sincere thanks also go to all colleagues in the LPP-ERM/KMS who had important impacts on this manuscript via discussions or their collaboration during my research. I would like to thank specially R. Koch, F. Louche, A. Křivká, D. Van Eester, K. Crombé, Y. Kazakov, R. Ragona, M. Vervier, A. Messiaen, E. Lerche, P. Dumortier, and J. Ongena. Without their precious support it would not be possible to conduct this research. During my Ph.D research I had the opportunity to work in many European research institutions. Part of the work was carried out at IPP-Jüllich, IPP-Garching, CCFE-Culham, and KIPT-Kharkov. For these fantastic collaborations I would like to thank specially V. Bobkov, D. Douai, R. D'Inca, J. Jacquot, R. Ochoukov, M. Usoltceva, V.E. Moiseenko, A.V. Lozin, R.O. Pavlichenko, M.M. Kozulya, M.B. Dreval, Yu.K. Mironov, A.N. Shapoval, V.V. Chechkin, L.I. Grigor'eva, the TEXTOR Team from IPP-Jüllich, the ASDEX Upgrade Team from IPP-Garching, the IShTAR Team from IPP-Garching, the JET Team from CCFE-Culham and the URAGAN 3-M Team from KIPT-Kharkov.

Brussels, December 2017
Matěj Tripský

Table of Contents

List of Acronyms

0-9

1D	One Dimensional

A

AUG	ASDEX Upgrade (Axially Symmetric Divertor EXperiment), Garching, Germany

C

C	Carbon
CS	Central Solenoid
CX	Charge exchange

D

D	Deuterium
D-IIID	Doublet III-Divertor experiment, San Diego, USA
DEMO	Demonstration Fusion Power Plant

E

ECR	Electron Cyclotron Resonance
ECRF	Electron Cyclotron Range of Frequencies
ECRH	Electron Cyclotron Resonance Heating
ECWC	Electron Cyclotron Wall Conditioning

EEDF	Electron Energy Distribution Function
EM	Electromagnetic

F

FS	Faraday Screen
FW	Fast Wave

G

GDC	Glow Discharge Conditioning

H

H	Hydrogen
He	Helium
HFS	High Field Side

I

IBW	Ion Bernstein Wave
ICRF	Ion Cyclotron Range of Frequencies
ICRH	Ion Cyclotron Resonance Heating
ICWC	Ion Cyclotron Wall Conditioning
IEDF	Ion Energy Distribution Function
IShTAR	Ion cyclotron Sheath Test ARrangement
ITER	International Thermonuclear Experimental Reactor, Cadarache, France

J

JET	Joint European Torus, Culham, UK

L

LFS	Low Field Side
LH	Lower Hybrid (heating)

M

MC	Monte Carlo
MCC	Monte Carlo Collision
MCCS	Monte Carlo Collision Scheme
MPI	Message Passing Interface

N

NPA	Neutral Particle Analyzer

P

PDM	Ponderomotive model
PDMI	Ponderomotive-Ionization model
PFC	Plasma Facing Components
PIC	Particle-In-Cell
PIC-MCC	Particle-In-Cell Monte Carlo Collision
PSI	Plasma Surface Interactions
PWI	Plasma Wall Interactions

R

RF	Radio Frequency
RMS	Root Mean Square

S

SEE	Secondary Electron Emission
SEY	Secondary Electron Yield
SOL	Scrape-Off Layer
SW	Slow Wave

T

T	Tritium
TEXTOR	Tokamak Experiment for Technology Oriented Research in the field of plasma wall interaction, Jülich, Germany
TF	Toroidal Field
TOMAS	TOroidal MAgnetic field System, Jülich, Germany
TORE SUPRA	Superconducting tokamak, Cadarache, France

V

VSWR	Voltage Standing Wave Ratio

W

W	Tungsten

Nederlandse samenvatting

Introductie

Een van de wereldwijde uitdagingen waarmee we op dit moment worden geconfronteerd is een toename van CO_2 in onze atmosfeer. Er bestaat consensus binnen de wetenschappelijke gemeenschap over de menselijke oorzaak van de temperatuurstoename op onze planeet door het teveel aan broeikasgassen waaronder CO_2. Het grootste deel van de broeikasgassen in onze atmosfeer is afkomstig van het verbranden van fossiele brandstoffen door energiecentrales en de industrie. Fossiele brandstoffen vertegenwoordigen ongeveer 81% van het energieverbruik op aarde. Het is cruciaal om onze fossiele brandstofcentrales te vervangen door energiebronnen die geen CO_2 uitstoten in onze atmosfeer. Een voornaam CO_2-arm alternatief is gebaseerd op kernsplijting. Kerncentrales kunnen een enorme hoeveelheid stroom produceren. Politiek is er echter weinig draagkracht voor kernenergie wegens onzekerheden omtrent veiligheid en nucleair afval. Vooral in Europa genieten hernieuwbare energiebronnen zoals windmolens en zonnepanelen momenteel de voorkeur als CO_2-arme energiebron. Helaas lijkt het onmogelijk om met deze technieken ons volledige energieverbruik te voorzien. Bovendien is de energieproductie van deze hernieuwbare energiebronnen afhankelijk van de weersomstandigheden. De elektriciteitsproductie is niet continu in de tijd waardoor energieopslag moet worden voorzien. Daarom is er een dringende behoefte aan nieuwe methoden voor energieproductie die aanzienlijke hoeveelheden energie produceren, geen broeikasgassen produceren en betrouwbaar en veilig zijn. De meest veelbelovende methode is magnetische fusie. Op dit moment wordt de grootste fusiereactor ooit gebouwd in het zuiden van Frankrijk nabij het CEA-onderzoekscentrum in Cadarache. Deze machine, ITER genoemd, is het internationale project van zeven aangesloten entiteiten: de Europese Unie, India, Japan, China, Rusland, Zuid-Korea en de VS. ITER belichaamt de overgang van experimentele fusie machines (zoals JET, ASDEX-upgrade, TORE SUPRA, TEXTOR) naar de eerste reactor die meer energie zal produceren dan dat ze verbruikt.

Kernfusie is de energiebron van onze zon. In de zon smelten waterstofatomen samen om uiteindelijk helium te produceren. In dit proces worden enorme hoeveelheden energie vrijgeven. Het onderzoek naar fusie-energie is voornamelijk gericht op de reacties tussen twee soorten waterstofisotopen: deuterium (D) en tritium (T). Deze waterstofisotopen produceren na het samensmelten een heliumkern dat niet radioactief is en een neutron met een gecombineerde energie van $17.6\,\mathrm{MeV}$: $D + T \rightarrow {}^4He\,(3.5\,\mathrm{MeV}) + n\,(14.1\,\mathrm{MeV})$. Als we kernfusie op onze planeet willen gebruiken, moeten we een manier vinden om de afstotende Coulomb-kracht tussen de geladen kernen te overwinnen, hetgeen op grote schaal veel energie vergt. In thermonucleaire fusie wordt een geladen brandstofgas, plasma, met een hoge dicht-

heid tot fusierelevante temperaturen verhit door extern aangelegd verhittingsvermogen en waarbij slechts een fractie van de brandstof voldoende energie zal bezitten om de Coulomb barrière te doorbreken. Men spreekt van een zelfonderhoudende fusiereactie (ignition) op het moment dat het plasma zichzelf verhit door de fusiereacties en de externe verhitting kan worden uitgeschakeld. Om ignition te bereiken, moeten de plasmaparameters het Lawson-criterium (of het triple product) overstijgen: $n_e T \tau_E \geq 3 \cdot 10^{21}\,\mathrm{m}^{-3}\mathrm{keVs}$, waarbij n_e de plasma-elektronendichtheid is, T de plasmatemperatuur en τ_E de karakteristieke tijdsduur van de energieopsluiting. Het fusieonderzoek van vandaag kent vele benaderingen om de juiste triple product-waarden te bereiken. Het meest veelbelovende concept is gericht op de magnetische opsluiting van het plasma in een donutvormige container gecreëerd door magnetische velden. Dit manuscript kadert binnen dit concept. De huidige torusvormige machines waarin fusieplasmas bestudeerd worden kunnen onderverdeeld worden in twee types: de tokamak en de stellarator. De beoogde waarden van het triple-product voor tokamaks zijn $T \approx 10 - 20\,\mathrm{keV}$, $n_e \approx 10^{20}\,\mathrm{m}^{-3}$ and $\tau_E \approx 3 - 5\,\mathrm{s}$.

Het magnetische veld van de tokamak bestaat uit twee componenten: toroïdale (sterkere) en poloïdale magnetische velden. Deze twee magnetische veldcomponenten creëren samen gesloten magnetische flux oppervlakken waarop de geladen deeltjes zijn vastgepind. Het toroïdale magnetische veld wordt geproduceerd door een reeks poloidale stroomspoelen die het plasma omgeven. In een tokamak induceert een primair transformatorcircuit een toroidale stroom in het plasma die de poloïdale magnetisch veldcomponent produceert. Stellaratoren gebruiken een andere benadering om de magnetische oppervlakken te creëren door gebruik te maken van uniek gevormde en ontworpen poloïdale spoelen. In dit manuscript presenteren we experimenten uitgevoerd op tokamaks TEXTOR (IPP-Jü llich, Germany) en ASDEX Upgrade (IPP-Garching, Duitsland), stellarator Uragan 3-M (Kharkiv, Oekraïne) en ook op de lineaire machine IShTAR (IPP-Garching, Duitsland).

Een van de moeilijkheden bij het bereiken van de noodzakelijke voorwaarden voor fusiereacties (Triple product) is het beheersen van de gevolgen van de interactie van het plasma met de wandmaterialen van de reactor. Deze interactie resulteert namelijk in de productie van onzuiverheden, de opslag en het weer loslaten van waterstof uit de wand en de opslag van radioactief tritium in de wand. Er bestaan verschillende methoden om de reactorwandoppervlakken te conditioneren en zo de vacuümcondities te verbeteren of de gevolgen van plasma-wandinteractie te controleren. De belangrijkste zijn opwarmen (baking)-, gloeiontladingen (GDC) en ion of elektron cyclotron-wandconditionering (ICWC en ECWC). Hoewel al deze vermelde methoden hun effectiviteit aantoonden, bestaan er belangrijke beperkingen voor het gebruik van de eerste twee methoden in ITER en andere toekomstige fusie-machines. GDC kan bijvoorbeeld niet worden toegepast in de aanwezigheid van magnetische velden. ITER zal supergeleidende toroïdale veldspoelen gebruiken voor het produceren van het toroïdale magnetische veld. Dit veld is quasi permanent aanwezig omdat de supergeleidende spoelen niet snel noch vaak kunnen worden uitgeschakeld b.v. wanneer er wandconditionering nodig is. Aangezien zowel ICWC als ECWC het magnetische veld nodig hebben voor hun werking, worden deze methoden door ITER als belangrijk beschouwd voor wandconditionering.

PhD doelstellingen

In dit manuscript onderzoeken we de initiatie van plasma-ontladingen door ICRF-antennes in het kader van de ontwikkeling van ICWC voor ITER. Hoewel ICWC met succes op alle tokamaks met ICRF-antennes was getest, was de initiële fase van het plasmaproductie proces door ICRF-antennes nog steeds niet goed begrepen. ICRF-antennes zijn ontworpen om radiofrequent vermogen te koppelen aan een reeds ontwikkeld plasma door het exciteren van snelle golven (Fast Waves), terwijl tijdens de ICWC-experimenten de ICRF-antennes eerst in het vacuüm worden aangedreven wanneer er nog geen plasmabelasting is. Het vermogen wordt volledig gedissipeerd door resistieve verliezen langs de transmissielijnen, het matchingsysteem en de omgeving van de antenne. Hierdoor, zelfs wanneer de antenne op de vacuümbelasting wordt afgestemd, wordt bijna al het vermogen dat bij de antenne arriveert, teruggekaatst naar het matchingsysteem. De voorwaartse en gereflecteerde golven tussen de antenne en het matchingsysteem creëren een staande golf met een aanzienlijk hogere amplitude dan die van de voorwaartse golf die door de generator in het matchingsysteem wordt gestuurd. De aanwezigheid van deze hoge spanningen in de transmissielijnen tussen het matchingsysteem en de antenne introduceert de potentieel gevaarlijke situatie van elektrische ontladingen in de transmissielijnen, op de antenne of andere RF-componenten die mogelijk het ICRF-systeem kunnen beschadigen. Daarom is het van cruciaal belang om het ICRF-systeem te gebruiken met antenneparameters en neutrale gasdruk die zorgen voor een snelle opbouw van het plasma in de torus en het verschijnen van de plasma-belasting voor de antenne. De tijdsvertraging tussen het activeren van de antenne en het verschijnen van het plasma voor de antenne wordt doorslagtijd genoemd (i.e. breakdown-tijd). Door de plasmabelasting in de torus vóór de antenne kan het voorwaartse vermogen van de generator in het plasma worden gedissipeerd. Als zodanig neemt het gereflecteerde vermogen dat teruggaat naar het matchingsysteem af, wat resulteert in een kleinere amplitude van de staande golf tussen het matchingssysteem en de antenne. Deze plotse daling van de antennespanning is de experimentele indicator van de doorslag. Andere experimentele indicatoren van de doorslag zijn (i) een burst in de H_α-emissie en (ii) een stijging van de plasmabelasting (plasma-geabsorbeerd RF-vermogen).

Het primaire doel van dit manuscript is het vinden van optimale parameters voor het antennesysteem (generatorvermogen, frequentie, fasering) en de neutrale gasdruk om de doorslagtijd tot een minimum te beperken en een veilige werking van het antennesysteem te verzekeren. Door de doorslagtijd te verkorten, verminderen we de tijdspanne waarin er zich hoge spanningen bevinden tussen het matchingcircuit en de antenne. We bestuderen de afhankelijkheden van de doorslagtijd van parameters zoals het generatorvermogen (elektrische veldsterkte), de RF-frequentie, de vorm van het veld, de fasering van de antenne en de neutrale gasdruk. We onderzoeken deze afhankelijkheden zowel experimenteel op fusie-relevante machines als door simulaties. We hebben een nieuwe aanpak gekozen om de ontlading-initiatie in het systeem te bestuderen gebaseerd op de ontwikkeling en het gebruik van Monte Carlo-modellen. Deze modellen hebben we voornamelijk ontwikkeld voor toroïdale machines waarin geladen deeltjes langs de toroidale veldlijnen bewegen en met het antennevacuümveld zullen interageren bij elke passage voor de antenne. Specifieke eigenschappen van ontladingsinitiatie werden onderzocht door het model aan te passen aan (i) de line-

aire geometrie van de lineaire machine IShTAr en (ii) de interne geometrie van een antenne.

Monte Carlo botsingsmodel `RFdinity1d`

De ontwikkelde modellen volgen de beweging van gyratiecentra van zowel elektronen als ionen in een smalle bundel van magnetische veldlijnen dicht bij de antenne. Deze 1D-benadering voor de beginfase van de ontlading wordt gerechtvaardigd door experimentele waarnemingen waarbij het eerste plasma zich als een toroïdaal homogene smalle bundel voordoet die zich in de nabijheid van de antenne bevindt. Na de doorslag breidt het plasma zich uit in het poloïdaal en toroïdaal homogene plasma dat nodig is voor effectieve wandconditionering. In ons eerste Monte Carlo-botsingsmodel `RFdinity1d` worden enkel elektronen in de nabijheid van de antenne versneld door de toroidale component van het elektrische veld E_z (of $E_\parallel$), dat gegenereerd wordt door de ICRF-antenne. Botsingen tussen de elektronen en neutrale atomen (waterstof of helium) worden behandeld in de drie dimensionale snelheidsruimte (v_x, v_y, v_z), waarbij v_z de parallelle snelheidscomponent is, en $v_\theta = \sqrt{v_x^2 + v_y^2}$ de component loodrecht op de toroidale magnetische veldlijnen. Het model beschrijft de cyclotrongyratie in de ruimte niet expliciet. De elektronen worden uitsluitend in de parallelle richting versneld (de richting van het magnetisch veld B_T), terwijl de loodrechte snelheid onveranderd blijft door het elektrische veld. Tijdens de botsingen in de 3D-snelheidsruimte wordt een deel van de parallelle snelheidscomponent verspreid in de loodrechte snelheid. We passen een Monte Carlo-procedure toe die voor elk elektron de weglengte tussen twee botsingen monstert. Als we de snelheid en deze weglengte kennen, kunnen we de exacte botsingstijd voor de elektronen in de simulatie schatten. Wanneer een botsing plaatsvindt, gebruiken we een tweede Monte Carlo-procedure om het botsingstype te bepalen. In ons model beschouwen we inelastische botsingen (ionisatie, excitatie, dissociatie), botsingen met elastische verstrooiing en recombinatiebotsingen. De Coulomb-botsingen tussen geladen deeltjes worden in het model in aanmerking genomen met behulp van de Takizuka-Abe-methode. We hebben echter aangetoond dat de Coulomb-botsingen alleen een rol gaan spelen bij hogere elektronendichtheden $n > 10^{15}\,\mathrm{m}^{-3}$. Vanuit onze simulaties kunnen we de evolutie van de elektronendichtheid in de loop van de tijd meten. Dit verloop komt overeen met de ionisatiesnelheid en is een indirecte meting van de doorslagtijd. Een hogere ionisatiesnelheid betekent een kortere doorslagtijd.

Het model toonde aan dat vanaf een bepaalde elektrische veldsterkte de ionisatiesnelheid scherp toeneemt van nul tot een maximale waarde. Vanaf deze maximale waarde blijft de ionisatiesnelheid bijna constant bij verder toenemende amplitude, terwijl ze afneemt met toenemende RF-frequentie. Volgens het bestaande PDM-model is de ionisatiesnelheid afhankelijk van de verhouding tussen de amplitude en frequentie van het elektrische veld. We hebben echter met ons nieuw model aangetoond dat simulaties met dezelfde verhouding maar verschillende waarden van de amplitude en frequentie van het elektrische veld zeer verschillende ionisatiesnelheid hebben. Verder duidt een drukscan in onze simulaties op een toenemende ionisatiesnelheid bij toenemende druk gegeven door $\nu_{\text{ion}} \sim \sqrt{p}$ terwijl de PDM methode een lineaire afhankelijkheid voorspelt. Dezelfde elektrische veldsterkte en drukafhankelijkheden van de

doorslagtijden als in onze simulaties werden waargenomen tijdens experimenten op TEXTOR en ASDEX-upgrade. In deze experimenten en simulaties is de ionisatiesnelheid bijna tien keer kleiner dan voorspeld door het PDM-model. Deze verschillen tonen aan dat het PDM-model een zeer ruwe benadering is voor ontladingsinitiatie door de ICRF-antennes en dat er meer geavanceerde modellen zoals de MC `RFdinity1d` nodig zijn. Ten slotte gaven onze simulaties een eerste aanwijzing over hoe de torusgrootte de ionisatiesnelheid beïnvloedt. De ionisatiesnelheid neemt af met de omtrek van de magnetische veldlijnen als $\nu_{\text{ion}} \sim C^{-1}$. Deze afhankelijkheid suggereert dat voor plasma productie met behulp van meerdere ICRF antennes in grote machines zoals ITER, deze antennes idealiter gespreid gepositioneerd worden in de torus. In werkelijkheid bevinden de ITER ICRF-antennes zich zeer dicht bij elkaar, slechts gescheiden door één poort. Niettegenstaande hebben we met onze simulaties aangetoond dat we zelfs met de grote ITER-omtrek een ontlading kunnen initiëren met één ITER ICRF-antenne.

Model upgrade naar Particle-In-Cell Monte Carlo botsingsmodel `RFdinity1d`

We hebben het Monte Carlo-botsingsmodel aangepast in een Particle-In-Cell Monte Carlo-botsingmodel `RFdinity1d`. Het nadeel van het eerste Monte Carlo-model is dat het de beweging van ionen negeert die tijdens ionisatiebotsingen zijn gecreëerd. Deze ionen hebben veel lagere snelheden dan de elektronen wat ladings-inhomogeniteiten zal creëren langs het toroidale simulatiedomein. Deze inhomogeniteiten zijn vooral van belang in de nabijheid van de antenne. Door de ladingsinhomogeniteit wordt een elektrostatisch veld gegenereerd waarvan het toroidale profiel kan worden bepaald door de vergelijking van Poisson op te lossen. Het PIC-MCC-model volgt de beweging van gyratiecentra van zowel elektronen als ionen, maar deze keer worden ze versneld door een som van twee elektrische velden: (i) het vacuüm RF elektrisch veld voor de ICRF-antenne E_z^{RF} en (ii) het zelf-gegenereerde elektrostatische veld E_z^P verkregen uit Poisson's vergelijking. De grootte van het elektrostatische veld E_z^P hangt af van de elektronendichtheid $|E_z^P| \sim n_e$. Voor een lage elektronendichtheid heeft het PIC-model een vergelijkbare elektronendichtheidsevolutie in de tijd als het eerste Monte Carlo-model zonder het elektrostatische veld E_z^P, omdat geladen deeltjes voornamelijk worden versneld door het antenneveld, $vert E_z^P| \ll |E_z^{RF}|$. Wanneer de elektrostatische veldsterkte vergelijkbaar wordt met het antenneveld zien we een verandering van de ionisatiesnelheid in de tijd. We hebben de elektronendichtheidsevolutie ingedeeld in fasen met verschillende dominante mechanismen. Elke fase wordt gemarkeerd door een andere ionisatiesnelheid en elektronenergieverdelingsfunctie (EEDF). In het Monte Carlo-model zonder het elektrostatische veld blijft de ionisatiesnelheid min of meer constant omdat de EEDF tijdens een simulatie niet significant verandert. De ionisatiesnelheid in de laatste fase van de gesimuleerde dichtheidsevolutie is in kwantitatieve overeenstemming met de ionisatiesnelheid geschat uit de toename in plasma-weerstand in het experiment op ASDEX-upgrade.

Door de plasma-geproduceerde E_z^P -component in het PIC-model op te nemen, wordt aangenomen dat de verandering van het vacuüm elektrisch veld bij toenemende plasmadichtheid consistent is opgenomen in een 1D (toroïdale) benadering. We heb-

ben aangetoond dat het RF-veld van de antenne verstoringen in de ladingsdichtheid-distributie veroorzaakt die propageren langs de magnetische veldlijnen wanneer de plasma frequentie de RF frequentie benadert $\omega_{p,e} \leq \omega_{RF}$. Deze waarneming is in goede overeenstemming met de theoretisch voorspelde plasmaoscillaties (Langmuir-plasmagolven). Deze langzame golven verhogen de energie van de laag-energetische elektronen en ionen. Dit is zichtbaar in zowel de elektronen- als de ionen-energieverdelingsfuncties en resulteert in een hogere ionisatiesnelheid. In simulaties wordt een initiële laag energetische Maxwell-energieverdeling voor elektronen eerst vervormd tot een bi-Maxwell-verdeling. Het grootste deel van de elektronen blijft hierbij laag energetisch met $T_e \approx 3\,\mathrm{eV}$ terwijl een klein deel van de elektronen ($< 1\%$) een hoog energetische Maxwell-verdeling vormt met $T_e > 1\,\mathrm{keV}$. Wanneer de toroidale plasma golven worden geëxciteerd, wordt de EEDF getransformeerd in een verdeling die afwijkt van een (bi-)Maxwell-energieverdeling. De EEDF komt echter overeen met een Kappa-verdeling. Deze lijkt op een Maxwell-verdeling bij lage energie, maar neemt af als een machtsfunctie bij de hogere energieën. Dezelfde observaties gelden voor de ionenenergieverdelingsfunctie (IEDF).

De gesimuleerde IEDF werpt een nieuw licht op de waargenomen energetische staarten in de IEDF tijdens ICWC-experimenten. NPA-metingen tonen het bestaan van energetische ionen ($\epsilon > 1\,\mathrm{keV}$) en suggereren inderdaad een Kappa-energiedistributiefunctie in plaats van een Maxwell-energieverdeling. De waarneming van Kappa-verdelingen in de simulaties en de experimenten is significant omdat wordt aangenomen dat ICWC-plasma een lage temperatuur heeft ($\approx 3 - 5\,\mathrm{eV}$). Wanneer deze NPA-gemeten distributies worden geïnterpreteerd door een Maxwell-energieverdeling, overschat deze interpretatie de temperatuur ($T > 200\,\mathrm{eV}$) van het ICWC-plasma. Door een Kappa-verdeling voor de experimentele gegevens aan te nemen verkrijgen we overeenstemming met zowel een meerderheid van ionen met een lage energie ($3 - 5\,\mathrm{eV}$) alsook met de energetische staarten die we waarnemen in de ICWC-experimenten. Voor de ICWC ontladingen op ASDEX Upgrade bij hoge magnetische veldsterkte wordt aangenomen dat de ionenpopulatie met hoge energieën voortkomt uit een resonante interactie van de ionengyratie beweging met het RF veld. Tot nu toe werd echter geen goede verklaring gegeven voor de waargenomen energetische ionenpopulatie in ontladingen met een lager magnetisch veld waarbij de resonantie koppeling veel minder sterk is. De simulaties met het PIC-model suggereren echter dat snelle ionen kunnen worden gecreëerd door de actie van plasmagolven via het parallelle elektrische veld $E_z = E_z^{RF} + E_z^P$, en reeds dit bij zeer lage elektronendichtheden $n_e > 10^{13}\,\mathrm{m}^{-3}$. Dit mechanisme zal altijd aanwezig zijn in de ICRF-ontladingen, ongeacht de toroïdale magnetische veldsterkte B_T.

Eén-elektronmodel

We hebben een theorie ontwikkeld die een beter inzicht geeft in de MCC- (en experimentele) resultaten in termen van de bewegingen van één enkel elektron. Wanneer een elektron het elektrisch veld voor de antenne nadert krijgt het ofwel energie van het antenneveld, of wordt het gereflecteerd door de ponderomotorische kracht aan de rand van het antenneveld zonder enige verandering in zijn energie (begin versus eind). Door middel van het vereenvoudigd model, waarbij de beweging wordt gesimuleerd van on-

afhankelijke en afzonderlijke elektronen en waarbij eventuele botsingen worden genegeerd, kunnen we de drempelenergie schatten waarboven het elektron zal versneld worden in de interactie met het elektrische veld of zelfs het antennegebied zal binnentreden. Deze drempelwaarde in energie is afhankelijk van de amplitude, vorm en frequentie van het elektrische veld. Uit de simulatieresultaten kon de nieuwe theorie worden afgeleid die de drempelenergie analytisch voorspelt. De theorie is voornamelijk gebaseerd op geldigheidslimieten van de reeksontwikkeling van het RF-elektrisch veld tot en met de tweede orde term. De analytisch verkregen drempelenergieën komen goed overeen met de simulatieresultaten van het één-elektronmodel. Bovendien geeft deze drempelenergie ook een indirecte indicatie van de ionisatiesnelheid die wordt waargenomen in simulaties met het volledige MCC-model `RFdinity1d`. Antenne parameters (amplitude, frequentie en vorm) die een lage drempelenergie geven, zullen resulteren in hoge ionisatiesnelheden omdat meer initiëel laag-energetische elektronen een energie boven de drempelwaarde hebben en in staat zullen zijn om versneld te worden door het antenneveld. Ten slotte verklaart deze nieuwe theorie waarom het eerste plasma in ICWC-experimenten steeds verschijnt op de radiale positie die zich het dichtst bij de antenne bevindt. Op deze radiale positie heeft het elektrische veld het steilste profiel, terwijl de toroidale gradiënt geleidelijk afneemt in radiale richting weg van de antenne.

Ontladingsinitiatie in een lineaire machine

Naast het onderzoek naar de ontladingsinitiatie door de ICRF-antennes in toroidale machines, werd het Monte Carlo-botsingsmodel `RFdinity1d` aangepast om de ontladingsinitiatie in een lineaire machine of binnen in de antenne zelf te simuleren. De simulatieresultaten werden vergeleken met experimentele observaties op de lineaire IShTAR machine. In het experiment onderzochten we de ontladingsinitiatie voor een lage en hoge RF-frequentie, respectievelijk $f = 5.22\,\mathrm{MHz}$ en $f = 42.06\,\mathrm{MHz}$. Voor $f = 5.22\,\mathrm{MHz}$ werd een homogene plasmakolom vóór de antenne gevormd. De minimale drukken waarboven het plasma kan geïnitieerd worden zijn afhankelijk van het vermogen van de generator en komen in kwalitatieve overeenstemming met de gemodelleerde voorspellingen. In experimenten met $f = 42.06\,\mathrm{MHz}$ wordt het plasma steeds in de antennedoos geproduceerd. We konden deze resultaten enkel reproduceren met simulaties door secundaire elektronenemissie aan het oppervlak van het antennemateriaal in ons model op te nemen. We hebben het effect van de secundaire elektronenemissie op de ontladingsinitiatie numeriek bestudeerd voor verschillende secundaire emissierendementen (SEY) en voor een breed gebied van elektrische veldsterktes en frequenties. Onze simulatieresultaten bevestigden dat voor de hoge frequentie ($f = 42.06\,\mathrm{MHz}$) het zeer waarschijnlijk is dat het plasma in de antennedoos wordt geïnitieerd, terwijl dit voor de lage frequentie ($f = 5.22\,\mathrm{MHz}$) zeer onwaarschijnlijk is. De simulaties geven verder aan dat voor tamelijk hoge maar realistische SEY, de secundaire elektronenemissie het dominante proces wordt voor de elektronenvermenigvuldiging en dichtheidsopbouw. De dichtheidstoename in simulaties met hoge SEY is onafhankelijk van de neutrale gasdruk, wat een zorg is voor het creëren van plasma in de antenne. Daarom is het noodzakelijk om (i) de antenne te maken uit materialen met een lage SEY, (ii) antenne-conditioneringstechnieken toe te passen

en/of (iii) de antenne op een lagere frequentie te gebruiken in plasma productie modus.

Extrapolatie naar ITER

Moderne fusie-machines met supergeleidende spoelen, zoals ITER, maken gebruik van conditioneringstechnieken voor de wandmaterialen die werken in de aanwezigheid van het toroïdale magnetische veld. ITER voorziet het gebruik van de Ion-Cyclotron-Wall-Conditioning (ICWC) techniek waarbij de conditioneringsontlading geïnitieerd word met behulp van ICRF-antennes. In dit manuscript bestuderen we de parametrische afhankelijkheden van ontladingsinitiatie door de ICRF-antenne. Wanneer deze afhankelijkheden gekend zijn kunnen we de ontladingsinitiatie op ITER optimaliseren. Dit komt neer op het minimaliseren van de elektrische spanningen in het ICRF systeem en de tijdspanne waarin hoge spanningen aanwezig zullen zijn. Als de ICRF-antenne gebruikt wordt met parameters die resulteren in lange plasma-doorslagtijden of te hoge spanningen bestaat het risico van doorslag in de transmissielijnen of de antenne zelf, met mogelijke beschadigingen als gevolg.

De ITER ICRF-antenne werkt in het bereik van $40 - 55\,\mathrm{MHz}$. Dit frequentiebereik is iets hoger dan de frequenties die op dit moment typisch gebruikt worden in ICRF-systemen op tokamaks en stellarators. Op basis van onze simulaties volgen hieruit verschillende potentiële nadelen voor ontladingsinitiatie met behulp van ICRF-antennes. Ten eerste gaven onze simulaties aan dat de ionisatiesnelheid afneemt met afnemende antennefrequentie. Hierdoor zou men dus de voorkeur moeten geven aan het werken met $f = 40\,\mathrm{MHz}$ tijdens ICWC op ITER. Ten tweede wezen simulaties in de antenne erop dat bij hogere frequenties het waarschijnlijker is dat het plasma in de antennedoos gecreëerd wordt als gevolg van secundaire elektronenemissie. We kunnen niet precies weten wat het secundaire elektronenemissierendement (SEY) is van de ITER-antenne opeervlakken. Maar we kunnen de kans op plasmaproductie in de antenne verminderen door ook hier met de laagst mogelijke frequentie te werken met de ITER-antenne ($f = 40\,\mathrm{MHz}$), en de SEY te verlagen door de antenne te conditioneren.

Verder vonden we dat de ionisatiesnelheid in simulaties afhangt van de vierkantswortel van de neutrale gasdruk, $\nu_{\mathrm{ion}} \sim \sqrt{p}$, voor het drukbereik in ICWC-experimenten $p < 5 \cdot 10^{-2}\,\mathrm{Pa}$. In simulaties met het vacuümantenneveld van ITER konden we het plasma efficiënt initiëren met een doorslagtijd van $\approx 2\,\mathrm{ms}$ bij $p = 10^{-2}\,\mathrm{Pa}$. We kunnen geen verdere substantiële afname van de doorslagtijd verkrijgen door bij hogere drukken te werken vanwege de vierkantswortelafhankelijkheid. Bovendien zal bij de lagere drukniveaus $p \leq 10^{-2}\,\mathrm{Pa}$ ook de kans verminderen dat het plasma in de antenne of zelfs in de transmissielijnen wordt gecreëerd.

Met betrekking tot het optimale vermogensniveau op de ITER ICRF-antennes voor plasma productie, vonden we in onze simulaties dat boven een specifiek generatorvermogen de doorslagtijd niet meer significant verbeterd. Onze simulaties gaven aan dat voor een relatief laag generatorvermogen van $P = 0.5\,\mathrm{MW}$ het plasma binnen de $2\,\mathrm{ms}$ gecreëerd wordt. Gebruik van ICWC op ITER met een hoger antennevermogen dan $0.5\,\mathrm{MW}$ heeft enkel als gevolg dat de spanning tussen de antenne en het matchingssysteem hoger zal zijn zodat de kans op schade bij doorslag in de transmissielijnen vergroot. Om de wandconditioneringsefficiëntie te verbeteren kan het

vermogen verhoogd worden zodra het plasma in de torus geïnitieerd is en de plasmabelasting verschijnt.

Ten slotte hebben we in onze simulaties gemeten dat de ionisatiesnelheid afneemt met een toenemende omtrek, $\nu_{\text{ion}} \sim C^{-1}$. Daarom zou het optimaal zijn om de ITER ICRF-antennes toroïdaal gespreid te positioneren. In werkelijkheid bevinden de ITER ICRF-antennes zich in naburige poorten. Onze simulaties voor ITER beschouwden slechts één ICRF-antenne. Hieruit blijkt dat de lange ITER-omtrek geen hindernis is voor ICRF plasma productie in ITER.

Nieuwe inzichten door dit doctoraatsonderzoek

Tijdens mijn doctoraat onderzocht ik ontladingsinitiatie met behulp van ICRF-antennes in het kader van de ontwikkeling van de wandconditioneringstechniek ICWC voor fusiemachines. Het initiële proces van het produceren van een plasmaontlading door een ICRF-antenne was nog steeds niet goed begrepen. Daarom heb ik nieuwe Monte Carlo-modellen ontwikkeld om dit proces te bestuderen. Deze modellen volgden rigoureus de bewegingen van geladen deeltjes langs de magnetische veldlijnen in de torus. Eerder ontwikkelde modellen gingen ervan uit dat het plasma in de nabijheid van de antenne wordt geïnitieerd en dat elektronen die het antennegebied verlaten, niet verder bijdragen aan de ontladingsinitiatie. Mijn modellen maken deze aannames niet. Ze toonden hierdoor aan dat de meeste ionisatiebotsingen buiten het antennegebied plaatsvinden en dat ook de periodiciteit van de torus een belangrijke rol heeft in ontladingsinitiatie: elektronen die het antenne gebied verlaten kunnen dit gebied opnieuw betreden nadat ze rond de torus zijn gereisd. Ten eerste heb ik het MCC-model textttt RFdinity1d gebruikt om de afhankelijkheden van de ionisatiesnelheden op de antenneparameters (elektrische veldamplitude, frequentie) en neutrale gasdruk te bestuderen. Deze uitgebreide parameterscans werden vergeleken met de experimentele observaties op TEXTOR en ASDEX Upgrade en gepresenteerd tijdens de 41e EPS-conferentie over plasmafysica in Berlijn:
[1] M. Tripsky et al. Monte Carlo simulation of ICRF discharge initiation at $\omega_{LHR} < \omega$. In European Conference Abstracts (ECA), volume 38.F., Berlin, Germany, June 2014.

Ik heb ook voor de eerste keer de mogelijkheid aangetoond van ontladingsinitiatie in ITER met behulp van het elektrische veld van de ITER ICRF-antenne. De resultaten van deze simulaties werden gepresenteerd op de 21ste Topical Conference on Radiofrequency Power in Plasmas in Lake Arrowhead, Californië:
[2] M. Tripsky et al. Monte Carlo simulation of ICRF discharge initiation in ITER. In AIP Conference Proceedings, volume 1689, page 060009, California, USA, 2015.

Vervolgens voerden we een gedetailleerd experimenteel onderzoek uit naar de ontladinginitiatie door de ICRF-antenne in URAGAN-3M. Ik heb deze experimentele bevindingen samengevat en gepresenteerd tijdens de 43e EPS-conferentie over plasmafysica in Leuven:
[3] M. Tripsky et al. Investigation of discharge initiation by ICRF antenna on URAGAN 3-M. ECA, 40A(P2.052), 2016.

Ik heb een nieuw Particle-in-Cell Monte Carlo Collision-model texttt RFdinit1d ontwikkeld. Dit model onthulde nieuwe natuurkundeverschijnselen die een rol spelen bij ontladingsinitiatie door ICRF-antennes. Bijvoorbeeld de waarneming van de Langmuirgolven in het plasmaproductieproces of de vorming van een Kappa-energiedistributie. Ik publiceerde de bevindingen van het PIC-MCC-model texttt RFdinit1d in Nuclear Fusion:
[4] M. Tripsky et al. A PIC-MCC code RFdinity1d for simulation of discharge initiation by ICRF antenna. Nucl. Fusion, 57:126043, 2017.

Ik voerde voor de eerste keer een gedetailleerde studie uit van ontladingsinitiatie in de antenne, zowel numeriek met behulp van MCC-model texttt RFdinity1d en experimenteel op de lineaire machine IShTAR uitgerust met een single-strap ICRF-antenne. Tijdens mijn analyse ontdekte ik de belangrijke rol van secundaire elektronenemissie bij het creëren van een ontlading in de antenne en het mogelijke gevaar van werken met een hoge RF-frequentie. De experimentele en simulatieresultaten werden gepubliceerd en gepresenteerd tijdens de 22nd Topical Conference on Radiofrequency Power in Plasmas in Aix-en-Provence.:
[5] M. Tripsky et al. Discharge initiation by ICRF antenna in IShTAR. EPJ Web of Conferences, 157:03056, May 30 - June 2 2017.

Tot slot hebben we samen met mijn supervisor Dr. Wauters een nieuwe en geavanceerde analytische beschrijving van elektronenversnelling ontwikkeld in ICRF-ontlading initiatie. Deze analytische beschrijving kan worden gebruikt als de eerste indicator voor het vinden van optimale parameters om een ICRF-ontlading te initiëren. Deze theorie werd geïntroduceerd tijdens de 22nd Topical Conference on Radiofrequency Power in Plasmas in Aix-en-Provence.:
[6] T.Wauters, M.Tripsky et al. Advanced ponderomotive description of electron acceleration in ICRF discharge initiation. EPJ Web of Conferences, 157:03064, May 30 - June 2 2017.

English summary

Introduction

One of the global challenges we are facing at this moment is an increase in the level of the greenhouse gases, i.e., CO_2 in our atmosphere. The worldwide scientific community reported that these greenhouse gases are the most prominent contributors to the increase in the temperature level on our planet. The excessive amount of the greenhouse gases in our atmosphere comes from the burning of fossil fuels in our power stations and industry. Nowadays, around 81% of the energy sources on the planet use fossil fuels. Therefore, it is crucial to replace our fossil fuel power stations with energy sources which do not release CO_2 into our atmosphere. The most efficient and CO_2-free power stations are based on nuclear fission. These power stations can produce a huge amount of power, but the public has a very negative opinion concerning the nuclear fission due to both the problem of nuclear waste storage and the safety of a nuclear power plant. Currently and especially in Europe, we are increasing our use of renewable sources of energy, i.e., wind turbines and solar panels as another CO_2-free source of energy. Unfortunately, we will have to build a lot of them to cover our total energy consumption. Furthermore, renewable sources of energy depend on the weather conditions and their electricity production is not continuous in time. Therefore, there is an urgent need for a new method of energy production that produce a considerable amount of energy, does not produce greenhouse gases, and is reliable and safe. The most promising method is using energy from magnetic fusion. At this moment, the largest tokamak device in construction is located in the south of France near the CEA research center in Cadarache. This device called ITER is the international project run by seven member entities: the European Union, India, Japan, China, Russia, South Korea and the USA. ITER will be the transition from experimental devices (JET, ASDEX Upgrade, TORE SUPRA, TEXTOR) to the first fusion device producing net energy. ITER is designed to demonstrate that we can produce with nuclear fusion more energy than it consumes.

Nuclear fusion takes place on our Sun where hydrogen nuclei merge to finally produce helium and in that process release vast amounts of energy. If we want to use nuclear fusion on our planet, we need to find a way to overcome the repulsive Coulomb force between charged nuclei, which requires a lot of energy on a large scale. In thermonuclear fusion, a charged fuel gas, plasma, with a high density is heated to fusion-relevant temperatures by externally applied heating power and only a fraction of the fuel will have enough energy to break the Coulomb barrier. Nowadays, research on fusion energy is focused on the D-T reaction. These hydrogen isotopes produce after merging a helium nucleus which is not radioactive and a neutron with a combined energy of $17.6\,\mathrm{MeV}$: $D + T \rightarrow {}^4He\,(3.5\,\mathrm{MeV}) + n\,(14.1\,\mathrm{MeV})$. One

speaks of a self-sustaining fusion reaction (ignition) at the moment that the plasma heats itself through fusion reactions (helium of DT reaction) and the external heating can be switched off. To reach ignition the plasma must have parameters overcoming the Lawson criterion (or the triple product): $n_e T \tau_E \geq 3 \cdot 10^{21} \mathrm{m}^{-3} \mathrm{keVs}$, where n_e is the plasma electron density, T the plasma temperature and τ_E the energy confinement time. Today's research adopts many approaches to reach the appropriate triple product value. However, the most promising concept and also related to this manuscript aims at achieving the ignition condition by confining the plasma in a donut-shaped container created by magnetic fields. These toroidal devices are divided into two types: the tokamak and the stellarator. The envisaged values of the triple product for tokamaks are $T \approx 10 - 20\,\mathrm{keV}$, $n_e \approx 10^{20}\,\mathrm{m}^{-3}$ and $\tau_E \approx 3 - 5\,\mathrm{s}$.

The magnetic field of the tokamak device consists of two components: toroidal (stronger) and poloidal magnetic fields. These two magnetic fields create together helicoidal magnetic field lines on which the particles are confined. The toroidal magnetic field is produced by a series of current coils. These coils encircle the plasma poloidally. In a tokamak a primary transformer circuit induces a current flowing toroidally in the plasma producing the poloidal magnetic field component. Stellarators use a different approach to create the magnetic field to confine the plasma by using uniquely shaped and designed poloidal coils. These coils then directly generate the helical magnetic field to confine the plasma. In this manuscript, we present experiments carried out on tokamaks TEXTOR (IPP-Jüllich, Germany) and ASDEX Upgrade (IPP-Garching, Germany), stellarator Uragan 3-M (Kharkiv, Ukraine) and also of the linear device IShTAR (IPP-Garching, Germany).

One of the difficulties in achieving the necessary conditions for fusion plasmas is the problem of controlling the consequences of the interaction of the plasma with the wall materials that face the plasma, namely impurity production, hydrogen fueling of the plasma by the wall and tritium (radioactive) retention in the wall. There exist several Wall Conditioning methods to improve vacuum conditions and to control recycling. The most important are baking, glow discharge conditioning (GDC) and Ion or Electron cyclotron wall conditioning (ICWC and ECWC). Although all these listed methods demonstrated their effectiveness as wall conditioning technique, important restrictions exist for the usage of the first two of the methods in ITER or future fusion devices. For example, GDC cannot be applied in the presence magnetic fields. ITER will have superconducting toroidal field coils for producing the toroidal magnetic field. This field is quasi permanently present as the superconducting coils cannot be turned off quickly nor frequently when e.g. wall conditioning is needed. Since both ICWC and ECWC need the magnetic field to be present to work, these methods are considered as wall conditioning techniques for ITER and W7-X.

PhD aims

In this manuscript, we study discharge initiation by ICRF antenna in the frame of the development of ICWC for ITER. Although ICWC had been successfully tested on all tokamaks with ICRF antennas, the initial process of producing a plasma by the ICRF antenna was still not well understood. The ICRF antennas are designed to couple radio-frequency power into already developed plasma by exciting Fast-Waves, whe-

reas during the ICWC experiments the ICRF antennas are powered first in the vacuum when no plasma loading nor plasma waves exist. The power is fully dissipated in resistive losses along the transmission lines, matching system and antenna surroundings. As a result, even when matching the antenna to the vacuum load, almost all forward antenna power arriving at the antenna is reflected back toward the matching system. These forward and reflected waves between the antenna strap and matching system create a standing wave with significantly higher amplitude than that of the forward power between the generator and matching system. The presence of these high voltages in the transmission lines between the matching system and antenna strap introduces a potentially dangerous situation of arcing inside the transmission lines, on the antenna or of other RF components which can potentially bring damage to the ICRF system. It is crucial to employ ICRF antenna parameters and neutral gas pressure to assure swift density build-up in front of the antenna and appearance of plasma loading. The time delay between the pulse start and the first appearance of plasma in front of the antenna is called breakdown time. When plasma is created in front of the antenna, a fraction of power from a generator can be dissipated in the plasma. As such the power reflected back towards the matching system decreases resulting in a smaller amplitude of the standing wave between the matching system and antenna strap. This drop in the antenna voltage is the experimental indicator of the breakdown. Other experimental signs of the breakdown are (i) a burst in the H_α emission and (ii) a rise of the plasma load (plasma absorbed RF power).

The primary goal of this manuscript is to study discharge initiation by ICRF antennas and its dependency on the parameters as the generator power (electric field strength), RF frequency, shape of the field, phasing of the antenna straps and neutral gas pressure in the vessel. Knowing these dependencies, we can propose optimal parameters for a safe ICRF plasma start-up during the ICWC operation with the shortest possible breakdown time. By reducing the breakdown time, we decrease the time where high voltages exist between the matching circuit and antenna strap. We investigate these dependencies both experimentally on fusion relevant devices and by simulations. We have adopted a new approach to study the discharge initiation in the vessel based on the development and usage of Monte Carlo models. These models were used primarily for toroidal devices in which charged particles, accelerated by the antenna vacuum field in front of the straps, encircle around the torus to again interact with the antenna. Specific features of discharge initiation were investigated by adapting the model to the linear geometry of the linear device IShTAr and the inside of an antenna box.

Monte Carlo collision model `RFdinity1d`

The developed models follow the motion of guiding centers of both electrons and ions in a narrow bundle of magnetic field lines close to the antenna straps. This 1D approximation for the initial phase of the discharge is justified by experimental observations where the first plasma is a toroidally homogeneous narrow bundle located in the antenna strap vicinity. After the breakdown, the plasma expands into the poloidally and toroidally homogeneous plasma that is required for the effective wall conditioning. In our first Monte Carlo collision model `RFdinity1d` only electrons are accelerated in

the antenna vicinity by the toroidal component of the electric field E_z (or $E_\parallel$), which is generated by the ICRF antenna. Collisions between the electrons and neutral atoms (hydrogen or helium) are treated in the 3D velocity space $(v_x,\, v_y,\, v_z)$, where v_z is the parallel velocity component, and $v_\theta = \sqrt{v_x^2 + v_y^2}$ the perpendicular velocity component. The model does not resolve the cyclotron gyration in space. The electrons are accelerated exclusively in the parallel direction (direction of the magnetic field B_T) while the perpendicular velocity remains unchanged by the electric field. During the collisions in the 3D velocity space, part of their parallel velocity component is scattered into the perpendicular velocity. We apply the Monte Carlo procedure to sample path length between two collisions for each electron in a simulation. Knowing the velocity and this path length, we can estimate the exact collision time for the electrons. When a collision occurs, we use another Monte Carlo procedure to decide the collision type. In our model, we include inelastic collisions (ionization, excitation, dissociation), elastic scattering collision and recombination collisions. The Coulomb collisions between charged particles are taken into account in the model using the Takizuka-Abe method. However, we have demonstrated that the Coulomb collisions start to play a role only for higher electron densities $n > 10^{15}\,\mathrm{m}^{-3}$. From our simulations, we can measure the electron density evolution over time. This increase in time corresponds to the ionization rate, and it is an indirect measurement of the breakdown time. A higher ionization rate means a shorter breakdown time due to a faster electron density increase in time.

The electric amplitude scan with this model demonstrated that above the certain amplitude threshold, the ionization rate increases sharply from zero until reaching a maximum value. After arriving at this maximum value, the ionization rate stays nearly constant with further increasing amplitude, while it decreases with increasing RF frequency. According to the PDM-model (Ponderomotive model), the ionization rate should be dependent on the ratio between the electric field amplitude and frequency. However, we showed with this model that simulations with the same ratio but different values of the electric field amplitude and frequency have very different ionization rates. The pressure scan in our simulations indicates increasing ionization rate with increasing pressure given by $\nu_{ion} \sim \sqrt{p}$ whereas the PDMI-model (Ponderomotive-Ionization model) predicts a linear dependency. Same electric field and pressure tendencies of the breakdown times than in our simulations were also detected during experiments on TEXTOR and ASDEX Upgrade. In these experiment and in our simulation we measure almost ten times smaller ionization rates than predicted by the PDMI-model. These discrepancies demonstrate that the PDM and PDMI-models are very crude approximations of the discharge initiation by the ICRF antennas and more sophisticated models like the MC `RFdinity1d` are needed.

Finally, our simulations indicated that the ionization rate decreases with the circumference length as $\nu_{ion} \sim C^{-1}$. The PDM-model does not include this circumference length dependency. Our model presents first indications on how the torus size influences the ionization rate. This dependence can help us to understand better influence of the toroidal positioning of the ICRF antennas in large fusion devices like ITER. Our simulations suggest that the optimal toroidal locations for two ITER ICRF antennas are at the toroidal location opposite to that of each other. In reality, the ITER ICRF antennas are located very close to each other separated only by one port. Nevertheless, we could demonstrate with our simulations that even with the large ITER

circumference length we can initiate the discharge by the ITER ICRF system.

Model upgrade to Particle-In-Cell Monte Carlo collision model `RFdinity1d`

We have modified the Monte Carlo collision model into a Particle-In-Cell Monte Carlo collision model (PIC-MCC). The disadvantage of the first Monte Carlo model is that it neglects the motion of ions created during ionization collisions. These ions have much lower velocities than electrons, and thus it will create charge inhomogeneities along the toroidal domain of a simulation. These inhomogeneities are especially significant in the antenna straps vicinity. Due to this charge inhomogeneity, an electrostatic field is generated, and its toroidal profile can be estimated by solving Poisson's equation. The PIC-MCC model follows the motion of guiding centers of both electrons and ions, but this time they are accelerated by a sum of two electric fields: (i) the vacuum RF electric field in front of the ICRF antenna E_z^{RF} and (ii) the self-generated electrostatic field E_z^P obtained from Poisson's equation. The magnitude of the electrostatic field E_z^P depends on the electron density $|E_z^P| \sim n_e$. For low electron density, the PIC model has a similar electron density evolution in time as the Monte Carlo model without the electrostatic field E_z^P, because charged particles are accelerated mostly only by the antenna field, $|E_z^P| \ll |E_z^{RF}|$. When the electrostatic field magnitude becomes comparable to the antenna field, we observe a change in the electron density evolution in time. We have divided the electron density evolution into phases with different dominating mechanisms. Each phase is marked by a different ionization rate and electron energy distribution function (EEDF). In the Monte Carlo model without the electrostatic field, the ionization rate stays more or less constant because the EEDF does not change significantly during a simulation. The ionization rate in the last phase of the density evolution simulated by our PIC model is in quantitative agreement with the ionization rate predicted from the fitting of the plasma resistance increase in the experiment on ASDEX Upgrade.

By including the plasma produced E_z^P component in the PIC model, the modification of the vacuum electric field due to the presence of a substantial plasma density is included self-consistently in a 1D (toroidal) approach. We have demonstrated that upon approaching, in the antenna vicinity, an electron density such that $\omega_{p,e} \leq \omega_{RF}$, the perturbations created by the RF field in front of the antenna, propagate away from the antenna region. This observation is in good agreement with the theoretically predicted plasma oscillations for a case with the RF frequency close to the electron plasma frequency (Langmuir plasma waves). These Slow Waves propagating in the toroidal direction increase the energy of low energetic electrons and ions and the ionization rate. Furthermore, due to the SW excitation, we detected a transition in the Electron and Ion energy distribution functions. In simulations, the initial low energetic Maxwell energy distribution for electrons is deformed into a superposition of two Maxwell distributions. The majority of electrons stays low energetic with $T_e \approx 3\,\mathrm{eV}$ while a small fraction of electrons ($< 1\%$) form a high energetic Maxwell distribution with $T_e > 1\,\mathrm{keV}$. When the SW are excited, the EEDF is transformed into a distribution that diverges from a Maxwell energy distribution. This EEDF corresponds to a Kappa distribution, which resembles a Maxwell distribution at low energy but falls off as a

power law at higher energies. This transition also happens to IEDF.

The simulated ion energy distributions shed new light on the observed energetic ion tails in ICWC experiments. These experiments with the NPA measurements show the existence of energetic ions ($\epsilon > 1\,\mathrm{keV}$) and suggest furthermore also a Kappa energy distribution function rather than a Maxwell energy distribution. The observation of Kappa distributions in the simulations and the experiments is significant because it is considered that ICWC plasma is low temperature ($\approx 3 - 5\,\mathrm{eV}$). When these NPA measured distributions are interpreted by a Maxwell energy distribution, this interpretation overestimates the plasma temperature ($T > 200\,\mathrm{eV}$) in the ICWC experiments. Whereas by assuming a Kappa distribution for the experimental data, we obtain agreement with a majority of ions having a low energy ($3 - 5\,\mathrm{eV}$) and also having the energetic tails that we observe in the ICWC experiments. Finally, the discharges on ASDEX Upgrade with the high magnetic field show a significant ion population at high energies supposedly caused by an acceleration of the ions at the Ion Cyclotron Resonance or its harmonics. However, until now no proper explanation was given for the fast ion population observed in discharges with the low magnetic field. The present modeling of ICRF discharge initiation with the PIC model suggests that these fast ions are already created at low electron density $n_e > 10^{13}\,\mathrm{m}^{-3}$ by the action of plasma waves via the parallel electric field $E_z = E_z^{RF} + E_z^P$. Furthermore, these mechanisms are always present in the ICRF discharges regardless of the applied toroidal magnetic field B_T.

Single electron model

We have developed a theory that provides a better understanding of the MCC (and experimental) results in terms of single electron motions. When an electron approaches the antenna field, it either gains energy from the antenna field, or it is reflected by the ponderomotive force without any change in its energy (initial vs. final). By means of a simplified model, simulating the motion of independent single electrons that approach the antenna electric field while neglecting any collisions, we can estimate the threshold energy above which the electron will be accelerated at the field edge or even enter into the antenna area. This threshold energy depends on the electric field amplitude, shape and frequency. From the simulation results a new theory could be derived to predict the threshold energy analytically based mainly on validity limits of the series expansion of the RF electric field, retaining up to the second order term. The analytically obtained threshold energies are in good agreement with the simulation results obtained by the single electron model. Furthermore, this threshold energy is also an indirect measurement of the ionization rate observed in our simulations with the full `RFdinity1d` MCC model. Antenna parameters (amplitude of the antenna RF electric field, its shape and frequency) that give a low threshold energy will result in high ionization rates because more initial low energetic electrons have energy above this threshold energy and will be able to gain additional energy from the antenna field. Finally, this developed theory using the single electron model explains why the first plasma during ICWC experiments appears always at the radial position closest to the antenna straps. At this radial position, the electric field has the steepest profile, whereas when moving radially further the vacuum toroidal field becomes

smoother.

Discharge initiation in linear device

In addition to the investigation of the discharge initiation by the ICRF antennas in toroidal devices, the Monte Carlo collision model `RFdinity1d` was modified to simulate the discharge initiation in front of the antenna in a linear device or inside the antenna box. The simulation results were compared with experimental observations on the IShTAR linear device equipped with one strap antenna. In the experiment, we investigated the discharge initiation for low and high RF frequency, resp. $f = 5.22\,\mathrm{MHz}$ and $f = 42.06\,\mathrm{MHz}$. For $f = 5.22\,\mathrm{MHz}$ the homogeneous plasma column in front of the antenna was formed. The minimum pressures above which the plasma was created depends on the generator power and are in qualitative agreement with the modeling predictions. While for experiments at $f = 42.06\,\mathrm{MHz}$, the plasma is always also created in the antenna box. We could reproduce these results in our simulations only after including the secondary electron emission into our model. We had studied the effect of the secondary electron emission on the discharge initiation with the model for different yields of the secondary electron emission, and for varying ratios between the electric field amplitude and frequency. Our simulation results indeed confirmed that for the high frequency ($f = 42.06\,\mathrm{MHz}$) it is very likely that the plasma is initiated inside the antenna box. Whereas for the low frequency ($f = 5.22\,\mathrm{MHz}$), it is very unlikely that the plasma is created inside the antenna box. The simulations further indicate that for rather high but realistic SEY, the secondary electron emission becomes the dominant process for the electron multiplication and density build-up. The density increase in simulations with the high SEY is independent of the neutral gas pressure which poses a concern for the plasma creation in the antenna box. Therefore, it is necessary to construct the antenna box using materials with already low SEY, perform antenna conditioning, or operating the antenna at a lower frequency.

Extrapolation to ITER

We have stated that future fusion devices with the superconducting coils, e.g., ITER, have to rely on wall conditioning techniques which can operate in the presence of the toroidal magnetic field. Ion-Cyclotron-Wall-Conditioning operates in the presence of the magnetic field and initiates the discharge used for wall conditioning by applying power from ICRF antennas. In this manuscript, we were studying the parametric dependencies of this discharge initiation by ICRF antenna. By knowing these dependencies, we can optimize the discharge initiation on ITER such that we can minimize time with high voltages on ITER antenna straps or inside the transmission lines. Operating the ICRF antenna at parameters with long breakdown times, or too high voltages, we risk damaging the antenna system by arcing in the transmission lines or the antenna box.

The ITER ICRF antenna will operate in the range of $40 - 55\,\mathrm{MHz}$. This frequency range is slightly higher than the frequencies ranges currently used in ICRF systems on tokamaks and stellarators. Based on our simulations this frequency range presents several potential disadvantages during the discharge initiation using ICRF antennas.

First, our simulations indicated that the ionization rate decreases with increasing antenna frequency. Thus, it may be preferred to operate with $f = 40\,\mathrm{MHz}$ during ICWC experiments on ITER. Secondly, simulations inside the antenna box indicated that at higher frequencies it is more probable to create the plasma inside the antenna box independently on the pressure due to the secondary electron emission. We will not know precisely the secondary electron emission yield in the ITER antenna box, but we can reduce the chance of creating the plasma inside the antenna box by operating at the lowest possible frequency with ITER antenna ($f = 40\,\mathrm{MHz}$).

Furthermore, we found that the ionization rate in simulations depends on the square root of the neutral gas pressure, $\nu_{\mathrm{ion}} \sim \sqrt{p}$, for the pressure range in ICWC experiments $p < 5 \cdot 10^{-2}\,\mathrm{Pa}$. In simulations with the ITER vacuum antenna field, we could efficiently initiate the plasma at $p = 10^{-2}\,\mathrm{Pa}$ with the breakdown time around $\approx 2\,\mathrm{ms}$. We will not gain substantial decrease in the breakdown time when operating at higher pressures due to the square root dependence on the pressure. Therefore, we propose that it will be sufficient to initiate ICWC experiments with pressure below $p \leq 10^{-2}\,\mathrm{Pa}$. Additionally, this lower pressure level will also decrease the probability of creating the plasma inside the antenna box or even in the transmission lines.

Concerning the optimal power level on the ITER ICRF antennas for plasma production, we found in our simulations that above a specific magnitude of the generator power the breakdown time saturates. The breakdown time does not further decrease upon increasing power. Our simulations indicated that already relatively moderate generator power of $P = 0.5\,\mathrm{MW}$ creates the plasma within $2\,\mathrm{ms}$. Operating the ICWC on ITER with higher antenna power than $0.5\,\mathrm{MW}$ will only increase the voltage between the antenna straps and matching system and potentially increase a chance of arcing in the transmission lines. After breakdown, when a plasma load appears, the power may be increased to enhance wall conditioning efficiency.

Finally, we found in our simulations that the ionization rate decreases with the increasing circumference length, $\nu_{\mathrm{ion}} \sim C^{-1}$. Therefore, it would be optimal to have the ITER ICRF antennas at the toroidal location opposite to that of each other. Unfortunately, the ITER ICRF antennas are located next to each other separated only by one port. However, our simulations for ITER were launched with only one ICRF antenna, and the long ITER circumference length was not a hurdle to initiate the plasma by the ICRF antenna. This circumference length dependence will be of use to optimize the toroidal locations of ICRF antennas the future machines.

Main findings and its specific contribution of the current state of knowledge

During my Ph.D. research, I focused on summarizing our understanding of discharge initiation by the ICRF antennas in the frame of the development of ICWC on fusion machines. This initial process of producing a plasma by the ICRF antenna was still not well understood. Therefore, I have developed new Monte Carlo models to study this process. These models rigorously followed the motions of charged particles along the magnetic field line around the torus. Previously developed models assumed that the plasma is first initiated in front of the antenna and electrons leaving the antenna region do not contribute anymore in the discharge initiation process. My models do

not make any of these assumptions. They showed that many of ionization collisions occur outside of the antenna region and electrons can be reaccelerated in the antenna region after traveling around the torus.

First, I have used the MCC-model `RFdinity1d` to study dependencies of the ionization rates on the antenna parameters (electric field amplitude, frequency) and neutral gas pressure. These comprehensive parameter scans were compared with the experimental observations on TEXTOR and ASDEX Upgrade and presented at 41st EPS Conference on Plasma Physics in Berlin:
[1] M. Tripsky et al. Monte Carlo simulation of ICRF discharge initiation at $\omega_{LHR} < \omega$. In European Conference Abstracts (ECA), volume 38.F., Berlin, Germany, June 2014.

I also for the first time demonstrated the possibility of discharge initiation in ITER using the electric field of the ITER ICRF antenna. The results of these simulations were presented at 21st Topical Conference on Radiofrequency Power in Plasmas at Lake Arrowhead, California:
[2] M. Tripsky et al. Monte Carlo simulation of ICRF discharge initiation in ITER. In AIP Conference Proceedings, volume 1689, page 060009, California, USA, 2015.

Then, we performed a detailed experimental study of discharge initiation by the ICRF antenna in URAGAN-3M. I have summarized these experimental findings and presented at 43rd EPS Conference on Plasma Physics in Leuven:
[3] M. Tripsky et al. Investigation of discharge initiation by ICRF antenna on URAGAN 3-M. ECA, 40A(P2.052), 2016.

I developed a new Particle-In-Cell Monte Carlo Collision model `RFdinit1d`. This model revealed new physics phenomena playing a role in discharge initiation by ICRF antennas. For example, the observation of the Langmuir waves in the plasma production process, or the formation of a Kappa energy distribution. I published the findings of the PIC-MCC model `RFdinit1d` in the Nuclear Fusion Journal:
[4] M. Tripsky et al. A PIC-MCC code RFdinity1d for simulation of discharge initiation by ICRF antenna. Nucl. Fusion, 57:126043, 2017.

I performed for the first time detailed study of discharge initiation inside the antenna box both numerically using MCC-model `RFdinity1d` and experimentally on the linear device IShTAR with one strap ICRF antenna. During my analysis, I discovered important role of the Secondary Electron Emission during discharge initiation inside the antenna box and possible danger of operating at high RF frequency. The experimental and simulation results were published and presented at 22nd Topical Conference on Radiofrequency Power in Plasmas in Aix-en-Provence:
[5] M. Tripsky et al. Discharge initiation by ICRF antenna in IShTAR. EPJ Web of Conferences, 157:03056, May 30 - June 2 2017.

Finally, together with my supervisor Dr. Wauters, we have developed a new and advanced analytical description of electron acceleration in the ICRF discharge initiation. This analytical description can be used as the first estimator for optimal parameters to

initiate ICRF discharge efficiently. This theory was introduced at 22nd Topical Conference on Radiofrequency Power in Plasmas in Aix-en-Provence:
[6] T.Wauters, M.Tripsky et al. Advanced ponderomotive description of electron acceleration in ICRF discharge initiation. EPJ Web of Conferences, 157:03064, May 30 - June 2 2017.

1 Introduction

The growing tendency of energy consumption in the world forces us to find new possible sources of the energy and to optimize their use most efficiently. Nowadays, fossil fuels are still the most important energy source on the planet: 81% (oil 31.3%, coal 28.6%, and natural gas 21.2%), while only 4.8% belongs to nuclear and 13.8% of other energy sources (hydro, peat, solar, wind, geothermal power, etc.) [1, 2]. Although the members of OECD are decreasing their use of fossil fuels and increasing their use of nuclear and renewable sources of energy, it will not change the status of fossil fuels as the dominant energy source on the planet. This dependency on fossil fuels will be problematic in future, as illustrated by the global fuel reserves shown in Table 1.1. However, the biggest problem is that using fossil fuels has the negative impact on climate. The electricity production by nuclear fission is of increasing importance. With the breeder technology, we could extend the fuels time reserve for thousands of years. However, the public has a very negative opinion concerning the nuclear fission both due to the problem with a nuclear waste storage or due to the safety of a nuclear power plant.

1.1 Fusion power

There is an urgent need for new methods of energy production. One possibility is using reverse action to fission, **fusion**. Fig. 1.1(a) shows the binding energy per a nucleon for different elements. The binding energy represents the minimum energy that would be required to take apart the nucleus of an atom into its component parts [3]. The curve has maximum around iron (most stable isotope). The products of nuclear reactions (fusion and fission) have different binding energies than their reactants. Thus, nuclear energy can be released in the fission of heavy particles (e.g. Uranium) into two or

Fuel	Reserve	Time Reserve (years)
Liquids	$1.4 \cdot 10^{12}$ Barrels	40-50
Gas	$6.6 \cdot 10^{15}$ Cubic Feet	50-60
Coal	$9.1 \cdot 10^{12}$ Tons	110-120
Uranium[1]	$5.4 \cdot 10^{6}$ Tons	230

Table 1.1: The global fuel reserves at the current rate of consumption [1, 2].

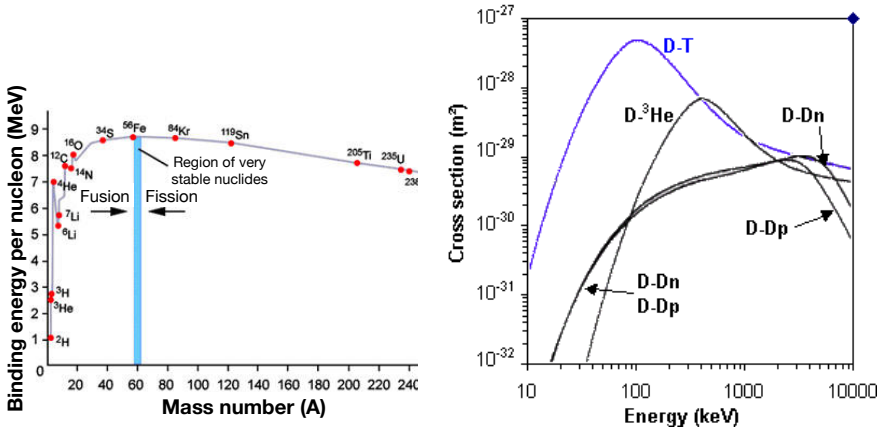

(a) (b)

Figure 1.1: (a) The binding energy for different elements with regions of nuclear fusion and fission [6], (b) Cross section for the reactions DD, DT and DHe^3. The two DD reactions (DDn and DDp) have a similar cross section [7].

more lighter nuclei, or in the fusion of lighter atoms into a heavier one [3, 4].

1.1.1 Nuclear fusion on the Sun

Nuclear fusion is the energy source of stars. All stars in the Universe gain their energy from fusing light elements into heavier ones. Our sun belongs to a group of the youngest stars, this type of stars combine hydrogen atoms (protons) to eventually produce helium (two proton and two neutrons) [3]. The main reaction cycle is represented by this scheme [5]:

reaction 1. $$p + p \rightarrow D + e^{+} + \nu + 1.42\,\mathrm{MeV}$$

reaction 2. $$D + p \rightarrow He^{3} + \gamma + 5.5\,\mathrm{MeV}$$

reaction 3. $$He^{3} + He^{3} \rightarrow He^{4} + p + p + 12.9\,\mathrm{MeV}\,.$$

1.1.2 Nuclear fusion on Earth

To initiate fusion the repulsive Coulomb force between charged nuclei must be overcome. The barrier is proportional to the product of nuclei charge number. The repul-

sive barrier between two hydrogen atoms on the Sun is overwhelmed by large gravitational forces. If we want to use nuclear fusion on our planet, we need to find a way to overcome the repulsive Coulomb force between charged nuclei, which requires a lot of energy on a large scale. In thermonuclear fusion, a charged fuel gas, plasma, with a high density is heated to fusion-relevant temperatures by externally applied heating power and only a fraction of the fuel will have enough energy to break the Coulomb barierr. Furthermore, the process on the Sun in which a proton is transformed into a neutron (reaction 1), is extremely slow. Nowadays, research on fusion energy is focused on the D-T reaction using hydrogen isotopes with one or two neutrons, Deuterium, and Tritium [8]. Then, the reaction cycle on Earth could be:

a) Reaction of two atoms of deuterium (DD reaction)

$$D + D \rightarrow T + H + 4.03MeV$$
$$D + D \rightarrow He^3 + n + 3.27MeV$$

b) Reaction of deuterium and tritium (DT reaction)

$$D + T \rightarrow He^4(3.5MeV) + n(14.1MeV)$$

c) Exotic reaction of deuterium and helium-3 (DHe^3 reaction)

$$D + He^3 \rightarrow He^4 + H + 18.3MeV$$

The cross section for the reactions is given in Fig. 1.1(b). The best candidate for the reaction in a future fusion reactor is the DT reaction. The maximum cross section of DT reaction occurs at just over 100keV. The cross sections of DD and DHe^3 reactions are lower than that for DT reaction except at high energies [9]. A difficulty of the DT reaction is that tritium is radioactive with a half-life equal to 12.3 years[2]. Tritium does not appear naturally on Earth, but it is possible to produce it via a reaction between lithium and neutrons from fusion reactions at the blanket of a reactor [8]:

$$\begin{aligned} Li^6 + n &\rightarrow T + He^4 + 4.8\,\mathrm{MeV} \\ Li^7 + n &\rightarrow T + He^4 + n - 2.5\,\mathrm{MeV}\,. \end{aligned} \tag{1.1}$$

Deuterium can be isolated from seawater and lithium is a common element on earth. Therefore, they would be cheap fuel for fusion reactors in future.

The cross sections for previous reactions given in the figure 1.1(b) indicate that the maximum cross section is below $< 100\,\mathrm{keV}$. It means that we have to heat the mixture of deuterium-tritium fuel to a sufficiently high temperature. The reaction rate coefficient for DT reaction, $\langle \sigma v \rangle$, has a maximum at a temperature of about 60 keV [9–11]. At such temperatures, the gas which is called *plasma* is fully ionized, and it exists as a macroscopically neutral collection of ions and unbound electrons [12].

[2]Because of tritium radioactivity, the reactor must comply to respect nuclear safety regulations. Activation of the walls of a fusion reactor will produce of course radioactive waste but much smaller amounts than that for a fission reactor

Power balance of reactor

It has been mentioned that the fusion on Earth can only work when nuclei have high energies to overcome their Coulomb barrier. It is achieved by injecting a lot of energy initially into the plasmas. If we want to use the thermonuclear fusion as a new and efficient source of energy on Earth, the energy output must be higher than the energy input to increase the temperature of the plasmas. For a description of this power balance between the input and output power, we define parameters relevant for the thermonuclear fusion.

The thermonuclear power per unit volume in DT plasma is

$$P_{\text{Th}} = n_D n_T \langle \sigma v \rangle \epsilon \,, \tag{1.2}$$

where n_D and n_T are deuterium and tritium densities, $\langle \sigma v \rangle$ is DT reaction rate, and ϵ is the energy released per reaction. The power is maximized for equal deuterium and tritium densities. Then, for a given electron density n the thermonuclear power is

$$P_{\text{Th}} = \frac{1}{4} n^2 \langle \sigma v \rangle \epsilon \,. \tag{1.3}$$

Four-fifths of this thermonuclear power (17.6 MeV per one DT reaction) is carried by the neutrons and the rest by α-particles. It is planned to use the energy of the α-particles ($\epsilon_\alpha = 3.5\,\text{MeV}$) to heat the plasma whereas the neutrons leave the plasma. Then this α-particle heating in volume V is expressed by

$$P_\alpha = \frac{1}{4} \overline{n}^2 \langle \sigma v \rangle \epsilon_\alpha V \,. \tag{1.4}$$

Plasma has a continuous loss of energy P_L which has to be replenished by a plasma heating. The total energy in plasma is

$$W = 3 \overline{n} \overline{T} V \,, \tag{1.5}$$

where $\overline{n}$ and $\overline{T}$ are the average density and temperature of the plasma in volume V. Important parameter of fusion devices is energy confinement time defined as

$$\tau_E = \frac{W}{P_L} \,. \tag{1.6}$$

It expresses the timescale of the loss of energy carried by the plasma particles. This power loss must be balanced by the externally supplied power and the α-particle power; thus the power balance is

$$P_H + P_\alpha = P_L \,. \tag{1.7}$$

Substituting Eq. (1.4) and Eq. (1.6) into above equation gives

$$P_H + \frac{1}{4} \overline{n^2} \langle \sigma v \rangle \epsilon_\alpha V = \frac{3 \overline{nT} V}{\tau_E} \,. \tag{1.8}$$

The ratio of fusion power to input power is called a Q-parameter,

$$Q = \frac{P_{\text{Th}}}{P_H} \,. \tag{1.9}$$

It is essential that the future fusion reactors have the Q-parameter as large as possible. When the Q-parameter is equal to 1, it is called **break even** or burn condition. We call **ignition** state when there is no need for the external heating power P_H. The energy of α-particles is enough to balance the power loss P_L in this ignition state. For the ignition condition $P_H = 0$ ($Q = \infty$) and:

$$P_\alpha > P_L \,, \tag{1.10}$$

From Eq. (1.4) and Eq. (1.6) we get

$$\frac{1}{4}\overline{n}^2 \langle \sigma v \rangle \epsilon_\alpha V > \frac{3\overline{n}\overline{T}V}{\tau_E} \,. \tag{1.11}$$

The confinement time τ_E is a function of temperature. It turns out that in the temperature range 10-20keV the reaction rate is represented to within 10% by

$$\langle \sigma v \rangle = 1.1 \cdot 10^{-24} T^2 \,\mathrm{m^3 s^{-1}} \,, \tag{1.12}$$

where T is in keV [9]. Then, using $\epsilon_\alpha = 3.5$MeV, the ignition condition, also called the triple product, becomes

$$\overline{n} T \tau_E > 3 \cdot 10^{21} \,\mathrm{m^{-3} keV s} \,. \tag{1.13}$$

This condition is valid only for a case when the temperature and density has a constant value in the whole plasma volume. Example values of densities, temperatures and confinement times of the triple product are presented in the next part giving a short introduction of fusion devices [9].

Fusion device concepts

Since fusion was considered as a new potential energy source, there were plenty of proposals to reach the appropriate triple product value. However, nowadays the major thermonuclear fusion research focuses on two types:

1. **Inertial confinement fusion**: The target (a DT pellet) is bombarded by laser beams or beams of ions. The target must be compressed to very high density before the fusion starts. The confinement times are in the order of nanoseconds. The triple product parameters for the inertial confinement plasma are $n \approx 10^{32}\,\mathrm{m^{-3}}$, $T \approx 30\,\mathrm{keV}$ and $\tau_E \approx 10^{-11}\,\mathrm{s}$ [3, 13].

2. **Magnetically confined plasma**: There are several approaches

   (a) *Magnetic mirrors*

   (b) *Pinches*

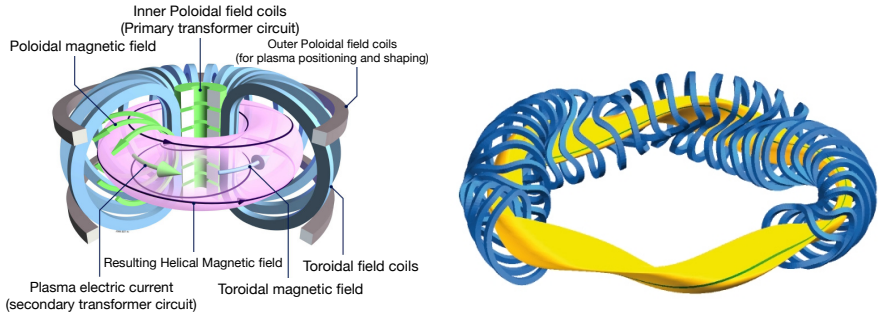

(a) (b)

Figure 1.2: (a) Scheme of a tokamak and magnetic field configuration [15]. (b) A stellarator design, as used in the Wendelstein 7-X experiment: A coil system (blue) surrounds plasma (yellow).

(c) *Toroidal systems*

The magnetic mirrors and pinches are opened on the ends. They lose particles and are found not sufficiently efficient. Up to now the best and the most promising experimental results were produced by toroidal systems, namely of a **tokamak** and a **stellarator** type [8, 9, 14]. The envisaged values of the triple product for tokamaks are $T \approx 10 - 20\,\mathrm{keV}$, $n \approx 10^{20}\,\mathrm{m}^{-3}$ and $\tau_E \approx 3 - 5\,\mathrm{s}$. As the theme of this thesis concerns toroidal systems, the concepts of a tokamak and stellarator are discussed in more details in the next section.

1.2 Toroidal fusion machines

Tokamak

The tokamak device is illustrated in Fig. 1.2(a). The magnetic field of the tokamak device consists of two components: toroidal (stronger) and poloidal magnetic fields. The toroidal magnetic field induced by toroidal field coils is radially non-uniform. It decreases from the center of the torus to the outer walls. The outer side of the vessel is called *Low field side (LHS)*, and the inner side is *High field side (HFS)*. A primary transformer circuit induces a *plasma current* producing the poloidal magnetic field. The combination of the toroidal and the poloidal magnetic fields results in a helical magnetic field. The outer poloidal field coils are there for plasma positioning and shape control [9].

In the presence of only a non-uniform toroidal magnetic field, there is a vertical motion of particles. This vertical drift is caused by grad-B and curvature drifts. They have the same direction, perpendicular to the magnetic lines. The drifts of ions and electrons have opposite direction [16]. It creates a separation of charges, and consequently, it produces a vertical electric field which together with the magnetic field

results in an additional drift of the plasma radially towards the low field side. This process is called $\vec{E} \times \vec{B}$ drift. The radial plasma drift is avoided by applying the poloidal magnetic field.

Stellarator

In tokamaks, the helical magnetic field is created by combining the toroidal and poloidal magnetic fields. Stellarators use a different approach to create a magnetic field to compensate for particle losses. Instead of inducing the current in a plasma to create poloidal magnetic field, stellarators use a special shape and design of the poloidal coils. These coils then directly generate the helical magnetic field to confine the fuel long enough to allow it to be heated to the point where fusion would take place. Fig. 1.2(b) shows the complicated geometry of the poloidal coils in Wendelstein 7-X.

1.2.1 Divertor and limiter

Even with the confining fields, the plasma might be in contact with walls. Special structures are designed to receive the plasma flux to protect the walls and to avoid releasing impurities from the walls into the plasma. The impurities in the plasma give rise to radiation losses and also dilute the fuel. Two techniques are used in tokamak and stellarator research. The first method defines the outer boundary of the plasma with a material limiter as shown in Fig. 1.3(a)(left). The second configuration is called divertor. It allows diverting the plasma at the plasma boundary away from the plasma core by locally changing the magnetic field, as shown in Fig. 1.3(a)(right). The limiter configuration has two main disadvantages: Firstly, the limiter itself could release impurities by an impact of the plasma on it, these impurities could degrade the plasma properties. Secondly, the ash (helium from fusion reactions) cannot be pumped away efficiently from a fusion reactor with limiter [9]. It is the reason why the divertor configuration is preferred on present big fusion devices like JET, ASDEX Upgrade and in future devices like ITER and DEMO.

1.2.2 Plasma heating systems in toroidal devices

There are several approaches to reach the required plasma temperature for fusion reactions ($10 - 20\,\mathrm{keV}$). The main plasma heating systems in tokamaks and stellarators are summarized in Fig. 1.3(b): **Ohmic Heating**, **Neutral Beam Injection Heating**, and **Radio-Frequency Heating**.

Ohmic heating

Ohmic heating is based on the fact that the plasma is a resistive medium. The plasma is heated by the Joule effect of the toroidal current in the tokamak. The heating power

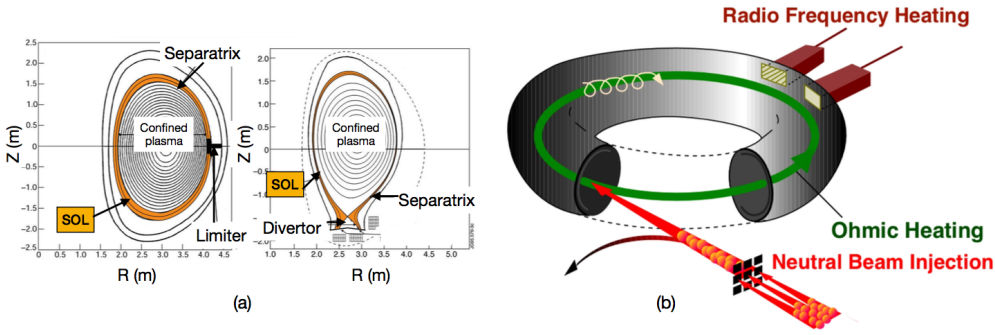

Figure 1.3: (a) Separation of plasma from a vacuum vessel by a limiter configuration (left) and a divertor configuration (right) [17]. The Scrape-Off Layer (SOL) refers to the plasma region characterized by open field lines [12]. (b) Summary of heating systems on toroidal machines: Radio Frequency heating, Ohmic heating, and Neutral Beam Injection.

can be expressed approximately by

$$P_{\mathrm{OH}}\,[\mathrm{MW/m^{-3}}] = 2.8 \cdot 10^{-15} \frac{Z_{eff} I^2\,[\mathrm{A}]}{a^4\,[\mathrm{m}]\; T_e^{3/2}\,[\mathrm{keV}]}\,, \tag{1.14}$$

where Z_{eff} is the effective ion charge, I is the toroidal plasma current, and a is the plasma minor radius. The biggest disadvantage of the ohmic heating is that with increasing temperature the ohmic heating efficiency decreases. The maximum temperatures we can reach with the ohmic heating alone are around $\approx 1\,\mathrm{keV}$ [12].

Neutral beam injection (NBI)

This heating method injects energetic hydrogen or deuterium atoms ($40\,\mathrm{keV} - 1\,\mathrm{MeV}$) into a plasma, where they are ionized. These energetic ions then transfer their energy to the plasma particles via Coulomb scattering. The injected particles must be neutral to penetrate the magnetic field surrounding the plasma. This technique is effective for higher plasma temperatures, and it can provide more energy than ohmic heating [13, 18].

Wave heating

Plasma is a medium that can host a mix of oscillations and waves. We can launch electromagnetic waves externally which are absorbed inside the plasma to increase the mean velocity of chaotic motion of particles. The use of electromagnetic waves to heat plasma is referred to as the radio-frequency (rf) heating. Three main frequency ranges of interest are:

1. electron cyclotron (ECH) $f = 100 - 150\,\mathrm{GHz}$
2. lower hybrid frequency (LHR) $f = 2 - 5\,\mathrm{GHz}$

3. ion cyclotron range of frequencies (ICRF) $f = 10 - 100\,\mathrm{MHz}$

The launched electromagnetic waves may propagate into the plasma where they are either absorbed via collisions or by resonant interactions, depending on the magnetic field strength B, the frequency of the launched wave and the plasma species [19].

Fusion alpha heating

Once a significant amount of fusion reactions take place, the alpha particles produced in DT reactions constitute a self-heating mechanism. The alpha particles are positively charged (He^{++}) and will be confined by the magnetic field together with ions and electrons. They will transfer their energy via collisions with the plasma particles [12].

1.2.3 International Thermonuclear Experimental Reactor

The largest tokamak device in construction is located in the south of France near CEA Cadarache Research Center. It is the international project run by seven member entities - the European Union, India, Japan, China, Russia, South Korea and USA. ITER should be a transition from experimental devices (JET, ASDEX Upgrade, TORE SUPRA, TEXTOR, etc.) into a fusion device to produce net energy. The highest fusion power was achieved by the European tokamak JET. In 1997, it generated $16\,\mathrm{MW}$ of fusion power from a total input power of $24\,\mathrm{MW}$ ($Q = 0.67$). ITER is designed for $Q = 10$, or $500\,\mathrm{MW}$ of fusion power from $50\,\mathrm{MW}$ of input power, for long pulses ($400 - 600\,\mathrm{s}$) [20]. The external heating will consist of Neutral Beam Injection ($33\,\mathrm{MW}$), Electron Cyclotron Heating ($20\,\mathrm{MW}$), Ion Cyclotron Heating ($20\,\mathrm{MW}$) and possible upgrade by Lower Hybrid Resonance Heating (20MW) [18, 21]. Table 1.2 summarizes the parameters of ITER and other European tokamaks, JET, TEXTOR and ASDEX Upgrade.

Tokamak	R_0 [m]	a/b [m]	V_{plasma} [m^3]	B_T [T]	I_p [MA]	Config.
ITER	6.2	2/3.7	840	5.3	15	Div.
JET	2.96	1.25/2.1	155	3.45	7	Div
ASDEX Upgrade	1.65	0.5/0.8	14	3.9	2	Div.
TEXTOR	1.75	0.5	7	3	0.8	Lim.

Table 1.2: Comparison of tokamaks JET, TEXTOR and ASDEX Upgrade with ITER: major radius R_0, minor radius (a/b), plasma volume (V_{plasma}), toroidal magnetic field strength (B_T), plasma current (I_p) and configuration (limiter or divertor) [4].

The magnetic system of ITER consists of 18 toroidal field coils, six poloidal field coils, a central solenoid and a set of correction coils. The magnetic system will be fully superconducting and cooled with helium around $4\,\mathrm{K}$. The cryostat provides thermal protection of the magnetic system. The material of the blanket will be made of low Z material beryllium. At the beginning of ITER design, there was a plan to

have a divertor from carbon in the first ITER operation stage, and then use second divertor make of tungsten. However, it was decided to install the tungsten divertor since the beginning of ITER operation. The ITER operation is divided into three campaigns: Hydrogen-Helium, Deuterium, Deuterium-Tritium [18, 21]. ITER will face a lot of technological challenges, e.g. high flux of neutrons and fuel atoms on the walls. An efficient method for wall conditioning in ITER is needed. Some of the wall conditioning methods are discussed in the next section.

1.3 Wall conditioning

One hurdle in achieving the necessary conditions for fusion plasmas is controlling the impurity production, hydrogen fueling of the plasma by the wall and tritium retention in the wall. There exist several Wall Conditioning methods to improve vacuum and control recycling. The most important are *baking, glow discharge conditioning* and *Ion* and *Electron cyclotron wall conditioning* (ICWC and ECWC).

Baking

The conditioning is based on thermal desorption of particles. The wall surfaces are heated up to temperatures above 500K. This procedure takes days and it is employed only after machine venting and in-vessel interventions to remove absorbed oxygen and water [4].

Glow discharge conditioning

This procedure is used routinely on almost all fusion devices. The simplest type of glow discharge (GD) is the direct current glow discharge (DC-GD). In this type of GD, the electrodes (anodes) are powered by a DC source. One or more electrodes are positioned within the vessel. The divertor and wall are set at ground potential and serve as cathodes. The ions are predominantly created in the negative glow and accelerated towards the cathode. Thus, the cathode is exposed to a flux of ions. GDC is carried out in a variety of gasses. Helium is used to remove hydrogen. Hydrogen glow discharge is used to remove impurities such as O & C via water formation, CO and CH_4. For improved removal efficiency, the walls can be heated to the temperature above 100° C.

However, a significant disadvantage of GDC is that it is inefficient in the presence of the toroidal magnetic field [4], and therefore not applicable in ITER or future fusion machines with super-conductive magnetic coils.

Ion cyclotron wall conditioning

Unlike the GDC, Ion Cyclotron Wall Conditioning (ICWC) can only be used in the presence of the magnetic field [4, 22, 23]. This is an important aspect especially for superconductive devices like ITER in which the toroidal magnetic field will be present

for long periods. ICRF plasma is produced and sustained by coupling RF power in the ion cyclotron range of frequencies. Details of the ICRF plasma production is studied in this thesis via experiments on TEXTOR, ASDEX Upgrade, JET, TORE Supra, URAGAN-3M and IShTAR, and modeling of the plasma initiation by ICRF antenna using Monte Carlo models.

Electron cyclotron wall conditioning

Electron cyclotron wall conditioning (ECWC) discharges are created by coupling RF waves in the electron cyclotron range of frequencies. The technique is less efficient than ICWC and GDC, and the discharges are not very homogeneous [24, 25].

1.4 PhD overview

This PhD manuscript aims to study the process of discharge initiation by the ICRF antenna relevant for applications such as ICWC. The ICWC technique is advantageous over the standard GDC technique due to its compatibility with the presence of a high toroidal magnetic field. For this reason, the ICWC will be applied in ITER, and it is necessary to understand better the plasma start-up by the ICRF antenna. The primary purpose is to study discharge initiation and to optimize the antenna parameters to swiftly initiate the discharge minimizing the time interval with the high voltage in the transmission lines and poor absorption of RF power. The optimization of the parameters is essential to avoid a possibility to initiate the parasitic plasma in the antenna box or transmission lines leading to potential damage of the ICRF antenna system.

In chapter 2, we present a general overview of discharge initiation in various configurations. First, we derive conditions for plasma initiation between two electrodes powered by a DC source. We derive conditions for the minimum voltage to initiate plasma between the electrodes as a function of pressure and distance between the electrodes. This dependency is called the Paschen curve. Then, we describe toroidal discharge during ohmic startup in tokamaks. We derive equations for the ionization and loss rates to describe the electron density evolution in time leading up to the plasma breakdown. At the chapter end, we summarize our present understanding of the discharge initiation by ICRF antennas. We show the experimental observations of the plasma breakdown during ICWC experiments, and we introduce two theoretical descriptions of the discharge initiation by ICRF antennas. The Ponderomotive model (PDM-model) investigates the acceleration of electrons in front of the antenna using the Taylor expansion of the vacuum antenna electric field around the oscillation center position. The conditions in the PDM-model for the discharge initiation are given as a function of the electric field strength and RF frequency. The Ponderomotive-Ionization model (PDMI-model) is based on the description given by the PDM-model, but it also adds the pressure dependency into the model.

Chapter 3 is dedicated to the description of our developed Monte Carlo collision model `RFdinity1d`. This model follows the motion of separate electrons around the

torus and their collisions with the neutral gas using Monte Carlo collision procedure. Electrons are accelerated by the vacuum antenna electric field in the parallel direction with respect to the toroidal magnetic field. The model investigates the electron density evolution in the time and dependency of this evolution on the antenna parameters (electric field strength, RF frequency, and antenna phasing), neutral gas pressure and torus circumference. Electrons undergo inelastic collisions with neutral molecules (or atoms). In the procedure, the model samples the path length between collisions for each electron. The model also contains Coulomb collisions between the charged particles (electron-electron and electron-ion collisions) using the Takizuka-Abe method.

In chapter 4, we present results of simulations using the Monte Carlo collision model `RFdinity1d` and their comparison with experimental observations on TEXTOR and URAGAN-3M. We also examine the discharge initiation with the ITER ICRF antenna using the MCC-model `RFdinity1d`. In the last part of this chapter, we describe a new method to find optimal parameters for discharge initiation using ICRF antennas. This derivation is based on the single electron model simulating the motion of a single electron in the antenna vacuum field. In this method, we study the threshold energy of an electron above which it can enter the antenna region and be accelerated by the electric field and its dependency on the antenna parameters (amplitude of the antenna RF electric field, its shape and frequency).

In chapter 5, we present a modification of the Monte Carlo collision model, combining a Particle-In-Cell method with the Monte Carlo collision model `RFdinity1d`. This PIC-MCC model follows the motion of guiding centers of both electrons and ions, whereas the Monte Carlo model in chapters 3-4 follows only the motion of electrons. First the techniques used in the PIC-MCC model are discussed in details, and then, the modeling results are presented. This chapter contains the most significant results as it shows direct relevance between the simulations results and experimental observations obtained on NPA diagnostics during the ICWC experiments on ASDEX Upgrade. These experimental observations had not been well understood, but we demonstrate that the NPA measurements can be explained using my PIC-MCC model `RFdinity1d`. The PIC-MCC model also demonstrated toroidal propagation of the Langmuir waves and their effect in the plasma production process.

In chapter 6, we introduce simulations using the MCC-model `RFdinity1d` in a linear configuration to study discharge initiation by ICRF antenna in front of the antenna or inside the antenna box. These simulations are based on the experiment performed on the linear device IShTAR with one strap ICRF antenna. We show in experiments and simulations a danger operating the ICRF antenna with high frequency. In the experiment, plasma is formed inside the antenna box, and our simulations show that this unsought phenomenon is due to the Secondary Electron Emission.

Chapter 6 summarizes the findings of this PhD manuscript and gives suggestions for optimal parameters of the discharge initiation by the ICRF antennas on toroidal machines and especially on ITER.

References

[1] Office of Integrated Analysis U.S. Energy Information Administration and Forecasting. *International Energy Outlook 2016*. Technical report, U.S. Department of Energy, Washington, DC 20585, 2016.

[2] International Energy Agency. *Key world energy statistics*. Electronic publication, 2016.

[3] G. McCracken and P. Stott. *Fusion The Energy of the Universe*. Elsevier, 2005.

[4] Tom Wauters. *Study and Optimization of Magnetized ICRF Discharges for Tokamak Wall Conditioning and Assessment of the Applicability to ITER*. PhD thesis, Universiteit Gent, 2012.

[5] L.T. Cox et al. Fusion Technology, 18(325), 1990.

[6] The Encyclopedia of Science, 2012. `http://www.daviddarling.info/encyclopedia/B/binding_energy.html`.

[7] CEA, 2001. `http://www-fusion-magnetique.cea.fr/gb/fusion/principes/principes01.htm`.

[8] J. SCHEFFEL and P. BRUNSELL. *Fusion Physics - introduction to the physics behind fusion energy*. KTH Stockholm, 2007.

[9] J. Wesson. *Tokamaks (second edition)*. Clarendon Press, Oxford, England, 1977.

[10] T. J. Dolan. *Fusion research*. Pergamon Press, New York, USA, 1982.

[11] Volodymyr Bobkov. *Studies of high voltage breakdown phenomena on ICRF (Ion Cyclotron Range of Frequencies) antennas*. PhD thesis, Technische Universitat Munchen Fakultat fur Physik, 2003.

[12] Jr. Weston M. Stacey. *An Introduction to the Physics and Technology of Magnetic Confinement Fusion*. A Wiley–Interscience publication, 1984.

[13] J. Mlynar. *Introduction to Thermonuclear Fusion*. University Lecture, 2011.

[14] F. F. Chen. *Introduction to plasma physics*. Plenum Press, 1974.

[15] *Energy fundamentals*, 2012. `http://uni-leipzig.de/~energy/ef/11.htm`.

[16] P. T. Gallagher. *Introduction to Plasma Physics*. University Lecture, 2012.

[17] EFDA. *Fusion-Limiters and Divertors*, 2012. `http://www.efda.org/fusion/focus-on/limiters-and-divertors/`.

[18] Tullio Bonicelli. *Heating Neutral Beam and Electron Cyclotron Power Supplies An overview of the Procurement*, 2009.

[19] T. H. Stix. *Waves in Plasmas*. Springer, New York, USA, 1992.

[20] ITER Organization. *Technical Description of ITER*, 2013. `http://www.iter.org/`.

[21] David Rasmussen. *Overview of ITER Heating and Current Drive Systems*. APS-DPP, USBPO ITER Town Meeting, 2011.

[22] A. Lyssoivan et al. *Simulation of ITER full-field ICWC scenario in JET: RF physics aspects*. Plasma Phys. Control. Fusion, 54, 2012.

[23] A. Lyssoivan et al. *Development of ITER relevant ICRF Wall Conditioning Technique on European Tokamaks*. Probl. At. Sci. Tech, Volume 1 of Plasma Physics:44–48, 2005.

[24] E. de la Cal et al. *Review of radio frequency conditioning dischares with magnetic fields in superconducting fusion reactors*. Plasma Phys. Control. Fusion, 47(2):197, 2005.

[25] J. Li et al. *Wall conditioning towards the utilization in ITER*. J. Nucl. Mater., DOI: 10.1016/j.jnucmat.2010.10.048, 2010.

2

Breakdown Phenomena in Gases

Gases are usually non-conducting. The process of transformation of a non-conducting material into a conductor as result of applying to it a sufficiently strong electric field is called **electrical breakdown**. This chapter will focus on basic physics of this process with a focus on the breakdown in RF fields which is the main subject of this thesis.

2.1 Electrical breakdown of gases: Townsend Mechanism

The non-conducting gas becomes conductive (electrical breakdown) as the result of applying electric field. A plasma is generated in a short time, usually between $10^{-8} - 10^{-4}$ s for glow discharges [1] and $10^{-4} - 10^{-1}$ s for ICRF discharges [2–5]. This spread of breakdown times is due to dependencies on many parameters. The simplest example of the electrical breakdown in neutral gas is a DC glow discharge. Two electrodes in a glass tube with separation d are connected to a DC power supply with voltage V. The electric field between the electrodes is homogeneous $E = V/d$, Fig. 2.1(a). The electric field accelerates primary electrons originating from cosmic rays and/or terrestrial radiation towards the anode. When the electron reaches the energy somewhat greater than the ionization potential of atoms or molecules inside of the tube, it may ionize a molecule or atom. The impact ionization results in two electrons that are again accelerated in the electric field, and an ionization avalanche can begin [6].

The **ionization rate**, ν_i, characterizes the rate of the ionization process. It is the number of ionization events performed by electron per second, $\mathrm{d}n_e/\,\mathrm{d}t = \nu_i n_e$. The better way to describe the ionization in an avalanche is by the **first Townsend coef-**

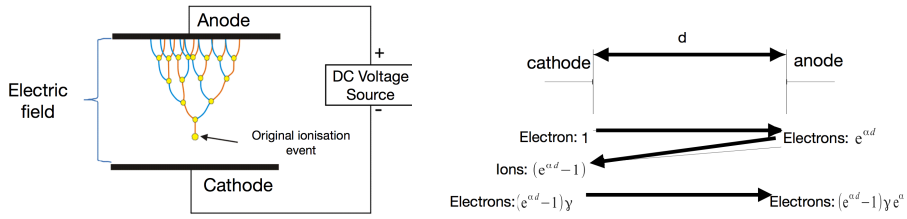

(a) (b)

Figure 2.1: (a) Visualisation of a Townsend avalanche [7], (b) Illustration of electrons and ions creation during the DC-discharge.

ficient α rather than by the ionization rate. Townsend's first coefficient α expresses how many ionizations on average are caused by one electron per meter along its path:

$$\frac{\mathrm{d}n_e}{\mathrm{d}x} = \alpha n_e \,. \tag{2.1}$$

If the ionization by electrons develops under unchanging conditions, $\nu_i = \text{const.}$ or $\alpha = \text{const.}$ and there are no losses of electrons during the process, the electron avalanche develops as $n_e = n_e(0)\exp(\alpha x)$ [6]. Experimental measurements have shown (for hydrogen [8, 9]) that in certain ranges the first Townsend coefficient α can be expressed by

$$\alpha = A \cdot p \cdot \exp\left(-\frac{B \cdot p}{E}\right) , \tag{2.2}$$

where pressure p is in Pascal and electric field E in V/m. Table 2.1 shows experimental constants A and B for different gases and the validity range E/p.

Gas	A $[\mathrm{m^{-1}Pa^{-1}}]$	B $[\mathrm{Vm^{-1}Pa^{-1}}]$	E/p $[\mathrm{Vm^{-1}Pa^{-1}}]$
He	2.3	25.5	15-113
Ne	3	75	75-300
Ar	9	135	75-450
Kr	13	180	75-750
Xe	20	263	150-600
Hg	15	278	113-450
H_2	3.8	94	113-450
N_2	9	257	75-450
Air	11	274	75-600
CO_2	15	350	375-750
H_2O	9.8	218	113-750

Table 2.1: Experimental constants A, B for different gases and the validity ranges E/p [6].

Whenever the electron ionizes an atom or molecule, a new electron and a new ion are created. The number of ions in the gap between the electrodes generated by

one primary electron equal to $\exp(\alpha d) - 1$. All the ions drift to the cathode. When they reach the cathode, they eject electrons from the cathode in the process called *secondary electron emission*. The probability of the secondary electron emission due to an ion impact on the cathode is expressed by the **second Townsend coefficient** γ. The parameter γ depends on the cathode material, state of the surface and type of gas. Typical values of γ in the electrical discharges are 0.01 to 0.1 [10].

Fig. 2.1(b) shows the process that creates a current between the electrodes. It starts with one electron near the cathode; the electron is accelerated towards the anode. It creates current at the anode proportional to $\exp(\alpha d)$, in the same time ions create $\gamma\left[\exp(\alpha d) - 1\right]$ electrons at the cathode, these electrons create current at the anode proportional $\gamma\left[\exp(\alpha d) - 1\right]\exp(\alpha d)$. The total current created by this avalanche process is equal to

$$i = i_0 \exp(\alpha d)\left(1 + \mu + \mu^2 + \mu^3 \cdots\right) \text{ with } \mu = \gamma(\exp(\alpha d) - 1) \tag{2.3}$$

The sum is convergent for $\mu < 1$, and we get:

$$i = \frac{i_0 \exp(\alpha d)}{1 - \gamma\left[\exp(\alpha d) - 1\right]} \tag{2.4}$$

The expression is called the **Townsend formula**, first derived in 1902 [10]. This derivation assumes no electron losses due to recombination or attachment. This equation gives a condition for initiating a self-sustaining discharge. As the applied voltage increases, $\exp(\alpha d)$ and $\gamma \exp(\alpha d)$ increases until $\mu \to 1$. Then the denominator in the equation becomes zero and the current $i \to \infty$. The current cannot be steady at this condition. On the other hand, if the $\mu < 1$, the current is steady and not self-sustained. It implies that the transition condition towards a self-sustained discharge is $\mu = 1$,

$$\gamma\left[\exp(\alpha d) - 1\right] = 1\,. \tag{2.5}$$

The formula represents the condition for the self-sustained current in a homogeneous electric field $E_t = V_t/d$, and V_t is called the threshold voltage for the plasma breakdown [10]. In other words, it means that the current flows even in the absence of an outside source of electrons. It is valid when one primary electron is replaced with one secondary electron by the secondary emission, $\mu = \gamma\left[\exp(\alpha d) - 1\right]$.

2.1.1 Breakdown voltage

The breakdown voltage V_t depends on the gas, the material of the cathode, the pressure, and the discharge gap width. By substituting the semi-empirical equation formula for the first Townsend coefficient α in Eq. (2.2) into the condition for the initiating a self-sustained discharge in Eq. (2.5), we can express the minimum voltage as

$$V_{\text{min}} = \frac{Bpd}{\ln \frac{A}{\ln(1/\gamma+1)} + \ln pd}\,. \tag{2.6}$$

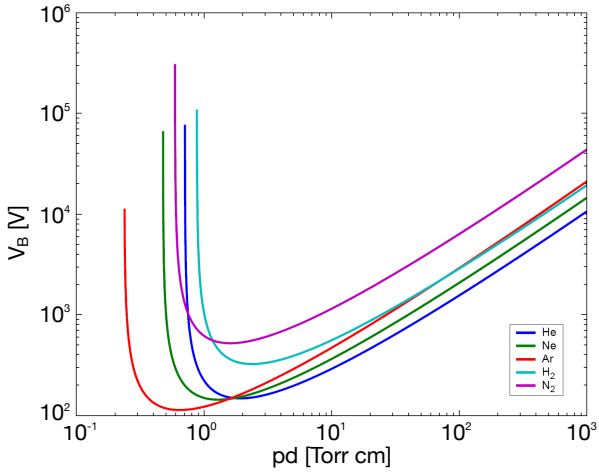

Figure 2.2: Paschen curves for different gases [11].

In this equation, we call C the first term in the denominator:

$$C = \ln \frac{A}{\ln\left(1/\gamma + 1\right)} \,. \tag{2.7}$$

The parameter C has no dependency on the pressure p or the width d. Finally, we can write the equation for the minimum voltage as

$$V_{\text{min}} = \frac{Bpd}{C + \ln pd} \,. \tag{2.8}$$

The breakdown voltage (Eq. (2.8)) depends on the product of the neutral gas pressure and the distance between the electrodes pd. This dependency is usually referred to as the **Paschen curve** [6, 10]. The experimental Paschen curves for different gases are shown in Fig. 2.2. All the curves have a minimum voltage point that corresponds to the easiest breakdown conditions:

$$V_{\text{min}} = \frac{eB}{A} \ln\left(1 + \frac{1}{\gamma}\right) \,, \tag{2.9}$$

where $e = 2.72$ is the base of natural logarithm [6, 10].

2.2 Toroidal discharges: ohmic startup

In the section above, we have described the electron avalanche process between two electrodes. Another example of the electron avalanche mechanism is the Ohmic startup in tokamaks. Here, we summarize the theoretical description of the breakdown phase during the low voltage Ohmic startup given by Lloyd [12] and Papoular [13], and which is based as well on the Townsend avalanche theory [8]. This theoretical

description is later compared with experimental observations obtained in DIII-D tokamak [12] and in my own simulations.

During the Ohmic startup, electrons are accelerated by a loop voltage generated by induction from the central solenoid (See Fig. 1.2(a)). The electrons travel around the torus following toroidal magnetic field lines to cause ionization of the neutral gas. The ionization by electron impact competes with the loss of electrons by various mechanisms, such as drift losses and direct loss along magnetic field lines. The evolution of the electron density is described by

$$n_e = n_{e,0} \exp\left[\left(\tau_{\text{ion}}^{-1} - \tau_{\text{loss}}^{-1}\right) t\right] , \tag{2.10}$$

where $n_{e,0}$ is the initial density of free electrons, τ_{ion}^{-1} is the ionization rate and τ_{loss}^{-1} is the loss rate. The recombination reactions are neglected as a loss mechanism because they become relevant only when the electron density reaches the magnitude of the neutral gas density. We will demonstrate the importance of the recombination reactions in Section 4.1. Therefore, these recombination reactions are omitted in the above equation describing the electron density evolution during the Ohmic startup.

2.2.1 Ionization rate

The theoretical predictions given in this section are compared with experimental studies of low voltage startup in DIII-D [12]. The experiment has been carried out in deuterium. Experimental measurements [8, 9] demonstrate that Townsend's first coefficient for deuterium is closely similar to those in hydrogen up to $E/p = 750\text{Vm}^{-1}\text{Pa}^{-1}$. Therefore, for the experiment in DIII-D in deuterium, we use the constants A and B for hydrogen (Table 2.1) to calculate Townsend's first coefficient α (Eq. (2.2)). Fig. 2.3(a) plots the first Townsend's coefficient α for hydrogen (deuterium) for several values of the electric field E.

According to Papoular [13] and experimental measurements [14], we assume that electrons achieve a constant drift speed, v_{De} proportional to E/p:

$$v_{De} = \eta E/p\,. \tag{2.11}$$

However, in this analysis, we have to presume frequent collisions. Otherwise, electrons may be accelerated at high velocities with a low collision probability. These electrons are called *runaway electrons*, and it is important to set a value of E/p to avoid them. The runaway electrons can achieve energies of $10-50\text{MeV}$ in the present large tokamaks [15] and in the worst scenario up to $500\,\text{MeV}$ in ITER [16]. Such energetic beam of electrons could melt part of the wall of the reactor when they bombard it. Measurements in hydrogen gives $\eta \simeq 5.7 \cdot 10^3$ [14]. Furthermore, the measurements define that Eq. (2.11) is applicable for $E/p \leq 150\text{V}\cdot\text{m}^{-1}\cdot\text{Pa}^{-1}$. Above this threshold of E/p ratio, runaway electrons may be produced and Eq. (2.11) is no longer valid [17]. The ionization rate for deuterium can be expressed for $E/p \leq 150\,\text{V}\cdot\text{m}^{-1}\cdot\text{Pa}^{-1}$ as

$$\tau_{\text{ion}}^{-1} = v_{De}\alpha = 5.7 \cdot 10^3\,(E/p) \times 3.8p \exp\left(-94p/E\right) . \tag{2.12}$$

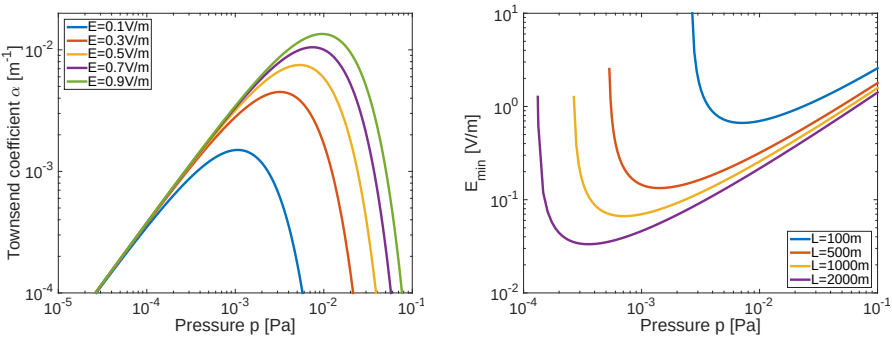

Figure 2.3: (a) Townsend's first coefficient α as a function of pressure for various values of the electric field in hydrogen. (b) The minimum electric field for the breakdown, E_{min}, in hydrogen, as a function of pressure for various values of toroidal connection length L.

2.2.2 Loss rate

During the avalanche process, we consider only two main particle loss mechanisms: (i) drift losses (curvature and ∇B drift) and (ii) direct loss along magnetic field lines. In tokamaks, the curvature and ∇B drifts always act together and can be expressed by

$$v_{\text{drift}} = v_R + v_{\nabla B} = \frac{1}{R\omega_{ce}} \left(v_{\parallel}^2 + \frac{1}{2} v_{\perp}^2 \right) , \tag{2.13}$$

where $\omega_{ce} = \frac{m_e}{q_e B_T}$ is the cyclotron frequency of electrons at toroidal magnetic field B_T. Setting $v_{\parallel}^2 \sim v_{\perp}^2 \sim 3k_B T_e / 2m_e$ gives

$$v_{\text{drift}} \sim \frac{1}{RB_T} \frac{T_e[\text{eV}]}{0.44} . \tag{2.14}$$

This drift is vertical, pointing upwards or downwards (depending on particle charge), therefore setting b as the minor radius in the vertical direction, the time loss can be expressed by

$$\tau_{\text{drift}} \sim 0.44 b R B_T / T_e . \tag{2.15}$$

For the tokamak DIII-D with $R = 1.67\,\text{m}$, $B_T = 2\,\text{T}$, $b \simeq 1\,\text{m}$, and since T_e is limited to $5 - 10\,\text{eV}$ until ionization is complete [18], we have

$$\tau_{\text{drift}} \simeq 150\,\text{ms} . \tag{2.16}$$

This time is much larger than the typical breakdown times in experiments.

The time for the direct losses along the magnetic field lines is given by

$$\tau_{\text{direct}} \sim L / v_{De} \simeq \frac{a_{\text{eff}} B_T / B_{\perp}}{v_{De}} , \tag{2.17}$$

where L ($\simeq a_{\text{eff}} B_T / B_\perp$) is the connection length and a_{eff} is the distance to the wall along the direction of $B_\perp$. Typically, on the DIII-D, $B_T = 2\,\text{T}$, $B_\perp = 10^{-3}\,\text{T}$, $a_{\text{eff}} \sim b \simeq 1\,\text{m}$ gives $L \sim 2000\,\text{m}$. Then, Eq. (2.17) equals to

$$\tau_{\text{direct}} \simeq 2.3\,\text{ms} \tag{2.18}$$

where we use drift speed for $E/p = 150\,\text{V} \cdot \text{m}^{-1} \cdot \text{Pa}^{-1}$. Hence, it is obvious that the dominant loss during the avalanche process is due to direct loss along magnetic field lines and, therefore,

$$\tau_{\text{loss}} \sim \tau_{\text{direct}} \simeq L / v_{De} \tag{2.19}$$

It is necessary that the ionization rate exceeds the loss rate in order to initiate a discharge. Therefore, the ionization length α^{-1} must be longer than the connection length L. We can derive the formula for the minimum electric field for breakdown by setting $\alpha^{-1} = L$. This gives, from Eq. (2.2) for hydrogen (deuterium) [12, 13]

$$E_{\text{min}} = \frac{94\,p\,[\text{Pa}]}{\ln\left(3.8\,p[\text{Pa}]\,L\,[\text{m}]\right)}\,. \tag{2.20}$$

This relationship is referred as a Paschen's law, and it is plotted in Fig. 2.3(b) as a function of pressure for various values of L.

2.2.3 Breakdown time

Inserting the relations for the ionization rate Eq. (2.12) and the loss rate Eq. (2.19) into Eq. (2.10) for the evolution of the electron density n_e during the avalanche process, gives

$$n_e = n_{e,0} \exp\left[v_{De} \left(\alpha - \frac{1}{L} \right) t \right]\,. \tag{2.21}$$

Then we can define the **breakdown time** t_{bkdn} as the moment reaching the critical electron density n_{bkdn}

$$t_{bkdn} = \frac{\ln\left(n_{bkdn}/n_{e,0}\right)}{v_{De}\left(\alpha - 1/L\right)}\,. \tag{2.22}$$

The critical electron density n_{bkdn} is reached at the moment when the electron-ion Coulomb collision frequency, ν_{CC}^{e-i}, exceeds the electron-atom collision frequency, ν^{e-H_2} [12, 13]. This condition is expressed by

$$n_{bkdn} \sigma_{CC}^{e-i} = \left(n_{H_2} - n_{bkdn}\right) \sigma^{e-H_2}\,, \tag{2.23}$$

where n_{H_2} is the hydrogen density and σ_{CC}^{e-i} and σ^{e-H_2} are cross-sections approximated by [13]

$$\sigma_{CC}^{e-i} \simeq 3 \cdot 10^{-19} T_e^{-1/2}\,[\text{m}^2] \tag{2.24}$$

$$\sigma^{e-H_2} \simeq 1.5 \cdot 10^{-16} T_e^{-2}\,[\text{m}^2]\,. \tag{2.25}$$

This gives

$$\frac{n_{bkdn}}{n_{H_2} - n_{bkdn}} \simeq \frac{n_{bkdn}}{n_{H_2}} \simeq 5 \cdot 10^{-3} T_e^{3/2}\,, \tag{2.26}$$

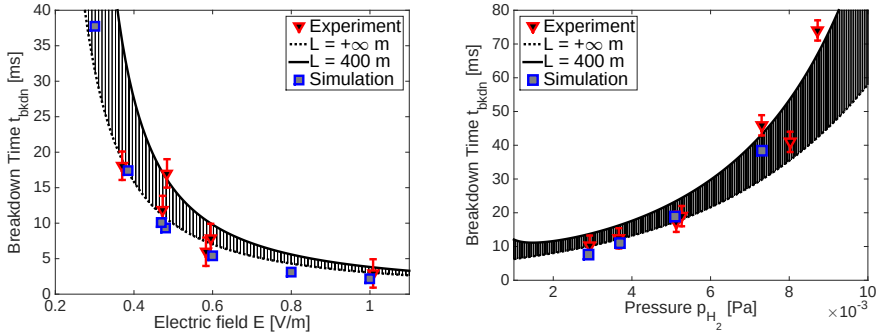

(a) (b)

Figure 2.4: Comparison of the theoretical predictions based on a Townsend avalanche and the experimental breakdown times measured during Ohmic start-up in DIII-D. (a) Breakdown time as a function of the electric field at $p = 5.2 \cdot 10^{-3}\,\mathrm{Pa}$, where the electric field on the axis corresponds to that at $R = R_0 - a/2$; (b) Breakdown time as a function of the pressure p at $E = 0.38\,\mathrm{V/m}$ corresponding to that at $R = R_0 - a/2$. The theoretical bands illustrate the extent of a variation of t_{bkdn} for the connection length $L = 400\,\mathrm{m}$ and $L = +\infty$.

or by defining the degree of ionization $\gamma = n_e/n_{H_2}$

$$\frac{\gamma}{1-\gamma} \simeq 5 \cdot 10^{-3} T_e^{3/2}\,. \tag{2.27}$$

Simulations have shown that T_e is limited to $5 - 10\,\mathrm{eV}$ during ohmic startup [18], and the degree of ionization γ is $< 15\%$. Unfortunately, it is a challenge to identify the start of the Coulomb phase in the experiments. Therefore, in practice, this definition is not applicable.

In the experiments, another definition is used corresponding to the peak H_α (or D_α) emission. This moment is associated with a minimum value of T_e and $\gamma = 0.5$ [12]. Thus, the breakdown moment is set to an electron density as $n_e = \frac{n_{H_2}}{2}\,\mathrm{m}^{-3}$. Setting $n_{bkdn} = \frac{n_{H_2}}{2}$ in Eq. (2.22) and using Eq. (2.2) and Eq. (2.11) we can evaluate t_{bkdn} for given values of E, p and L, and compare it with the experimental measurements.

Fig. 2.4(a) shows the theoretical predictions of the breakdown time t_{bknd} as a function of the electric field at $p = 5.2 \cdot 10^{-3}\,\mathrm{Pa}$ for two connection lengths ($L = 400\,\mathrm{m}$ and $L = +\infty$). We have chosen to set $\ln(n_{bkdn}/n_{e,0}) = 41$, which corresponds to $p = 5.2 \cdot 10^{-3}\,\mathrm{Pa}$ at $T_{gas} = 400\,\mathrm{K}$ and $n_{e,0} = 1\,\mathrm{m}^{-3}$. It is important to underline the difficulties regarding the correct value of electric field employed for the comparison between the experimental data and the theoretical predictions. Visible bremsstrahlung emission measurements during the low voltage Ohmic start-up indicate that the discharge initiates at the low major radius, where the electric field E is the highest. Therefore, assigning to the experimental data the E fields at $R = R_0 - a/2$ in Fig. 2.4(a) is showing good agreement with the theoretical breakdown predictions. The theoretical band in Fig. 2.4(a) illustrates the variation of t_{bkdn} for varying values

of L. The upper theoretical line for $L = 400\,\mathrm{m}$ indicates good agreement for upper limits of the experimental breakdown times. Choosing $L = +\infty$ as the lower limit of the experimental breakdown times is equivalent to selecting the special case without any electron losses. The theoretical prediction given by Townsend avalanche theory is valid only up to $E/p \leq 150\,\mathrm{V \cdot m^{-1} \cdot Pa^{-1}}$ corresponding to $E \leq 0.78\,\mathrm{V \cdot m^{-1}}$ at $p = 5.2 \cdot 10^{-3}\,\mathrm{Pa}$. The dependency of t_{bkdn} as a function of the pressure p is plotted in Fig. 2.4(b) for $E = 0.38\,\mathrm{V/m}$ (the value at $R \simeq R_0 - a/2$ for $E = 0.3\,\mathrm{V/m}$ at $R = R_0$). Again, the experimental breakdown times are in good agreement with the Townsend avalanche theory, Eq. (2.22). The validity limit for Townsend avalanche theory at this electric field is $p > 2.5 \cdot 10^{-3}\,\mathrm{Pa}$.

Additionally, both experimental and theoretical breakdown times are in quantitative agreements with model results using our `RFdinity1d` model (blue squares in Fig. 2.4). The model will be introduced in detail in Chapter 3. It describes the motion of electrons along the magnetic field line and simulates the collisions between electrons and neutral gas molecules for a given loop voltage. The evolution of the electron density obtained from this model follows an exponential increase in time, and the breakdown time is obtained as the moment when the density overcomes the theoretical condition for the breakdown described by Lloyd [12] and Papoular [13] $n_{\mathrm{bkdn}} = n_{H_2}/2$.

2.3 Discharge initiation by ICRF antennas

In the DC discharges or during the Ohmic Startup, both electrons and ions are accelerated by a constant electric field. While in the RF discharge, charge particles perform very complicated motion under action of the antenna oscillating electric field. Therefore, we cannot define the drift velocity v_{De} by Eq. (2.11). In addition, the definition of the ionization rate ν_i in Eq. (2.12) using the first Townsend coefficient α is not applicable to describe the discharge initiation by RF systems. A simplified analytical description was introduced to approximate this chaotic motion of the charged particles in the RF field in toroidal devices. The basics of the RF physics aspects of the ICWC discharges, and discharge initiation by ICRF antennas have been summarized by *Carter* et al. [19] and *Schüller* et al. [20]. Another difference between the DC and RF discharges is the excitation of plasma waves initiated by antenna systems. These waves play an important role in further acceleration of the charged particles (increasing the ionization rate) and expansion of the plasma column during the discharge initiation. The waves can start propagating in the plasma when certain conditions are matched [2, 21–25]. This chapter gives an overview of the ICRF plasma production, coupling properties of the ICRF power to the plasma, and presents basic models describing the breakdown conditions of the RF plasmas as a function of the discharge parameters: RF frequency, RF field strength, and neutral gas pressure.

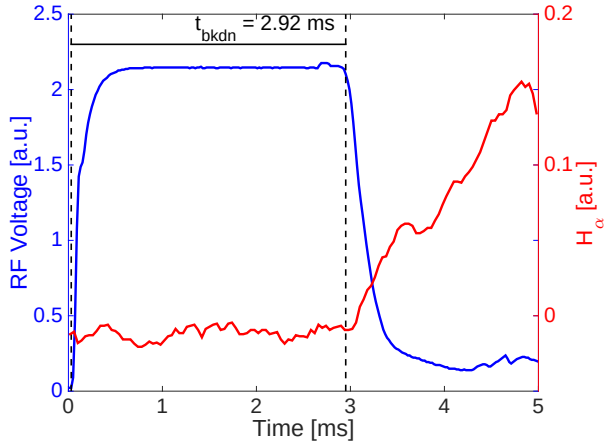

Figure 2.5: Time evolution of the antenna voltage and H_α signal during ICWC experiment in TEXTOR (shot number #120195). The breakdown time is highlighted as a difference between the time when the antenna is turned on and time when the antenna voltage drops and H_α signal rises.

2.3.1 Discharge breakdown in ICWC experiments

The standard ICRF antenna is designed to couple the RF power into the plasma via excitation and absorption of the Plasma Waves, mainly Fast wave (FW) [2, 26]. Concept and theoretical description of the Ion Cyclotron Resonant Heating (ICRH) was first systematically described by *Stix* [26]. Using the Stix formulation, we write the plasma dielectric tensor $\overline{\overline{K}}$ in the cold approximation as:

$$\overline{\overline{K}} = \begin{bmatrix} S - \frac{k_\parallel^2}{k_0^2} & -iD & \frac{k_\perp k_\parallel}{k_0^2} \\ iD & S - \left(\frac{k_\parallel^2}{k_0^2} + \frac{k_\perp^2}{k_0^2}\right) & 0 \\ \frac{k_\parallel k_\perp}{k_0^2} & 0 & P - \frac{k_\perp^2}{k_0^2} \end{bmatrix}, \tag{2.28}$$

where $k_\parallel$ and $k_\perp$ are resp. the parallel and perpendicular components of the wave vector with respect to magnetic field B_0 [2, 26, 27]. In the Stix formulation, the elements S, D and P are defined in [26] as:

$$S = 1 - \sum_s \frac{\omega_{p,s}^2}{\omega^2 - \Omega_s^2} \tag{2.29}$$

$$D = \sum_s \frac{\omega_{p,s}^2 \Omega_s}{\omega(\omega^2 - \Omega_s^2)} \tag{2.30}$$

$$P = 1 - \sum_s \frac{\omega_{p,s}^2}{\omega^2}, \tag{2.31}$$

where $\omega_{p,s}$ and Ω_s are the plasma frequency and the cyclotron frequency of the s-species, respectively. In these equations, P is much bigger than S and D because of the difference between the ion and electron masses. Using this fact we can simplify Eq. (2.28) and we obtain the two solutions of the dispersion relation, a fast wave (FW) and a slow wave (SW) [2, 26, 27]:

$$k_{\perp,FW}^2 = \frac{\left(k_0^2 S - k_\parallel^2\right)^2 - \left(k_0^2 D\right)^2}{k_0^2 S - k_\parallel^2} \tag{2.32}$$

$$k_{\perp,SW}^2 = \frac{P}{S}\left(k_0^2 S - k_\parallel^2\right) . \tag{2.33}$$

The wavelength of the slow wave is significantly shorter than that of the fast wave. The fast wave has a cut-off at $\left(k_0^2 S - k_\parallel^2\right) = k_0^2 D$. The slow wave has a cut-off for $P = 0$ and a resonance at $S = 0$ referred as the lower hybrid resonance (LHR).

During the ICRF discharge initiation experiments on TEXTOR, ASDEX Upgrade, JET and TORE SUPRA, a breakdown event is defined as the moment when the antenna voltage V^{RF} drops, an increase in H_α signal is detected and antenna resistance rises [21, 23]. These definitions are illustrated in Fig. 2.5 showing the discharge initiation during an ICWC experiment in TEXTOR.

The ICRF antenna operated in the plasma production mode is matched close to vacuum load to overcome safely a transition from vacuum to plasma load, which is higher at sustained discharge phase ($R_{\text{pl}} > R_{\text{vac}}$). On applying the RF power to the antenna strap(s) at time $t = 0$ms (Fig. 2.5), the RF voltage immediately builds up to a high value defined by the R_{vac} and given RF power level. In this manuscript, the RF voltages or voltages on the strap are measured by probes in the transmission lines or in the antenna strap vicinity. The voltage measurements shown in this manuscript are taken directly from diagnostics and use arbitrary units.

At the time instance when a sufficient plasma density is created, the forward power from the generator starts to be coupled into the plasma due to a change in load inside of the vessel. This moment defines the experimentally observed breakdown of the neutral gas with the standard ICRF antenna. It shows up a clear correlation between a sudden drop in the antenna RF voltage, a rise of the plasma load (plasma absorbed RF power) and a burst in the H_α emission as described in [21, 28] and shown in Fig. 2.5 ($t_{\text{bkdn}} \approx 2.92\,\text{ms}$). The experimental indication of the breakdown moment, i.e., the voltage drop is independent whether the probe measurements are taken in the transmission lines or antenna strap vicinity.

2.3.2 Review of theory of ICRF plasma breakdown

In this section, we introduce two models describing the discharge initiation by the ICRF antenna. These models use crude approximations to capture the complex RF physics to give breakdown conditions of RF plasmas as a function of the discharge parameters: RF frequency, RF field strength and shape, and neutral gas pressure.

Choosing the proper parameters is crucial to create swiftly the discharge for ICWC and to assure the antenna safety.

2.3.2.1 Dependency on amplitude and frequency of RF field

The PDM-model described in [19] determines the breakdown conditions as a function of the RF field and frequency. The PDM-model describes the electron motion due to the Lorentz force in the near antenna parallel electric field (parallel with the toroidal magnetic field) [29]. The model does not include the pressure dependency because it neglects any electron collisions. The model describes the initial phase of the neutral gas ionization before the plasma wave excitation (pre-wave phase) and investigates the parameters of the RF field necessary to accelerate electrons above sufficient energy for an ionization reaction. The Lorentz force acting on the electrons in the parallel direction is given by:

$$F_L = m_e \frac{\mathrm{d}v_z}{\mathrm{d}t} = -q_e E_z \,. \tag{2.34}$$

The parallel electric field on the right-hand side is driven at a frequency ω and will be parametrized by a factor $\cos(\omega t + \phi_0)$. The model relies on a possibility to simplify Eq. (2.34) and then solve the equation analytically for regions where the field is roughly constant over the length of the particle excursion in an RF cycle [2]. Then the electron motion can be separated into a fast oscillation and a slower drift around the oscillation center. The velocity and position are written as $v_z = v_0(t) + v_1(t)$ and $z = z_0(t) + z_1(t)$. The electric field is expressed in a Taylor series expansion around the slowly varying coordinate z_0:

$$E_z\left(z = z_0(t) + z_1(t)\right) = \sum_{n=0}^{\infty} \frac{z_1^n}{n!} \frac{\mathrm{d}^n E_z}{\mathrm{d}z^n}(z_0) \,. \tag{2.35}$$

In the work of *Carter* et al. [2, 19], the Taylor series keeps only the 0^{th}- and 1^{st}-order term.

$$E_z\left(z = z_0(t) + z_1(t)\right) = E_z(z_0) + z_1 \frac{\mathrm{d}E_z}{\mathrm{d}z}(z_0) \,. \tag{2.36}$$

However, our recent findings expanded the theory, and for that reason, we will introduce as well the 2^{nd}-order term in Section 4.5 to explain the electron motion in the RF field.

Relying on the assumptions that z_0 is changing slowly in comparison with z_1, we can write Eq. (2.34) regarding fast a_1 and slow dynamics a_0 with two individual equations of motion

$$\frac{\mathrm{d}v_1}{\mathrm{d}t} = -\frac{q_e}{m_e} \underbrace{E_z(z_0)}_{0^{\text{th}}\text{-order}} \cos(\omega t) \tag{2.37}$$

$$\frac{\mathrm{d}v_0}{\mathrm{d}t} = -\left\langle \frac{q_e}{m_e} \underbrace{z_1 \frac{\mathrm{d}E_z}{\mathrm{d}z}(z_0)}_{1^{\text{st}}\text{-order}} \cos(\omega t) \right\rangle \,. \tag{2.38}$$

The $\langle \ldots \rangle$ represents an average over the fast oscillation period.

The second equation (Eq. (2.38)) illustrates that the spatial non-uniformity of the electric field cause a slow z_0-drift of the electrons. The first equation (Eq. (2.37)) with only 0^{th}-order term for the fast motion around the z_0 is easily integrated. Assuming $z_1 = v_1 = \phi_0 = 0$ at time $t = 0$,

$$z_1 = \frac{q_e}{m_e \omega^2} E_z(z_0) \left[\cos(\omega t) - 1\right] \tag{2.39}$$

Inserting the above expression into Eq. (2.38), we can express the acceleration causing the zero order drift in the form:

$$\begin{aligned} a_0 = \frac{\mathrm{d}v_0}{\mathrm{d}t} &= -\left\langle \frac{q_e^2}{m_e^2 \omega^2} E_z \frac{\mathrm{d}E_z}{\mathrm{d}z}(z_0) \left[\cos^2(\omega t) - \cos(\omega t)\right] \right\rangle = \ldots \\ &= -\frac{q_e^2}{m_e^2 \omega^2} E_z \frac{\mathrm{d}E_z}{\mathrm{d}z}(z_0) \left[\underbrace{\left\langle \cos^2(\omega t) \right\rangle}_{=\frac{1}{2}} - \underbrace{\left\langle \cos(\omega t) \right\rangle}_{=0} \right] \end{aligned} \tag{2.40}$$

The acceleration a_0 (Eq. (2.38)) can be finally written as

$$a_0 = -\frac{\mathrm{d}}{\mathrm{d}z} \left[\frac{q_e}{2 m_e \omega} E_z(z_0) \right]^2 . \tag{2.41}$$

The associated force is called the *ponderomotive force* with a potential [29]:

$$\Phi_p = \left[\frac{q_e E_z(z_0)}{2\sqrt{m_e}\omega} \right]^2 . \tag{2.42}$$

It is important to define validity conditions for the present ponderomotive expansion. In the work of Lyssoivan [2], it is discussed that the 1^{st}-order term in the Taylor expansion of E_z should be much smaller than the 0^{th}-order term, i.e. $|a_0/a_1| \ll 1$ or

$$\left| \frac{\mathrm{d}E_z}{\mathrm{d}z} \right| \ll \frac{2 m_e \omega^2}{q_e} . \tag{2.43}$$

Given this approximation of the electron motion in the RF field, we can estimate the maximum energy reached by an electron for a given electric field strength as:

$$\epsilon_{\text{pdm}} = \frac{1}{2} m_e v_1^2 = \frac{1}{2 m_e} \left(\frac{q_e E_z}{\omega} \right)^2 . \tag{2.44}$$

In the PDM-model, the electron multiplication is initiated by the parallel electric field when the oscillation energy exceeds the ionization threshold ϵ_i. This condition is a lower value for the electric field of the breakdown criterion in the PDM-model [2, 19, 30, 31].

$$E_z > E_{z,\text{min}} = \sqrt{2 m_e \epsilon_i} \frac{\omega}{q_e} \tag{2.45}$$

The PDM-model assumes that a build-up of electron density by the electron multiplication reactions occurs primarily in front of the antenna. Therefore, the model defines

the upper criterion for the breakdown as the electric field strength for which an electron stays in the antenna region. The condition is expressed by

$$2\Delta z_1 < L_z \tag{2.46}$$

$$\Delta z_1 = \left| \frac{q_e E_z}{m_e \omega^2} \right| , \tag{2.47}$$

where L_z is the toroidal length of the region over which the E_z antenna field is significant), and Δz_1 is the spatial oscillation amplitude from Eq. (2.39) [2, 30, 31]. Finally, the upper condition in the PDM-model for the maximum electric field is expressed as

$$E_z < E_{z,\max} = \frac{m_e \omega^2 L_z}{2 q_e} . \tag{2.48}$$

In summary, the criteria for the breakdown in the antenna region given by the PDM-model are: the electric field strength (i) must be strong enough to accelerate electrons above the ionization threshold energy ϵ_i, and (ii) should be substantially lower than $E_{z,\max}$ to avoid expelling of all electrons from the antenna region.

$$\frac{\omega}{q_e} \sqrt{2 m_e \epsilon_i} \leq E_z \leq \frac{m_e \omega^2 L_z}{2 q_e} \tag{2.49}$$

The PDM-model assumptions and approximations suffer from a few drawbacks [20]:

1. The model does not consider that electrons expelled from the antenna might contribute to a build-up of electron density by ionization collisions outside the antenna region. It was indicated by *Schüller et al.* [20] that expelled electrons can obtain enough energy to ionize along the torus. It was shown during my master research [32], that outside of the antenna region electrons have a higher probability of a collision as a typical path length between collisions is several meters. Furthermore, the PDM-model ignores the possibility of an expelled electron to reenter the antenna region after it encircled around the torus which is an important effect as we will show later in the thesis.

2. Another remark by *Schüller et al.* [20] is related to the upper limit of the electric field strength in Eq. (2.48). It gives only the criterion for the validity limit of the Taylor expansion to the Lorentz force. In principle, it does not exclude the electric field strength above $E_{z,\max}$ to accelerate electrons to cause ionization either in the antenna region or away from the antenna. However, the lower limit in Eq. (2.49) can be applied to determine the minimum electric field above which an electron may obtain sufficient energy for the ionization.

3. The most significant drawback of the PDM-model is neglecting the pressure dependency for the antenna safety. The breakdown criterion describing the dependency on the neutral gas pressure is given by *Schüller et al.* [20].

2.3.2.2 Dependency on pressure

In the work of *Schüller et al.* [20], two regions of possible ionization collisions are distinguished: (1) ionization inside the antenna region and (2) ionization by electrons expelled from the antenna region by the ponderomotive force. The first case of ionization inside the antenna region is critical for the antenna safety. This PDMI-model (Ponderomotive-Ionization model) defines the probability of creating a new electron due to ionization during one oscillation by the ratio between $4z_1$ (Eq. (2.47)) and the mean free path length for the time-averaged ionization collision cross-section $\langle\sigma_{\text{ion}}\rangle$. The ionization rate for the antenna region ν_{ion}^{RF} is given in Eq. (2.50). For electron ionization outside of the antenna region, we can derive the ionization rate ν_{ion}^{PDM} as a ratio between the velocity of an electron v_{pdm} (Eq. (2.44)) expelled from the antenna region and the mean free path for ionization $\lambda = (n_{H_2}\sigma_{\text{ion}})^{-1}$ [20].

$$\nu_{\text{ion}}^{RF} \approx 4z_1 n_{H_2}\langle\sigma_{\text{ion}}\rangle f = 1.78\cdot 10^7 \frac{E_z\ [\text{kV/m}]}{f\ [\text{MHz}]} n_{H_2}\langle\sigma_{\text{ion}}\rangle \quad [\text{s}^{-1}] \tag{2.50}$$

$$\nu_{\text{ion}}^{PDM} \approx n_{H_2}\sigma_{\text{ion}}\sqrt{\frac{2q_e\epsilon_{\text{pdm}}}{m_e}} = 1.98\cdot 10^7 \frac{E_z\ [\text{kV/m}]}{f\ [\text{MHz}]} n_{H_2}\sigma_{ion} \quad [\text{s}^{-1}] \tag{2.51}$$

The ionization cross-section σ_{ion} depends on the ponderomotive energy ϵ_{pdm}. Both ionization rates are compared in Fig. 2.6 as a function of the ratio between the magnitude of E_z-field and RF frequency f. It is clear that both rates are very similar. However, it is important to mention that the toroidal length outside the antenna area is much larger than inside of the antenna. For that reason, it is evident that the electron multiplication rate is dominated by the ionization outside of the antenna region (red curve). Additionally, these theoretical ionization rates and their dependencies on the electric field and frequency will be compared with the ionization rates obtained by our MC model `RFdinity1d` in Section 4.1.

According to *Schüller et al.* description in the PDMI-model, we can define the criterion for the pressure above which plasma formation is expected in the antenna region (or inside the antenna box). It corresponds to the pressure for which the residence time of the oscillating electron in front of the antenna is longer that the characteristic time for an ionization $1/\nu_{\text{ion}}^{RF}$. The crude approximation of this constraint on the pressure is given by

$$p_{H_2}\,(W_{\text{ant}} + L_z) \ll 1\,[\text{Pa.m}]\,, \tag{2.52}$$

where W_{ant} is the width of the antenna region and L_z is the toroidal width of the region over which the E_z antenna field is significant. The analysis of *Schüller et al.* indicates that we should avoid pressure values above 10^{-1}Pa in the ICWC experiments [20].

The presented PDM-model and its expansion by *Schüller et al.* into PDMI-model provide criteria for plasma formation by the RF field as a function of the electric field strength, frequency, and neutral gas pressure. However, as mentioned already by *Schüller et al.*, the criteria are more relevant only to the plasma formation inside the antenna box. To define criteria for the plasma formation along the whole length of the magnetic field lines, one needs to take into account ionization outside of the antenna region. The argument that the ionization takes place everywhere along the

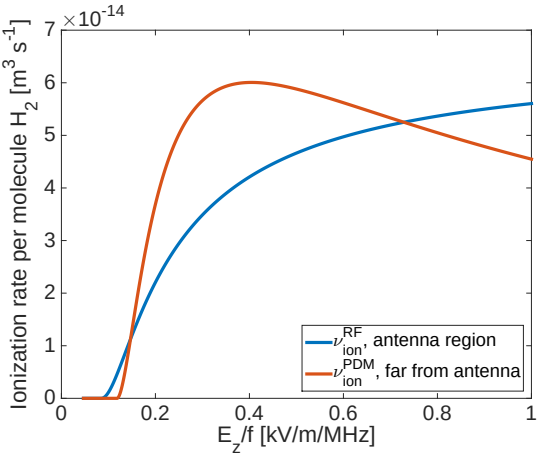

Figure 2.6: The ionization rates per molecule H_2 in the antenna region due to oscillatory movement of the electrons (ν_{ion}^{RF}), and outside of the antenna due to the ponderomotive drift as a function of the ratio between the magnitude of E_z-field and RF frequency f.

magnetic field line is in agreement with the experimental observation. In the experiments, the Balmer-line emission (the excitation cross-sections are not very different from the ionization cross-section) is toroidally symmetric. Therefore, within this dissertation thesis, we study the plasma formation with a more sophisticated approach by following the motion of the electrons around the torus.

2.3.3 Review of ICRF antenna and matching

An ICRF antenna is usually located at the LFS due to easier access compared to HFS, top or bottom of the vessel. The antennas are designed to couple the highest possible fraction of the generator power to the plasma. The poloidal loop-type antenna shown in Fig. 2.7 with two current-carrying straps are constructed to excite efficiently the Fast Wave (FW) into the plasma. A Faraday screen oriented along the external magnetic field is used to reduce the electric field of the waves along the magnetic field. Fig. 2.8 illustrates a simple ICRF system [33, 34]. The generator power is delivered to the plasma via transmission lines. Generally, the impedance of the plasma load varies from the impedance of generator and transmission lines. Therefore, the part of the generator power is reflected back due to this mismatch. The power transmitted to the antenna $P_{\text{tr,Ant}}$ is the forward minus reflected power $P_{\text{R,Ant}}$:

$$P_{\text{tr,Ant}} = P_{\text{F,Ant}} - P_{\text{R,Ant}} \,. \tag{2.53}$$

To maximize power transmission from the generator to plasma, we need to construct a matching system between the RF generator and antenna. The matching systems are

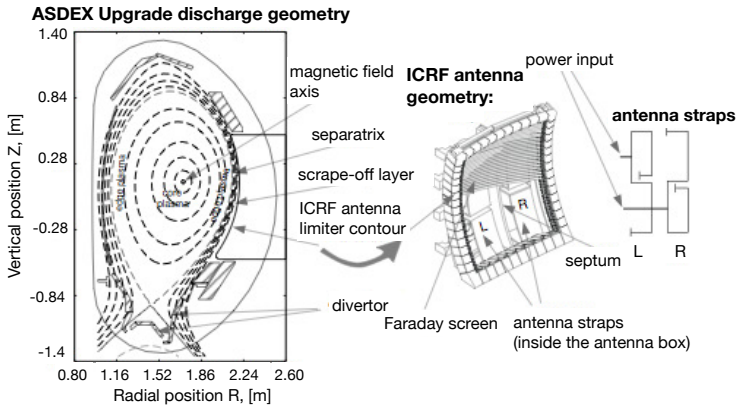

Figure 2.7: Geometry of the two strap ICRF antenna system on ASDEX Upgrade [33].

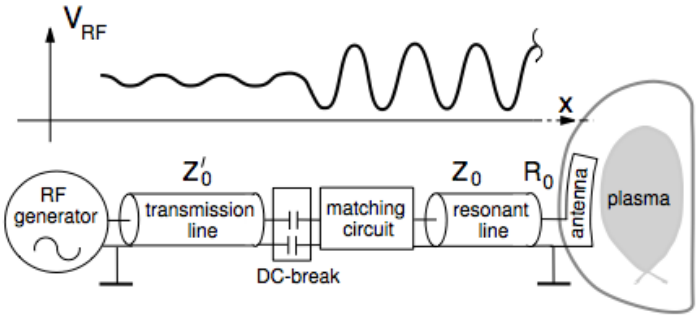

Figure 2.8: Layout of a simple ICRF system [33].

constructed such that the load impedance is real and equal to the source impedance [35, 36].

A standing wave is developed between the antenna and matching system due to the presence of both forward and reflected waves. These standing waves store the energy which is partially dissipated in the transmission lines. The stored wave energy results in a build-up of a high voltage on the antenna strap. This voltage as we will see later is employed for ICRF plasma production. The standing waves can even result in arcing inside the transmission lines [33].

By employing the matching system, we can minimize the power reflection from the matching circuit back to the generator. The ratio between the forward and reflected

power is called the reflection coefficient:

$$\Gamma_L = \frac{V_{\mathrm{R}}}{V_{\mathrm{F}}} = \frac{Z - Z_0}{Z + Z_0}\,, \tag{2.54}$$

where $Z = V/I$ is a complex impedance at any point along the transmission line, and Z_0 is the characteristic impedance of the transmission line [33]. We are interested in the impedance at the end of the transmission line Z_{Ant} where the antenna is located. The transmitted power to the antenna results in

$$P_{\mathrm{tr,Ant}} = \frac{1}{2} V_{\mathrm{Ant}}^2 \mathrm{Re}\left(\frac{1}{Z_{\mathrm{Ant}}^*}\right)\,. \tag{2.55}$$

The antenna impedance Z_{Ant} consist of the real part in the form of resistance R_{Ant} and the imaginary part in an inductive nature $X_{\mathrm{Ant}} = \omega L_{\mathrm{Ant}}$. The imaginary part is inductive in nature and linear with respect to frequency because the typical length of the ICRF antenna strap is shorter than the wavelength for the ICRF frequency range ($f = 5 - 60\,\mathrm{MHz}$). The antenna resistance consists of ohmic losses due to dissipation on antenna structure and transmission line and the actual plasma loading: $R_{\mathrm{Ant}} = R_{\mathrm{v.loss}} + R_{\mathrm{pl}}$ [33, 34]. Finally, we get

$$P_{\mathrm{tr,Ant}} = \frac{V_{\mathrm{Ant}}^2}{2} \frac{R_{\mathrm{v.loss}} + R_{\mathrm{pl}}}{X_{\mathrm{Ant}}^2} \approx P_{\mathrm{G}}\,. \tag{2.56}$$

The power absorbed by the plasma can be expressed based on Eq. (2.56) as

$$P_{\mathrm{pl}} = \frac{V_{\mathrm{Ant}}^2}{2} \frac{R_{\mathrm{pl}}}{X_{\mathrm{Ant}}^2}\,. \tag{2.57}$$

The fraction of the generator power that is coupled to the plasma is called the antenna coupling efficiency and can be written with Eq. (2.56) and Eq. (2.57) as [33, 34]:

$$\eta = \frac{P_{\mathrm{pl}}}{P_{\mathrm{G}}} = \frac{R_{\mathrm{pl}}}{R_{\mathrm{v.loss}} + R_{\mathrm{pl}}}\,. \tag{2.58}$$

Fig. 2.8 illustrates a difference between the relative amplitudes of the waves for regions between (i) the RF generator and matching circuit, and (ii) the matching circuit and antenna strap. As we have already mentioned, the purpose of the matching system is to minimize the reflected power towards the RF generator, and in the ideal case, only the forward wave exists between the matching circuit and the RF generator [33]. The amplitude of the standing waves between the matching circuit and antenna is much higher than the amplitude between the RF generator and matching circuit. This high voltage drops during the plasma breakdown. Therefore, the primary goal of this thesis is to find optimal parameters of the antenna system (generator power, frequency, phasing) and neutral pressure to minimize the breakdown time to assure the antenna system safety. By reducing the breakdown time, we decrease time with the high voltage between the matching circuit and antenna strap. Otherwise, we risk creating a discharge in the antenna box or transmission lines which can potentially destroy the ICRF system [33].

2.4 Conclusion

In this chapter, we introduced the basics concept of discharge initiation in gases. First, we described the electrical breakdown of gases called a DC glow discharge. In this configuration, charged particles are accelerated by a constant electric field $E = V/d$ towards the anode (electrons) and cathode (ions). We defined and explained the Townsend's first coefficient α as a number of ionizations on average caused by one electron per meter along its path. The coefficient depends on the gas type, pressure, electric field strength and distance between the anode and cathode. For a specific ratio of these parameters, an avalanche process is created between the electrodes such that it generates a self-sustained discharge. This parameter dependency is usually visualized by the Paschen curve expressing the minimum voltage dependency on the pressure and distance to initiate the self-sustained discharge between the electrodes.

Then, we studied discharge initiation in toroidal devices during the Ohmic startup. In this process, electrons are accelerated by the constant electric field along the magnetic field line around the torus. We derived formulas to describe the ionization and loss rate during the Ohmic startup. The electron density build-up in time follows exponential increase with the exponent equal to a difference between the ionization and loss rate $n_e \sim \exp\left[(\nu_{\text{ion}} - \nu_{\text{loss}})\, t\right]$. According to the experimental data, and theoretical description by *Papoular* and *Lloyd*, the breakdown time corresponds to a moment when the critical density is reached. This breakdown density is approximated in the Ohmic startup by $n_{bkdn} \approx n/2$, where n is the density of the neutral gas in the vessel. At the end of this section, we presented the comparison of the breakdown times obtained in experiments at DIII-D with the theoretical predictions. Both the theoretical and experimental results were also in a good agreement with modeling results given by my MCC-model `RFdinity1d`. This model will be introduced in the next chapter.

The last part of the chapter gives a summary of discharge initiation by ICRF antennas. We started with the definition of the breakdown in the experiments and its detection. We showed an example discharge obtained during the ICWC experiment at TEXTOR. The breakdown corresponds to a moment when the antenna voltage drops and H_α-signal rises. Following sections presented approximated description of discharge initiation by the ICRF antenna by explaining the movements of electrons in the RF field. These movements are described by an approximation of the RF field in which electrons are accelerated by the ponderomotive force. We introduce the PDM-model assuming the discharge initiation only in front of the ICRF antenna based on the ponderomotive force. The PDM-model derive conditions for the electric field strength and frequency to initiate the ICRF discharge in front of the antenna. Then, we presented the PDMI-model based on the PDM-model, but it also takes into account (1) the ionization along the whole circumference of the torus and (2) the pressure dependency for the ICRF discharge initiation.

References

[1] Ch. Helling et al. *Ionization in atmospheres of Brown Dwarfs and Extrasolar planets. III. Breakdown condition for mineral clouds*. Astrophysical Journal, 767(2), 2013.

[2] A. Lyssoivan et al. *Simulation of ITER full-field ICWC scenario in JET: RF physics aspects*. Plasma Phys. Control. Fusion, 54, 2012.

[3] M. Tripský et al. *Monte Carlo simulation of ICRF discharge initiation at* $\omega_{LHR} < \omega$. In European Conference Abstracts (ECA), volume 38.F. of *http://doi.org/10.1063/1.4864556*, Berlin, Germany, June 2014.

[4] M. Tripský et al. *Discharge initiation by ICRF antenna in IShTAR*. EPJ Web of Conferences, 157:03056, May 30 - June 2 2017.

[5] M. Tripský et al. *Investigation of discharge initiation by ICRF antenna on URAGAN 3-M*. ECA, 40A(P2.052), 2016.

[6] Y. P. Raizer. *Gas Discharge Physics*. Springer–Verlag, Moscow, 1987.

[7] Wikipedia. *Plagiarism — Wikipedia, The Free Encyclopedia*, 2012. `http://en.wikipedia.org/wiki/File:Electron_avalanche.gif#filelinks`.

[8] A. Von Engel. *Ionized Gases (2nd edn)*. Clarendon Press, Oxford, England, 1965.

[9] D. J. Rose et al. Phys. Rev., 104(273), 1956.

[10] A. Fridman and L. A. Kennedy. *Plasma Physics and Engineering*. Taylor and Francis Group, USA, 1991.

[11] 2009. `http://en.wikipedia.org/wiki/File:Paschen_Curves.PNG`.

[12] B. Lloyd et al. *Low Voltage Ohmic and Electron Cyclotron Heating Assisted Startup in DIII-D*. Nuclear Fusion, 31(11):2031–2053, 1991.

[13] R. Papoular et al. *The Genesis of Toroidal Discharges*. Nuclear Fusion, 16(1):37–45, 1976.

[14] L. G. H. Huxley and R. W. Crompton. *The Diffusion and Drift of Electrons in Gases*. Wiley, New York, USA, 1974.

[15] R. Paprok et al. *Simulations of Runaway Electrons*. In WDS'11 Proceedings of Contributed Papers, Part II, pages 208–214, 2011.

[16] R. Jaspers et al. Nuclear Fusion, 36(367), 1996.

[17] A. V. Gurevich et al. Sov. Phys. - JETP, 904(12), 1961.

[18] A. Tanga, P. R. Thomas, and J. G. Cordey. *Tokamak Start-up*. Plenum Press, New York, USA, 1986.

[19] M. D. Carter et al. *Plasma production using radiofrequency fields near or below the ion cyclotron range of frequencies*. Nuclear Fusion, 30(723), 1990.

[20] F. Schuller et al. *Report on Applications of ICWC on ITER*. Technical Report IO/2009/ADM-014 report version 3, ITER - IO, 13115, St. Paul-lez-Durance, France, November 2009.

[21] A. Lyssoivan et al. *Development of ICRF wall conditioning technique on divertor–type tokamaks ASDEX Upgrade and JET*. Journal of Nuclear Materials, 456:337–39, 2005.

[22] A. Lyssoivan et al. *ICRF Plasma Production in TORE SUPRA: Analysis of Antenna Coupling and Plasma Properties*. In Europhysics Conference Abstract of the 26th EPS Conf. on Contr. Fusion and Plasma Physics, Volume 23J:737–740, 1999.

[23] A. Lyssoivan et al. *New scenarios of ICRF wall conditioning in TEXTOR and ASDEX Upgrade*. J. Nucl. Mater., 363-365:1358–1363, 2007.

[24] M. K. Paul et al. *Plasma and Antenna Coupling Characterization in ICRF–Wall Conditioning Experiments*. Fusion Engineering and Design, Volume 87, Issue 2:98–103, 2012.

[25] V.E. Moiseenko et al. Plasma Physics Reports, 39(873), 2013.

[26] T. H. Stix. *Waves in Plasmas*. Springer, New York, USA, 1992.

[27] T. H. Stix et al. *Fast Wave Heating of a Two Component Plasma*. Nucl. Fusion, 15(4):737, 1975.

[28] A. Lyssoivan et al. *Wave aspect of neutral gas breakdown with ICRF antenna in ICWC operation mode*. In European Conference Abstracts. Vol. 38.F. European Conference Abstracts (ECA), Berlin, Germany, June 2014.

[29] A.V. Gaponov et al. JETP, 34(242), 1958.

[30] A. Lyssoivan et al. *Analysis of ICRF plasma production in large scale tokamaks*. Nucl. Fusion, 32:1361–1372, 1992.

[31] M. Verviers. *ICWC in TEXTOR*. In CCIC–09 Meeting, Cadarache, July 2011.

[32] Matěj Tripský. *Monte Carlo Simulation of Initial breakdown Phase of Magnetized toroidal ICRF discharges*. Master's thesis, Universtiteit Gent, Belgium, 2013.

[33] Volodymyr Bobkov. *Studies of high voltage breakdown phenomena on ICRF (Ion Cyclotron Range of Frequencies) antennas*. PhD thesis, Technische Universitat Munchen Fakultat fur Physik, 2003.

[34] Tom Wauters. *Study and Optimization of Magnetized ICRF Discharges for Tokamak Wall Conditioning and Assessment of the Applicability to ITER*. PhD thesis, Universiteit Gent, 2012.

[35] Frederick Fasseur. *Study of an RF-system for plasma production on TOMAS*. Master's thesis, ROYAL MILITARY ACADEMY, Brussels, 2017.

[36] D. M. Pozar. *Microwave Engineering*. John Wiley & Sons (Asia) PTE. LTD., third edition, 1989.

3

MCC-model RFdinity1d for Simulation in Toroidal Devices

In the previous chapter, we have illustrated the PDM-model for a description of the plasma initiation by the ICRF antenna [1]. This model has fundamental drawbacks: (i) neglecting possible ionization outside of the antenna region, (ii) independence on neutral gas pressure, and (iii) overestimating electric field strength and frequency conditions for the breakdown. Some of the drawbacks were addressed by *Schüller et al.* [2], who introduced ionization rate formulas in the PDMI-model for two regions: (i) in front of the antenna, and (ii) outside the antenna region. These formulas contain as well the pressure dependency. To further improve the description of the plasma initiation by the ICRF antenna, we have developed a new model using **Monte Carlo** methods. In this model, we follow the motion of separate electrons around the torus and their collisions with the neutral gas. This section is dedicated to the description of the model (`RFdinity`) developed at LPP-ERM/KMS. The model development started during my master thesis [3] and continued thereafter during the first part of my PhD. In Chapter 5, we will include the plasma self-produced electric field in the model by modifying it into a Particle-In-Cell Monte Carlo collision model.

3.1 Monte Carlo Collision model `RFdinity1d`

Our Monte Carlo model includes the dependency on the frequency, strength, and shape of the vacuum electric field, neutral gas pressure and size of the torus. The model (1D in displacements) follows the motion of guiding centers of electrons around the torus in a narrow bundle of magnetic field lines close to the antenna straps. This 1D approximation for the initial phase of the discharge is justified by experimental observations.

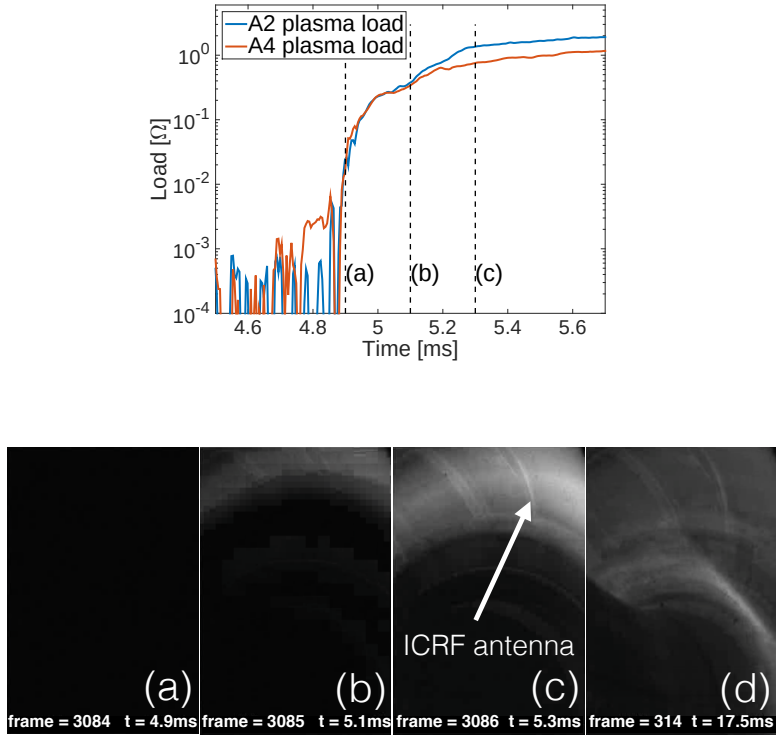

Figure 3.1: (Upper figure) Appearance of the plasma load in front of the A2 and the A4 ICRF antennas on ASDEX Upgrade (shot #29002), and (Bottom figure) images recorded by fast camera during one of our ICWC experiment on ASDEX Upgrade. "Breakdown", experimentally defined as drop in RF voltage (or the appearance of the plasma load), occurs close to antenna strap (image (b)).

Fig. 3.1 shows the discharge initiation in an ICWC experiment on ASDEX Upgrade. It shows the first appearance of the plasma load seen by the antennas (Fig. 3.1(Upper)) and four images of the fast cameras looking from the vessel top toward the ICRF antenna at different times (Fig. 3.1(Bottom)). Image (a) corresponds to the moment when the plasma load appears, while no radiation is registered yet, whereas image (b) $0.2\,\mathrm{ms}$ later contains the first visible appearance of the plasma column following the magnetic field line close to the ICRF antenna. This plasma column in the image (b) is toroidally homogeneous following the magnetic field bundles close to the ICRF antenna. Image (c) illustrates the plasma expansion after the plasma breakdown, and image (d) shows the final poloidally and toroidally homogeneous plasma column $12\,\mathrm{ms}$ after the breakdown moment.

Electrons are accelerated in the antenna vicinity by the toroidal component of the electric field E_z (or $E_{\|}$), which is generated electrostatically and inductively by the ICRF antenna [4]. The generation and shape of this parallel electric field of the an-

tenna are discussed in more details in section 3.1.2. Electrons might be accelerated up to the ionization potential, and an electron avalanche can be triggered. Our model can be used to find optimal conditions for the antenna parameters (electric field strength, frequency and antenna phase) and the neutral pressure inside of the torus to swiftly initiate the discharge in the shortest possible time. To find parameters with the shortest breakdown time is necessary for the antenna safety. Because after the breakdown the antenna voltage drops and the antenna power is coupled into the plasma (See section 2.3).

3.1.1 Description of the electron motion

The charged particles are accelerated in the parallel direction with respect to the magnetic field B_T by the Lorentz force:

$$m_e \frac{\mathrm{d}v_z}{\mathrm{d}t} = F_L = q_e E_z(z) \cos(\omega t) \,, \tag{3.1}$$

where $v_z \times B_T$ term is omitted ($v_z \parallel B_T$). To optimize the run-time of the model, we have divided the circumference length into *A-region* and *B-region*. The A-region represents the antenna region and its vicinity. In this region, the electrons feel the antenna electric field ($|E_z(\text{A-region})| \neq 0$), and their movements are driven by Eq. (3.1). While the B-region is the rest of the circumference where the antenna electric field equal to zero ($|E_z(\text{B-region})| = 0$). The Eq. (3.1) becomes $\frac{\mathrm{d}v_z}{\mathrm{d}t} = 0$ in the B-region. Electrons are moving with a constant velocity, and their trajectory or energy can be changed only via collisions. We distinguish two families of electron collisions: (1) with neutral atom or molecule, and (2) Coulomb collisions (electron-electron or electron-ion). More details concerning the collisions will be introduced in the next section.

The Newton equation of motion in this model for finite time steps are solved by using the explicit forward Euler's method given by:

$$\begin{aligned} z_{\text{new}} &= z_{\text{old}} + v_{\text{old}} \Delta t \\ v_{\text{new}} &= v_{\text{old}} + \frac{q_e}{m_e} E_z(z_{\text{old}}, t) \Delta t \,, \end{aligned} \tag{3.2}$$

where $E_z(z_{\text{old}}, t)$ is the antenna electric field at the position z_{old} and in time t, and Δt is a time step. The time step was chosen equal to $\Delta t = 10^{-11}$s to assure the stability of the forward Euler's method. However, some electrons in the simulations have such high velocities that they cannot fulfill the requested spatial precision of the model set at $\Delta z = 5 \cdot 10^{-4}$m. Therefore, the time step of these electrons was dynamically changed as a function of the velocity. This time step recalculation is only needed in the A-region. The position and velocity of an electron in the B-region are updated only when it enters into the A-region, or it undergoes a collision. This division of the toroidal length into A and B-regions introduces a significant computational improvement because we do not have to follow the electrons in B-regions explicitly with this extremely small time step of $\Delta t = 10^{-11}$ s.

3.1.2 Antenna-near E_z^{RF}-field in vacuum

The antenna vacuum electric field E_z^{RF} is a result of the RF potential difference between the antenna strap and the side parts of the antenna box (antenna protection side RF limiters) [4, 5].

$$E_{z,\text{elst}} \approx V_{\text{RF}}/d\,, \tag{3.3}$$

where V_{RF} is the maximum RF voltage on the strap, d is the toroidal gap between the current strap and the antenna box. The parallel E_z^{RF}-field is also induced inductively from the RF voltage between Faraday screen (FS) bars by the time-varying magnetic flux generated by RF current in the antenna straps if the FS bars are tilted with respect to the toroidal magnetic field lines [4, 5]. Details of a distribution of the vacuum E_z^{RF}-field for the ASDEX Upgrade ICRF antenna with two straps phased in dipole is shown in Fig. 3.2(a) [6]. This field is calculated using the finite-element code HFSS[1]. Important points to note about the typical vacuum E_z^{RF}-field:

- The E_z^{RF} field (i) is highest in the gaps between the antenna straps and side walls, and there (ii) peaks close to the strap edge (Fig. 3.2(a)).
- The amplitude of the E_z^{RF}-field decreases in poloidal direction with a maximum at the feeding point.
- In the radial direction the magnitude of the E_z^{RF}-field decays roughly exponentially, $E_z^{RF}(r) \propto \exp\left[-k_z \Delta r\right]$, with an inverse decay length k_z typical of the antenna-near field spectrum, which depends on the antenna toroidal size and the phasing between the antenna straps [5]. This decay is visible in figure 3.2(b) with a profile of the antenna E_z^{RF}-field in vacuum of an ICRF antenna with one strap at IShTAR machine [7, 8] for two radial positions, $r = 2\,\text{cm}$ and $r = 3\,\text{cm}$.

The toroidal profile of E_z^{RF} for each strap is in the present study approximated by an analytic formula, for example, two Gaussians with opposite sign centered around the two gaps between the strap and the antenna box (Fig. 3.2(b), blue line). Such profile is a good approximation of the E_z^{RF} profiles obtained by 3D CST Microwave Studio simulations with the actual design of a one-strap ICRF antenna. Earlier reported work with simulations for the ITER antenna employed E_z^{RF} profiles [9] obtained by 3D CST Microwave Studio [10] simulations with the actual design of the ICRF antenna.

3.1.3 Initial positions and velocities

Initially, electrons are uniformly distributed around the whole torus circumference with velocities sampled from a Maxwell distribution at $T = 0.5\,\text{eV}$:

$$f(E) = \frac{2}{T\sqrt{\pi}} \sqrt{\frac{E}{T}} \exp\left(-\frac{E}{T}\right), \tag{3.4}$$

[1] HFSS (high frequency structure simulator), www.ansys.com.

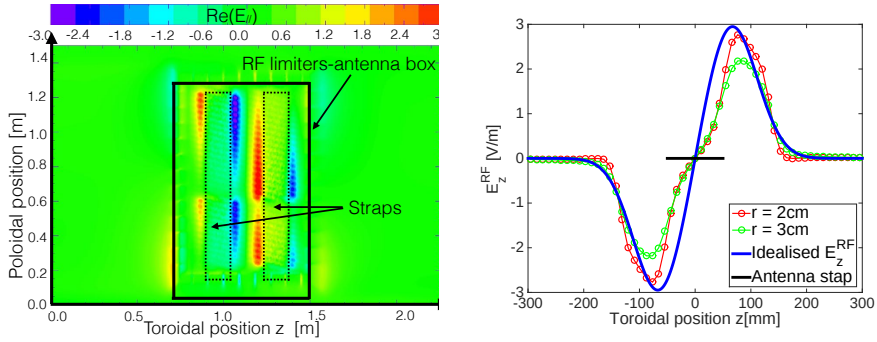

(a) (b)

Figure 3.2: (a) Calculations of $E_{\|}$ by HFSS in front of the ASDEX Upgrade ICRF antenna with two straps ($f = 30\,\mathrm{MHz}$, dipole phasing). Antenna strap locations are shown schematically with dashed contours and antenna limiters with solid line. The ASDEX Upgrade ICRF antenna configuration is shown in Fig. 2.7. (b) The toroidal profile of the vacuum E_z^{RF}-field for IShTAr one strap antenna (antenna strap width $w_{\mathrm{ant}} = 10\,\mathrm{cm}$, $f = 10\,\mathrm{MHz}$, $P = 1\,\mathrm{W}$) at two radial positions from the antenna strap, $r = 2\,\mathrm{cm}$ and $r = 3\,\mathrm{cm}$. The idealized profile of the E_z^{RF}-field approximated by the sum of two Gaussians with opposite sign centered around the two gaps between the strap and the antenna box.

According to the direct random sampling from Maxwellian, the energy is sampled as

$$E \longleftarrow kT\left[-\log\xi_1 - \log\xi_2 \cos^2\left(\frac{\pi\xi_3}{2}\right)\right], \tag{3.5}$$

where ξ_1, ξ_2 and ξ_3 are three different random numbers [11]. All random numbers used in my models are uniformly distributed between 0 and 1, and uncorrelated. The velocity magnitude $|\vec{v}|$ from the sampled energy is then $|\vec{v}| = \sqrt{2E/m_e}$. The velocity directions in 3D isotropic distribution, $\vec{\Omega} = (a\,,\, b\,,\, c)$, are sampled according to

$$\begin{aligned} a &\longleftarrow 2\cdot\xi_4 - 1 \\ b &\longleftarrow \sqrt{1-a^2}\cdot\cos(2\pi\xi_5) \\ c &\longleftarrow \sqrt{1-a^2}\cdot\sin(2\pi\xi_5) \end{aligned}$$

where ξ_4 and ξ_5 are two different random numbers between 0 and 1. Finally, the velocity components $(v_x\,,\, v_y\,,\, v_z)$ equal to

$$\begin{aligned} v_x &= |\vec{v}|b \\ v_y &= |\vec{v}|c \\ v_z &= |\vec{v}|a\,. \end{aligned} \tag{3.6}$$

Collisions between the electrons and neutral atoms are treated in the 3D velocity space $(v_x,\, v_y,\, v_z)$, where v_z is the parallel velocity component (direction of the magnetic field B_T) and $v_\theta = \sqrt{v_x^2 + v_y^2}$ the perpendicular velocity component [12]. However,

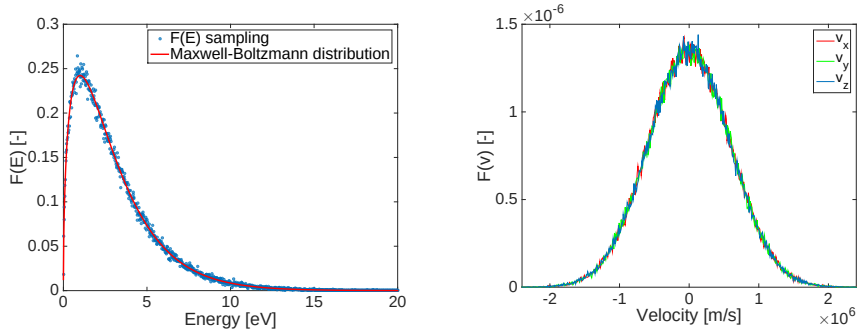

(a) (b)

Figure 3.3: (a) Maxwell-Boltzmann energy distribution Eq. (3.4) and comparison with sampled Maxwell-Boltzmann distribution produced by Eq. (3.5), (b) Sampled velocity components v_x, v_y, v_z corresponding to the sampled energy.

it is important to emphasize that the model does not include the cyclotron gyration. The electrons are accelerated solely in the parallel direction, but during the collisions in the 3D velocity space, part of their parallel velocity component is scattered into the perpendicular velocity. By this mechanism, the electrons slow down in the toroidal direction not only by the energy loss during the inelastic collision but also by the scattering. Fig. 3.3 shows an example of sampled energy and velocity distributions. The plot was produced by a sampling of 10^5 electrons with the initial electron temperature $T_0 = 2\,\mathrm{eV}$. The left figure demonstrates agreement between the sampled energy distribution (Eq. (3.5)) and a Maxwell-Boltzmann energy distribution (Eq. (3.4)). Right figure illustrates the isotropic velocities generated from sampling by Eq. (3.6).

3.1.4 Monte Carlo Collision schema

The model uses Monte Carlo Collision Schema (**MCCS**) on inelastic collision in hydrogen and helium gas. The model samples an actual path length of each electron between collisions according to the MC procedure given by

$$\lambda^{MC} = -\frac{1}{n\sigma_T(\epsilon)} \log(1-\xi)\ , \tag{3.7}$$

where $\sigma_T(\epsilon)$ is the sum of cross sections for all collisions between the electron and the neutral gas with density n for a given energy ϵ and ξ is a random number $(0 \leq \xi < 1)$ [11]. This equation represents a sampling from the negative exponential distribution with the mean value $(n\sigma_T(\epsilon))^{-1}$ called the mean free path length. For example for hydrogen, the path length between electrons and hydrogen molecules H_2, hydrogen molecule ions H_2^+ and hydrogen atom ions H^+ is equal to

$$\lambda^{MC} = -\frac{1}{n_{H_2}\sigma_T^{e-H_2}(\epsilon) + n_{H_2^+}\sigma_T^{e-H_2^+}(\epsilon) + n_{H^+}\sigma_T^{e-H^+}(\epsilon)} \log(1-\xi)\ . \tag{3.8}$$

However, the hydrogen ion species start to play a role only at the later stage of the discharge initiation. At the start, the neutral gas density is much larger ($n_{H_2} \gg n_{H_2^+}$ and $n_{H_2} \gg n_{H^+}$) and therefore, only the inelastic collisions between the electrons and hydrogen molecules are the dominant ones at the early stage of the discharge initiation.

Index	Collision species	Before	After
1	Ionization of H_2	$e + H_2$	$e + H_2^+ e$
2	Vibration excitation of H_2	$e + H_2$	$e + H_2^*$
3	Electronic excitation of H_2	$e + H_2$	$e + H_2^*$
4	Dissociation of H_2	$e + H_2$	$e + H + H$
5	Dissociation ionization of H_2	$e + H_2$	$e + H^+ + H + e$
6	Ionization of H_2^+	$e + H_2^+$	$e + H^+ + H^+ + e$
7	Dissociation of H_2^+	$e + H_2^+$	$e + H^+ + H$
8	Dissociation recombination of H_2^+	$e + H_2^+$	$H + H^*$
9	Recombination of $H+$	$e + H^+$	$H + h\nu$

Table 3.1: Included collisions in the MCC model `RFdinity1d` [13, 14].

3.1.4.1 Probability array

When a collision takes place, the type of the collision is decided by the MC procedure. For example, the MCC model `RFdinity1d` for hydrogen plasma contains 9 inelastic collisions: 5 collisions between electron and hydrogen molecule H_2, 3 collisions between electron and hydrogen molecular ion H_2^+ and one collision between electron and hydrogen ion H^+. These collisions are summarized in Table 3.1. We define the cumulative probability array P_j for an electron with energy ϵ undergoing a collision of type j (corresponding to the index in Table 3.1) as

$$P_j(\epsilon) = \frac{\sum\limits_{s\in(H_2,H_2^+,H^+)} \sum\limits_{k=1}^{k\leq j} n_s \sigma_k(\epsilon)}{n_{H_2}\sigma_T^{e-H_2}(\epsilon) + n_{H_2^+}\sigma_T^{e-H_2^+}(\epsilon) + n_{H^+}\sigma_T^{e-H^+}(\epsilon)} \tag{3.9}$$

where $\sigma_k(\epsilon)$ is the cross section for the reaction k (index in Table 3.1), n_s is the density of the s-th target species (n_{H_2}, $n_{H_2^+}$, n_{H^+}), $\sigma_T(\epsilon)$ is the sum of all cross sections at energy ϵ for a given type ($e - H_2$, $e - H_2^+$, $e - H^+$). By construction, the cumulative probability array P_j, Eq. (3.9), is an array of numbers between 0 and 1. The width of each interval reflects the weight of the collision type at the energy ϵ.

When a collision occurs a random number is generated. The interval into which this number falls, decides which collision takes place. Cross sections for the inelastic collisions are based on experimental and theoretical fit constants [13]. The code uses

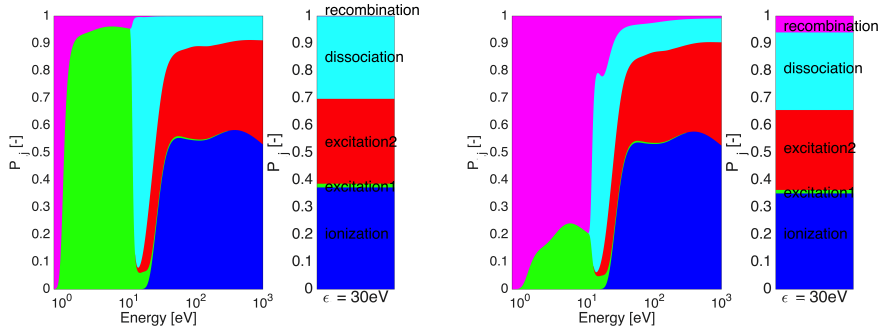

Figure 3.4: The probability array $P_j(\epsilon)$ as a function of the electron energy, and a zoom at the probability function $P_j(\epsilon)$ for $\epsilon = 30\,\mathrm{eV}$. Two scenarios: (a) $n_{H_2} = 10^{18}\,\mathrm{m}^{-3}$ and $n_{H_2^+} = 10^{16}\,\mathrm{m}^{-3}$; (b) $n_{H_2} = 10^{18}\,\mathrm{m}^{-3}$ and $n_{H_2^+} = 8 \cdot 10^{17}\,\mathrm{m}^{-3}$.

these external data files to calculate the cross section for each electron as a function of its energy. We group all inelastic collisions of same type (ionization, excitation, dissociation, etc.) and with similar threshold energies. List of all inelastic collisions included in the `RFdinity1d` model for hydrogen and helium are attached in Appendix A.

The probability array $P_j(\epsilon)$ as a function of the electron energy for hydrogen is shown in Fig. 3.4 for two different scenarios. For a better readability of the probability array, we do not plot all inelastic collisions in hydrogen. We plot four out of five inelastic reaction collisions with hydrogen molecule H_2 (ionization, excitation 1, excitation 2 and dissociation) and only one out of three collision with hydrogen molecular ion H_2^+ (recombination). Both figures zoom in energy level $\epsilon = 30\,\mathrm{eV}$ for a better visualization of the probability arrays and their ratios between each reaction types. Two scenarios correspond to different density ratios between hydrogen molecules and hydrogen molecule ions. Fig. 3.4(a) corresponds to the scenario with $n_{H_2} \gg n_{H_2^+}$ and Fig. 3.4(b) represents the scenario in which both densities are similar, $n_{H_2} \simeq n_{H_2^+}$. It demonstrates that the probability array varies during the simulations due to density evolution. When hydrogen molecules are dominant targets for the electrons, the inelastic collisions with hydrogen molecules have a much higher proportion of the probability array for the whole energy spectrum. In the second scenario, the probability array changes especially for low energetic collisions with a larger proportion of the electron collisions with hydrogen molecule ions.

3.1.4.2 Post-collision energy

When a collision type is assigned to an electron undergoing the collision, the model calculates a post-collision energy of an incident electron. In case of ionization, the MC algorithm divides energy between the newborn electron (rejected electron) and incoming electron according to the scheme described by *Vahedi* and *Surendra* [15],

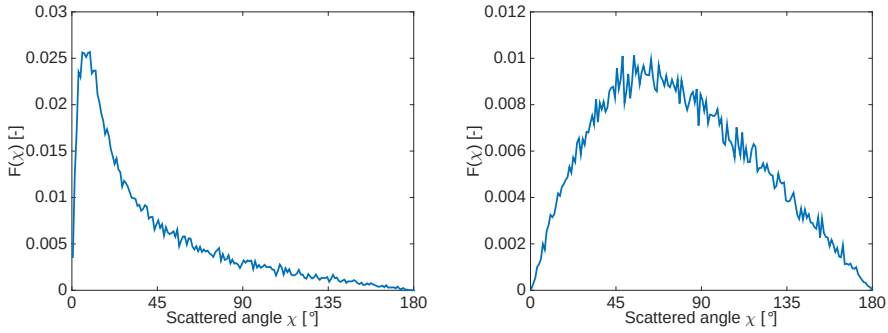

(a) (b)

Figure 3.5: The scattered angle χ according to Eq. (3.12) with distribution over interval $[0°, 180°]$ for (a) high incoming energy electron (300 eV), and (b) low incoming energy electron (2 eV). Both distributions were produced with 10^5 collisions.

and by *Opal* et al. [16].

The incident electron scatters through an angle χ determined with an approximate differential cross section of the electron given by

$$\frac{\sigma\left(\epsilon_{\text{inc}}, \chi\right)}{\sigma\left(\epsilon_{\text{inc}}\right)} = \frac{\epsilon_{\text{inc}}}{4\pi\left[1 + \epsilon_{\text{inc}} \sin^2\left(\chi/2\right)\right] \log\left(1 + \epsilon_{\text{inc}}\right)}, \tag{3.10}$$

where ϵ_{inc} is the energy of the incident electron in eV. This equation has solution for $\cos\chi$ from

$$\xi_1 = \frac{\int_0^{\chi} \sigma\left(\epsilon_{\text{inc}}, \chi'\right) \sin\chi' \mathrm{d}\chi'}{\int_0^{\pi} \sigma\left(\epsilon_{\text{inc}}, \chi'\right) \sin\chi' \mathrm{d}\chi'}, \tag{3.11}$$

where ξ_1 is a random number, $0 \leq \xi_1 < 1$ to get

$$\cos\chi = \frac{2 + \epsilon_{\text{inc}} - 2\left(1 + \epsilon_{\text{inc}}\right)^{\xi_1}}{\epsilon_{\text{inc}}} \tag{3.12}$$

Eq. (3.12) gives the scattered angle χ independently on the collision type. The angle χ is strongly dependent on the incoming electron energy ϵ_{inc}. The dependency is shown in Fig. 3.5 for two cases of the incoming energy. When the incoming energy is high ($\epsilon_{\text{inc}} = 300$ eV), Eq. (3.12) gives mostly small scattering angles (forward scattering). Fig. 3.5(a) demonstrates an existence of the peak around $10°$ for this incoming energy. While, for the case with the low incoming energy ($\epsilon_{\text{inc}} = 2$ eV), the scattering is more isotropic Fig. 3.5(b).

The azimuth angle ϕ is uniformly distributed in the interval $[0,\ 2\pi]$ and is calculated as

$$\phi = 2\pi\xi_2, \tag{3.13}$$

where ξ_2 is another random number between 0 and 1.

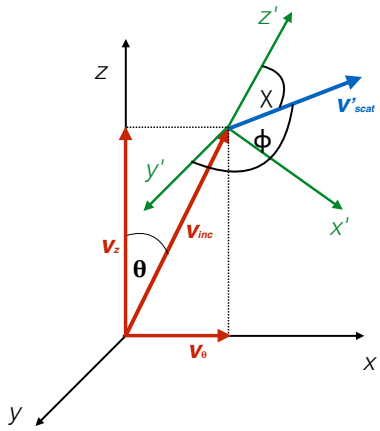

Figure 3.6: Vector diagram for collisions between the electron and the neutral atom with its scatted and azimuth angles.

Knowing the scattering angles χ and ϕ, the scattered velocity $\vec{v}_{\text{scat}}$ is obtained based on geometric considerations illustrated in Fig. 3.6. Directions of scattered velocities are chosen according to the following schema: vector $\vec{v}_z$ is parallel to the z axis and vector $\vec{v}_\theta$ is set parallel to x axis in (x, y, z) frame. Then a collision frame (x', y', z') is defined with the z' axis oriented parallel to the incoming vector $\vec{v}_{\text{inc}}$ in x-z plane. It means that the collisions frame (x', y', z') is the frame (x, y, z) rotated around the y axis though the angle $\theta = \text{atan}(v_\theta / v_z)$. The scattered velocity vector $\vec{v}'_{\text{scat}}$ is located in (x', y', z') frame defined by the scattering angles χ and ϕ. Finally the scattered velocity vector $\vec{v}'_{\text{scat}}$ is transformed back into (x, y, z) frame as

$$\vec{v}_{\text{scat}} = T_y(\theta)\,\vec{v}'_{\text{scat}} = \begin{pmatrix} \cos\theta & 0 & \sin\theta \\ 0 & 1 & 0 \\ -\sin\theta & 0 & \cos\theta \end{pmatrix} |\vec{v}'_{\text{scat}}| \begin{pmatrix} \sin\chi\sin\phi \\ \sin\chi\cos\phi \\ \cos\chi \end{pmatrix}. \tag{3.14}$$

For non-ionization reaction collisions, the scattered electron energy (or velocity $|\vec{v}'_{scat}|$) is simply a difference between the incoming energy and the potential energy of specific reaction: $\epsilon_{\text{scat}} = \epsilon_{\text{inc}} - \Delta E$. While in the case of ionization, next to the scattered electron (with the scatter energy ϵ_{scat}), we have a newborn electron as well ejected with the energy ϵ_{ej}. Energy balance for the ionization can be expressed as

$$\epsilon_{\text{scat}} + \epsilon_{\text{ej}} = \epsilon_{\text{inc}} - \Delta E \tag{3.15}$$

Therefore, we have to define an algorithm dividing the energy between the scattered and ejected electrons. In the model developed for my Master Thesis [3], we used an algorithm in which the remaining energy after the ionization was divided between the scattered and ejected electron as

$$\epsilon_{\text{ej}} = \xi \cdot (\epsilon_{\text{inc}} - \Delta E_{\text{ion}}) \tag{3.16}$$

$$\epsilon_{\text{scat}} = (1 - \xi) \cdot (\epsilon_{\text{inc}} - \Delta E_{\text{ion}}) \tag{3.17}$$

where ξ is a random number between 0 and 1. This rather simple implementation undervalues a fundamental difference between the ejected and scattered electron. Therefore, we use a different algorithm in the `RFdinity1d` model. In this algorithm introduced by *Opal* et al. [16], the scattered electron takes a substantial proportion of the remaining energy. It uses a simplified form of the differential ionization cross section to derive an equation to sample the ejected energy as:

$$\epsilon_{\text{ej}} = B(\epsilon_{\text{inc}}) \tan\left[\xi \arctan\left(\frac{\epsilon_{\text{inc}} - \Delta E_{\text{ion}}}{2B(\epsilon_{\text{inc}})}\right)\right], \tag{3.18}$$

where $B(\epsilon_{\text{inc}})$ is a known function, for hydrogen $B(\epsilon_{\text{inc}}) \simeq 8.3\,\text{eV}$ and for helium $B(\epsilon_{\text{inc}}) \simeq 15.8\,\text{eV}$ [16]. When the incident energy ϵ_{inc} is just above the threshold energy ΔE_{ion}, i.e., $(\epsilon_{\text{inc}} - \Delta E_{\text{ion}})/(2B(\epsilon_{\text{inc}}) \ll 1$, Eq. (3.18) reduces to

$$\epsilon_{\text{ej}} \simeq \xi \cdot \left(\frac{\epsilon_{\text{inc}} - \Delta E_{\text{ion}}}{2}\right). \tag{3.19}$$

It means that on average the remaining energy is divided equally between the two electrons. After the energy assignment, the calculation of scattering and azimuth angles χ and ϕ is performed according to Eq. (3.12) and Eq. (3.13) for the scattered and ejected electrons.

Fig. 3.7 plots energy spectra of the ejected electron calculated by two methods: algorithm (A) Eq. (3.16) and algorithm (B) Eq. (3.18) for two scenarios: low incoming energy $\epsilon_{\text{inc}} = 30\,\text{eV}$ in Fig. 3.7(a), and (b) high incoming energy $\epsilon_{\text{inc}} = 300\,\text{eV}$ in Fig. 3.7(b). First, we can see that the ejected energy spectrum is homogeneous for the algorithm (A) Eq. (3.16). It means that there is no distinction between the ejected and scattered electrons. Whereas for the algorithm (b) Eq. (3.18), we can observe in Fig. 3.7 that the ejected electron has energy always smaller than $(\epsilon_{\text{inc}} - \Delta E_{\text{ion}})/2$. Furthermore, it is evident that the ejected electron is more likely to have much smaller energy than the scattered one. This behavior is especially visible for the high incoming energy in Fig. 3.7(b) where the ejected electron spectrum has a clear peak for the low ejected energy.

3.1.5 Coulomb collisions

The model also includes interactions between the charged particles, i.e., electron-ion Coulomb collisions and electron-electron Coulomb collisions. In our model, we use the Monte Carlo binary collision model proposed by T. Takizuka & H. Abe (**TA-method**) [17].

The collision model of Takizuka and Abe

Coulomb collisions in plasma can be recognized as many continuous small-angle binary collisions between charged particles. The Fokker-Planck equation describes the time evolution of the particle distribution in a spatially homogeneous, non-equilibrium

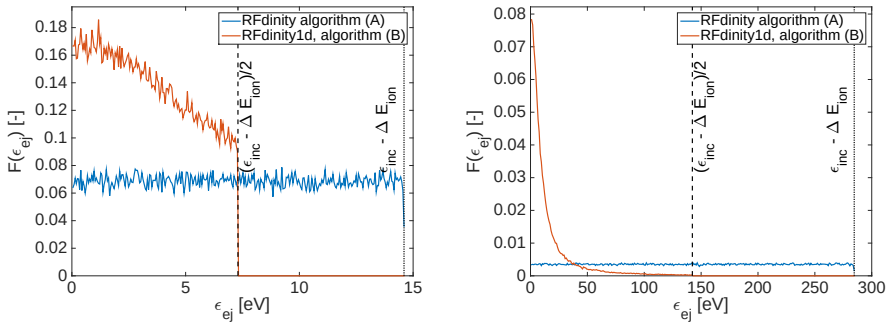

(a) (b)

Figure 3.7: Energy spectrum of 10^5 ejected electrons calculated with algorithm (A) Eq. (3.16) and algorithm (B) Eq. (3.18) for two levels of the incoming energy: (a) $\epsilon_{\text{inc}} = 30\,\text{eV}$ and (b) $\epsilon_{inc} = 300\,\text{eV}$.

plasma as:

$$\frac{\partial f_\alpha}{\partial t} = \left(\frac{\delta f_\alpha}{\delta t}\right)_{\text{coll}}, \tag{3.20}$$

where f_α is a distribution function of the α species and $\left(\frac{\delta f_\alpha}{\delta t}\right)_{\text{coll}}$ is a collision operator:

$$\left(\frac{\delta f_\alpha}{\delta t}\right)_{\text{coll}} = -\sum_\beta \frac{\partial}{\partial v_j}\frac{e_\alpha^2 e_\beta^2 \log\Lambda}{8\pi\epsilon_0 m_\alpha}\int \mathrm{d}v' \left[\frac{\delta_{jk}}{u} - \frac{u_j u_k}{u^3}\right]\left[\frac{f_\alpha}{m_\beta}\frac{\partial f'_\beta}{\partial v'_k} - \frac{f'_\beta}{m_\alpha}\frac{\partial f_\alpha}{\partial v_k}\right], \tag{3.21}$$

where $\vec{u} = \vec{v_\alpha} - \vec{v_\beta}$, $u = |\vec{u}|$ and $f'_\beta = f_\beta(\vec{v'})$. Bobylev and Nanbu [18] derived approximated solution of the Fokker-Planck equation over a time step Δt given by

$$f_\alpha\left(\vec{v}, t+\Delta t\right) = \sum_{\beta=1}^{n} \pi_{\alpha\beta}\int_{R^3\times S^2} \mathrm{d}\vec{v_\beta}\mathrm{d}\vec{n} D_{\alpha\beta}\left(\frac{\vec{g}\cdot\vec{n}}{g}, A_{\alpha\beta}\frac{\Delta t}{g^3}\right) f_\alpha(\vec{v'_\alpha}, t) f_\beta(\vec{v'_\beta}, t)\,, \tag{3.22}$$

and a set of conditions on the kernel $D_{\alpha\beta}$ to ensure that f is the approximate solution of the Fokker-Planck equation [18, 19].

The TA-method is based on Monte Carlo simulations of the integral (Eq. (3.22)) for a specific choice of $D_{\alpha\beta}$ [17]:

$$D_{\text{TA}}(\mu,\tau) = (2\pi)^{-1}(2\pi)^{-\frac{1}{2}}\exp\left(-\frac{\zeta^2}{2\tau}\right)\left(\frac{\mathrm{d}\zeta}{\mathrm{d}\mu}\right) \tag{3.23}$$

in which

$$\tau = \langle\zeta^2\rangle = \left(\frac{e_\alpha^2 e_\beta^2 n_L \log\Lambda}{8\pi\epsilon_o^2 m_{\alpha\beta}^2 u^3}\right)\Delta t_{\text{CC}}\,. \tag{3.24}$$

The scattering angle θ is defined by

$$\begin{aligned} \theta &= 2\arctan\zeta \\ \mu &= \cos\theta\,, \end{aligned} \tag{3.25}$$

where e_α and e_β are the electric charges for the species α and β, n_L is the smaller density of the particle species α and β, Λ is the Coulomb logarithm, $u = |\vec{v_\alpha} - \vec{v_\beta}|$ is the relative speed, Δt_{CC} is the time step of Coulomb collisions (varying from the time step used in the equation of motion, Eq. (3.2)), and $m_{\alpha\beta} = m_\alpha m_\beta/(m_\alpha + m_\beta)$ is the reduced mass [20, 21].

The Monte Carlo algorithm of the TA-method consists of 4 steps described in [20]:

1. Randomly select two particles with velocity v_α and v_β from the distributions f_α and f_β. It must be done in a way that no particle is selected more than once. This corresponds to the term $f_\alpha f_\beta$ in Eq. (3.23).

2. Sample a value of $\mu = \cos(2\arctan\zeta)$, where ζ has to be a sampled random number from a Gaussian distribution with mean 0 and variance $\tau = \langle\zeta^2\rangle$. Variance τ is defined by Eq. (3.24) using $u = |v_\alpha - v_\beta|$. The scattered angle θ is equal to $2\arctan\zeta$. This step represents the factor $(2\pi)^{-\frac{1}{2}} \exp\left(-\frac{\zeta^2}{2\tau}\right)\left(\frac{\mathrm{d}\zeta}{\mathrm{d}\mu}\right)$ of the kernel D_{TA} in Eq. (3.23).

3. The azimuth angle ϕ is uniformly sampled from the interval $[0,\, 2\pi]$. This is the factor $(2\pi)^{-1}$ in the kernel in D_{TA}.

4. The new velocities $\vec{v}'_\alpha$ and $\vec{v}'_\beta$ with known scattered θ and azimuth ϕ angles are calculated by

$$\begin{aligned} \vec{v}'_\alpha &= \vec{v}_\alpha + \frac{m_{\alpha\beta}}{m_\alpha}\Delta\vec{u} \\ \vec{v}'_\beta &= \vec{v}_\beta - \frac{m_{\alpha\beta}}{m_\beta}\Delta\vec{u}\,, \end{aligned} \tag{3.26}$$

where Δu is given by

$$\begin{aligned} \Delta u_x &= \frac{u_x}{u_\perp}u_z\sin\theta\cos\phi - \frac{u_y}{u_\perp}u\sin\theta\sin\phi - u_x(1-\cos\theta) \\ \Delta u_y &= \frac{u_y}{u_\perp}u_z\sin\theta\cos\phi + \frac{u_x}{u_\perp}u\sin\theta\sin\phi - u_y(1-\cos\theta) \\ \Delta u_z &= -u_\perp\sin\theta\cos\phi - u_z(1-\cos\theta) \\ \vec{u} &= \vec{v}_\alpha - \vec{v}_\beta \\ u_\perp &= \sqrt{u_x^2 + u_y^2}\,. \end{aligned} \tag{3.27}$$

We tested the TA-method implementation and its behavior. The `RFdinity1d` model was modified to neglect all inelastic collisions and acceleration by the antenna parallel field. In the end, the model follows only the motion of electron moving freely

around the torus. This version of the model then studies only the Coulomb collisions between electrons and ions using the TA-method.

The first step of the TA-method is randomly select two particles from the f_e (electron) and f_i (ion) energy distributions. Unfortunately, the model does not follow the motion of ions, and thus we do not have the exact shape of the ion energy distribution. For the TA-method test, we decided to sample the ions during the Coulomb collisions from a Maxwell energy distribution with temperature T_i. This temperature is lower than the mean temperature of electrons. Therefore, electrons transfer energy to ions and the ion temperature T_i will change during a simulation. For the test, the initial energy distribution of electrons corresponds to a square distribution with energies between 0 and 6eV. Fig. 3.8(a) plots the initial electron distribution in blue color.

If the Coulomb collisions are implemented correctly, the initial square distribution of the electrons should evolve into a Maxwell distribution, and both electrons and ions should have the same mean energy. We can see in Fig. 3.8(a) that indeed the initial square distribution of the electrons is transformed into a Maxwell energy distribution with $T_e = 1.5\,\mathrm{eV}$. During this transformation, the majority of high energetic electrons in the square distribution loses the energy with slower ions transforming this energy into ions population. The ion cloud corresponds in this simulation to a Maxwell energy distribution at $T_{i,0} = 1\,\mathrm{eV}$. The ion temperature increases in time and at the end the ions population reach an equilibrium with the electrons population with the same Maxwell energy distribution at $T_i \approx T_e \approx 1.5\,\mathrm{eV}$.

Furthermore, Fig. 3.8(b) demonstrates that both species reach equilibrium for the mean energy $\langle\epsilon\rangle \approx 2.25\,\mathrm{eV}$. This mean energy corresponds to the temperature of $T = 1.5\,\mathrm{eV}$ from $\langle\epsilon\rangle = \frac{3}{2}kT$. The initial mean energy of the system (electrons and ions) is equal to $\langle\epsilon_T\rangle = 4.5\,\mathrm{eV}$ as the mean energy of the initial square for electrons is $\langle\epsilon_{e,0}\rangle = 3\,\mathrm{eV}$ and the ion population with a Maxwell distribution has initially $\langle\epsilon_{i,0}\rangle = 1.5\,\mathrm{eV}$. The total energy of $\langle\epsilon_T\rangle = 4.5\,\mathrm{eV}$ is conserved through the whole simulation.

In the next subsections, we give a summary of each for the TA-method implementation of the Coulomb collision (electron-ion, electron-electron) in the `RFdinity1d` model to simulate the discharge initiation in toroidal machines by ICRF antennas.

Electron-ion Coulomb collisions in the `RFdinity1d` model

The electron-ion collision frequency equals to

$$\nu_{cc}^{ei} = \frac{e_\alpha^2 e_\beta^2 n_L \log\Lambda_{ei}}{2\pi\epsilon_o^2 m_{\alpha\beta}^2 v_T^3}\,, \tag{3.28}$$

where n_L is the smaller density of the electrons or ions ($n_L = n_e = n_i$), $v_T = \sqrt{\frac{3k_BT}{m_e}}$ is the thermal velocity. The typical electron energy distribution in our simulations does not correspond to a Maxwell distribution, but it consists of a low energy Maxwell-like distribution with a high-velocity tail. Therefore, the thermal velocity cannot be calculated via $\langle E\rangle = \frac{3}{2}k_BT$, and it is approximated in our model by assuming that the electron thermal velocity equals to a median of the electron velocities,

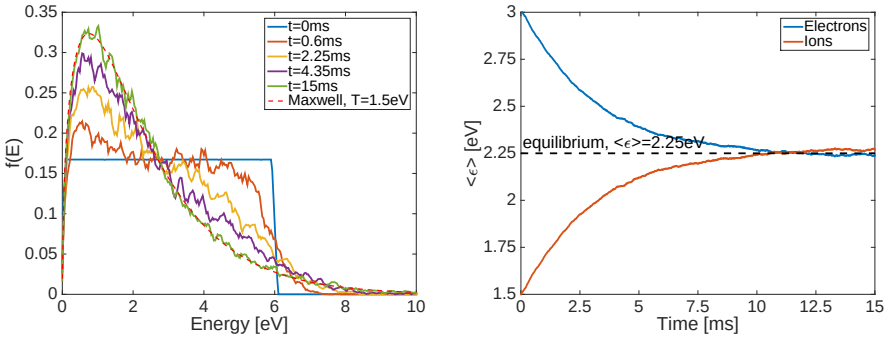

(a) (b)

Figure 3.8: (a) Evolution of electron energy distribution in time, initial square distribution tends to convert into a Maxwell energy distribution, (b) Time evolution of the mean electron and ion energy $\langle\epsilon\rangle$, the equilibrium energy is highlighted by the black line at $\langle\epsilon\rangle = 2.25\,\mathrm{eV}$.

$v_T = \mathrm{median}(f_e(v))$. Λ_{ei} is the Coulomb logarithm for electron ion collisions calculated from [22].

We already mention that the `RFdinity1d` model follows only the motion of electrons, as such, we have the exact information only regarding the electron distribution f_e (f_α in TA-method). We have decided to approximate the ion distribution function f_i (f_β in TA-method) by a Maxwell energy distribution. The TA-method for electron-ion Coulomb collisions:

1. A particle pair undergoing Coulomb collisions is selected, an electron is randomly picked from the electron distribution, an ion is sampled from a Maxwell distribution. In the model, we assume that ions created via ionizations of a neutral atom are sampled with the energies corresponding to a Maxwell distribution with the initial temperature $T_{i,0} = 0.5\,\mathrm{eV}$, which is gradually increasing due to an energy gain from the Coulomb collisions with energetic electrons.

2. For a calculation of the scattering angle between the electron and ion according to the TA-method, we need to estimate the τ parameter in Eq. (3.24). All terms in this equation are straightforward to calculate except the time step of Coulomb collisions Δt_{CC}. This time step varies from the time step used in the simulations $\Delta t = 10^{-11}\,\mathrm{s}$. The Δt_{CC} is estimated based on the collision frequency of Coulomb collisions ν_c in Eq. (3.28) to fulfill the condition, $\nu_c \Delta t_{CC} < 1$, given by the TA-method [17, 20]. The safety margin was set at 10 $\Delta t_{\mathrm{CC}} = 10/\nu_c$. However at the low electron densities the value of ν_c can be extremely small, and the time step Δt_{CC} would be large. Therefore we decided to set the maximum possible time step of Coulomb collisions at $\Delta t_{\mathrm{CC}} = 10^{-6}\,\mathrm{s}$.

   Knowing the parameter τ, we estimate ζ by sampling it from a Gaussian distri-

bution with mean 0 and variance τ:

$$\zeta = \sqrt{-2\tau \cdot \log \xi}\,, \tag{3.29}$$

where ξ is a random number between 0 and 1 [11]. Finally, the scattered angle θ is calculated as $\theta = 2 \arctan \zeta$ [17, 20].

3. The azimuth angle ϕ is sampled as $\phi = 2\pi\xi$, where ξ is a random number between 0 and 1.

4. The last step is to insert the calculated angles θ and ϕ into the system of equations 3.26 to calculate the post-collision velocities.

Electron-electron Coulomb collisions in the `RFdinity1d` model

In the previous section describing the Electron-Ion Coulomb collisions implementation in our model, we have shown that it is a process of an electron colliding with an ion cloud corresponding to a Maxwell distribution. We decided to apply the same approach for Electron-electron Coulomb collisions, such that electrons are colliding with an electron cloud with the energy distribution of electrons in the system.

Neglecting Coulomb collisions in the model

We already mentioned that at the beginning of a simulation, Coulomb collisions could be neglected due to low collision rates when compared with the electron-neutral collisions [9, 23]. The Coulomb collision rates for both electron-ion and electron-electron collisions depend on the electron density $\nu_{CC} \sim n_e$ (Eq. (3.28)). Therefore, we include the Coulomb collisions during a simulation only after a certain threshold electron density is reached.

We determine the threshold electron density above which Coulomb collisions cannot be neglected by a comparison of their collision rates with the electron-neutral reaction rates. We found that the electron-ion Coulomb collisions starts to dominate above the electron density $n_e = 10^{17}\,\mathrm{m}^{-3}$. We use a safety margin of 10^3 to employ our implementation of the TA-method in the model above the threshold density $n_e^{\mathrm{tr}} = 10^{14}\mathrm{m}^{-3}$. The electron-electron Coulomb collisions begin to play a role at lower density around $10^{14}\,\mathrm{m}^{-3}$ according to our analysis. Setting the same safety margin of 10^3, we obtain the threshold density for the electron-electron Coulomb collisions at $n_e^{\mathrm{tr}} = 10^{11}\,\mathrm{m}^{-3}$. However, running the model, we see the first effect of the electron-electron Coulomb collisions above $10^{15}\,\mathrm{m}^{-3}$. For that reason, we set both threshold densities at $n_e = 10^{14}\,\mathrm{m}^{-3}$.

3.1.6 Electron losses in the `RFdinity1d` model

The model includes electron losses due to **recombination** and **electron drifts**. Both mechanisms become relevant only at higher electron densities ($n_e > 10^{15}\,\mathrm{m}^{-3}$ for recombinations) and in the later stage of the discharge initiation (electron drifts).

The model is a closed system of particles, e.g. for hydrogen:

$$N_{H_2} + 2N_H + N_{H_2^+} + 2N_{H^+} = \text{const.} \tag{3.30}$$

$$N_{H_2^+} + N_{H^+} = N_e \tag{3.31}$$

For every newborn electron, a H_2^+ or H^+ ion is created (Eq. (3.31)). The number of hydrogen molecules or atoms is then adjusted accordingly concerning Eq. (3.30) in order to fulfill. In the case of a recombination, one electron is lost from the system, hydrogen molecule H_2 or hydrogen atom H is added into the system, and one H_2^+ or H^+ is removed. When an electron hits the wall due to drifts, one hydrogen molecular ion H_2^+ is recycled from the wall. This recycled hydrogen molecular ion H_2^+ is then recombined and added as an H_2 molecule into the simulation system. The recombination reactions taken into account in the model for hydrogen and helium are listed in Appendix A.

The drift losses exist in our system due to the presence of the inhomogeneity and curvature of the toroidal magnetic field. These two drifts mechanisms always act together, and they are referred to as the '$\vec{B} \times \nabla B$' drift [12]. The drift velocity is

$$v_{\vec{B}\times\nabla B} = \frac{m_e}{q_e} \frac{\vec{R_k} \times \vec{B}}{R_k^2 B^2} \left(v_\parallel^2 + \frac{1}{2} v_\perp^2 \right) , \tag{3.32}$$

where $\vec{R_k}$ is the curvature radius, $\vec{B}$ is the toroidal magnetic field, and $v_\parallel$, $v_\perp$ are the parallel and perpendicular velocities of an electron with respect to the magnetic field line. The drift of the electrons is upwards or downwards depending on the direction of the magnetic field, and ions always drift in the opposite direction. Using Eq. (3.32), we calculate a drift length per increment time for each electron. When the drift length exceeds the torus dimensions for an electron, this electron hits the wall and recycles hydrogen ion. Note, the electron losses due to drifts are not significant, especially for simulation time below 1ms.

3.2 Conclusion

In this chapter, we have introduced our Monte Carlo Collision model `RFdinity1d`. This MCC-model follows the motion of guiding centers of electrons around the torus in a narrow bundle of magnetic field lines close to the antenna straps. The model investigates the electron density evolution in time and dependency of this evolution on the antenna parameters (electric field strength, RF frequency, and antenna phasing), neutral gas pressure and torus circumference.

In the model, electrons are accelerated in the antenna vicinity by the toroidal component of the vacuum electric field. We have described the Monte Carlo procedure for inelastic collisions between electrons and neutral gas. The procedure samples the path length between collisions for each electron. Upon a collision, the procedure selects a collision type based on the electron energy and cross section for this energy. The post-collision energies are calculated according to the procedure described by *Vahedi* and *Surendra*. Furthermore, the model contains Coulomb collisions between the

charged particles (electron-electron and electron-ion collisions). These collisions start to play a role only in the later stage of the simulations above certain threshold electron density, $n_e^{tr} = 10^{14}\,\mathrm{m}^{-3}$. We have used the Monte Carlo binary collision model proposed by T. Takizuka & H. Abe (**TA-method**) to describe the Coulomb collisions in the MCC-model.

References

[1] M. D. Carter et al. *Plasma production using radiofrequency fields near or below the ion cyclotron range of frequencies*. Nuclear Fusion, 30(723), 1990.

[2] F. Schuller et al. *Report on Applications of ICWC on ITER*. Technical Report IO/2009/ADM-014 report version 3, ITER - IO, 13115, St. Paul-lez-Durance, France, November 2009.

[3] Matěj Tripský. *Monte Carlo Simulation of Initial breakdown Phase of Magnetized toroidal ICRF discharges*. Master's thesis, Universtiteit Gent, Belgium, 2013.

[4] A. Lyssoivan et al. *Final Report on ITER Design Task*. Laboratory Report No 114, LPP-ERM/KMS, 1998.

[5] A. Lyssoivan et al. *Simulation of ITER full-field ICWC scenario in JET: RF physics aspects*. Plasma Phys. Control. Fusion, 54, 2012.

[6] V. Bobkov et al. Nuclear Fusion, 53(9), 2013.

[7] K. Crombé et al. *Studies of RF sheaths and diagnostics on IShTAR*. In AIP Conference Proceedings, volume 1689 of *http://doi.org/10.1063/1.4936471*, page 030006, California, USA, 2015.

[8] F. Louche et al. *Designing the IShTAR antenna: Physics and engineering aspects*. In AIP Conference Proceedings, volume 1689 of *https://doi.org/10.1063/1.4936523*, page 070016, California, USA, 2015.

[9] M. Tripský et al. *Monte Carlo simulation of ICRF discharge initiation in ITER*. In AIP Conference Proceedings, volume 1689 of *http://doi.org/10.1063/1.4936507*, page 060009, California, USA, 2015.

[10] CST STUDIO SUITE (R), http://www.cst.com. *CST AG*, 2015.

[11] F.B. Brown and T.M. Sutton. *Monte Carlo Fundamentals*. Lockheed Martin Company, Knolls Atomic Power Laboratory, Schenectady, New York, USA, 1996.

[12] F. F. Chen. *Introduction to plasma physics*. Plenum Press, 1974.

[13] D. Reiter. *Elementary Processes in Hydrogen-Helium Plasmas*. Springer, Forschungszentrum Jülich GmbH 52425 Jülich, Germany, 1987.

[14] D. Reiter. *The data file HYDHEL, Atomic and Molecular Data for EIRENE*. Technical report, Forschungszentrum Jülich GmbH, 52425 Jülich, Germany, 2002.

[15] V. Vahedi and M. Surendra. *A Monte Carlo collision model for particle-in-cell method: applications to argon and oxygen discharges*. Computer Physics Communications, 87:179–198, 1995.

[16] C.B. Opal et al. J. Chem. Phys., 55:992–1001, 1971.

[17] T. Takizuka and H. Abe. J. Comput. Phys., 25:205–219, 1977.

[18] A. V. Bobylev and K. Nanbu et al. Physical Review E, 61(4):4576–4582, 2000.

[19] C. Wang et al. *Particle simulation of Coulomb collisions: Comparing the methods of Takizuka & Abe and Nanbu*. J. Comput. Phys., 227, 2008.

[20] R. Caflisch. *A Hybrid Method for Accelerated Simulation of Coulomb Collisions in a Plasma*. Laboratory Report UCRL-JRNL-235460, Lawrence Livermore National Laboratory, 2007.

[21] I. Fujino et al. *Analysis of electron energy distribution of an arc-discharge H^- ion source with Monte Carlo simulation*. Review of Scientific Instruments, 79, 2008.

[22] J. D. Huba. *NRL Plasma Formulary*. Laboratory Report NRL/PU/6790–11-551, Naval Research Laboratory, 2001.

[23] M. Tripský et al. *Monte Carlo simulation of ICRF discharge initiation at $\omega_{LHR} < \omega$*. In European Conference Abstracts (ECA), volume 38.F. of *http://doi.org/10.1063/1.4864556*, Berlin, Germany, June 2014.

4

Discharge Initiation in Experiments and Comparison with the MCC-model `RFdinity1d`

The first parametric scans and their benchmarking with experimental results were presented in my master thesis [1] and at the 20^{th} Topical Conference on Radio Frequency Power in Plasmas in Sorrento [2]. These scans were obtained with our first model `RFdinity`. This model neglects Coulomb collisions, includes only collisions with hydrogen molecules H_2, and it describes collisions only in 1D velocity space. Here, we present results obtained with the updated version of the code `RFdinity1d` described in the previous chapter.

We study dependencies of the ionization rates on the electric field strength E_0, frequency f, phasing between the antenna straps, neutral gas p, and torus size. We investigated the plasma initiation with the ITER ICRF antenna. The shape of the electric field for the ITER antenna varies with the radial distance from the antenna straps. This version of the model is also applied to compare the breakdown time predictions with the experimental observations on tokamaks TEXTOR, ASDEX Upgrade and stellarator URAGAN-3M.

4.1 Ionization rate dependency in simulations

In this section, we present results of simulations using the `RFdinity1d` model studying ionization rate dependencies on the electric field strength, RF frequency, neutral gas pressure and torus size.

The electron density evolution in time follows an exponential increase given by

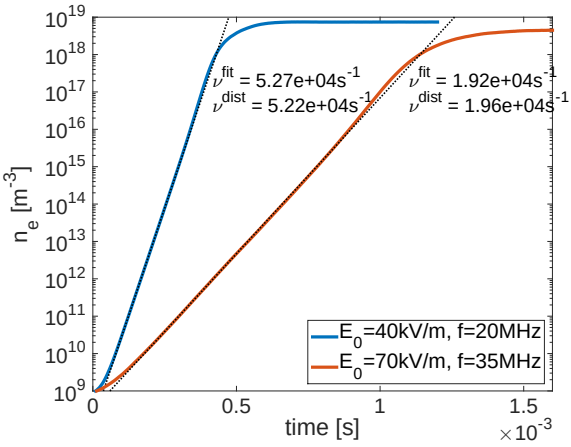

Figure 4.1: Electron density evolution in time during simulation for two sets of parameters, $E_0 = 40\,\mathrm{kV/m}$, $f = 20\,\mathrm{MHz}$, and $E_0 = 70\,\mathrm{kV/m}$, $f = 35\,\mathrm{MHz}$ at $p_{H_2} = 0.05\,\mathrm{Pa}$ in hydrogen.

the difference between the ionization rate and loss rate (Eq. (2.10)). The electron density increase per time increment $\mathrm{d}t$ can be written as

$$\frac{\mathrm{d}n_e}{\mathrm{d}t} = n_e \left(\nu_{\mathrm{ion}} - \nu_{\mathrm{loss}}\right) , \tag{4.1}$$

where n_e is the electron density, ν_{ion} and ν_{loss} are the ionization and loss rates. However, it has been already mentioned that the loss rate in our simulations depends on the electron density (in case of recombination) and time (drift losses). For that reason, in our simulations, the loss rate is negligible compared to the ionization rate ($\nu_{\mathrm{loss}} \ll \nu_{\mathrm{ion}}$) for the low electron densities $n_e < 10^{16}\,\mathrm{m}^{-3}$ and in the early stage of simulations. Taking this into account, we rewrite the equation for electron density increase into

$$\frac{\mathrm{d}n_e}{\mathrm{d}t} \approx n_e \nu_{\mathrm{ion}} . \tag{4.2}$$

The ionization rate can be calculated as

$$\nu_{\mathrm{ion}} = n_n \langle v \cdot \sigma_{\mathrm{ion}} \rangle = n_n \int v \cdot \sigma_{\mathrm{ion}}\left(v\right) \cdot f\left(\boldsymbol{v}\right) \mathrm{d}^3\boldsymbol{v} , \tag{4.3}$$

where σ_{ion} is the ionization cross section, n_n is the neutral gas density and $f\left(v\right)$ is the normalized velocity distribution function of all electrons in the simulation. This equation allows calculating the ionization rate at any moment as we have information about the velocity distribution of electrons moving around the torus.

Together with Eq. (4.3), we can also calculate the ionization rate ν_{ion} in our analysis based on Eq. (4.2) by fitting the exponential electron density increase in time. Fig. 4.1 presents the electron density evolution in time for two simulations with a one

strap antenna electric field for two sets of parameters, $E_0 = 40\,\mathrm{kV/m}$, $f = 20\,\mathrm{MHz}$, and $E_0 = 70\,\mathrm{kV/m}$, $f = 35\,\mathrm{MHz}$. Both simulations were launched in hydrogen at the neutral gas pressure $p_{H_2} = 0.05\,\mathrm{Pa}$ with the maximum electric field amplitude from the start. In the experiment, we see a time delay before the voltage on the antenna strap reaches its maximum. The time evolution of these two simulations as predicted by Eq. (4.2), follows an exponential growth with a constant slope corresponding to the ionization rate ν_{ion}. The fits for both simulations are visualized in the figure. They show that the ionization rate is constant during the electron density evolution, especially at lower density $n_e < 10^{16}\,\mathrm{m^{-3}}$. Above this electron density, the ionization rate starts to vary with time as the result of modifications in the electron energy distribution. These changes of the electron energy distribution are caused by the Coulomb collisions [3]. Loss mechanisms such as recombination and drifts start to play a role above $10^{18}\,\mathrm{m^{-3}}$, and the density evolution is slowed down. At this high electron densities, the loss rate ν_{loss} in eq. (4.1) balances the ionization rate to reach a plateau in the electron density evolution ($\nu_{\mathrm{loss}} = \nu_{\mathrm{ion}}$).

Fig. 4.1 illustrates values of the ionization rates in the simulations obtained by Eq. (4.2) as ν^{fit} and by Eq. (4.3) as ν^{dist} for a moment with the electron density $\approx 10^{15}\,\mathrm{m^{-3}}$. As expected, both definitions give identical results of the ionization rate. In the later sections presenting the parametric dependencies of the ionization rate, we use only Eq. (4.2) (ν^{fit}) to estimate the ionization rate in simulations.

Electric field strength and frequency dependencies

In this section, we present results of the ionization rate dependencies on the electric field strength and frequency for one strap antenna electric field (See Fig. 4.3(a)). We display results of the ionization rate obtained by simulations as a function of the electric field amplitude E_0 and frequency for the TEXTOR torus circumference at $p = 0.05\,\mathrm{Pa}$ in Fig. 4.2. We can see that for each simulated frequency, the ionization rate has a similar dependency on the electric field amplitude E_0. First, above the certain threshold of the amplitude, the ionization rate abruptly increases from zero reaching a maximum value of the ionization rate at rather low electric field amplitude $E_0 = 10 - 30\,\mathrm{kV/m}$. After arriving at this maximum value, the ionization rate stays nearly constant with an increasing amplitude E_0.

In contrast to the electric field dependency, the ionization rate decreases with the applied frequency f for a given electric field amplitude in Fig. 4.2. We observed that above $f = 50\,\mathrm{MHz}$ the ionization rate is zero even for the high electric field amplitude $E_0 = 70\,\mathrm{kV/m}$. The results of these simulations introduce a potential complication for a plasma initiation at high antenna frequency. For example, the ITER ICRF antenna will operate in the frequency band of $40 - 55\,\mathrm{MHz}$. We will show later that it is possible to initiate the electron density increase with the ITER antenna electric field. However, the simulations indicate that the ionization rate is higher when operating at the lower range of frequencies in ITER, $\nu_{\mathrm{ion}}(f = 40\,\mathrm{MHz}) > \nu_{\mathrm{ion}}(f = 55\,\mathrm{MHz})$.

Both electric field amplitude and frequency dependencies are partially consistent

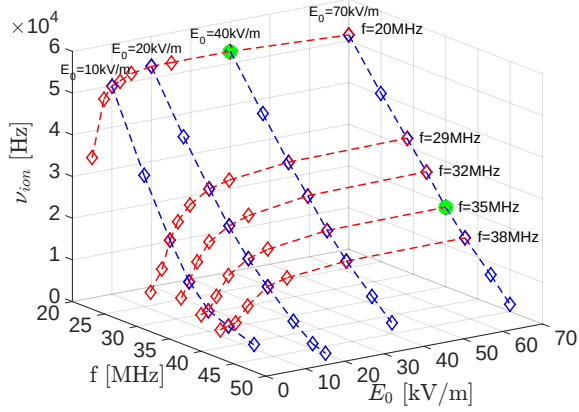

Figure 4.2: Ionization rate ν_{ion} dependency on the electric field strength E_0 and frequency f with one strap antenna for TEXTOR size torus at $p_{H_2} = 0.05\,\text{Pa}$. Two green points correspond to simulations in Fig. 4.1 with different E_0 and f but identical E_0/f ratios.

with the PDM and PDMI models [4, 5] presented in Section 2.3.2.1. In these models, the ionization rate was dependent on the ratio of the electric field strength and frequency E_0/f. In their analysis, two equations of the ionization rate are derived with E_0/f dependency for regions: in front of the antenna $\nu_{\text{ion}}^{\text{RF}}$ (Eq. (2.50)) and outside of the antenna region $\nu_{\text{ion}}^{\text{PDM}}$ (Eq. (2.51)). In Table 4.1, we summarize the ionization rates $\nu_{\text{ion}}^{\text{fit}}$ obtained in simulations for the E_0/f ratios with different values of the electric field amplitude and frequency ($E_0/f = [0.25,\ 1.25,\ 2.0]\,\text{kV/m/MHz}$). The results of the ionization rates in simulations are compared with the theoretical predictions given by Eq. (2.50) and Eq. (2.51). First, we can see that the ionization rates in simulations are approximately ten times smaller than the theoretical ionization rates $\nu_{\text{ion}}^{\text{PDM}}$, $\nu_{\text{ion}}^{\text{RF}}$. Secondly, we observe a difference between the simulated ionization rates $\nu_{\text{ion}}^{\text{fit}}$ for a given E_0/f ratio although according to the PDM description should give an identical ionization rates. Furthermore, we visualize this difference between the simulated ionization rates for the same E_0/f ratio in Fig. 4.1 for (i) $E_0 = 40\text{kV/m}$ and $f = 20\text{MHz}$, and (ii) $E_0 = 70\,\text{kV/m}$ and $f = 35\,\text{MHz}$. The values of the ionization rates for these two simulations are highlighted in Fig. 4.2 by two green points. We can conclude that the theoretical ionization rates overestimate the ionization rates and they cannot be described solely by the E_0/f ratio. We demonstrated that the description given by the PDM-model does not adequately capture the discharge initiation by the ICRF antenna and we need more detailed numerical models to describe and understand it (e.g., MC `RFdinity1d` model).

E_0 [kV/m]	f [MHz]	E_0/f [kV/m/MHz]	$\nu_{\text{ion}}^{\text{fit}}$ [s^{-1}]	$\nu_{\text{ion}}^{\text{PDM}}$ [s^{-1}]	$\nu_{\text{ion}}^{\text{RF}}$ [s^{-1}]
5	20	0.25	$3.3 \cdot 10^4$	$4.5 \cdot 10^5$	$2.7 \cdot 10^5$
8	32	0.25	$6.7 \cdot 10^3$		
25	20	1.25	$5.3 \cdot 10^4$	$3.7 \cdot 10^5$	$5.3 \cdot 10^5$
40	32	1.25	$2.5 \cdot 10^4$		
40	20	2.0	$5.3 \cdot 10^4$	$2.8 \cdot 10^5$	$5.5 \cdot 10^5$
70	35	2.0	$2.0 \cdot 10^4$		

Table 4.1: The ionization rate obtained in simulations for three ratio of $E_0/f = [0.25,\ 1.25,\ 2.0]\,\text{kV/m/MHz}$ with different combinations of the electric field amplitude E_0 and frequency f. The ionization rates $\nu_{\text{ion}}^{\text{RF}}$ and $\nu_{\text{ion}}^{\text{PDM}}$ are calculated using Eq. (2.50) and Eq. (2.51).

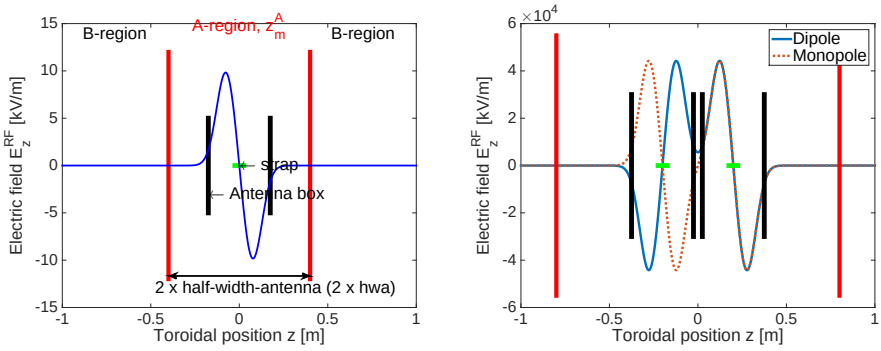

(a) (b)

Figure 4.3: Idealized vacuum electric fields used in the MC model `RFdinity1d` for (a) one strap and (b) two straps antenna (monopole and dipole phasing).

Pressure dependency

We investigated the ionization rate dependency on the hydrogen pressure for three sets of the antenna parameters:

1. $E_0 = 20\,\text{kV/m},\ f = 29\,\text{MHz},\ \frac{E_0}{f} \approx 0.69\ \frac{\text{kV/m}}{\text{MHz}}$
2. $E_0 = 5\,\text{kV/m},\ f = 29\,\text{MHz},\ \frac{E_0}{f} \approx 0.17\ \frac{\text{kV/m}}{\text{MHz}}$
3. $E_0 = 20\,\text{kV/m},\ f = 38\,\text{MHz},\ \frac{E_0}{f} \approx 0.53\ \frac{\text{kV/m}}{\text{MHz}}$

For this scan, we were using the vacuum electric field with two straps in monopole phasing (Fig. 4.3(b)). Fig. 4.4(a) summarizes the results of simulations at these parameters as a function of the hydrogen pressure. The pressure range for this scan was $p_{H_2} \in \langle 0.0083; 0.08 \rangle\,\text{Pa}$, although in practice, the ICWC experiments remain always below the maximum pressure set at $0.05\,\text{Pa}$. In the plot, the ionization rate dramatically increases with pressure for $p_{H_2} < 0.02\,\text{Pa}$. While above this pressure, the

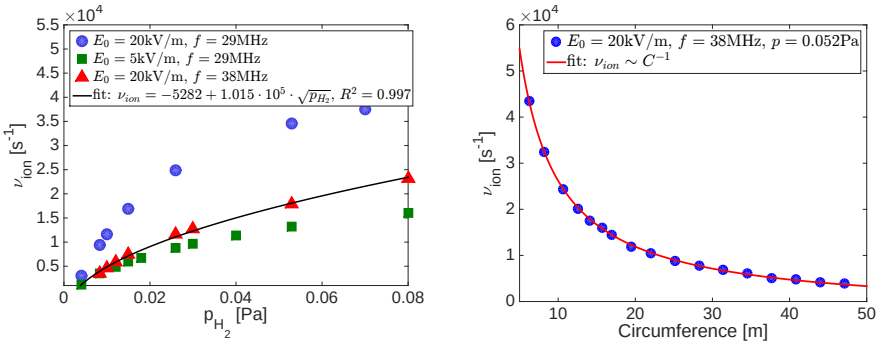

(a) (b)

Figure 4.4: (a) Ionization rate ν_{ion} as a function of the pressure p_{H_2} for 3 different set of antenna parameters: (1) $E_0 = 20\,\mathrm{kV/m}$, $f = 29\,\mathrm{MHz}$, (2) $E_0 = 5\,\mathrm{kV/m}$, $f = 29\,\mathrm{MHz}$, (3) $E_0 = 20\,\mathrm{kV/m}$, $f = 38\,\mathrm{MHz}$ with a square root fit: $\nu_{ion} = -5282 + 1.015 \cdot 10^5 \cdot \sqrt{p_{H_2}}$, $R^2 = 0.997$. (b) Ionization rate ν_{ion} as a function of the torus circumference length for $p_{H_2} = 5.2 \cdot 10^{-2}\,\mathrm{Pa}$, $f = 38\,\mathrm{MHz}$ and $E_0 = 20\,\mathrm{kV/m}$.

ionization rate increases slowly. The theoretical formulas in the PDMI-model for the ionization rate derived in Section 2.3.2.1 suggest a linear dependency on the pressure (Eq. (2.50) and Eq. (2.51)). Whereas, the results of the ionization rates in our simulations imply a square root dependency on the pressure, $\nu_{\mathrm{ion}} \sim \sqrt{p_{H_2}}$ as shown by a square root fit (black line with $R^2 = 0.997$) of the ionization rates for $E_0 = 20\,\mathrm{kV/m}$ and $f = 38\,\mathrm{MHz}$ in Fig. 4.4(a).

Dependency on torus circumference length

The ionization rate ν_{ion} as a function of the torus circumference length is illustrated in Fig. 4.4(b) at $p_{H_2} = 5.2 \cdot 10^{-2}\,\mathrm{Pa}$, $f = 38\,\mathrm{MHz}$ and $E_0 = 20\,\mathrm{kV/m}$. The ionization rate decreases with the circumference length. The ionization rates are very well fitted by $\nu_{ion} \sim C^{-1}$ (red line). Longer circumference means for an electron longer time before it can reenter the antenna region and be accelerated again. During the time in between the acceleration from the antenna, an electron looses energy for every inelastic collision it undergoes. When the electron is slowed down below certain energy, it is very difficult for the electron to re-enter the antenna region. We will study this minimum energy to re-enter and be re-accelerated by the antenna field in Section 4.5.

4.2 Benchmarking of the MC model `RFdinity1d` to ICWC experiments

4.2.1 Breakdown time in simulations

As mentioned earlier, the experimental breakdown time corresponds to the moment with a drop of antenna voltage or increase in H_α signal [6–8] (See Section 2.3). Unfortunately, our MC model `RFdinity1d` does not have any direct interaction between the antenna field and plasma medium. The model applies during the whole simulation only the vacuum electric field without any modification when the electron density increases. We overcame this drawback of the MC model `RFdinity1d` when we modified the model into a PIC-MCC model `RFdinity1d`. We present this PIC-MCC `Rfdinity1d` in Chapter 5. For the comparison of the breakdown times in the simulations and experiments, we have to adopt different definitions of the breakdown moment in our simulations using the MC model `RFdinity1d`.

Here, we discuss three definitions of the breakdown used in our model. Two definitions are based on the hypothesis of strongly increased collisionality during the transition from single ionization events to an avalanche (gas breakdown moment) [9]. At this moment, ionization rate and energy losses due to ionization collisions equal to Coulomb collision frequency and energy losses during Coulomb collisions. The third theoretical definition was presented by *Lyssoivan* et al. [10] as the moment when electron density overcomes the critical density for the low hybrid resonance ($\omega = \omega_{\text{LHR}}$) $n_{\text{e,crit}}^{\text{SW(LHR)}}$. It is important to mention that this critical density is above another critical density: (SW) excitation ($\omega = \omega_{p,e}$) $n_{\text{e,crit}}^{\text{SW(cut-off)}}$, which is a first principle validity limit of the present code version. Upon slow wave excitation, the $E_\parallel$ field will diverge from the vacuum field $E_{\parallel,0}$ used in the MC model. We will show later in Chapter 5 that the electrostatic field E^P generated by charge inhomogeneities interferes with the vacuum electric field $E_{\parallel,0}$. The resulting sum of these two fields, $E_\parallel = E_{\parallel,0} + E^P$, will have very different shape and magnitude from the vacuum field. On approaching the LHR, where $E_\parallel$ becomes very strong the vacuum field cannot be used further, and simulation results beyond this density with the present code version are not valid. The numerical definition of the breakdown moment in simulations was in this study nevertheless put at the upper validity limit $n_{\text{e,crit}}^{\text{SW(LHR)}}$ [3, 10] without the modification of the antenna electric field above the first critical density $n_{\text{e,crit}}^{\text{SW(cut-off)}}$. We will see that no matter which critical density for the breakdown is used the time difference between reaching the $n_{\text{e,crit}}^{\text{SW(cut-off)}}$ and $n_{\text{e,crit}}^{\text{SW(LHR)}}$ is small and predictable via ν_{ion}.

Below we summarize the numerical definitions of the breakdown moment in the model:

i. The critical density $n_{\text{e,crit}}^{\text{SW(LHR)}}$ is determined by the lower-hybrid resonance (LHR) condition, $k_{\perp,\text{SW}} \to \infty$:

$$1 = \sum_s \frac{\omega_{p,s}^2}{\omega^2 - \Omega_{c,s}^2}\,, \omega^2 = \omega_{\text{LHR}}\,, \tag{4.4}$$

where s refers to all plasma species, ω is RF frequency, $\omega_{p,s}$ is the plasma frequency of the species s, $\Omega_{c,s}$ is the cyclotron frequency of the species s [6]. In the ICRF band and for the low densities considered, we have: $\omega^2 \ll \Omega_{c,e}^2$ and $\omega_{p,e}^2 \ll \Omega_{c,e}^2$. Thus the electron term can be omitted in the equation (4.4), and it can be rewritten as

$$1 \approx \sum_i \frac{\omega_{p,i}^2}{\omega^2 - \Omega_i^2}\,, \tag{4.5}$$

where i now represents all ion species. For example in case of hydrogen, Eq. (4.5) can be expressed as

$$n_{e,crit}^{SW(LHR)} = \frac{\frac{\epsilon_0 m_p}{q_e^2}\frac{R_H+1}{R_H}}{\left(\frac{\frac{1}{2}}{\omega^2 - \frac{q_e^2 B_T^2}{4m_p^2}} + \frac{\frac{1}{R_H}}{\omega^2 - \frac{q_e^2 B_T^2}{m_p^2}}\right)}\,, \tag{4.6}$$

where m_p is mass of the proton, B_T is the toroidal magnetic field strength and R_H is the ratio between the ions H_2^+ and H^+ ($R_H = \frac{n_{H_2^+}}{n_{H^+}}$). In our simulations, the ratio R_H stays close to constant below $n_e = 10^{17}\,\mathrm{m}^{-3}$ with value around $\frac{n_{H_2^+}}{n_{H^+}} \approx 30$. For $B_T = 1.9\,\mathrm{T}$, $f = 29\,\mathrm{MHz}$) and $R_H = 30$, Eq. (4.6) gives the critical density $n_{e,crit}^{SW(LHR)} = 1.4 \cdot 10^{15}\,\mathrm{m}^{-3}$, while the critical density for the SW excitation is two orders lower: $n_{\mathrm{e,crit}}^{\mathrm{SW(cut\text{-}off)}} = 1.04 \cdot 10^{13}\,\mathrm{m}^{-3}$.

ii. The Coulomb collisions frequency ν^{CC} exceeds the ionization rate ν_{ion}: $\nu_{e-H_2^+}^{CC} \geq \nu_{\mathrm{ion}}$ and $\nu_{e-e}^{CC} \geq \nu_{\mathrm{ion}}$.

iii. The electron energy losses due to electron-ion Coulomb collisions $dE_{CC}^{e-H_2^+}$ exceed the energy losses due to ionization reactions dE_{ion}: $dE_{CC}^{e-H_2^+} \geq dE_{\mathrm{ion}}$

We compare these three numerical definitions with the experimental one in Fig. 4.5 for a scenario with the initial antenna voltage ramp-up in simulation corresponding to the antenna voltage ramp-up during the discharge in TEXTOR. The previously presented results of the ionization rates in Section 4.1 correspond to simulations in which the antenna amplitude was maximum from the start. While in experiments it takes some time to reach the maximum voltage at the antenna strap ($\approx 2 - 4 \cdot 10^{-4}\,\mathrm{s}$). When we include the time dependency of the voltage start-up into the model, the electron density evolution in simulations is slowed down during the low voltage. However, it does not affect the final ionization rate ν_{ion} obtained from the exponential fit of the electron density increase at the stage when this evolution has a steady increase in time.

The simulations were launched with $E_0 = 20\,\mathrm{kV/m}$, $f = 29\,\mathrm{MHz}$, $p = 0.026\,\mathrm{Pa}$ and using the monopole vacuum electric field with two straps (Fig. 4.3(b)). The experimental discharge on TEXTOR was carried out at $p = 0.0257\,\mathrm{Pa}$, $f = 29\,\mathrm{MHz}$ using one ICRF antenna at generator power $P = 100\,\mathrm{kW}$ and toroidal magnetic field in the center $B_T = 1.9\,\mathrm{T}$. In the figure, we illustrate the threshold densities for this

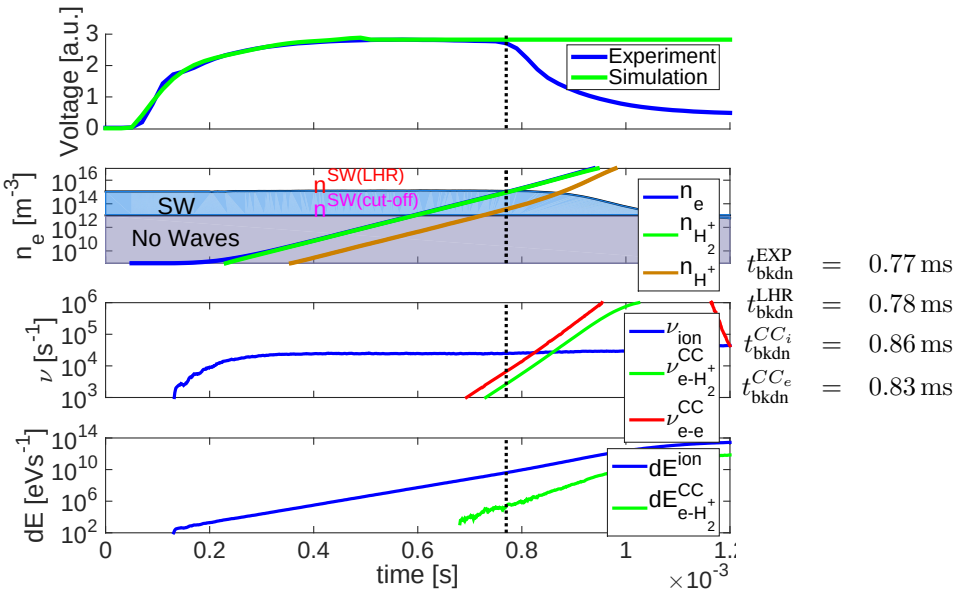

Figure 4.5: Comparison of the breakdown moment definitions: (i) experimental breakdown time $t_{\text{bkdn}}^{\text{EXP}}$ corresponding to the antenna voltage drop for ICWC experiment on TEXTOR ($P_G = 100\,\text{kW}$, $f = 29\,\text{MHz}$, $p_{H_2} = 0.0257\,\text{Pa}$, $B_T = 1.9\,\text{T}$), numerical breakdown times (ii) $t_{\text{bkdn}}^{\text{LHR}}$ as the moment when the LHR density is reached, (iii) t_{bkdn}^{CC} as the moment when the Coulomb collision rate exceeds the ionization rate, and (iv) the moment when the Coulomb collisions energy losses exceed the ionization collision energy losses.

simulation, the threshold densities for SW excitation and Lower Hybrid Resonance equal to $n_{\text{e,crit}}^{\text{SW(cut-off)}} = 1.04 \cdot 10^{13}\,\text{m}^{-3}$ and $n_{e,crit}^{SW(LHR)} = 1.4 \cdot 10^{15}\,\text{m}^{-3}$.

Fig. 4.5 shows experimental measurement of the antenna voltage in the top subplot. We can see the voltage start-up profile and breakdown corresponding to the moment with the antenna voltage drop at $t_{\text{bkdn}}^{\text{EXP}} = 0.77\,\text{ms}$. The experimental breakdown time t_{bkdn} is highlighted in the figure by a dashed vertical line in each subplot. Our simulations were launched with the identical time dependency of the electric field amplitude E_0 as for the experimental discharge (the top subplot). The remaining subplots investigate the numerical definitions of the breakdown moment: $t_{\text{bkdn}}^{\text{LHR}} = 0.78\,\text{ms}$ for the moment when electron density overcomes the critical density for lower-hybrid resonance, $t_{\text{bkdn}}^{\text{CC}_i} = 0.86\,\text{ms}$ for the moment electron-ion Coulomb collisions have higher frequency than ionization collisions or $t_{\text{bkdn}}^{\text{CC}_e} = 0.83\,\text{ms}$ for electron-electron Coulomb collisions. The last subplot in Fig. 4.5 illustrates electron energy losses due to ionization and Coulomb collisions. As we can see, the numerical definition of the breakdown moment when $dE_{CC}^{e-H_2^+} \geq dE_{\text{ion}}$ is not satisfied in our simulations.

The numerical definitions of the breakdown $t_{\text{bkdn}}^{\text{LHR}}$, $t_{\text{bkdn}}^{\text{CC}_i}$ and $t_{\text{bkdn}}^{\text{CC}_e}$ have a very good quantitative agreement in this case with the experimental breakdown time $t_{\text{bkdn}}^{\text{EXP}}$. How-

ever, it is very misleading to link the numerical breakdown times directly to the experimental breakdown moment, because they are dependent on the initial electron density in our simulations. Obviously, we can tune the value of the numerical breakdown time by starting with different initial electron density $n_{e,0}$. In this particularly case, we had started with the initial electron density $n_{e,0} = 9{\cdot}10^8\,\mathrm{m}^{-3}$ resulting in $t_{\mathrm{bkdn}}^{\mathrm{LHR}} = 0.78\,\mathrm{ms}$. If we started our simulation with $n_{e,0} = 9 \cdot 10^6\,\mathrm{m}^{-3}$ (or $n_{e,0} = 9 \cdot 10^{10}\,\mathrm{m}^{-3}$), the numerical breakdown times would be around $t_{\mathrm{bkdn}} \approx 1\,\mathrm{ms}$ (or $t_{\mathrm{bkdn}} \approx 0.52\,\mathrm{ms}$). It does not represent a significant change in the numerical breakdown time, but we would prefer a variable less dependent on initial conditions when we compare simulations and experiments. Therefore, we are mainly interested in the ionization rate dependency on the input parameters in our simulations rather than direct predictions of the breakdown time. Knowing the ionization rate gives us indirectly the breakdown time dependency by assuming that with higher ionization rate, the critical density for the breakdown is reached in shorter time.

Another reason why it is hard to link our simulations with experiments directly is due to missing excitation of the slow waves above $n_{e,crit}^{SW(cut-off)}$ ($\omega = \omega_{p,e}$) in our model. In reality, the slow waves help to accelerate the electrons and ions and thus increase the ionization rate. This additional source of the acceleration of the electrons should increase the electron density increase above $n_{e,crit}^{SW(cut-off)}$. In Chapter 5, we will introduce PIC-MCC model that includes the excitation of the waves above the critical density ($\omega = \omega_{p,e}$). Indeed, we observe with the PIC-MCC model an additional increase in the electron density above this critical density.

4.2.2 Breakdown time dependency in experiment on TEXTOR

Fig. 4.6 illustrates the experimental breakdown time dependency on the neutral gas pressure on TEXTOR for $f = 29\,\mathrm{MHz}$, $B_T = 1.9\,\mathrm{T}$ and two generator powers $P = 100\,\mathrm{kW}$ and $P = 25\,\mathrm{kW}$. The experimental results are compared with the numerical breakdown times estimated according to the definition (1)-$t_{\mathrm{bkdn}}^{\mathrm{LHR}}$ for simulations with $f = 29\,\mathrm{MHz}$ and two electric field amplitudes $E_0 = 20\,\mathrm{kV/m}$ and $E_0 = 5\,\mathrm{kV/m}$. We selected these two amplitudes E_0 because they serve as two extremes for the numerical breakdowns. Referring to Fig. 4.2, we can see that the minimum and maximum ionization rates correspond approximately to amplitudes $E_0 = 5\,\mathrm{kV/m}$ and $E_0 = 20\,\mathrm{kV/m}$ for $f = 29\,\mathrm{MHz}$. In a similar approach, we can select two generator power levels representing the minimum and maximum powers. According to our experiences during the ICWC experiment on TEXTOR, we selected $P_G = 25\,\mathrm{kW}$ as the minimum power and $P_G = 100\,\mathrm{kW}$ as the maximum power. Indeed, we will show later that above specific generator power, the experimental breakdown time does not decrease with the generator power and stays constant. The ICWC discharges with power below $P_G = 25\,\mathrm{kW}$ were not always successful because of too low power. Pressure scans with different generator powers will have approximately the breakdown times between these two experimental curves in Fig. 4.6 or overlap with the curve for $P_G = 100\,\mathrm{kW}$ when the generator power will be higher than $100\,\mathrm{kW}$.

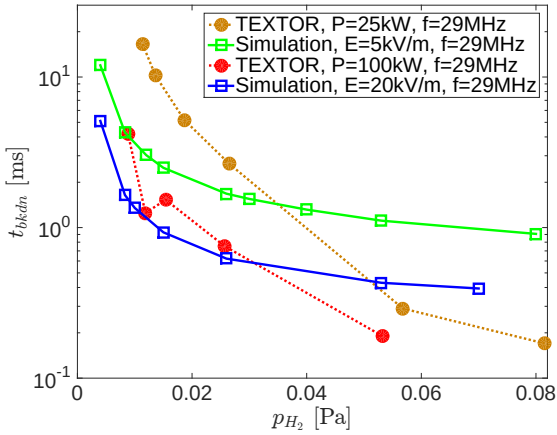

Figure 4.6: Comparison of the breakdown times in TEXTOR experiment and simulations as a function of the neutral gas pressure. The TEXTOR experiment was carried out for two generator powers $P_G = 25\,\mathrm{kW}$ and $P_G = 100\,\mathrm{kW}$ at frequency $f = 29\,\mathrm{MHz}$ ($B_T = 1.9\,\mathrm{T}$). The simulations were launched for two electric field strengths $E_0 = 5\,\mathrm{kV/m}$ and $E_0 = 20\,\mathrm{kV/m}$.

We can see that the experimental data have a similar tendency for both generator power levels. As expected, the experimental breakdown times are longer for the lower generator power. We can notice that the simulation results for the selected amplitudes have an identical shape. The breakdown times for simulations at $E_0 = 5\,\mathrm{kV/m}$ are lower by a factor of 2.5 from the breakdown times at $E_0 = 20\,\mathrm{kV/m}$. However, the experimental dependency has a stronger decrease of the breakdown time with pressure. The difference between the experiments and simulations are primarily noticeable at high neutral gas pressure $p > 0.05\,\mathrm{Pa}$. This extremely low breakdown time ($\sim 0.2\,\mathrm{ms}$) at the higher pressure can be connected to an increased probability of creating the plasma in the antenna strap vicinity. In the presented MC model `RFdinity1d`, we assume that the electron spatial distribution is rather homogeneous over the whole circumference length to estimate the average electron density. However, we will show in Chapter 5 with the Particle-In-Cell MC model that there is an accumulation of electrons in the antenna vicinity just before the breakdown moment. This local electron density is higher than the average electron density thus this electron density in the antenna vicinity reaches the critical electron density for the breakdown in a shorter time. Therefore, we can assume that the first plasma in experiments is very localized in the antenna strap vicinity and can trigger the antenna voltage drop (the experimental indication of the breakdown) before the plasma is homogeneously created around the vessel. The spatial distribution of electron will be illustrated in Chapter 5.

Breakdown times as a function of the electric field (antenna power) in experiment and simulations are plotted in Fig. 4.7. The results demonstrate qualitative agreement between the experiment and simulations. Both dependencies show an existence of the

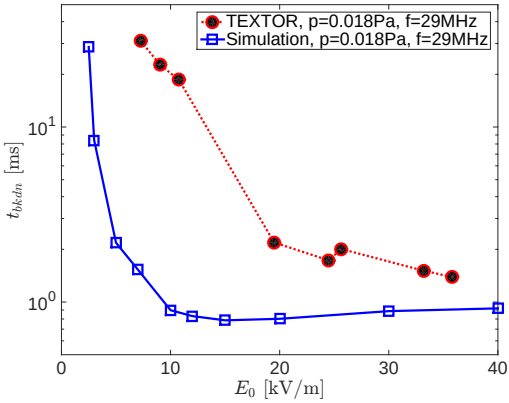

Figure 4.7: Comparison of the breakdown times in TEXTOR experiment and simulations as a function of the electric field strength at $p_{H_2} = 0.018\,\mathrm{Pa}$ and $f = 29\,\mathrm{MHz}$.

optimal power above which the breakdown time does not change significantly with the generator power. The values for the experimental plot were estimated at best effort from the voltage at the feeding point of the strap via transmission line voltage measurements taking into account the radial exponential decay of the $E_{\|}$ field in the torus. The saturation in the experiments occurs around $E_0 \approx 20\,\mathrm{kV/m}$ ($P_G = 60\,\mathrm{kW}$) while the saturation in the simulations starts around $E_0 \approx 10\,\mathrm{kV/m}$. This existence of the optimal minimum power above which the breakdown time does not significantly change with power is important because it demonstrates that there is no need to go towards higher generator power to achieve the faster initiation. An identification of this optimal power will be necessary to assure the ICRF antenna safety in ITER.

4.3 Discharge initiation by ICRF antenna on URAGAN 3-M

The experiments on ICRF discharge initiation were performed on the $l = 3$ URAGAN 3-M (U-3M) torsatron with a natural helical divertor located in Kharkiv, Ukraine. The results were presented at the 43rd EPS Conference on Plasma Physics in Leuven [11]. The experimental motivations were: (i) to study the dependencies of the breakdown time on the neutral gas pressure and the antenna power and (ii) investigate the hypothesis for the gas breakdown trigger as the moment of LHR generation in the antenna-field vicinity [10] by Langmuir probe measurements. The standard Frame antenna [12] was operated at $f = 8.6\,\mathrm{MHz}$, variable RF power ($P = 15 - 130\,\mathrm{kW}$, RF voltage at a generator, $V_{RF} = 3 - 9\,\mathrm{kV}$), confining magnetic field $B_T = 0.01 - 0.72\,\mathrm{T}$ to produce RF plasma in hydrogen at a continuous gas flow with pressure range $p_{H_2} \approx 1 \cdot 10^{-3} - 2 \cdot 10^{-2}\,\mathrm{Pa}$. Whereas sustaining a fully ionized hydrogen RF plasma takes place in the Alfvén wave range of frequencies ($\omega < \omega_{ci}$) for the given

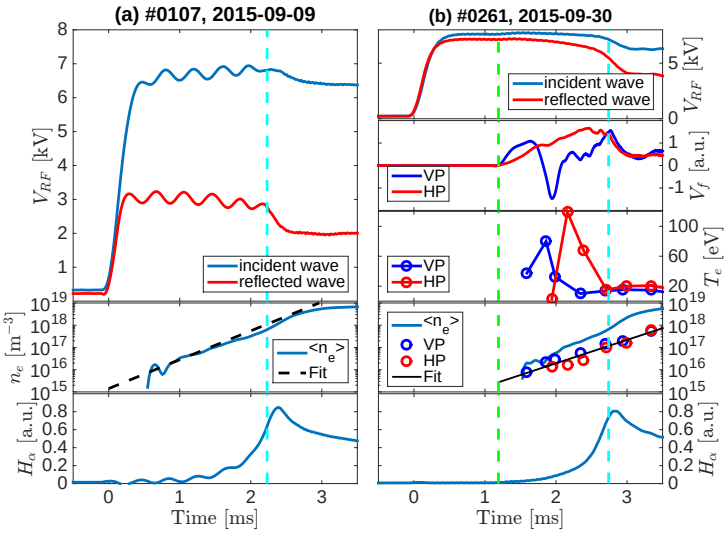

Figure 4.8: Comparison of experimentally observed indications of gas breakdown during ICWC in U-3M for the shot at $V_{RF} = 6\,\mathrm{kV}$, $p_{H_2} = 6.3 \cdot 10^{-3}\,\mathrm{Pa}$ and $B_0 = 0.72\,\mathrm{T}$ (a) in the first part of the experiment with oscillations of the signals and (b) improved measurement without oscillations. Time traces of forward (blue) and reflected (red) RF power delivered to the Frame antenna from the generator, average electron density $\langle n_e \rangle$, and H_α signal, additionally in (b) floating potential registered by the antenna-near vertical and horizontal Langmuir Probes (VP and HP), electron temperature T_e, electron density n_e by the Langmuir Probes and by the interferometer.

operating frequency at higher magnetic fields ($B_T \sim 0.72$T). The hydrogen gas RF breakdown moment is characterized by a dominant concentration of the molecular hydrogen ions H_2^+ [10]. It results in the breakdown performance in the U-3M case in the frequency range $\omega > \omega_{ci}$, which allows the existence of the LHR for all tested B_T values.

4.3.1 Experimental results

During the ICRF discharge initiation experiments on TEXTOR, ASDEX Upgrade, JET and TORE SUPRA, a breakdown event was defined as the moment when the antenna voltage V_{RF} drops and H_α signal rises [13]. This definition is adopted as well during the experiments on the U-3M. It is observed that the signals of antenna voltage V_{RF} and H_α showed uncontrolled low amplitude oscillations caused by EM interference between RF heating and diagnostic electronics and hindering correct estimation of the breakdown time t_{bkdn} as shown in Fig. 4.8(a). The figure shows the V_{RF} and H_α signals for a typical shot on U-3M together with the time evolution of the average electron density $\langle n_e \rangle$ obtained from a microwave interferometer located in the vicinity of the Frame antenna. The rise in H_α signal and drop in V_{RF} signal occur clearly at different time instances: the antenna voltage drop occurs around

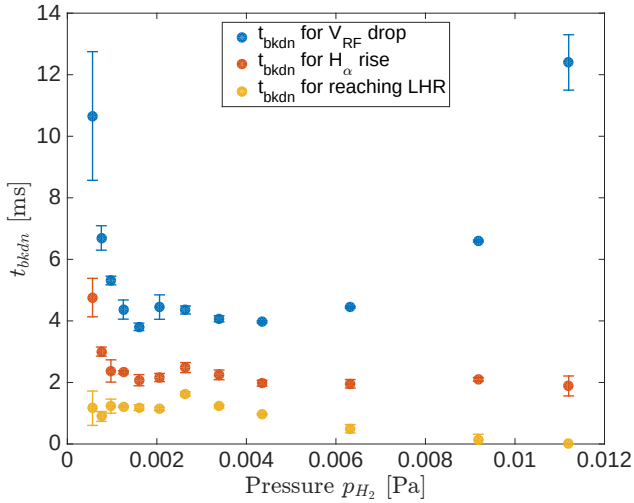

Figure 4.9: Breakdown time dependency on the neutral gas pressure for the strap voltage $V_{RF} = 4\,\mathrm{kV}$. Comparison of three breakdown definitions used in the experiment: (i) V_{RF} drop, (ii) H_α signal rise and (iii) the electron density reaching the LHR.

$\approx 2.2\,\mathrm{ms}$ (cyan dashed vertical line) and corresponds to $\langle n_e \rangle \approx 6 \cdot 10^{17}\,\mathrm{m}^{-3}$, and the H_α signal rises around $\approx 1.1\,\mathrm{ms}$. The $\langle n_e \rangle$ signal is extrapolated (black dashed line) to reach the LHR density in the U-3M antenna vicinity ($n_{e-LHR} \approx 3 \cdot 10^{15}\,\mathrm{m}^{-3}$ at $f = 8.6\,\mathrm{MHz}$, $B_{ant} \approx 0.64\,\mathrm{T}$, on-axis $B_0 = 0.72\,\mathrm{T}$, and $n_{H_2^+}/n_{H^+} = 20$), resulting in a breakdown time of about $\approx 0.4\,\mathrm{ms}$. Nevertheless, this fit is not very trustworthy as the fitted densities are close to the detection limits. Furthermore, it is visible that the discharge is already initiated at the moment of the V_{RF} drop.

In a selected number of shots, 40 out of 540, the oscillations could be successfully mitigated by improved grounding of the antenna generator. In this part of the experiment additional measurements of the plasma floating potential, electron density and temperature were obtained using vertical and horizontal arrays of the Langmuir probes illustrated in Fig. 4.8(b). One of the LP arrays (*vertical probes*, **VP**) was inserted into the vacuum chamber from the top in the Frame antenna vicinity: at $\sim 3\,\mathrm{cm}$ from the antenna edge and $14.5\,\mathrm{cm}$ from the torus midplane. Another LP array (*horizontal probes*, **HP**) was placed horizontally from the LFS far from the antenna at $\sim 0.5\,\mathrm{cm}$ inside from the plasma edge. The first response of the antenna voltage V_{RF} in this improved measurement is visible around $\approx 1.2\,\mathrm{ms}$ (green dashed vertical line). This moment coincides with the first response on the floating potential V_f measurements by the antenna-near vertical (VP) and horizontal (HP) Langmuir probes, and also with the rise of the H_α signal. The drop in V_{RF} again occurs later at the electron density $\langle n_e \rangle \approx 6 \cdot 10^{17}\,\mathrm{m}^{-3}$ (cyan vertical line). The floating potential in the I-V characteristics of the Langmuir probe corresponds to the voltage for which the current is zero due

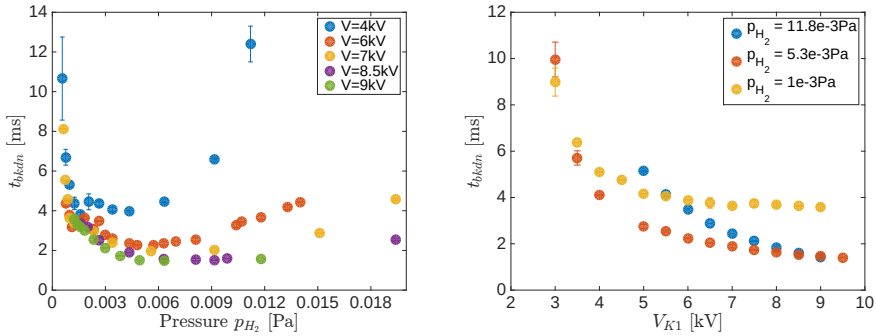

(a) (b)

Figure 4.10: The breakdown time t_{bkdn} (V_{RF} drop) dependency on (a) the varying neutral gas pressure for different strap voltages ($V_{RF} = [4; 6; 7; 8.5; 9]\,\text{kV}$), and (b) the varying strap voltages for different pressure levels ($p_{H_2} = [11.8; 5.3; 1] \cdot 10^{-3}\,\text{Pa}$).

to the same flow of ions and electrons on the probe. The results of the n_e and T_e evolutions are also illustrated in Figure 4.8(b) (third and fourth figure from top). Due to strong RF perturbations, the electron density n_e and temperature T_e could be reliably analyzed starting with delay $\sim 0.4\,\text{ms}$ after the first increase in V_f ($n_e \approx 7 \cdot 10^{15}\,\text{m}^{-3}$, $T_e \approx 37\,\text{eV}$). Extrapolation of the density curve to the gas breakdown moment defined as the first appearance of the radiation, assuming constant ionization rate (black line), indicates the electron density of the order of $\sim 3 \cdot 10^{15}\,\text{m}^{-3}$, which is in agreement with the predicted LHR density in the U-3M antenna vicinity.

The discrepancy between the different defined breakdown moments (i) drop in the antenna voltage V_{RF}, (ii) rise in H_α signal and (iii) possible theoretical breakdown definition (LHR threshold density) shows the challenge in defining the breakdown moment in ICRF plasma initiation. All mentioned breakdown definitions were tested and compared in Fig. 4.9 showing the breakdown time dependency t_{bkdn} on the neutral pressure p_{H_2} for the strap voltage $V_{RF} = 4\,\text{kV}$. All three definitions show slightly different dependencies, but only the definition by the voltage drop could be consistently registered during the whole experiment. Extrapolating from the interferometry density data to LHR resonance was not reliable, while the H_α signal was challenging to interpret due to its low amplitude oscillations. Therefore, we use the experimental breakdown definition as the antenna voltage drop (cyan dashed line in Fig. 4.8) to study the breakdown moment dependency on the neutral gas pressure and the antenna power for all 500 shots.

The dependencies of the experimental breakdown time on the neutral gas pressure and the antenna voltage are plotted in Fig. 4.10. In the case of the varying pressure Fig. 4.10(a), the data show the existence of an optimal value for the pressure which results in the lowest breakdown time for each antenna voltage. This optimal pressure is shifting towards higher values with increasing antenna voltage. In Fig. 4.10(b), we can see the breakdown time is decreasing with increasing magnitude of the voltage on

the strap.

4.4 Simulation of ICRF discharge initiation in ITER

We study the electron multiplication rate as a function of the RF discharge parameters (i) antenna input power ($0.1 - 5\,\mathrm{MW}$), and (ii) the neutral pressure (H_2) for two antenna phasing (monopole $[0000]$-phasing and small dipole $[0\pi0\pi]$-phasing). Furthermore, we investigate the electron multiplication rate dependency on the distance from the antenna straps. This radial dependency results from the decreasing electric amplitude and field smoothening with increasing distance from the antenna straps [14].

The performed simulations use the parallel electric field profiles as obtained by 3D Microwave Studio (***MWS*** [15]) computations for the current design of the ITER antenna without Faraday screen. The ITER ICRF antenna has 4 columns of straps in the toroidal direction, each column consisting of 2 poloidal triplets of straps fed in parallel by one transmission line per triplet. The ITER ICRF antenna configuration is shown in Fig. 4.11(a) together with the planes on which we performed our simulations. The results in this contribution are restricted to electric fields in two horizontal planes located at the top of the antenna and the center of the upper half of the antenna. Fig. 4.11(b) shows the absolute values of the E_z-field in $(r - Z)$-coordinates for two different toroidal antenna strap phasings in the mid-upper-plane: (a) Small dipole (**SmD**), (b) Monopole (**M**). Fig. 4.12 takes a closer look at the electric fields at two distances from the antenna strap ($r = 2.25$cm and $r = 9.25$cm) and for two antenna-phasings (***M*** and ***SmD***). The figures demonstrate that not only the amplitude of the electric field changes radially but also the shape.

Pressure dependency for SmD and M-phasing

A dependency of the breakdown time t_{bkdn} on the neutral pressure p_{H_2} was studied at ITER relevant ICWC pressure interval ($5 \cdot 10^{-3} - 1 \cdot 10^{-2}\,\mathrm{Pa}$) at constant antenna power $P = 5$MW and frequency $f = 40$MHz. We applied the numerical definition of the breakdown corresponding to the moment when the critical density $n_{e,crit}^{SW(LHR)}$ is reached.

Fig. 4.13(a) illustrates the dependency of the t_{bkdn} on the radial distance from the antenna in the mid-upper plane for three pressure levels for the **SmD**-phasing. The breakdown time t_{bkdn} is lower for higher neutral pressures p_{H_2} at a same radial distance from the antenna. The dependency on the radial distance is related to the varying shape of the E_z and decreasing amplitude when moving away from the antenna strap. The figure implies that the most effective area for the discharge initiate is below 50mm.

For these simulations, it is found that the varying pressure has little effect on the shape of the velocity distribution. Fig. 4.13(b) shows the velocity distributions with varying pressure and for the **M** and **SmD**-phasing, together with the ionization cross section. The distributions for **M** and **SmD** are slightly different: (i) the **M** distributions extend wider than for the **SmD** to velocities that do not contribute any more to

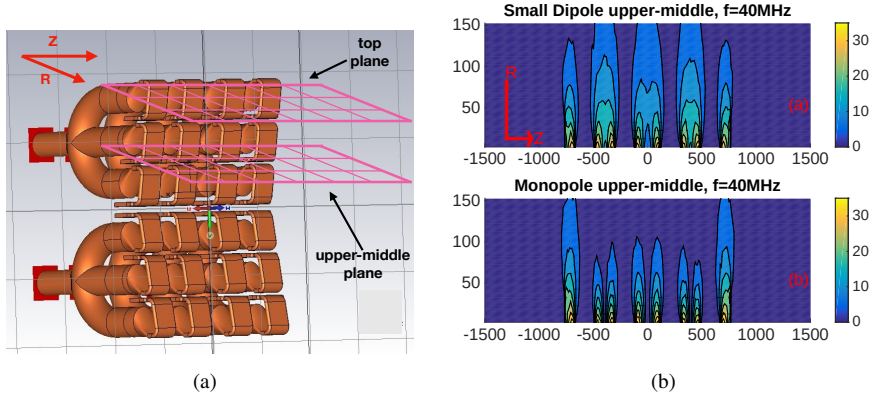

(a) (b)

Figure 4.11: (a) ITER ICRF antenna configuration: 4 columns of straps in the toroidal direction, each column consisting of 2 poloidal triplets of straps fed in parallel by one transmission line per triplet. The upper-middle plane shows the plane used in our model. (b) Contour plot of the absolute value of the E_z-field in $(R-Z)$-coordinates simulated with the MWS code for four-strap ITER antenna in mid-upper plane, r is relative distance from antenna strap ($f = 40\,\mathrm{MHz}$, $P = 0.5\,\mathrm{W}$): (a) Small dipole $[0\,\pi\,0\,\pi]$-phasing, (b) Monopole $[0\,0\,0\,0]$-phasing.

ionization, (ii) for **SmD**, between velocities of $10^7\,\mathrm{m/s}$ and $10^8\,\mathrm{m/s}$, the distribution is two times larger than for **M**. These small differences result in a slightly faster breakdown for **SmD** than for **M** in our simulations. However, this may be in discrepancy with the experimental observations on tokomaks TORE SUPRA or TEXTOR where the monopole-phasing is more efficient for plasma initiation than dipole-phasing [16].

Power dependency for SmD

The power scan was performed in the top-plane at $f = 40\,\mathrm{MHz}$ and $p_{H_2} = 1\cdot10^{-2}\,\mathrm{Pa}$ for the **SmD**-phasing. The vacuum electric field strength is determined by the input power as well as by the distance from the antenna straps. Results of the breakdown time dependency on the antenna power are illustrated in Fig. 4.14(a).

We observed that the breakdown time (t_{bkdn}) does not change dramatically with the varying antenna power ($P = 1 - 5\,\mathrm{MW}$). The value of the t_{bkdn} increases exponentially with radial distance from the antenna strap, due to decaying electric field and the smoothness of the electric field profiles. Simulations for the lowest power $P = 0.1\,\mathrm{MW}$ have relatively low t_{bkdn} only close to the straps. Above $R > 45\,\mathrm{mm}$ the t_{bkdn} for this power becomes much larger than for the simulations at higher power. The simulation results indicate that the most effective power is $P = 1\,\mathrm{MW}$ with the lowest breakdown time in the studied radial range. This result is encouraging for the future ICWC operation on ITER to avoid using excessive high generator power.

Fig. 4.14(b) illustrates the velocity distribution $F(v)$ during plasma production taken at $R = 45\,\mathrm{mm}$ for the different antenna powers, together with the ionization cross section. The velocity distributions for $P = 0.5\,\mathrm{MW}$ and $P = 1\,\mathrm{MW}$ have the largest electron population at the interval where the ionization cross section is the

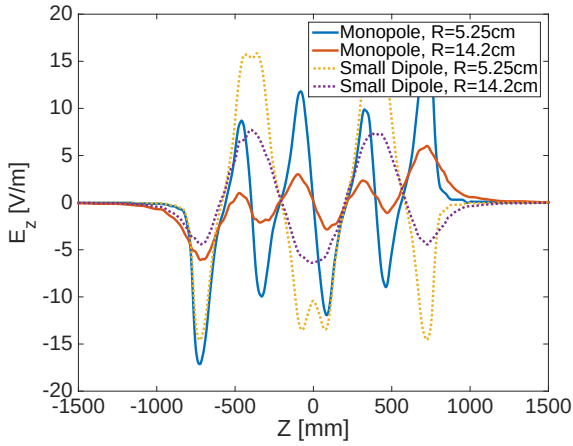

Figure 4.12: E_z-field in Monopole and Small dipole phasing at $r = 5.25\,\mathrm{cm}$ or $r = 14.2\,\mathrm{cm}$ used in the model.

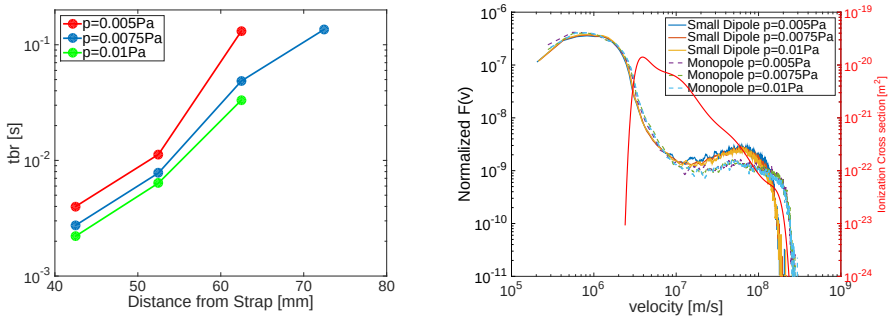

(a) (b)

Figure 4.13: (a) The breakdown time t_{bkdn} radial dependency with varying neutral pressure for **SmD**-phasing in mid-upper plane. (b) Velocity distribution for varying pressure $p = [5,\, 7.5,\, 10] \cdot 10^{-3}\,\mathrm{Pa}$ for one radial distance $R = 4.25\,\mathrm{cm}$ and for two antenna phasings **M** and **SmD** together with the ionization cross section as a function of velocity (red line).

most significant, $v = \left(3 \cdot 10^6 - 1 \cdot 10^7\right)\,\mathrm{m/s}$. The width of the velocity distribution increases with a square root of power, $\Delta \sim \sqrt{P}$ [1]. The depopulation of electrons from the velocity interval relevant for ionization reactions results in longer breakdown times at higher input power.

Fig. 4.15 shows the ionization frequency as a function of the radial position and gradient of the E_z-field (dE_z/dz) at the edge of the antenna box in the top-plane (see Fig. 4.11 at $Z = 750\,\mathrm{mm}$) as a function of the radial position for two antenna powers $P = 5\,\mathrm{MW}$ and $P = 0.1\,\mathrm{MW}$. Although the electric field amplitude for $P = 0.1\,\mathrm{MW}$ is seven times lower than for $P = 5\,\mathrm{MW}$, we can see that close to the

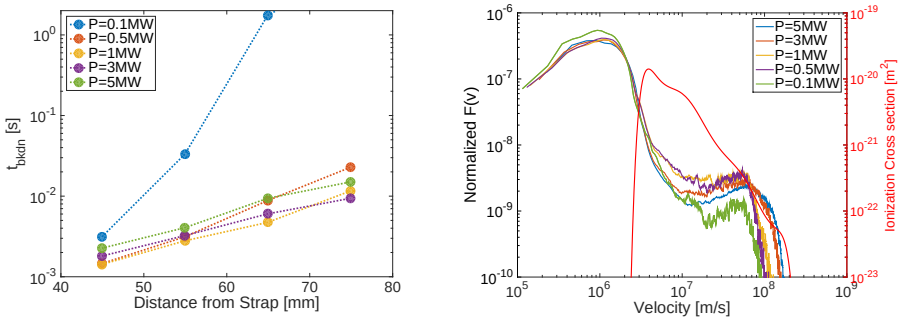

(a) (b)

Figure 4.14: (a) The breakdown time t_{bkdn} radial dependency with the varying antenna power for **SmD**-phasing in top plane. (b) Velocity distribution for varying antenna power $P = [5,\ 3,\ 1,\ 0.5,\ 0.1]\,\text{MW}$ at radial distance $R = 4.5\,\text{cm}$ with **SmD**-phasing together with the ionization cross section as a function of velocity (red line).

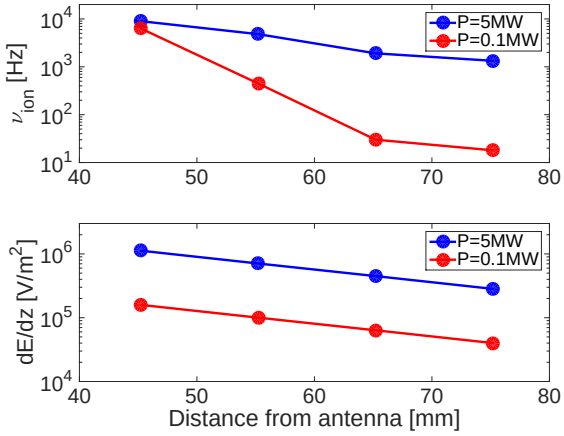

Figure 4.15: Dependencies of the function ν_{ion} and dE_z/dz on the radial distance at $P = 5\,\text{MW}$ and $P = 0.1\,\text{MW}$.

antenna strap ($R = 45\,\text{mm}$) the ionization rates have a similar magnitude for both powers. The ionization rate decays exponentially with the distance from the strap, and this decay is stronger for the lower power. This tendency is correlated with the $\mathrm{d}E_z/\,\mathrm{d}z$, which is found to be a measure for low energy electrons to gain energy in the oscillating electric field when approaching the antenna area. This theoretical description based on the $\mathrm{d}E_z/\,\mathrm{d}z$ is related to the PDM-model description of electron motion in the antenna electric field (See Section 2.3.2.1). More detail analysis and comparison with simulations will be presented at the end of this chapter in Section 4.5.

4.5 Advanced ponderomotive description of electron acceleration in ICRF discharge initiation

In this chapter, we illustrated the ionization dependencies on the electric field, frequency, pressure, circumference length and as well on the shape of the antenna field in case the simulations with the ITER ICRF antenna (as a function of the radial distance from the straps). To understand and study these dependencies on the antenna RF electric field (amplitude, frequency, shape), we have modified the MC-model `RFdinity1d` into the model following only the electrons motions without collisions (single electron model). Using this model, we introduce a new analysis of the PDM-model (See Section 2.3.2.1) developed during my research and presented by *Wauters et al.* [17]. In the PDM-model [4] and PDMI-model [5], no conditions are derived for an electron to reenter and be re-accelerated by the antenna electric field. In practice, only a small fraction of electrons can enter the antenna region from outside due to ponderomotive force expelling low energetic electrons. Fig. 4.16 plots the energy distribution of electrons in the later stage of a simulation at $E_0 = 20\,\mathrm{kV/m}$, $f = 29\,\mathrm{MHz}$, $p = 0.01\,\mathrm{Pa}$ with one strap antenna. The figure also illustrates a Maxwell energy distribution with $T = 3\,\mathrm{eV}$. We can imminently see that the majority of the electrons are low energetic: 83% of electrons have energy less than $3\,\mathrm{eV}$. Although the initial electrons are sampled from a Maxwell distribution with $T = 0.5\,\mathrm{eV}$, these low energetic electrons in the later stage of the simulation correspond to a Maxwell distribution with $T = 3\,\mathrm{eV}$ as this low energetic distribution is mainly populated by newborn electrons (ejected electrons) after ionization collisions. We showed in Section 3.1.4.2 (Fig. 3.7(a)) that the ejected electrons inclined to be low energetic.

Fig. 4.16 indicates that electrons in the energetic tail ($\epsilon > 100\,\mathrm{eV}$) are minority in the simulations (less than 1% of the electrons) and correspond to a Maxwell energy distribution with $T = 3.7\,\mathrm{keV}$. These high energies could be obtained only when they enter the antenna region to be accelerated by the antenna electric field. The majority of the electrons stays low energetic because the antenna field has never substantially accelerated them. The conditions for an electron to be able to gain energy from the antenna field depends on its energy when it approaches the antenna region. Only electrons with energies above certain energy threshold can overcome the ponderomotive repulsive force to enter or penetrate far enough into the antenna region to gain some energy. We will show in Chapter 5 that these two Maxwell energy distribution (low and high energetic distributions in Fig. 4.16) form energy distribution which can be fitted by one distribution function so-called **Kappa energy distribution**.

For the purpose of studying the movements of electrons and their interaction with the antenna electric field, we use the MC-model `RFdinity1d` without collisions. As such, the model follows solely the motion of the initial electrons around the torus accelerated by the vacuum electric field in the antenna region. Fig. 4.17 illustrates the results of such simulations. It plots trajectories of two electrons with initial energy of (a) $\epsilon = 1\,\mathrm{eV}$ and (b) $\epsilon = 10\,\mathrm{eV}$. Both figures indicate the shape of the electric

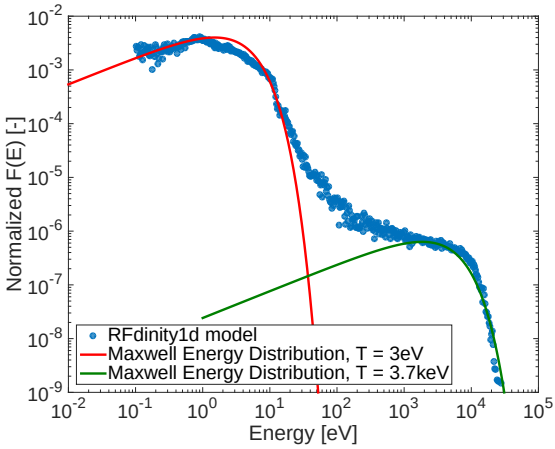

Figure 4.16: Energy distribution function of electrons for a simulation at $E_0 = 20\,\mathrm{kV/m}$ $f = 29\,\mathrm{MHz}$ $p = 0.01\,\mathrm{Pa}$. The majority of the electrons corresponds to low energetic Maxwell distribution with $T = 3\,\mathrm{eV}$. The energetic tail with the minority of electrons ($< 1\%$ of electrons) corresponds to high energetic Maxwell distribution with $T = 3.7\,\mathrm{keV}$.

field as a solid black line. In Fig. 4.17(a), an electron with the initial energy of $1\,\mathrm{eV}$ is approaching the antenna region, but it is reflected. The electron then continues with approximately same energy ($\approx 1\,\mathrm{eV}$), but with opposite sign in the parallel velocity. The electron encircles the torus and approaches the antenna region from the opposite side. The electron is again reflected without gaining any energy from the antenna field. In the simulations, we follow each electron for the time it needs to encircle the torus eight times to assure that an electron is reflected many times before it is definite that an electron does not obtain any energy from the antenna field. Fig. 4.17(b) illustrates the trajectory of the electron with the initial energy of $10\,\mathrm{eV}$. This electron has high energy enough to enter the antenna region and be accelerated even towards higher energies by the antenna electric field.

We launched simulations with electrons starting with different initial energies ϵ_i ranged between $10^{-1}-10^{3}\,\mathrm{eV}$ and different initial time shift. Thus electrons approach the antenna field at different phases of the oscillating RF field for each initial energy level. In our simulations, it was always 12 electrons starting at the same energy but shifted in time ($\Delta t = \frac{1}{12}\frac{2\pi}{f}$) to cover the period of the oscillating field. Afterwards, we plot the difference between the initial and final electron energy, $\Delta\epsilon = |\epsilon_f - \epsilon_i|$, as a function of the initial energy. Here, the final electron energy ϵ_f is calculated as an average value of the final electron energies $\tilde{\epsilon_f}$ for these 12 electrons starting with the same initial energy ϵ_i but with different initial time shift. We observed that the spread of these final energies $\tilde{\epsilon_f}$ is very small and the time shift does not play a significant role.

We can determine an existence of the threshold energy ϵ_{tr} above which the electron can gain some energy from the antenna electric field. This threshold energy can

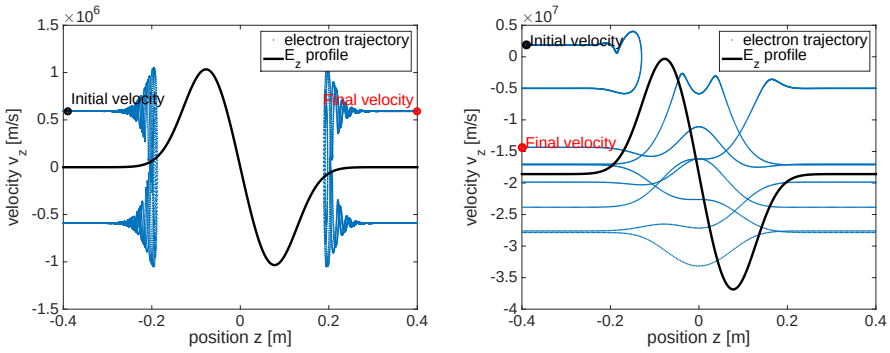

Figure 4.17: Electron trajectories in vicinity of the antenna electric field for two initial energies (a) 1 eV (b) 10 eV.

be easily identified because it is associated with a sudden increase in the difference between the initial and final energies $\Delta\epsilon$. Fig. 4.18 illustrates the threshold energy $\epsilon_{tr} \approx 1.5\,\mathrm{eV}$ determined by a step in $\Delta\epsilon$ dependency on the initial energy ϵ_i for a simulation at $E_0 = 20\,\mathrm{kV/m}$, $f = 29\,\mathrm{MHz}$ and $\sigma = 0.075\,\mathrm{m}$. In the next part, we investigate the threshold energy value using a single electron model. Then, we study parametric dependencies on the electric field amplitude E_0, frequency f, and shape of the electric field σ. In the simulations, we use the electric field profile given by a sum of two Gaussians with opposite sign given by:

$$E(z,t) = E_0 \left(\mathrm{e}^{\left(-(z+7.5\,\mathrm{cm})^2/\sigma^2\right)} - \mathrm{e}^{\left(-(z-7.5\,\mathrm{cm})^2/\sigma^2\right)} \right) \cos(2\pi f t)\,. \tag{4.7}$$

The parameter σ in the equation is used to study the dependency of the threshold energy on the electric field shape.

We can also study the threshold energy dependencies on E_0, f, and σ using theoretical description given by PDM-model in Section 2.3.2.1 [4]. Here, we summarize the equations presented in Section 2.3.2.1 to derive conditions for the threshold energies. We have already mentioned during the description of the PDM-model that this model retains only the zeroth- and first-order term of the Taylor series expansion [4, 6]. In my analysis, we introduce as well the quadratic term to derive an additional validity condition. The Taylor expansion of Eq. (2.35) retaining up to the 2$^{\mathrm{nd}}$-order term is written as

$$E_z\left(z = z_0(t) + z_1(t)\right) = E_z(z_0) + z_1 \frac{\mathrm{d}E_z}{\mathrm{d}z}(z_0) + \frac{z_1^2}{2}\frac{\mathrm{d}^2 E_z}{\mathrm{d}z^2}(z_0)\,. \tag{4.8}$$

The second order term is introduced in the equation of the movement of the fast oscillation as its sign will determine whether the oscillation is focusing around z_0 or defocussing (unstable) [17]. The Taylor expansion of the E_z field in Eq. (4.8) to describe the motion of an electron around z_0 is valid only when the first and second

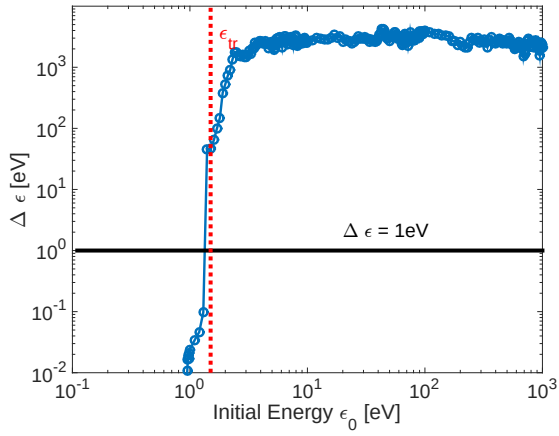

Figure 4.18: Difference between the initial and final electron energy $\Delta\epsilon = |\epsilon_f - \epsilon_i|$ as a function of the initial electron energy ϵ_i for $E_0 = 20\,\mathrm{kV/m}$, $f = 29\,\mathrm{MHz}$ and $\sigma = 0.075\,\mathrm{m}$. The threshold energy ϵ_{tr} obtained by noting the substantial increase in $\Delta\epsilon$.

order terms are smaller than the zeroth and first order term by factor $\xi_{v,1}$ and $\xi_{v,2}$ respectively,

$$z_1 \frac{\mathrm{d}E_z}{\mathrm{d}z}(z_0) < \xi_{v,1} E_z(z_0) \tag{4.9}$$

$$\frac{z_1^2}{2} \frac{\mathrm{d}^2 E_z}{\mathrm{d}z^2}(z_0) < \xi_{v,2} z_1 \frac{\mathrm{d}E_z}{\mathrm{d}z}(z_0)\,, \tag{4.10}$$

where z_1 is the fast motion around z_0 derived in Eq. (2.39) with the amplitude $z_1 = \frac{q_e}{m_e\omega^2} E_z(z_0)$. Finally, we can express the conditions as

$$\xi_{v,1} > \xi_1 = \frac{q_e}{m_e\omega^2} \frac{\mathrm{d}E_z}{\mathrm{d}z} \tag{4.11}$$

$$\xi_{v,2} > \xi_2 = \left(\frac{\mathrm{d}E_z}{\mathrm{d}z}\right)^{-1} \frac{q_e E_z}{2m_e\omega^2} \frac{\mathrm{d}^2 E_z}{\mathrm{d}z^2} \tag{4.12}$$

To further explore the relationship between the conditions Eq. (4.11) and Eq. (4.12) and the threshold energy ϵ_{tr}, we introduce a definition of the threshold point z_{tr}. It corresponds to the toroidal location at which the threshold energy is equal to the ponderomotive potential, $\Phi_P(z_{tr}) = \epsilon_{tr}$. The ponderomotive potential is defined as

$$\Phi_P = \left[\frac{q_e E_z}{2\sqrt{m_e}\omega}\right]. \tag{4.13}$$

Now, we consider only electrons with the energy $\epsilon_i < \max(\Phi_p)$, because electrons with higher energies will always enter the antenna region to be accelerated (passing electrons). For an electron ($\epsilon_i < \max(\Phi_p)$) approaching the antenna region from the

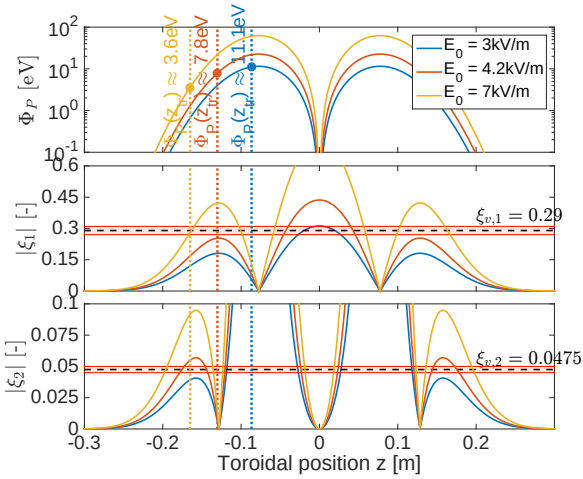

Figure 4.19: The reflection points z_r corresponding to a location for which the threshold energy ϵ_{tr} equals to the Ponderomotive potential Φ_p for three different electric field strengths $E_0 = [3\ 4.2\ 7]$kV/m at $f = 29$MHz and $\sigma = 0.075$m.

outside, the ponderomotive potential increases. At certain toroidal location, the electron will be reflected by the ponderomotive force. This reflection point is unique for each electron as it depends on its initial energy. Electrons, which are reflected before threshold point z_{tr}, will not gain any energy from the vacuum antenna field ($\epsilon_i \approx \epsilon_f$). Whereas, electrons, which pass the threshold point will obtain some acceleration from the antenna field.

The locations of the threshold point z_{tr} and also the threshold energies ϵ_{tr} for three simulations with different electric field strengths $E_0 = [3\ 4.2\ 7]\,\mathrm{kV/m}$ at $f = 29\,\mathrm{MHz}$ using the electric field profile E_z with $\sigma = 0.075\,\mathrm{m}$ in Eq. (4.7) are visualized in Fig. 4.19. The upper subplot shows the profile of the ponderomotive potential Φ_P (Eq. (4.13)) with the threshold points z_{tr}. The threshold energies were obtained from simulations, and the threshold points z_r correspond to the points where $\Phi_P(z_r) = \epsilon_{tr}$. Two other subplots illustrate the profiles of the validity conditions ξ_1 and ξ_2 (Eq. (4.11) and Eq. (4.12)). We identify three scenarios for which we can analytically estimate the reflection point z_r and threshold energy ϵ_{tr}:

1. At high electric field amplitude (E_0), low frequency (f), and steep profiles (low σ) we observe that the threshold energy is linked to the breaking of validity condition ξ_1 (Eq. (4.11)). This situation corresponds to the yellow line ($E_0 = 7\,\mathrm{kV/m}$) in Fig. 4.19. The oscillation center z_0 of an electron that approaches the antenna climbs on the potential up to the point where the initial energy equals the ponderomotive potential ($\Phi_p(z) = \epsilon_0$). The initial energy equals the final energy ($\epsilon_0 \approx \epsilon_f$) as long as $\xi_1 < \xi_{v,1} \approx 0.29$. We have found that electrons acquire energy from the electric field in the case $\xi_1(z_R) > \xi_{v,1}$ at the location of their reflections. The threshold energy ϵ_{tr} can, therefore, be taken

as the ponderomotive potential at the place where $\xi_1 = \xi_{v,1} = 0.29$ [17].

2. In the second scenario, when the validity limit $\xi_{v,1}$ is fulfilled for the entire electric field shape at the antenna edge ($\xi_1 < \xi_{v,1} = 0.29$), but the validity limit (Eq. (4.12)) is above $\xi_2 > \xi_{v,2} \approx 0.0475$ at the antenna edge. Then, the threshold energy ϵ_{tr} corresponds to the ponderomotive potential at which ξ_1 has a local maximum (the second derivative of the electric field profile turns negative). This situation corresponds to the red line ($E_0 = 4.2$kV/m) in Fig. 4.19. Our simulations showed that the final energy after reflection might differ from the initial energy as soon as the oscillation center enters the area with the negative quadratic term in Eq. (4.8). In the equation, a positive quadratic term focuses the oscillating electron around the slowly varying coordinate, while a negative quadratic term leads to an unstable oscillation (defocussing) [17].

3. Last of the three scenarios for which we can estimate the threshold energy analytically; when both conditions Eq. (4.11) and Eq. (4.12) are fulfilled. At such situation, the threshold energy ϵ_{tr} equals to the maximum ponderomotive potential. Only electrons with initial energy larger than the maximum ponderomotive potential $\epsilon_i > \max(\Phi_p)$ can enter into the antenna area and gain energy. The blue line in Fig. 4.19 ($E_0 = 3\,\mathrm{kV/m}$) indicates that indeed when the both conditions are fulfilled, the threshold energy in simulations equals to the maximum ponderomotive potential [17].

Parametric scans of the threshold energies in simulations for the electric field amplitude E_0, frequency f and shape σ are plotted in Fig. 4.20, resp. subfigures (a), (b) and (c). All presented scenarios are highlighted by different colors in each subplot. The observed tendencies are in ideal agreement with the numerical predictions of the threshold energies based on the previously introduced conditions. The transitions from each scenario are accompanied with the visible step in the threshold energy. These transitions are well captured in our numerical predictions for all parameter scans.

4.5.1 Ionization rate prediction using ponderomotive description

We can use these dependencies of the threshold energy on the vacuum electric field to explain ionization rate tendencies presented earlier in this chapter. The ionization rate and threshold energy have an inverse relationship: a simulation with the electric field parameters such that it has low threshold energy will have high ionization rate. For low threshold energy, more low energetic initial electrons can gain energy from the antenna field and overcome the ionization potential to undergo ionization collision reaction. As such, we can study a fraction of electrons from the initial Maxwell energy distribution with energies above this threshold energy.

We have seen in Section 4.4 that the antenna vacuum electric field changes its toroidal profile and magnitude with the radial distance from the antenna strap (Fig. 4.11). Therefore, we study the fraction of electrons $\int_{\epsilon_{tr}}^{\infty} f_{maxw.}(0.5\mathrm{eV})$ in a Maxwellian energy distribution of $0.5\,\mathrm{eV}$ that has energy above the threshold energy ϵ_{tr} as a function

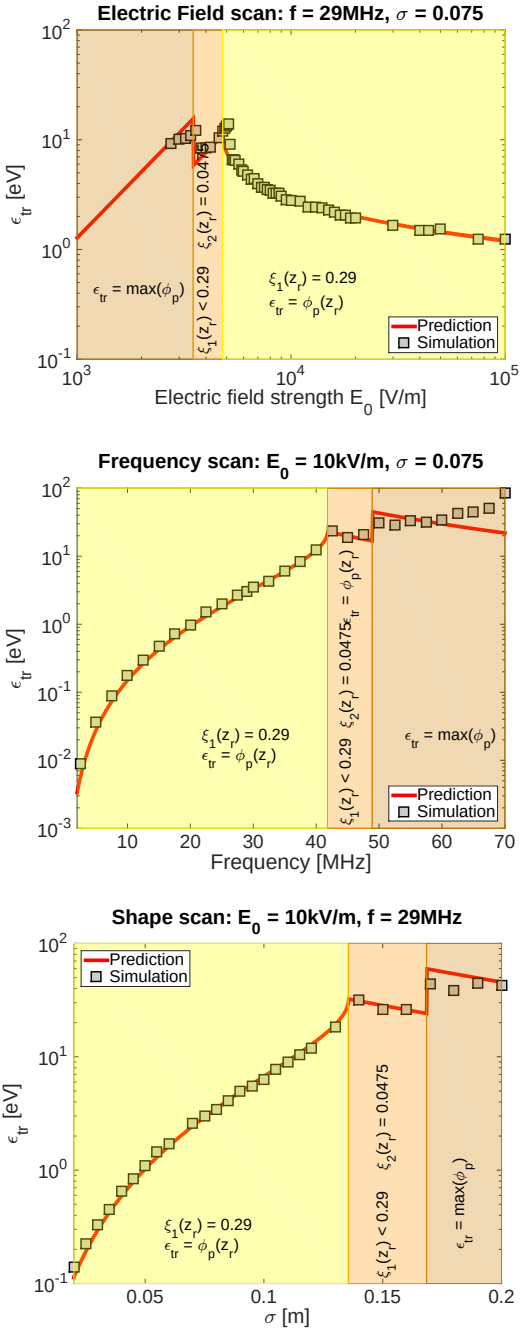

Figure 4.20: Threshold energy ϵ_{tr} as a function of (a) the electric field amplitude E_0, (b) frequency f, and (c) shape σ of the parallel electric field (Eq. (4.7)). The observed tendencies in the numerical experiments (rectangles) result from the electric field threshold Eq. (2.45) and validity limits Eq. (4.11) and Eq. (4.12).

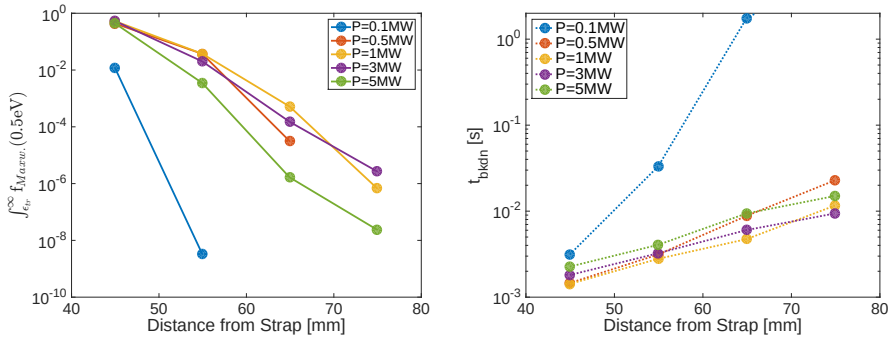

(a) (b)

Figure 4.21: (a) $\int_{\epsilon_{tr}}^{\infty} f_{maxw.}(0.5\text{eV})$, and (b) the breakdown time t_{bkdn} radial dependencies with the varying antenna power for **SmD**-phasing in top plane at $f = 40\,\text{MHz}$.

of the radial distance from the antenna strap and compare it with the breakdown time t_{bkdn} in the simulations. Fig. 4.21(a) plots the radial dependence of the fraction of the electrons above the threshold energy. We observe that the fraction decreases exponentially with radial distance from the strap. This dependency is in agreement with the experimental observations in which we see the first plasma at the magnetic field lines closest to the antenna strap (see Fig. 3.1(b)).

Additionally, Fig. 4.21 shows that for the lowest power $P = 0.1\,\text{MW}$ the fraction of the electrons above the threshold energy is very low close to the strap suggesting lower ionization rate (longer breakdown time). While with a small increase in the power to $P = 0.5\,\text{MW}$, the fraction of the electrons above the threshold energy substantially inceases (higher ionization rate and shorter breakdown time). These results are in agreement with the breakdown times obtained in simulations with the MC model `RFdinity1d` for ITER in Fig. 4.21(b) (or Fig. 4.14(a)). We can see in Fig. 4.21(a) that the fraction of the electrons above the threshold energy has maximum already for the powers $P = 0.5 - 1\,\text{MW}$ and increasing the power further is not usefull to reach shorter breakdown time (Fig. 4.21(b)).

We have indicated that using the PDM-model with our new understanding; we can preliminary estimate the parameters E_0, f with the lowest threshold energy ϵ_{tr}. With the lower threshold energy, we can expect higher ionization rate and thus shorter breakdown time t_{bkdn} in experiments. However, this preliminary analysis has also certain limitations and drawbacks. We have derived the validity limits for the vacuum electric field created by the ICRF antenna with one strap. We can apply these conditions for the ICRF antennas with more straps, but the final ionization rates will be also affected by the acceleration in the antenna area and not only on edge. We can demonstrate it using the vacuum electric field of the ITER ICRF antenna (See Fig. 4.11(b) and Fig. 4.12). This antenna consists of 4 columns of straps in the toroidal direction, each column consisting of 2 poloidal triplets of straps fed in parallel by one transmis-

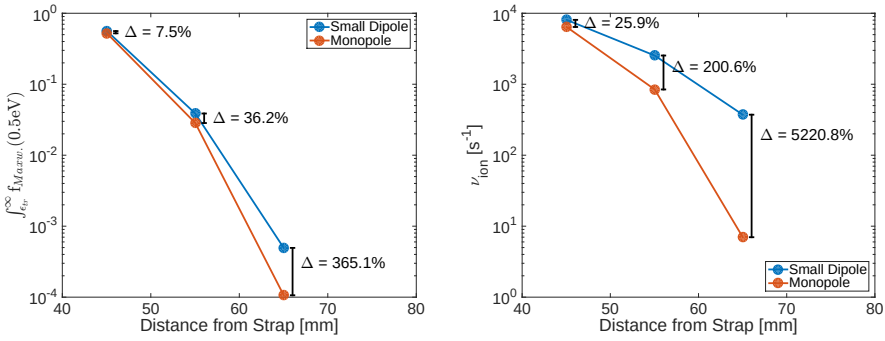

(a) (b)

Figure 4.22: (a) $\int_{\epsilon_{tr}}^{\infty} f_{maxw.}(0.5\text{eV})$, and (b) the ionization rate radial dependencies for the Small dipole and Monopole phasing in the upper middle plane at $P = 5\,\text{MW}$, $f = 40\,\text{MHz}$ and $p = 0.0075\,\text{Pa}$.

sion line per triplet, Fig. 4.11(a). We compare two different antenna phasing: Small dipole $[0\,\pi\,0\,\pi]$-phasing, Monopole $[0\,0\,0\,0]$-phasing. The shapes of the electric fields for these two phasing are similar at the antenna edge. Therefore, the threshold energies for these phasing depending exclusively on the electric field at the edge should be similar as well. Fig. 4.22(a) shows the radial dependence of the fraction of the electrons above the threshold energy. We illustrated the relative difference Δ between the values of the fraction of electrons for the Monopole x_m and Small Dipole x_d phasing:

$$\Delta = \frac{x_d - x_m}{x_m} \times 100\,[\%]\,. \tag{4.14}$$

The difference Δ of the electrons fraction in Fig. 4.22(a) increases with the radial distance from the antenna strap. If the ionization rate depends solely on the acceleration at the antenna edge and the fraction of the electrons above the threshold energy, then we should see comparable differences between the ionization rates for the monopole and small dipole phasing as in Fig. 4.22(a). However, we can see that in Fig. 4.22(b) that the relative differences between the ionization rates for the monopole and small dipole are more substantial than in Fig. 4.22(a). This difference is caused by varying velocity distributions for these two phasing (shown in Fig. 4.13(b), and it cannot be predicted solely by the ponderomotive description discussed in this section. We can use this ponderomotive description to obtain preliminary estimations of the ionization rate dependencies on E_0, f and σ, but ultimately we have to use more sophisticated models, e.g., `RFdinity1d` to explore the dependencies in more details.

4.6 Conclusion

In this chapter, we have discussed simulation results obtained with the MCC-model `RFdinity1d` and their comparison with the experimental observations of discharge

initiation by the ICRF antenna in TEXTOR and URAGAN-3M. First, we showed the electron density evolution in our simulations. As predicted by theory, the electron density has exponential evolution in time. The slope of this exponential increase corresponds to ionization rate ν_{ion}. The ionization rate can also be calculated in our simulations using the electron velocity distribution. Both methods give almost identical values of the ionization rate in our simulations. In later analysis, we are usually using the ionization rate obtained by fitting the electron density exponential increase in time.

We studied ionization rate dependency on the electric field amplitude E_0, frequency f, neutral gas pressure p and circumference length. The electric amplitude scan demonstrated that above a certain amplitude threshold, the ionization rate abruptly increases from zero reaching a maximum value of the ionization rate at rather low electric field amplitude $E_0 = 10 - 30\,\mathrm{kV/m}$. After arriving at this maximum value, the ionization rate stays nearly constant with the increasing amplitude E_0. We found that the ionization rate decreases monotonically with the applied frequency f. According to the PDM-model, the ionization rate should be dependent on the ratio between the electric field amplitude and frequency E_0/f. However, we showed with the MCC-model that simulations with the same ratio but different values of the electric field amplitude and frequency have very different ionization rates. Furthermore, we observed almost ten times smaller ionization rates in our simulations than predicted by the PDMI-model. This discrepancy demonstrates that more detailed models like MCC `RFdinity1d` are needed to better describe and understand discharge initiation by the ICRF antennas. The pressure scan of the ionization rate indicated increasing rate with the pressure given by $\nu_{\mathrm{ion}} \sim \sqrt{p}$. This relationship is again in discrepancy with the PDMI-model suggesting a linear dependency on the pressure. Furthermore, the ionization rate in our simulations decreases with the circumference length as $\nu_{\mathrm{ion}} \sim C^{-1}$.

Then, we introduced numerical definitions of the breakdown time applied in the MCC-model to benchmark it with the experimental breakdown times. In the experiment, we identify the breakdown as a moment of the antenna voltage drop and rise in the H_α signal. We cannot employ either of these experimental definitions in our model due to missing interaction between the antenna field and electron density in front of the ICRF antenna. Therefore, we proposed three numerical definitions of the breakdown time: (i) a moment when electron density overcomes the critical density for the low hybrid resonance ($\omega = \omega_{\mathrm{LHR}}$) $n_{\mathrm{e,crit}}^{\mathrm{SW(LHR)}}$ and moments when (ii) ionization rate and (iii) energy losses due to ionization collisions equal to Coulomb collision rate and energy losses during Coulomb collisions. We compared all the numerical definitions in our simulations with the experimental observation of the antenna voltage drop. In the simulations, we did not observe that the electron energy losses due to electron-ion Coulomb collisions exceed the energy losses due to ionization reactions. Therefore, we could not apply this definition in our analysis. The numerical breakdown time definitions (i) and (ii) showed a good agreement with the experimental observations. However, we discussed that we have to be careful with the direct comparison of the numerical and experimental breakdown times because the value of the numerical breakdown time depends on the chosen initial electron density in

our simulations. By selecting lower or higher initial electron density, we can obtain longer or shorter breakdown time. For this reason, in our analysis, we are more interested in the ionization rate dependencies on the parameters and to get the breakdown time indirectly by assuming that for a higher ionization rate we will measure a shorter breakdown time.

Nevertheless, we compared our simulations with the experimental observations on TEXTOR. This comparison between the simulation and experimental breakdown times resulted in a good agreement for the pressure and generator power dependencies. The agreement was visible for rather low neutral gas pressure ($p < 0.03\,\mathrm{Pa}$), at higher pressure, the experimental breakdown time is shorter than suggested by our simulations. We indicated that due to high pressure the plasma might be first locally initiated in front of the antenna in the experiments and later the discharge spreads toroidally into a vessel. Indeed, we observed in our simulations that the local density in the antenna vicinity is slightly higher than at places further from the antenna. In our simulations, we use the average electron density to define the moment when the critical density $n_{\mathrm{e,crit}}^{\mathrm{SW(LHR)}}$ is reached. As such, this localized electron density could reach the critical density in a shorter time to decrease the numerical breakdown time. The breakdown times in TEXTOR experiment as a function of the electric field strength showed a qualitative agreement with the simulation results. Both dependencies demonstrated the existence of the optimal electric field strength above which the breakdown time does not significantly change.

Then, we examined the discharge initiation with the ITER ICRF antenna. Although, the previously presented dependencies suggested meager ionization rates for the high RF frequencies, the simulations with the ITER antenna field demonstrated that it is possible to initiate a discharge with the ITER ICRF antenna even above $40\,\mathrm{MHz}$. However, our simulations stated that we should use the lowest operation frequency of the ITER ICRF antenna for the most efficient discharge initiation. Furthermore, our simulations demonstrated that the discharge would be initiated very locally in the antenna vicinity; $R < 5$cm from the antenna strap. We found that the optimal operation generator power is around $0.5\,\mathrm{MW}$, and operating the antenna during the ICWC experiments with a higher generator power will not decrease the breakdown time. The simulations also indicated that discharge can be safely obtained even for low hydrogen pressure, $p \leq 0.01\,\mathrm{Pa}$. Our results implied that the Small dipole phasing for the ITER antenna is more favorable for discharge initiation than the Monopole phasing, while, the experiments on ASDEX Upgrade and TEXTOR indicated shorter breakdown times for the monopole phasing rather than for dipole phasing.

In the last part of this chapter, we have described a new method to find threshold parameters for the discharge initiation using ICRF antennas. The method uses an approach derived from the PDM-model, but instead of describing the conditions to accelerate the electrons above the ionization potential in front of the antenna, we seek the parameters of the electric field such that the electron can enter into the antenna region from outside and be accelerated by antenna vacuum field. We found that an electron must have energy above a certain threshold to be able to gain any additional energy from the antenna field. The ponderomotive force reflects electrons with energies be-

low this threshold without gaining any acceleration from the antenna field. We derived analytic formulas to find the threshold energy for the combination of E_0, f, and σ (the shape of the E_z). There is unexpectedly good agreement between the analytically obtained threshold energies and simulations results. Then, using this new method, we could describe our simulation results presented in this chapter. The threshold energy and ionization rate have an inverse relationship, the lower the threshold energy, the more low energetic electrons can be accelerated by the antenna field and contribute to ionization collisions (higher ionization rate).

References

[1] Matěj Tripský. *Monte Carlo Simulation of Initial breakdown Phase of Magnetized toroidal ICRF discharges*. Master's thesis, Universtiteit Gent, Belgium, 2013.

[2] M. Tripský et al. *Monte Carlo Simulation of Initial Breakdown Phase for Magnetised Toroidal ICRF Discharge*. In AIP Conf. Proc., volume 1580, page p. 334, Sorrento, Italy, June 2013.

[3] M. Tripský et al. *Monte Carlo simulation of ICRF discharge initiation at* $\omega_{LHR} < \omega$. In European Conference Abstracts (ECA), volume 38.F. of *http://doi.org/10.1063/1.4864556*, Berlin, Germany, June 2014.

[4] M. D. Carter et al. *Plasma production using radiofrequency fields near or below the ion cyclotron range of frequencies*. Nuclear Fusion, 30(723), 1990.

[5] F. Schuller et al. *Report on Applications of ICWC on ITER*. Technical Report IO/2009/ADM-014 report version 3, ITER - IO, 13115, St. Paul-lez-Durance, France, November 2009.

[6] A. Lyssoivan et al. *Simulation of ITER full-field ICWC scenario in JET: RF physics aspects*. Plasma Phys. Control. Fusion, 54, 2012.

[7] Volodymyr Bobkov. *Studies of high voltage breakdown phenomena on ICRF (Ion Cyclotron Range of Frequencies) antennas*. PhD thesis, Technische Universitat Munchen Fakultat fur Physik, 2003.

[8] R. Koch et al. *Ion cyclotron resonance heating on TEXTOR*. Fusion science and technology, 47:97–107, 2005.

[9] R. Papoular et al. *The Genesis of Toroidal Discharges*. Nuclear Fusion, 16(1):37–45, 1976.

[10] A. Lyssoivan et al. *Wave aspect of neutral gas breakdown with ICRF antenna in ICWC operation mode*. In European Conference Abstracts. Vol. 38.F. European Conference Abstracts (ECA), Berlin, Germany, June 2014.

[11] M. Tripský et al. *Investigation of discharge initiation by ICRF antenna on URAGAN 3-M*. ECA, 40A(P2.052), 2016.

[12] V. V. Chechkin et al. Plasma Physics Reports, 40:601–610, 2014.

[13] A. Lyssoivan et al. *Development of ICRF wall conditioning technique on divertor–type tokamaks ASDEX Upgrade and JET*. Journal of Nuclear Materials, 456:337–39, 2005.

[14] M. Tripský et al. *Monte Carlo simulation of ICRF discharge initiation in ITER*. In AIP Conference Proceedings, volume 1689 of *http://doi.org/10.1063/1.4936507*, page 060009, California, USA, 2015.

[15] CST STUDIO SUITE (R), http://www.cst.com. *CST AG*, 2015.

[16] A. Lyssoivan et al. J. Nucl. Mater., 415, 2011.

[17] T. Wauters and M. Tripský et al. *Advanced ponderomotive description of electron acceleration in ICRF discharge initiation*. EPJ Web of Conferences, 157:03064, May 30 - June 2 2017.

5

Particle-In-Cell model Monte Carlo Collision model RFdinity1d

In the previous two chapters, we have introduced the Monte Carlo collision model `RFdinity1d` following the motion of electrons along the magnetic field line around the torus. The parallel electric field accelerates electrons in front of the ICRF antenna. Although the model improves our understanding of the discharge initiation by the ICRF antenna, it neglects waves excitation above specific threshold densities. It is expected that upon reaching these critical densities, the waves will play an essential role in the discharge initiation. Additionally, our MC model `RFdinity1d` operates only with the vacuum electric field of the antenna during a simulation. Using the vacuum electric field is reasonable for a low electron density. However, for a higher electron density $n_e > 10^{13}\,\mathrm{m}^{-3}$, we must assume that the antenna electric field will be modified by a presence of the medium in front of the antenna. To include the interaction between the antenna electric field and plasma, we modified the MC model `RFdinity1d` into a Particle-In-Cell Monte Carlo collision model. This model includes the plasma self-produced electric field created by the charge inhomogeneity generated by the antenna electric field. Then, the final field acting at charged particles is a sum of the parallel vacuum antenna electric field and the electrostatic field [1].

5.1 PIC MCC model `RFdinity1d`

The PIC MCC model is partially based on MC model previously presented in Chapter 3. The PIC-MCC model `RFdinity1d` (1D in displacements) follows the motion of guiding centers of both electrons and ions in a narrow bundle of magnetic field lines close to the antenna straps. Collisions between the electrons and neutral atoms

are treated in the 3D velocity space (v_x, v_y, v_z), where v_z is the parallel velocity component (direction of the magnetic field B_T) and $v_\theta = \sqrt{v_x^2 + v_y^2}$ the perpendicular velocity component. However, we have to stress that the model does not resolve the cyclotron gyration in space. The electrons are accelerated exclusively in the parallel direction while the perpendicular velocity remains unchanged by the electric field. During the collisions in the 3D velocity space, part of their parallel velocity component is scattered into the perpendicular velocity [1]. Both electrons and ions are treated kinetically and self-consistently by the numeric Leapfrog scheme. The charged particles are accelerated in the parallel direction with respect to the magnetic field B_T by the Lorentz force:

$$m\frac{\mathrm{d}v_z}{\mathrm{d}t} = F_L = q\left(E_z^{RF} + E_z^P\right) , \tag{5.1}$$

where $v_z \times B_T$ term is omitted ($v_z \parallel B_T$). The Lorentz force F_L results from the sum of two electric fields: (i) the vacuum RF electric field in front of the ICRF antenna E_z^{RF} and (ii) the self-generated electrostatic field E_z^P obtained from Poisson's equation. The magnitude of the electrostatic field E_z^P depends on the electron density, $|E_z^P| \sim n_e$. We will show that for low electron density the electrostatic field is much smaller than the RF antenna field, $|E_z^P| \ll |E_z^{RF}|$, and the above equation 5.1 simplifies to Eq. (3.1) used in the MC `RFdinity1d` model, $F_L \approx qE_z^{RF}$. Therefore, at low electron densities, the number of electrons evolves identically in time in both models. However, these evolutions diverge from each other when the magnitude of the electrostatic field increases and is comparable to the RF antenna field. We will show this comparison in the section with the results (Section 5.2.1).

Again, we use the concept of so-called **super-particles** for the computational particles (electrons, ions) in our PIC model. These super-particles represent many real particles to rescale the number of particles. A super-particle follows the same trajectory as the real particles because the Lorentz force depends only on the charge-to-mass ratio [2].

First, we describe the schema of the model, and later on, we go into more details to comment on each step of the model. The algorithm of the model is

- Set the initial position and velocity distributions of charged particles. We employ the algorithm described in Section 3.1.3 to distribute initial energies of electrons and ions using a Maxwell energy distribution with temperatures $T_{e,0} = 0.5\,\mathrm{eV}$ for electrons and $T_{i,0} = 0.04\,\mathrm{eV}$ for ions. The charged particles are again distributed uniformly around the whole torus circumference.

- Repeat the following steps to update the positions and velocities of the charged particles.

  - Compute the charge density on the grid, ρ, defined as:

$$\rho = q_e\left(n_i - n_e\right) , \tag{5.2}$$

    where n_e and n_i are the electron and ion densities.

– The electrostatic electric field is determined by first solving Poisson's equation in 1D to obtain electric potential ϕ,

$$\frac{\partial^2 \phi}{\partial z^2} = \frac{\rho}{\epsilon_0} \,. \tag{5.3}$$

Then, we take the gradient of the electric potential to estimate the electrostatic field E^P

$$E^P = -\nabla \phi \,. \tag{5.4}$$

– Updating the velocities and positions of the charged particles using the Leap-frog schema. The charged particles are accelerated by a sum of two electric fields: antenna electric field E^{RF}, and electrostatic electric field E^P.

– Electrons undergo collisions with the neutral gas. We apply Monte Carlo collisions schema using null-collision method to select colliding electrons and type of the collision.

Selection of the particle shape function

In the *particle-in-cell* models, the macro-quantities (charge density, electrostatic potential, and field) are calculated only on the mesh points, while particles can be located anywhere on the continuous domain. These macro-quantities are then assigned to particles by a weighting method. First, we define the shape function to estimate how a particle at the coordinate z_p is distributed over the spatial coordinate z: $S_z\,(z - z_p)$. For the purpose of general derivation, we use ξ as the spatial coordinate. The shape function is usually symmetric: $S_\xi\,(\xi - \xi_p) = S_\xi\,(\xi_p - \xi)$, and conserves quantities:

$$\int_{-\infty}^{+\infty} S_\xi\,(\xi - \xi_p)\,\mathrm{d}\xi = 1 \,. \tag{5.5}$$

PIC models usually apply the so-called b-splines as the spatial shape functions [3]. These b-spline functions are defined as series of consecutively higher-order functions acquired from each other by integration:

$$b_l(\xi) = \int_{-\infty}^{+\infty} b_{l-1}(\xi') b_0(\xi - \xi')\,\mathrm{d}\xi' \,. \tag{5.6}$$

The first b-spline is the flat-top function described as

$$b_0(\xi) = \begin{cases} 1 & \text{for } |\xi| < 1/2 \\ 0 & \text{else}\,. \end{cases} \tag{5.7}$$

The first two b-splines, $b_0(\xi)$ and $b_1(\xi)$, are illustrated in Fig. 5.1(a). The shape function using the b-spline function is given by

$$S_\xi(\xi - \xi_p) = \frac{1}{\Delta_p} b_l\left(\frac{\xi - \xi_p}{\Delta_p}\right) , \tag{5.8}$$

where Δ_p refers to the scale-length of the support of the shape function. In our PIC model Δ_p equals to grid size Δz. We already mentioned one purpose of the shape function in PIC models: to determine how physical particles are distributed to cells. Next to it the shape function is applied to calculate how the electric field on the grid-points interpolates to the location of the physical particles.

We describe the procedure in the model to obtain the charge distribution on the grid points and how the resulting electrostatic field at grid points is interpolated to the particle locations. We estimate the charge density at grid points ρ_i (centers of the cells) as the average of the charge distribution ρ over the cells [3, 4]. In our one-dimensional case, the cell average of ρ is

$$\rho_i = \frac{1}{\Delta z} \int_{z_{i-1/2}}^{z_{i+1/2}} \rho(z)\, \mathrm{d}z\,. \tag{5.9}$$

The above equation is modified using the definition of the b-spline of order 0:

$$\rho_i = \frac{1}{\Delta z} \int_{-\infty}^{+\infty} b_0 \left(\frac{z - z_i}{\Delta z} \right) \rho(z)\, \mathrm{d}z\,. \tag{5.10}$$

Charge density $\rho(z)$ can be expressed using the shape function $S_z(z - z_p)$:

$$\rho(z) = \sum_p q_p S_z(z - z_p)\,. \tag{5.11}$$

Then the average charge density over each cell is

$$\rho_i = \frac{1}{\Delta z} \sum_p \int_{-\infty}^{+\infty} b_0 \left(\frac{z - z_i}{\Delta z} \right) q_p S_z(z - z_p)\, \mathrm{d}z\,, \tag{5.12}$$

where q_p is the elementary charge of a particle ($-q_e$ for an electron and q_e for hydrogen ion H_2^+), z_i refers to the grid point i, z_p is the location of the particle, and z is the toroidal coordinate. We define the interpolation function $W(z_i - z_p)$ to simplify Eq. (5.12)

$$W(z_i - z_p) = \int_{-\infty}^{+\infty} b_0 \left(\frac{z - z_i}{\Delta z} \right) S_z(z - z_p)\,. \tag{5.13}$$

From the definition of the b-spline functions and because the shape function S_z is the b-spline function of order l, the interpolation function $W(z_i - z_p)$ equals to the b-spline function of order $l + 1$ [3, 4]:

$$W(z_i - z_p) = b_{l+1} \left(\frac{z_i - z_p}{\Delta z} \right)\,. \tag{5.14}$$

Evaluation of the charge density

Following the expression of the average cell charge density, $\rho_i = \sum_p \frac{q_p}{\Delta z} W(z_i - z_p)$, we can describe the evaluation of the charge density of the cell. In our PIC model, we use the b-spline function of order 0, meaning that our interpolation function, $W(z_i -$

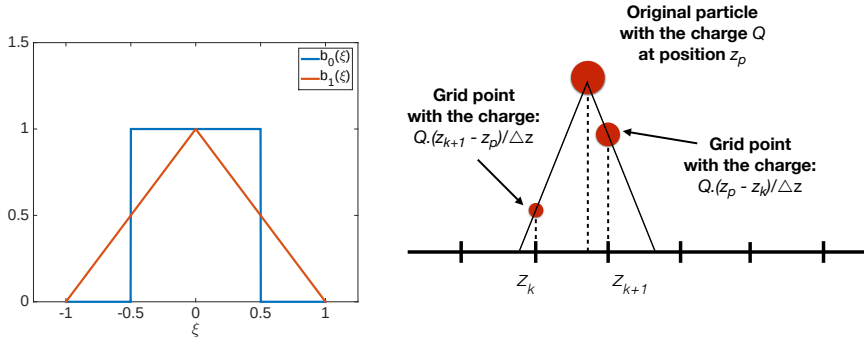

(a) (b)

Figure 5.1: (a) The first two b-splines $b_0(\xi)$ and $b_1(\xi)$. (b) Illustration of the charge density evaluation using the b-spline functions.

z_p), is the b-spline function of order 1 resulting in simple linear interpolation. For a particle (electron or ion) with position z, we can identify which two grid points the particle lies between. Suppose that the particle lies between z_j and z_{j+1}, then the charges ρ_j and ρ_{j+1} at this grid points are modified by the particle as

$$\rho_j = \rho_j + \frac{q_s}{\Delta z}\frac{z_{j+1} - z}{\Delta z} \tag{5.15}$$

$$\rho_{j+1} = \rho_{j+1} + \frac{q_s}{\Delta z}\frac{z - z_j}{\Delta z}\,. \tag{5.16}$$

Evaluation of the electrostatic potential and field

The toroidal domain is $[-z_m,\, z_m[$, where the variable z_m refers to a half of the circumference length $z_m = \pi\,(R_0 + a)$. In our geometry, the ICRF antenna is located at zero, and the periodic boundary conditions are applied to the location opposite the antenna as shown in Fig. 5.2. The periodic boundary conditions for charge distribution ρ, electrostatic potential ϕ, and electrostatic electric field E_z^P are defined as

$$\rho(-z_m) = \rho(z_m) \tag{5.17}$$

$$\phi(-z_m) = \phi(z_m) \tag{5.18}$$

$$E_z^P(-z_m) = E_z^P(z_m)\,. \tag{5.19}$$

We apply Fourier transformation method to solve the one-dimensional Poisson equation given by

$$\frac{\partial^2\phi}{\partial z^2} = -\frac{\rho}{\epsilon_0}\,, \tag{5.20}$$

where $\epsilon_0 = 8.8541 \times 10^{-12}\,\mathrm{F}\cdot\mathrm{m}^{-1}$ is the vacuum permittivity. The Fourier transfor-

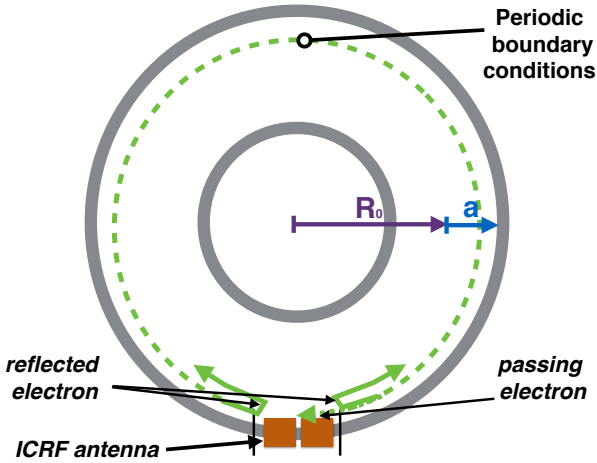

Figure 5.2: Top view on the mid-plane of a tokamak with one ICRF antenna. Low energetic electron is reflected at the antenna edge and either it is reflected again on the opposite side or it passes into the antenna region when it has sufficient energy to overcome the ponderomotive barrier at the antenna edge. The simulation domain in the toroidal direction is given by $2\pi\,(R_0 + a)$. The periodic boundary conditions are applied at the toroidal location opposite to that of the ICRF antenna.

mation of the left-hand side of the above equation is written

$$\begin{aligned}\int_{-\infty}^{+\infty} \frac{\partial^2 \phi}{\partial z^2} e^{ikz}\,\mathrm{d}z &= -k^2 \int_{-\infty}^{+\infty} \phi e^{ikz}\,\mathrm{d}z \\ &= -k^2 \hat{\phi}(k)\,, \end{aligned} \tag{5.21}$$

where $\hat{\phi}(k)$ is the Fourier transformation of $\phi(z)$ [4, 5]. The right-hand side of Eq. (5.20) is replaced by the Fourier transformation of the charge distribution $\rho(z)$ into

$$\hat{\rho}(k) = \int_{-\infty}^{+\infty} \rho(z) e^{ikz}\,\mathrm{d}z\,. \tag{5.22}$$

Using these expressions, we write the Fourier transformation of Eq. (5.20) as

$$\hat{\phi}(k) = \frac{\hat{\rho}(k)}{\epsilon_0 k^2}\,. \tag{5.23}$$

When the electric potential in k-space $\hat{\phi}(k)$ is calculated, the electric potential $\phi(z)$ is eventually recalculated via the inverse Fourier transformation

$$\phi(z) = \frac{1}{2\pi} \int_{-\infty}^{+\infty} \hat{\phi}(k) e^{-ikz}\,\mathrm{d}k\,. \tag{5.24}$$

We divide the circumference length into grid points with a uniform spacing Δz: $z_j = j\Delta z$ for $j = 0,\, 1,\, 2,\, \ldots,\, N-1$. The number of grid points N is determined by the

PIC constraint, $\Delta z \sim \lambda_D$ (λ_D is the Debye length) [3, 5]. The charge distribution $\hat{\rho}$ in Eq. (5.22) is discretized by the Discrete Fourier Transformation (DFT) from the charge distribution ρ at the grid points. We denote $\hat{\rho}_j$ and $\hat{\phi}_j$ corresponding to the DFT of $\rho_j = \rho(z_j)$ and $\phi_j = \phi(x_j)$ to illustrate the algorithm. The wave-number k of $\hat{\rho}_j$ is given by $k = j2\pi/L$ for $j = 0, 1, \ldots, N/2$ and $k = (j - N)2\pi/L$ for $j = N/2 + 1, \ldots, N - 1$, where $L = N\Delta z$ is the length of the space domain. Using these expressions, we write the discrete form of Eq. (5.23) as [4]

$$\hat{\phi}_j = \frac{\hat{\rho}_j}{\epsilon_0 \left[j2\pi/L\right]^2} \tag{5.25}$$

for $j = 1, 2, \ldots, N/2$ and

$$\hat{\phi}_j = \frac{\hat{\rho}_j}{\epsilon_0 \left[(j - N)2\pi/L\right]^2} \tag{5.26}$$

for $j = N/2 + 1, \ldots, N - 1$. We have to express a special case for $j = 0$ because in this case $k = 0$ appears in the denominator of Eq. (5.23). For this wave-number, Eq. (5.22) becomes only the overall integration over the charge distribution $\int_{-\infty}^{+\infty} \rho \, \mathrm{d}z$. Since we have the overall charge neutrality, this integral equals to zero implying that $\hat{\rho}_0 = 0$. Therefore, we set in our model $\hat{\phi}_0 = 0$. Finally, we can obtain ϕ_j through the inverse DFT from $\hat{\phi}_j$ [4, 5].

When we know the electrostatic potential ϕ_j, we can obtain the electrostatic field E_j^P through the following central difference scheme:

$$E_j^P = -\left.\frac{\partial \phi}{\partial z}\right|_{z=z_j} = -\frac{\phi_{j+1} - \phi_{j-1}}{2\Delta z} \,. \tag{5.27}$$

Knowing the electrostatic field E_j^P at the grid points, we have to use the corresponding interpolation function to estimate the electric field on the particle's location. As we discussed earlier, we use the zero-order b-spline function b_0 for the spatial shape of particles. Therefore, the corresponding interpolation function (Eq. (5.14)) is b_1 corresponding to linear interpolation [3, 4]. The electrostatic field $E^P(z_p)$ on a particle at the location z_p between z_j and z_{j+1} is given by

$$E^P(z_p) = E_j \frac{z_{j+1} - z_p}{\Delta z} + E_{j+1} \frac{z_p - z_j}{\Delta z} \,. \tag{5.28}$$

Electron collisions with neutral gas

In the previously MC model `RFdinity1d` in Section 3, we have described the MC method for electron collisions with molecules and ions. In this method, we sampled for each electron a path length between two collisions. Knowing the path length and following the motion of each electron, we can quickly estimate when the electron collides. However, this method might be computationally slow, because we have to check every time-step all electrons for a collision. In this section, we describe another more optimized method of the Monte Carlo Collision schema (MCC) usually applied

in PIC models [2, 6, 7]. It is called *null collision* method, and it is used as well in our PIC-MCC model `RFdinity1d`.

We use this MCC schema only on inelastic collisions between electrons and neutral hydrogen molecules ($e - H_2$). It includes 12 collisions grouped into 5 inelastic collision types (*ionization, vibrational excitation, excitation, dissociation, dissociative ionization*) and *elastic scattering*. The collisions taken into account are summarized in Table 5.1.

Index	Collision species	Before	After	ΔE [eV]
1	Ionization	$e + H_2\left(X^1\Sigma_g^+\right)$	$e + H_2^+(v) + e$	15.43
2	Vibration excitation	$e + H_2\,(v = 0)$	$e + H_2^*(v = 1)$	0.5
			$e + H_2^*(v = 2)$	1.0
3	Electronic excitation	$e + H_2\left(X^1\Sigma_g^+\right)$	$e + H_2^*\left(B^1\Sigma_u^+ 2p\sigma\right)$	12.1
			$e + H_2^*\left(C^1\Pi_u 2p\pi\right)$	12.4
			$e + H_2^*\left(E, F^1\Sigma_g^+\right)$	12.7
4	Dissociation	$e + H_2\left(X^1\Sigma_g^+\right)$	$e + H(1s) + H(1s)$	10.5
			$e + H(1s) + H^*(2s)$	10.5
			$e + H^*(2p) + H^*(2s)$	10.5
			$e + H(1s) + H^*(n = 3)$	10.5
5	Dissociation ionization	$e + H_2(X^1\sum_g^+)$	$e + H^+ + H(1s) + e$	21.1
6	Elastic scattering	$e + H_2$	$e + H_2$	–

Table 5.1: Included collisions in the PIC-MCC `RFdinity1d` model with their threshold energies ΔE [8, 9].

The kinetic energy of the incident ith electron is given by

$$\epsilon_i = \frac{1}{2} m_e v_i^2 = \frac{1}{2} m_e \left(v_z^2 + v_\theta^2\right) , \tag{5.29}$$

where v_z is the velocity in the toroidal direction driven by Eq. (5.1), and v_θ is the velocity in the perpendicular direction. The total cross section $\sigma_T^{e-H_2}$ for a collision between the incident ith electron at energy ϵ_i and the hydrogen molecule is given by a sum of cross sections for each collision taken from [9]:

$$\sigma_T^{e-H_2}\left(\epsilon_i\right) = \sum_{j=1}^{6} \sigma_j\left(\epsilon_i\right), \tag{5.30}$$

where $\sigma_j\left(\epsilon_i\right)$ is the cross section of the jth collision (Index in Table 5.1). In the null collision method, an additional collision process is included with a collision rate such that the total collision rate $n_{H_2}\sigma_T^{e-H_2}\left(\epsilon\right) v$, gives a constant value over all energies ϵ. This constant collision rate is represented by the maximum value of the total collision rate

$$\nu^\star = n_{H_2} \max_\epsilon \left(\sigma_T^{e-H_2} v\right) . \tag{5.31}$$

Knowing this collision rate, $\nu^\star$, independent on the incoming energy, we can express the fraction of the total number of electrons in the simulation undergoing collisions

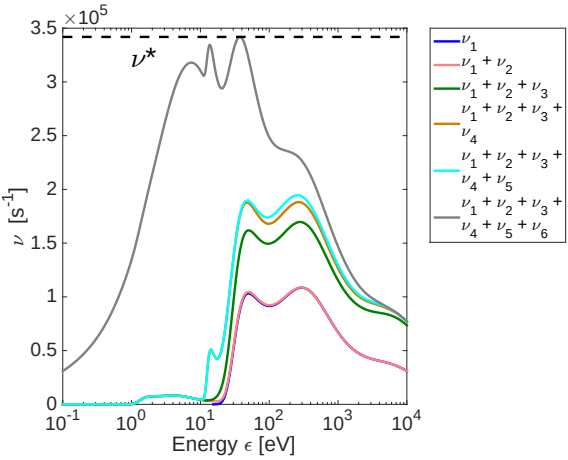

Figure 5.3: Accumulation of collision frequencies ($\nu_n = \sum_{j=1}^{n} \nu_j$, $n \in (1, 2, \ldots 6)$). The introducing the null collision process results in a constant frequency, $\nu^\star$, over all energies ϵ, at $p_{H_2} = 10^{-2}$ Pa and at the gas temperature $T_{gas} = 400\,\mathrm{K}$ (0.035 eV).

within a time step Δt. First, we express the probability of a collision P_{null}:

$$P_{\text{null}} = 1 - \exp\left(-\nu^\star \Delta t\right) . \tag{5.32}$$

The number of colliding electrons per time-step Δt corresponds to a product of the number of electrons N_e and collision probability P_{null}. The colliding electrons, $N_e P_{\text{null}}$, are randomly chosen from all electrons N_e, and for each chosen electron the type of collision is determined using

$$\begin{aligned}
\xi &\leq \nu_1(\epsilon)/\nu^\star && \text{(Collision type 1)} \\
\nu_1(\epsilon)/\nu^\star < \xi &\leq (\nu_1(\epsilon) + \nu_2(\epsilon))/\nu^\star && \text{(Collision type 2)} \\
&\vdots \\
\sum_{j=1}^{6} \nu_j(\epsilon)/\nu^\star &< \xi && \text{(Null collision)}
\end{aligned}$$

where ξ is a random number, $\xi \in [0, 1]$ [2, 6, 7]. These accumulated collision frequencies are visualized in Fig. 5.3 together with a constant collision frequency $\nu^\star$. When the null collisions occurs in the above schema, it means that no collision happens, and selected electrons continues without any change in its energy and velocity components. The time-step for sampling collisions in our simulations is set at $\Delta t = 10^{-8}$ s. We have decided to use this collision time-step Δt because the P_{null} parameter in PIC simulations is typically on the order of 10^{-2} [6]. For our maximum pressure during ICWC experiments $p = 5 \cdot 10^{-2}$ Pa, the parameter P_{null} equals to $\approx 1.7 \cdot 10^{-2}$. As such only $1.7 \cdot 10^4$ of 10^6 electrons will collide and need to be checked for the collision type (collision type in Table 5.1 and the null collision). The calculation of the

post-collision velocities in our PIC-MCC `RFdinity1d` is identical to the method for the previously presented MC model in Section 3.1.4.2.

5.1.1 Model Constraints and Limitations

As mentioned earlier the model in the present version includes the collisions between electrons and hydrogen molecules. The hydrogen molecules are assumed to be uniformly distributed over the whole length of the torus. The assumptions are justified at the early stage of the discharge initiation. Upon reaching higher densities, other species (H_2^+, H^+, H) created via $e - H_2$ collisions become important. It was deduced for the typical neutral pressure range in the ICWC experiments ($p_{H_2} = 10^{-3} - 5 \cdot 10^{-2}\,\mathrm{Pa}$) that (i) $e - H_2^+$ collisions can be ignored up to $n_e \leq 10^{16}\,\mathrm{m}^{-3}$, where the collision rate of these collisions is much smaller than $e - H_2$ collisions, $\nu^{e-H_2} \geq 10^3 \cdot \nu^{e-H_2^+}$, (ii) recombination collisions $e - H^+$ can be ignored even higher up to $n_e \leq 10^{17}\,\mathrm{m}^{-3}$, $\nu^{e-H_2} \geq 10^3 \cdot \nu^{e-H^+}$. Ion-neutral collisions are neglected in this version of the model due to their ten times smaller collision frequency than the electron-neutral collisions. However, it is expected that they will play a role in temperature isotropization of ions in the parallel and perpendicular direction at higher electron densities. In our model, ions are accelerated solely in the parallel direction, and their perpendicular velocity components do not change during a simulation. The isotropization is needed to justify a comparison of the ion temperature in the perpendicular direction obtained by NPA measurements in experiments with simulations observations in which ions have most of their energy in the parallel direction. In this version of the model, we also ignore Coulomb collisions between charged particles since, for low-density weakly-ionized discharges, interactions between charged and neutral species are the dominant collision mechanisms [10]. In the previous model, in which Coulomb collisions were included, their effect became noticeable only above $n_e > 10^{15}\,\mathrm{m}^{-3}$ (See Section 3.1.5) [11, 12].

In this chapter, we present results of simulations using the toroidal profile of E_z^{RF} for each strap approximated by an analytic formula, for example, two Gaussians with opposite sign centered around the two gaps between the strap and the antenna box (Fig. 3.2(b), blue line). The model constraint concerning ICRF physics is related to the critical density $n_{e,cr}^{LHR}$ determined by the lower-hybrid resonance condition:

$$\omega^2 \approx \sum_{i=H_2^+,H^+} \left(\Omega_i^2 + \omega_{p,i}^2\right), \tag{5.33}$$

where Ω, ω_p correspond to the cyclotron and plasma frequencies [13, 14]. For a discharge at $f = 29\,\mathrm{MHz}$, $B_T = 2\,\mathrm{T}$ and a hydrogen plasma ($n_{H_2^+}/n_{H^+} \approx 25$), the LHR zone close to the antenna strap appears at the critical density $n_{e,cr}^{LHR} \approx 2.6 \cdot 10^{16}\,\mathrm{m}^{-3}$. Approaching this critical density in our model, $k_\perp \to \infty$ ($\lambda_\perp \to 0$), it is not possible to neglect anymore the physics in the perpendicular direction. This concludes that our PIC-MCC model is valid up to densities in the range $10^{15} - 10^{16}\,\mathrm{m}^{-3}$. By including the plasma produced E_z^P component to the equation of the charged particles (Eq. (5.1)) it is considered that the modification of vacuum electric field upon

increasing plasma density is self-consistently included in the model within the adopted 1D (toroidal) approach.

Constraints on Δt and Δz

In PIC models, the time step and the grid size must be well chosen that the shortest time and length scale phenomena are properly resolved in the simulation. The grid size Δz in PIC models should be smaller than the natural length scale in the plasma given by the Debye length λ_D [3]:

$$\Delta z < \lambda_D = 7.4 \cdot 10^3 \sqrt{\frac{k_B T}{n_e}} \,. \tag{5.34}$$

However, the formula for the Debye length λ_D assumes that the plasma has a Maxwell energy distribution. In our simulations, we have a majority of electrons low energetic but there are as well electrons with high energies resulting in a bi-Maxwell energy distribution. Therefore, we decided after testing a stability of our model to use the grid size $\Delta z \approx 2 \cdot 10^{-3}\,\mathrm{m}$ already from the start of our simulations at low electron densities ($\approx 10^7\,\mathrm{m}^{-3}$). This grid size decreases further with increasing electron density in our simulations.

The time step must resolve the highest frequency present in a simulation. In our situation, it is the RF frequency of the ICRF antenna ω_{RF}:

$$\omega_{RF} \Delta t < 0.2 \,. \tag{5.35}$$

However, in our simulations, the electron density increases with time, and from a specific moment, the electron plasma oscillations $\omega_{p,e}$ ($\omega_{p,e} \approx 18\pi\sqrt{n_e}$) have a higher frequency than the RF frequency of the ICRF antenna. Thus, at higher electron densities when $\omega_{p,e} > \omega_{RF}$, we have to fulfill the time step constraint given by [3]

$$\omega_{p,e} \Delta t < 0.2 \,. \tag{5.36}$$

In practice, it means that the time step in our simulations is around $10^{-9}\,\mathrm{s}$ for the electron density below $n_e < 10^{11}\,\mathrm{m}^{-3}$. Then, the time step is decreased by an order of magnitude ($\Delta t \sim 10^{-10}\,\mathrm{s}$) for the electron density up to $n_e < 10^{12}\,\mathrm{m}^{-3}$. Afterwards, the time step is again decreased by order of magnitude ($\Delta t \sim 10^{-11}\,\mathrm{s}$) to resolve the plasma oscillations starting to play a role around $n_e \sim 10^{13}\,\mathrm{m}^{-3}$.

5.2 Simulation results

Fig. 5.4 presents the electron density evolution in time for a simulation with a one strap antenna electric field (the idealized E_z^{RF}-field in Fig. 3.2(b)) obtained with the PIC-MCC model and the MCC model neglecting the electrostatic field E_z^P. The parameters of both simulations are identical with the amplitude $E_0^{RF} = 10\,\mathrm{kV/m}$, frequency $f = 29\,\mathrm{MHz}$ and at the neutral gas pressure $p_{H_2} = 0.04\,\mathrm{Pa}$ with the circumference length of $14\,\mathrm{m}$. The simulated toroidal domain is $[-7,\, 7[\,\mathrm{m}$ with the periodic

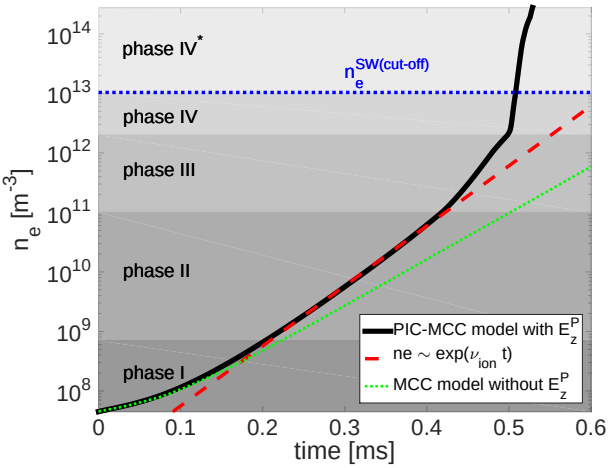

Figure 5.4: Time evolution of the electron density n_e for the PIC-MCC model and the MCC model ignoring the electrostatic field at $E_0 = 10\,\mathrm{kV/m}$, $f = 29\,\mathrm{MHz}$, $p_{H_2} = 0.04\,\mathrm{Pa}$. The evolution for the PIC-MCC model is divided into four phases with different ionization rates corresponding to different EEDFs (Fig. 5.5) and different mechanisms dominating in each phase. The exponential increase is fitted by red line for the PIC-MCC model in phase II, $n_e \sim \exp(\nu_{\mathrm{ion}} \cdot t)$.

boundary conditions applied at the outer points and the antenna located at zero. In Section 4.1, we have indicated that the electron density follows an exponential increase in time, $n_e \sim \exp[\nu_{\mathrm{ion}} \cdot t]$. The slope of this electron density evolution in time is called ionization rate, ν_{ion}. In the MCC `RFdinity1d` model, the ionization rate stays more or less constant over time. However, in the PIC-MCC `RFdinity1d` model including the electrostatic field E_z^P, the ionization rate varies in time as the electron density increases. We distinguish different phases of the electron density evolution with a different ionization rate, ν_{ion}. These phases are highlighted in Fig. 5.4.

The ionization frequency is defined in Eq. (4.3) as

$$\nu_{\mathrm{ion}} = n_{H_2} \int v \cdot \sigma_{\mathrm{ion}}(v) \cdot f(v)\, \mathrm{d}^3 v\,. \tag{5.37}$$

In the above figure, we showed the simulation results with only one antenna strap. However, the simulations with a two straps antenna electric field have similar behavior, and the electron density evolution for these simulations can be divided into the same phases as for the simulation with one strap (Fig. 5.4). For each phase, we can identify mechanisms responsible for the variation in the shape of the Electron Energy Distribution Function (EEDF).

Here, we give a summary of each phase with a description of the dominant mechanisms responsible for the electron density increase.

1. Each simulation starts with an assumed number of initial free electrons and

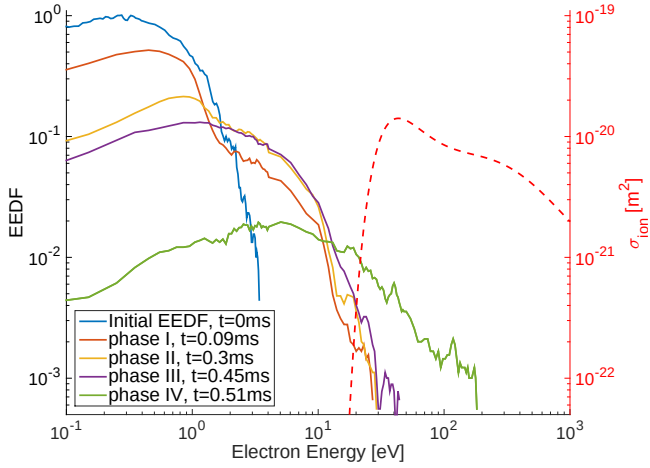

Figure 5.5: Evolution of the EEDFs in the PIC simulation with $E_0 = 10\,\mathrm{kV/m}$, $f = 29\,\mathrm{MHz}$, $p_{H_2} = 0.04\,\mathrm{Pa}$. The initial EEDF corresponds to the Maxwell energy distribution at $T = 0.5\,\mathrm{eV}$. The EEDFs correspond to different phases in the electron density evolution (Fig. 5.4) and their overlaps with the ionization cross section σ_{ion} give the ionization rates in each phase.

ions. These electrons and hydrogen ions are sampled from Maxwell energy distributions with $T_{e,0} = 0.5\,\mathrm{eV}$ and $T_{i,0} = 0.04\,\mathrm{eV}$ (Fig. 5.5, $t = 0\,\mathrm{ms}$) and are homogeneously distributed over the torus circumference. In phase I ($n_e < 7 \cdot 10^8\,\mathrm{m}^{-3}$), as soon as the antenna is powered, the initial Electron Energy Distribution Function (EEDF) deforms into a Maxwell-like distribution with an energetic tail (Fig. 5.5, $t = 0.09$ms). During this phase, the electrostatic field E_z^P is much smaller than the antenna field, $\left|E_z^P\right| \ll \left|E_z^{RF}\right|$. For that reason, all charged particles are mainly affected only by the antenna field, $F_L \approx qE_z^{RF}$. Most of the initial electrons being low energetic are reflected at the antenna edge by the ponderomotive force without gaining energy. The role of the ponderomotive force was discussed in Section 4.5. We have shown that depending on the antenna field only a small fraction of the electrons have sufficient energy to be either accelerated during the reflection at the antenna edge or to enter into the antenna area. These electrons can be accelerated towards energies exceeding the ionization threshold energy ($\Delta E^{ion} = 15.43\,\mathrm{eV}$).

An illustration of the electron trajectory in the initial phase of the ICRF discharge with the reflections at the antenna edge by the E_z^{RF}-field is drawn in Fig. 5.2. For example for the time delay of $t = 0.2\,\mathrm{ms}$ (time delay between phases I and II), an electron with the energy $E = 0.5\,\mathrm{eV}$ can travel $28\,\mathrm{m}$. As such it will encounter the antenna area and be reflected at least twice at the antenna edge for a simulation with the circumference $L \approx 13.5\,\mathrm{m}$ (ASDEX Upgrade). Furthermore, this distance is shorter than the mean free path length λ

for collisions of electrons with energies below $10\,\mathrm{eV}$ within the normal neutral pressure for the ICWC experiment, $p_{H_2} = 10^{-3} - 5 \cdot 10^{-2}\,\mathrm{Pa}$, $\lambda = 10^3 - 24\,\mathrm{m}$. Therefore, the trajectories are rarely influenced by collisions. At the end of phase I the EEDF stabilizes. A constant fraction of the electrons will have sufficient energy to enter into the antenna region while the remaining fraction with low energies is only reflected by the ponderomotive force without gaining any energy from the E_z^{RF}-field.

In contrast, the electron density evolution with the MCC-model without E_z^P-field has after phase I a constant ionization frequency. The variation between the models starts in phase II in which the electrostatic field slightly increases the ionization rate in the PIC-MCC model. The difference between the models is small in phase II as the electrostatic field E_z^P is still weak compared to the RF field.

A spatial distribution develops showing a lack of electrons right in front of the antenna. We visualize the distribution as a difference between numbers of ion and electron super-particles in each cell ($N_i - N_e$) along the toroidal position z for each phase in Fig. 5.6. As the RF field is strong in front of the antenna (the center of the antenna strap at $z = 0$m), electrons are immediately expelled from this area. The ions, because of their lower mobility, will reside longer in the antenna region. In phase I and II (Fig. 5.6(a-b)), it creates a positive charge (blue color) in front of the antenna strap while a negative charge (red color) is located in the antenna vicinity. We see no significant accumulation of the charge further away from the antenna region, demonstrating that most of the toroidal circumference has charge neutrality.

2. It was observed that the EEDF stays constant during phase II in the electron density range $7 \cdot 10^8 - 10^{11}\,\mathrm{m}^{-3}$. In this phase, the electron density evolution can be described by an exponential function, $n_e \propto \exp\left[\nu_{ion} \cdot t\right]$ with the ionization rate representing the slope of the curve (Fig. 5.4). Eq. (5.37) shows that the ionization rate has a constant value during phase II indicating that the EEDF remains constant as well.

   The negative charge accumulation in the antenna vicinity in phase I and II is caused by the shape of the resulting electric field E_z^P. This field is acting to cancel out the charge inhomogeneities introduced by the antenna field E_z^{RF}. The shape of the E_z^P-field is visualized in Fig. 5.7(a). This E_z^P-field will attract electrons into the antenna. However, during phase I-II the E_z^P-field remains sufficiently low not to affect the EEDF nor the ionization rate significantly ($|E_z^P| \ll |E_z^{RF}|$). The E_z^P-field has the maximum amplitude near the point where the E_z^{RF}-field reflects the majority of the low energetic electrons. In Fig. 5.6(b) for phase II, we can identify an accumulation of the negative charge (two red peaks) in the antenna vicinity while the positive charge dominates in front of the antenna strap (at $z = 0\,\mathrm{m}$).

3. Although the E_z^P-field magnitude is still smaller than the E_z^{RF}-field ($|E_z^P| <$

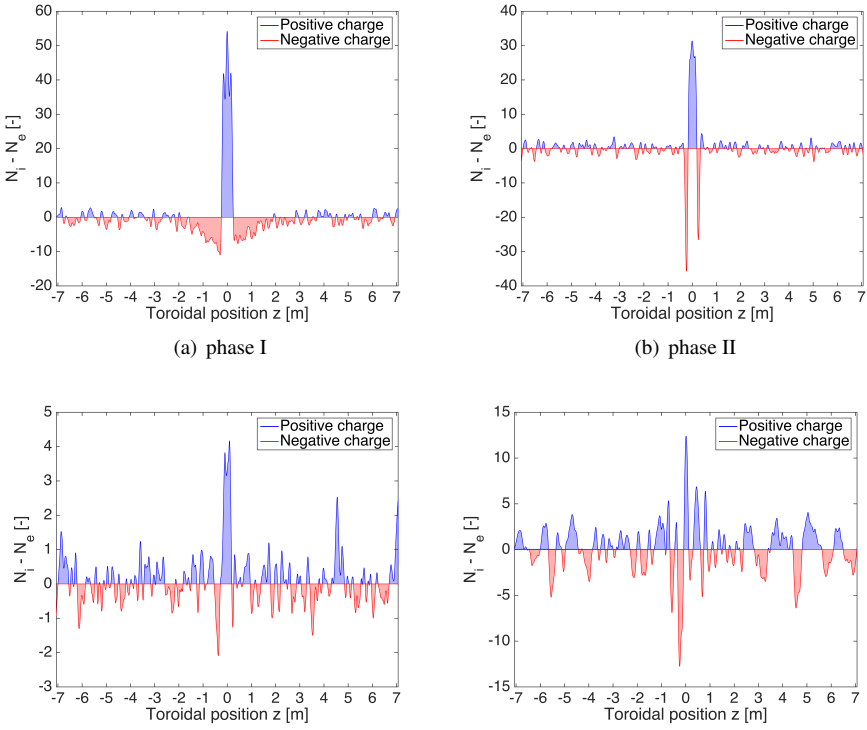

(a) phase I

(b) phase II

(c) phase III

(d) phase IV

Figure 5.6: Numbers of ion and electron super-particles in each cell ($N_i - N_e$) along the toroidal position z for each phase. Positive charge is visualized by blue color and negative by red color.

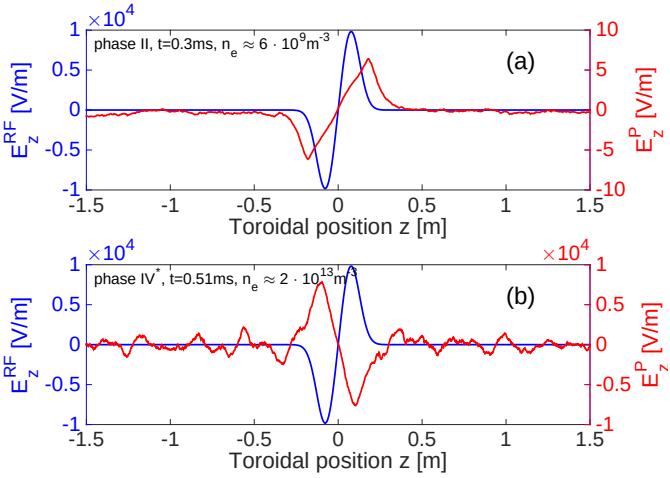

Figure 5.7: Distributions of the (i) E_z^{RF}-field (blue) and (ii) E_z^P-field (red) in the phase II at $t = 0.3\,\mathrm{ms}$, $n_e = 6 \cdot 10^9\ \mathrm{m}^{-3}$ and in the phase IV at $t = 0.51\,\mathrm{ms}$, $n_e = 2 \cdot 10^{13}\ \mathrm{m}^{-3}$.

$|E_z^{RF}|$) in phase III ($n_e \approx 10^{11} - 2 \cdot 10^{12}\,\mathrm{m}^{-3}$), the E_z^P slowly starts to play a role putting low energetic electrons into the antenna area. The EEDF is reshaped, and the ionization frequency $\nu_{ion}^{e-H_2}$ slightly increases due to a better overlap between the EEDF (Fig. 5.5, $t = 0.45\,\mathrm{ms}$) and the ionization cross section $\sigma_{ion}^{e-H_2}$ (dashed line in Fig. 5.5). The EEDF has less low energetic electrons than in the previous phases. The charge distribution in this phase (Fig. 5.6(c)) starts to be more uniform, and the positive charge in front of the strap becomes less dominant. We do not observe the negative charge accumulated in the antenna vicinity because these electrons can enter the antenna region to cancel out the positive charge.

4. Then another dramatic increase in the electron multiplication rate is visible reaching the electron density around $n_e \simeq 2 \cdot 10^{12}\,\mathrm{m}^{-3}$ at the beginning of phase IV. The ionization rate before the transition in Fig. 5.4 is $\approx 2.5 \cdot 10^4\,\mathrm{s}^{-1}$ while in phase IV the ionization rate increases to $\approx 2 \cdot 10^5\,\mathrm{s}^{-1}$. This ionization rate is in quantitative agreement with the ionization rate predicted from the fitting of the plasma resistance increase before the breakdown in the experiment on ASDEX Upgrade. We re-plot Fig. 3.1 showing the evolution of the plasma load for A2 ICRF antenna during the discharge initiation in the ICWC experiment on ASDEX Upgrade together with the fit of the plasma load increase prior of the breakdown (red line). Fig. 5.8 shows the first appearance of the plasma load seen by the antenna. Point (a) corresponds to the moment when the plasma load appears, while no radiation is registered yet, whereas point (b) contains the first visible appearance of the plasma column following the magnetic field line close to the ICRF antenna (See Fig. 3.1(right)). The signal of the

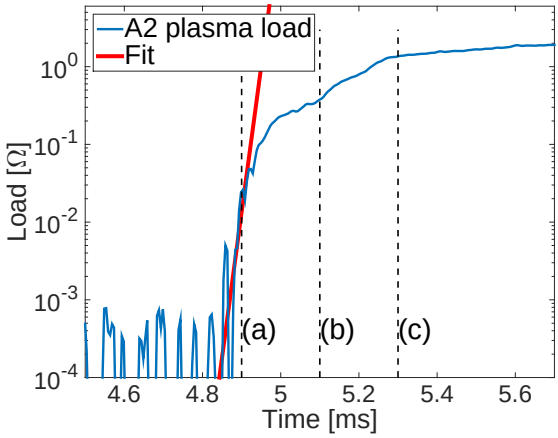

Figure 5.8: Appearance of the plasma load in front of the A2 ICRF antenna at ASDEX Upgrade (shot #29002). Red curve corresponds to the fit of the plasma load increase prior of the breakdown.

plasma load in the figure is in the early stage of the plasma initiation (around the point (a)) assumed to be monotonically increasing with the radially localized electron density. Therefore, the rate of increase of the logarithm of the plasma resistance may give a rough estimate of the ionization rate at the plasma breakdown. The ionization rate in this example is around $\nu_{ion} \sim 10^5\,\mathrm{s}^{-1}$. In this discharge phase, the electron density follows an exponential increase, $n_e = n_{e,0}\exp[\nu_{ion}t]$. It is not realistic to assume that the ionization rate is a constant from the start of the first application of power on the straps. Indeed, for a typical electron density in ICRF discharges, $n_e \approx 10^{16} - 10^{17}\,\mathrm{m}^{-3}$, using the above ionization frequency in the equation for the density evolution would give an unrealistic initial electron density, $n_{e,0} < 10^{-80}\,\mathrm{m}^{-3}$. This experimental observation suggests the existence of a dramatic change in the ionization rate in the experiments: low at the beginning of the shot into high just before or at the plasma breakdown. Here, we demonstrated changes in the electron density evolution observed in PIC `RFdinity1d`.

This transition occurs when the magnitude of the E_z^P-field is comparable to the magnitude of the E_z^{RF}-field, $|E_z^P| \sim |E_z^{RF}|$. The shape and the magnitude of the E_z^P-field in phase IV are visualized in Fig. 5.7(b). The figure demonstrates that the E_z^P-field attempts to cancel out the vacuum RF field in phase IV. Therefore more electrons can access the antenna region to be subsequently accelerated towards higher energies as seen in the significant change of the energy distribution in the IVth phase (Fig. 5.5, $t = 0.51\,\mathrm{ms}$). Understandably, the EEDF has less low energetic electrons compared to the EEDFs in the previous phases. Instead, it has a high population of electrons at energy levels above the

ionization threshold ($\Delta E^{\text{ion}} = 15.4\,\text{eV}$). Therefore this EEDF has improved overlap with the ionization cross section $\sigma_{ion}^{e-H_2}$ and the highest ionization rate. In the next subsection, we use the advanced ponderomotive description of electron acceleration (See Section 4.5) to explain how the electrostatic field E_z^P can boost the ionization rate.

Fig. 5.9 illustrates an evolution of the charge distribution over one RF period $T = 1/f$ oscillating with angular frequency $\omega = 2\pi f$ near the end of phase IV ($n_e = 10^{13}\,\text{m}^{-3}$). This density is close to the cut-off density at $f = 29\,\text{MHz}$ ($n_{e,crit}^{SW(cut-off)} = 1.04 \cdot 10^{13}\,\text{m}^{-3}$). It shows how the perturbations, created by the RF field in front of the antenna, propagate away from the antenna region. We have selected two phases of the oscillations, highlighted in solid and dashed lines, to follow their movements over this period. Both phases move $\lambda \approx 0.32\,\text{m}$ ($k \approx 19.6\,\text{m}^{-1}$) over the period. This observation is explained by the theoretically predicted plasma oscillations for a case with the RF frequency close to the electron plasma frequency (Langmuir plasma waves) propagating with a dispersion relation:

$$\omega^2 = \omega_{p,e}^2 + \frac{3}{2} v_{e,th}^2 k^2\,, \tag{5.38}$$

where $\omega_{p,e}$ is plasma frequency, and $v_{e,th} = \sqrt{2k_B T_e/m_e}$ is the electron thermal velocity [15]. At the averaged electron density $n_e = 10^{13}\,\text{m}^{-3}$, the electron temperature in the simulation is $T_e \approx 19\,\text{eV}$, and from the above equation, we obtain the plasma waves with the wavelength of $\lambda = 0.57\,\text{m}$ ($k = 11.1\,\text{m}^{-1}$). In Fig. 5.9, the oscillations are damped when moving further away from the antenna $z < -0.3\,\text{m}$ or $z > 0.3\,\text{m}$. It is caused by the local density at this toroidal location being slightly higher $n_e^L \approx 1.5 \cdot 10^{13}\,\text{m}^{-3}$ than the cut-off density $n_{e,crit}^{SW(cut-off)}$. The local density inside of the antenna region is below the threshold density to allow the oscillations to start propagating.

(iv*) Upon reaching the electron densities, $\omega_{p,e} = \omega$, the Slow Waves (**SW**) start propagating also in the perpendicular direction [13]. The physics underlying radial propagation of plasma oscillations is not included in the present 1D (toroidal) model. Despite this limitation the result above indicates that (i) propagation in the parallel direction occurs already at lower density in phase IV ($\omega_{p,e} < \omega$, See Fig. 5.9) (ii) a dramatic increase in the ionization rate occurs already below the threshold density for perpendicular propagation and (iii) the cold plasma wave description ignoring thermal motion of particles may be insufficient for describing the breakdown phase of ICRF plasma. The cut-off density at $f = 29\,\text{MHz}$ is $n_{e,crit}^{SW(cut-off)} = 1.04 \cdot 10^{13}\,\text{m}^{-3}$ (highlighted in Fig. 5.4).

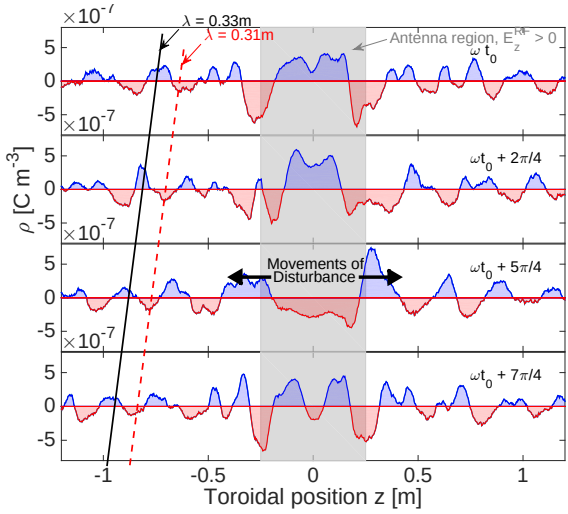

Figure 5.9: Evolution of the charge distribution, $\rho = q_e(n_e - n_i)$ near by the antenna (located at zero) in one RF period of the antenna during the PIC simulation at $n_e = 10^{13}\,\mathrm{m}^{-3}$.

5.2.1 Transition from phase III into phase IV

We have shown that the electron density evolution transition from phase III into phase IV (See Fig. 5.4) is accompanied with a significant increase in the ionization rate. The transition occurs at the electron density $n_e \approx 2 \cdot 10^{12}\,\mathrm{m}^{-3}$ which is still below the critical density for SW excitation, $n_{e,crit}^{SW(cut-off)} = 1.04 \cdot 10^{13}\,\mathrm{m}^{-3}$ for $f = 29\,\mathrm{MHz}$. Therefore, we have to assume that the reason for this transition is due to different mechanisms than the wave excitation in the antenna vicinity. In Section 4.5, we have shown that we can use the pondermotive potential to describe the threshold energy of an electron ϵ_{tr} below which it cannot enter or be accelerated from the parallel vacuum electric field E_z^{RF}. We have developed the model investigating the motion of a single electron in the antenna field and theoretical description to find the threshold energy ϵ_{tr} as a function of the electric field amplitude, RF frequency, and electric field shape (See Fig. 4.20). In this single electron model, an electron is accelerated solely by the parallel vacuum electric field E_z^{RF}. In this section, we employ this model to see how the threshold energy is changed when an electron is accelerated by a sum of the parallel vacuum electric field and electrostatic field from the Poisson equation, $E_z = E_z^{RF} + E_z^P$.

The electrostatic field E_z^P results from a collective motion of all electrons and ions and it cannot be calculated directly in this single electron model following only one electron. Therefore, we have first to make specific approximation concerning the shape of the electrostatic field E_z^P obtained in the PIC simulations. We have demonstrated in Fig. 5.7 that the E_z^P-field has such shape in phases I-III to attract electrons into the antenna area to cancel out the positive charge in front of the strap (See Fig. 5.6(a-c)). Although this toroidal profile of the electrostatic field varies ev-

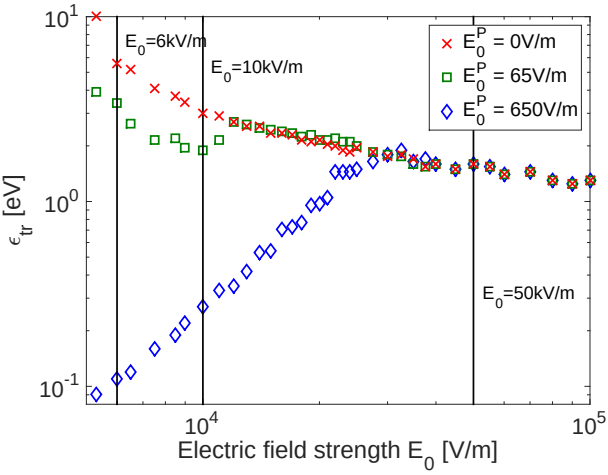

Figure 5.10: Dependence of the threshold energy on the antenna E_z^{RF}-field amplitude E_0 obtained with the single electron model for different amplitude E_0^P of the approximated electrostatic field in the antenna vicinity. Solid black lines highlight the situations for $E_0 = [6,\ 10,\ 50]\ \mathrm{kV/m}$.

ery time-step due to motions of the charges, the shape has two distinct peaks in the antenna vicinity as shown in Fig. 5.7(Phase II). These peaks with opposite signs have more or less stable shape during phases I-III and can be approximated by an analytical function. The amplitude of these peaks increases with the electron density. Additionally, these peaks are located precisely at the edge of the E_z^{RF}-field. Therefore at this location, they have an important impact on the reflections of electrons at the antenna field edge.

We have launched simulations using the single electron model to investigate the threshold energy dependency on the antenna electric field strength E_0 for two amplitudes of the approximated E_z^P-field in the antenna vicinity: (i) $E_0^P = 65\,\mathrm{V/m}$ and (ii) $E_0^P = 650\,\mathrm{V/m}$. The amplitude, $E_0^P = 650\,\mathrm{V/m}$, is set at the amplitude of the E_z^P-field in our PIC simulations corresponding to the transition from phase III to phase IV at the electron density $n_e \approx 2 \cdot 10^{12}\,\mathrm{m}^{-3}$. The threshold energy dependency on the antenna electric field strength E_0 is illustrated in Fig. 5.10. The simulations with $E_0^P = 0$V/m represent the situation solely with the antenna vacuum electric field E_z^{RF} without the electrostatic field E_z^P. As shown in Fig. 5.10, the threshold energy is influenced by the electrostatic field E_z^P. At low amplitude of the E_z^P field (green squares, $E_0^P = 65\,\mathrm{V/m}$), the threshold energies diverge from the situation without the E_z^P-field only for low amplitudes E_0 of the vacuum RF field (below $10\,\mathrm{kV/m}$). While above $E_0 > 10\,\mathrm{kV/m}$ the threshold energies equal to each other. This observation indicates that the threshold energy in the situation when the electrostatic field is present depends on the ratio between the amplitudes of the antenna E_z^{RF} and electrostatic E_z^P fields.

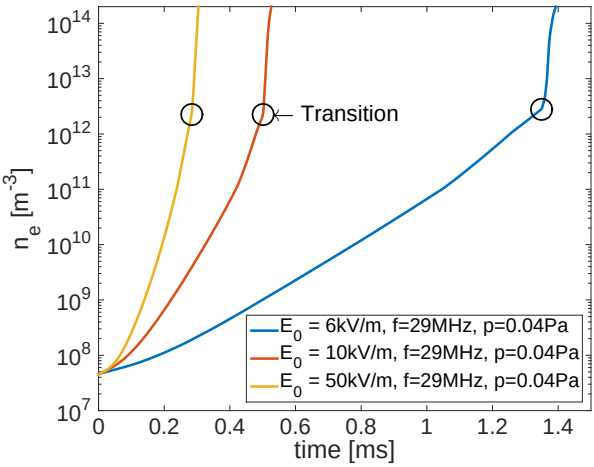

Figure 5.11: Time evolution of the electron density for PIC simulations with $E_0 = [6,\ 10,\ 50]\,\mathrm{kV/m}$ at $f = 29\,\mathrm{MHz}$ and $p = 0.04\,\mathrm{Pa}$. The transitions from phase III into phase IV is marked by black circles for $n_e \approx 2 \cdot 10^{12}\,\mathrm{m}^{-3}$.

As we can see in Fig. 5.10 for the situation with the electrostatic field amplitude at $E_0^P = 650\,\mathrm{V/m}$, the threshold energies have an obvious deviation from the situation without the electrostatic field. The differences in threshold energies ϵ_{tr} between these two situations are even one order of magnitude for the RF amplitude $E_0 < 20\,\mathrm{kV/m}$. Above $20\,\mathrm{kV/m}$, all three situations merge and have same threshold energies for the high RF amplitude E_0. These simulations obtained with the single electron model delivered fascinating results. The transition from phase III into phase IV (See Fig. 5.4) will be more significant for the lower values of the RF antenna field. For example for the RF amplitude of $E_0 = 10\,\mathrm{kV/m}$, the threshold energy without electrostatic field E_z^P is around $\approx 3\,\mathrm{eV}$, whereas with the electrostatic field E_z^P (blue diamonds in Fig. 5.10) this threshold energy decreases at $\epsilon_{\mathrm{tr}} \approx 0.3\,\mathrm{eV}$. This significant decrease in the threshold energy means that more electrons from the low energetic Maxwell distribution (See Fig. 4.16) can be accelerated towards higher energies. More energetic electrons in the simulations mean more collisions and an increase in the ionization rate as we can see in Fig. 5.4 at the transition from phase III into phase IV. Interestingly, when the amplitude of the RF field is high, we do not observe a change in the threshold energy for the situation with and without the electrostatic field E_z^P. Therefore, based on the observations with the single electron model, we can predict that it will be challenging to observe any changes in the electron density evolution in PIC simulations for a high antenna amplitude.

Therefore, we have launched three PIC simulations with varying amplitude of the antenna field $E_0 = [6,\ 10,\ 50]\,\mathrm{kV/m}$ at $f = 29\,\mathrm{MHz}$ and $p = 0.04\,\mathrm{Pa}$. The electron density evolution in time for these simulations are plotted in Fig. 5.11. The

black circles highlight the transitions from phase III into phase IV. As illustrated, the most significant increase in the ionization rate (slope of the density evolution) is for the simulation at the lowest amplitude $E_0 = 6\,\mathrm{kV/m}$, whereas the transition at $E_0 = 50\,\mathrm{kV/m}$ is difficult to recognize. These simulations are in agreement with the threshold energy observations in Fig. 5.10 where the solid black lines highlight situation for these free amplitude E_0 of the antenna field E_z^{RF}. At the simulation start when the electrostatic field is much smaller than the antenna RF field, $|E_z^P| \ll |E_z^{RF}|$, the PIC simulation with $E_0 = 50\,\mathrm{kV/m}$ has, compared to the 6 and $10\,\mathrm{k}V/m$ cases, the the lowest threshold energy (red crosses in Fig. 5.10), and thus it will have the highest ionization rate. At the transition density, $n_e \approx 2 \cdot 10^{12}\,\mathrm{m}^{-3}$, the ionization rate increases by a factor of 3 for $E_0 = 50\,\mathrm{kV/m}$, 5.5 for $E_0 = 10\,\mathrm{kV/m}$ and 10 for $E_0 = 6\,\mathrm{kV/m}$. Although the single electron model does not detect any change in the threshold energy, we observe a small increase in the ionization rate for $E_0 = 50\,\mathrm{kV/m}$ in our PIC simulations. This discrepancy may be caused by using the approximated electrostatic field E_z^P in the single electron model. Also, at these transition densities, the SW excitation starts to play a role because the local density in the antenna vicinity is slightly higher than the average density n_e. This higher local density at the antenna vicinity allows the excitation of SW and it will accelerate even low energetic electrons. These newly accelerated electrons may afterwards collide more frequently and increase the ionization rate. However, we can conclude remarkable relevance between the predictions of the single electron model and transitions in the PIC simulations.

5.2.2 Electric field in phase IV

As we have mentioned, the electrostatic field E_z^P has a magnitude comparable to the amplitude of the E_z^{RF}-field, $|E_z^P| \sim |E_z^{RF}|$. We have shown in Fig. 5.7(b) that the electrostatic field E_z^P in front of the antenna has an identical shape as the RF E_z^{RF}-field with opposite sign. This electrostatic field also oscillates with the same RF frequency as the E_z^{RF}-field. The charged particles are disturbed by the RF field, and resulting charge distribution creates the electrostatic field E_z^P acting against this disturbance created by the RF E_z^{RF}-field. Since phase IV, the electrostatic field E_z^P will always have a shape of the E_z^{RF}-field with the opposite sign. Fig. 5.12 and Fig. 5.13 demonstrate the shape of the E_z^P-field in front of the antenna in the electron density range $n_e = 10^{13} - 10^{14}\,\mathrm{m}^{-3}$ and for different time phases of the E_z^{RF}-field oscillating with $\cos(\omega t)$. Especially, Fig. 5.13 illustrates that the resulting E_z^P-field can have a more complicated shape of the dipole phasing with two straps while Fig. 5.12 shows simulation results obtained with one strap antenna.

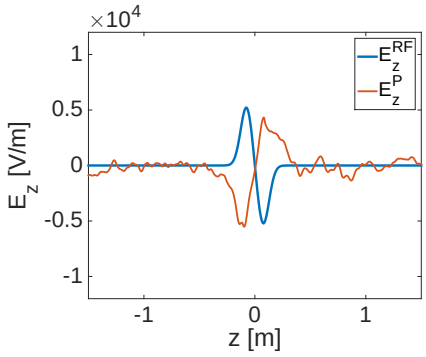

(a) $n_e = 1.4 \cdot 10^{13}\,\mathrm{m}^{-3}$ $T = 0.161 \cdot 2\pi$

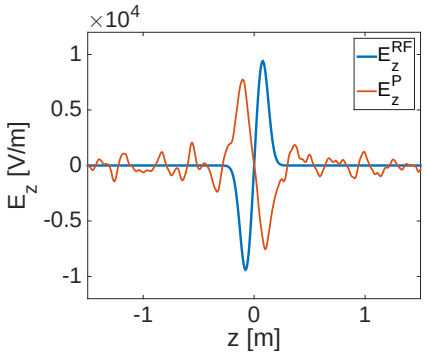

(b) $n_e = 2.0 \cdot 10^{13}\,\mathrm{m}^{-3}$ $T = 0.547 \cdot 2\pi$

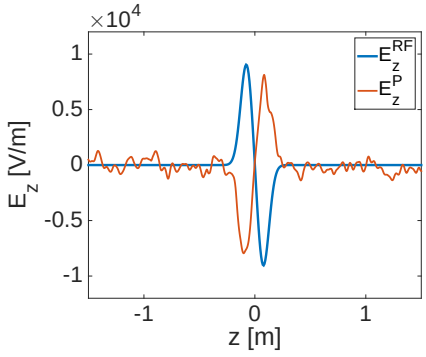

(c) $n_e = 3.0 \cdot 10^{13}\,\mathrm{m}^{-3}$ $T = 0.064 \cdot 2\pi$

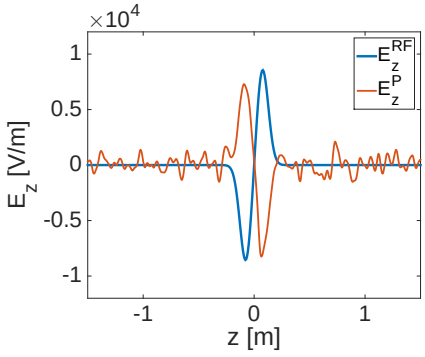

(d) $n_e = 4.5 \cdot 10^{13}\,\mathrm{m}^{-3}$ $T = 0.582 \cdot 2\pi$

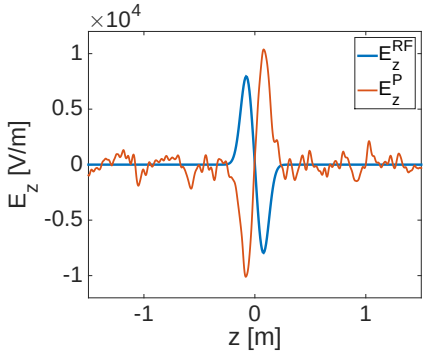

(e) $n_e = 6.8 \cdot 10^{13}\,\mathrm{m}^{-3}$ $T = 0.9 \cdot 2\pi$

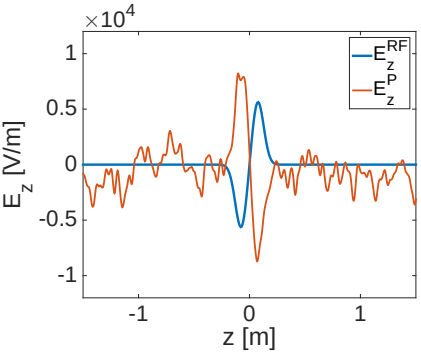

(f) $n_e = 1.0 \cdot 10^{14}\,\mathrm{m}^{-3}$ $T = 0.347 \cdot 2\pi$

Figure 5.12: Evolution of the electrostatic E_z^P and one strap antenna E_z^{RF}-fields in the antenna vicinity in phase IV for density range $n_e = 10^{13} - 10^{14}\mathrm{m}^{-3}$.

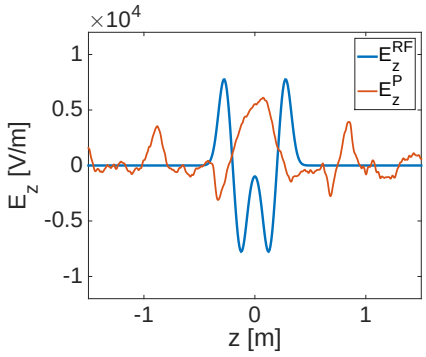

(a) $n_e = 1.5 \cdot 10^{13}\,\mathrm{m}^{-3}$ $T = 0.605 \cdot 2\pi$

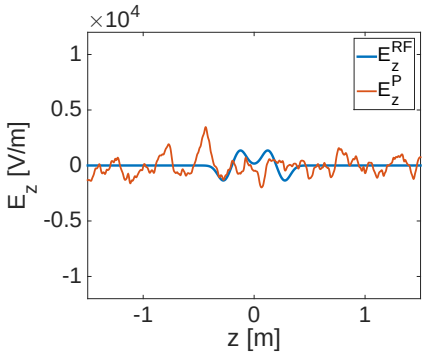

(b) $n_e = 2.4 \cdot 10^{13}\,\mathrm{m}^{-3}$ $T = 0.772 \cdot 2\pi$

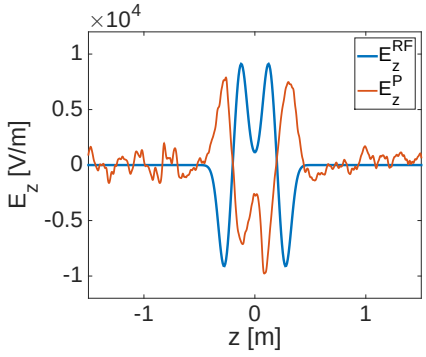

(c) $n_e = 3.6 \cdot 10^{13}\,\mathrm{m}^{-3}$ $T = 0.939 \cdot 2\pi$

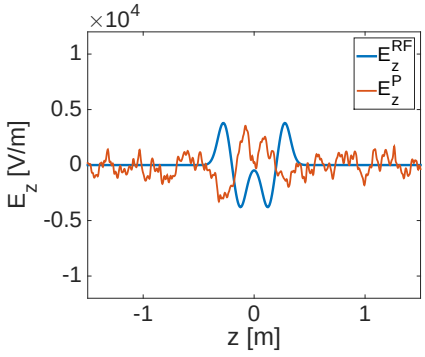

(d) $n_e = 5.2 \cdot 10^{13}\,\mathrm{m}^{-3}$ $T = 0.687 \cdot 2\pi$

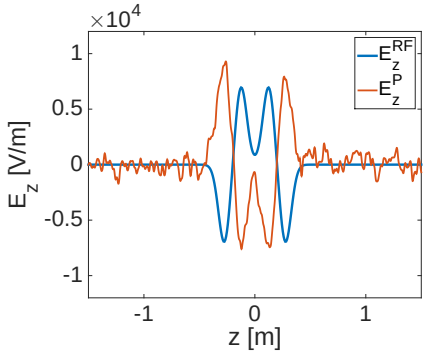

(e) $n_e = 7.8 \cdot 10^{13}\,\mathrm{m}^{-3}$ $T = 0.875 \cdot 2\pi$

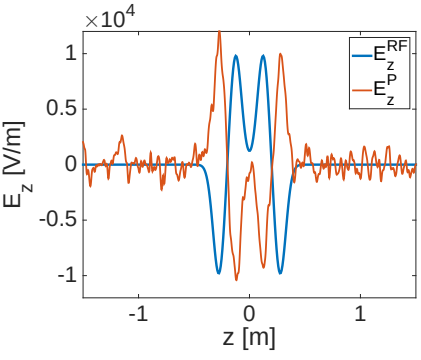

(f) $n_e = 1.2 \cdot 10^{14}\,\mathrm{m}^{-3}$ $T = 0.012 \cdot 2\pi$

Figure 5.13: Evolution of the electrostatic E_z^P and two strap antenna E_z^{RF}-fields in dipole phasing in the antenna vicinity in phase IV for density range $n_e = 10^{13} - 10^{14}\mathrm{m}^{-3}$.

5.3 Simulated energy distributions

The evolution of the EEDF in the PIC simulation was illustrated by plotting the distribution of each phase in Fig. 5.5. The initial energy distribution in simulation was set as a Maxwell distribution with $T = 0.5\,\mathrm{eV}$. The EEDFs within phase II and III correspond to two Maxwell energy distributions (low and high energetic maxwellian). This bi-Maxwell energy distribution is show in Fig. 4.16. Whereas the EEDF in phase IV is modified into a distribution that diverges from a Maxwell energy or a bi-Maxwell distribution. This EEDF corresponds to a Kappa distribution, which resembles a Maxwell distribution at low energy but falls off as a power law at higher energies. The kappa distribution is known to exist in systems in which there is on-going heating, such as wave-particle interactions [16, 17].

The isotropic Maxwellian distribution f_M and the isotropic kappa energy distribution f_κ are given by

$$f_M = \frac{2}{\sqrt{\pi}} \frac{1}{T^{\frac{3}{2}}} \sqrt{\epsilon} \cdot \exp\left[-\frac{\epsilon}{T}\right] \tag{5.39}$$

$$f_\kappa = A_\kappa \frac{2}{\sqrt{\pi}} \frac{1}{T_\kappa^{\frac{3}{2}}} \sqrt{\epsilon} \left[1 + \frac{\epsilon}{(\kappa - 3/2) T_\kappa}\right]^{-(\kappa+1)} \tag{5.40}$$

$$A_\kappa = \Gamma(\kappa + 1)/(\Gamma(\kappa - 1/2)(\kappa - 3/2)^{3/2}), \tag{5.41}$$

where A_κ is the normalization constant. The parameter κ ranges from $3/2$ to ∞, where for $\kappa = \infty$ the f_κ converges into a Maxwell distribution f_M, while smaller values of κ correspond to an increasingly non-thermal distribution. The kappa temperature T_κ is defined so that the average energy of the particles is $E_{avg} = (3/2) k_B T_\kappa$. The low energy part of the kappa distribution resembles a Maxwell distribution f_M with approximated Maxwellian temperature $T = T_\kappa \left(\kappa - 3/2\right)/\kappa$ [18]. The fraction of particles at low energies where the distribution function more closely resembles a Maxwell is expressed by [19]

$$C = 2.718 \frac{\Gamma\left(\kappa + 1\right)}{\Gamma\left(\kappa - 1/2\right)} \kappa^{-3/2} \left(1 + \frac{1}{\kappa}\right)^{-(\kappa+1)}. \tag{5.42}$$

Then, $R_N = 1 - C$ is the fraction of non-thermal particles (non-Maxwellian), which is largest for small κ [19].

Fig. 5.14(a) compares the EEDF obtained from the PIC simulation with $E_0 = 50\,\mathrm{kV/m}$, $f = 29\,\mathrm{MHz}$, $p_{H_2} = 0.04\,\mathrm{Pa}$ at the electron density $n_e \approx 2.6 \cdot 10^{15}\,\mathrm{m}^{-3}$ with a Maxwell and a Kappa energy distribution. We can observe an agreement between all three distributions for low energies ($\epsilon < 40\,\mathrm{eV}$), but the energetic tail of the EEDF in our PIC simulation undoubtedly corresponds to a Kappa distribution with $T_\kappa = 300\,\mathrm{eV}$ and $\kappa = 1.6$.

The PIC simulations show that also the Ion Energy Distribution Function (IEDF) is transformed into a Kappa distribution in phase IV. Fig. 5.14(b) shows two IEDFs at $n_e = 7.8 \cdot 10^{11}\,\mathrm{m}^{-3}$ (phase III, red line) and $n_e = 2.6 \cdot 10^{15}\,\mathrm{m}^{-3}$ (phase IV, blue line). In the PIC model hydrogen ions H_2^+, created during the ionization collisions,

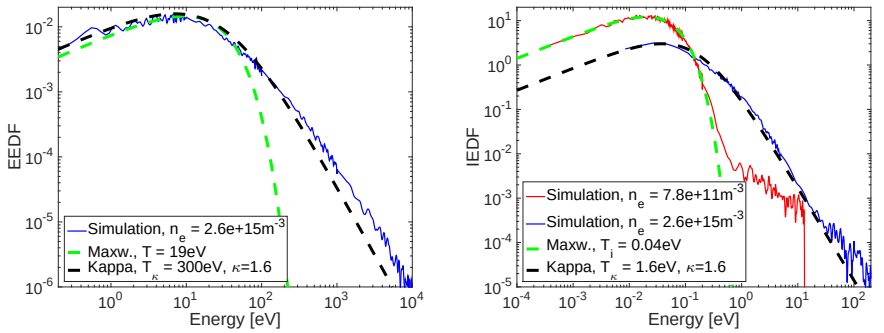

(a) (b)

Figure 5.14: (a) Electron Energy Distribution Function (EEDF) for PIC simulation with $E_0 = 50\,\mathrm{kV/m}$, $f = 29\,\mathrm{MHz}$, $p_{H_2} = 0.04\,\mathrm{Pa}$ fitted by a Maxwell energy distribution at $T = 19\,\mathrm{eV}$ and by a Kappa energy distribution with $T_\kappa = 300\,\mathrm{eV}$ and $\kappa = 1.6$. (b) Ion Energy Distribution Functions (IEDF) for PIC simulation with $E_0 = 50\,\mathrm{kV/m}$, $f = 29\,\mathrm{MHz}$, $p_{H_2} = 0.04\,\mathrm{Pa}$ at two electron densities: (i) $n_e = 7.8 \cdot 10^{11}\,\mathrm{m}^{-3}$ in the phase III fitted by a Maxwell energy distribution at $T_i = 0.04\,\mathrm{eV}$, and (ii) $n_e = 1.6 \cdot 10^{15}\,\mathrm{m}^{-3}$ in the phase IV fitted by a Kappa energy distribution at $T_\kappa = 1.6\,\mathrm{eV}$ and $\kappa = 1.6$.

are sampled from a Maxwell energy distribution at $T_{gas} = 400\,\mathrm{K}$ ($T_i \approx 0.04\,\mathrm{eV}$). At the low electron densities in the phases I-III the IEDF corresponds still to a Maxwell energy distribution at $T_i \approx 0.04\,\mathrm{eV}$ with a small fraction of energetic ions. As mentioned earlier, the effect of the perpendicular RF field on the ions is not included in the model. The energetic tail of the IEDF at low density in the PIC simulations is formed of ions created in ionization collisions that occur in the antenna region. The E_z^{RF}-field accelerates these newborn ions in the antenna region. It results in a small tail in the Maxwell energy distribution of $T_i = 0.04\,\mathrm{eV}$. Whereas in phase IV the E_z^{RF}-field is partially canceled out by the E_z^P field, more low energetic ions can enter the antenna region, as in the case of the low energetic electrons, and be accelerated by the total field ($E_z^{RF} + E_z^P$) in front of the antenna as well as by E_z^P outside of the antenna area. The IEDF transformation is visible in Fig. 5.14(b). The IEDF in phase IV corresponds to a Kappa distribution with $T_\kappa = 1.6\,\mathrm{eV}$ and $\kappa = 1.6$.

5.3.1 Energy distribution in experiment

The simulated ion energy distribution shed a new light on the observed energetic ion tails in ICWC experiments. Fig. 5.15 plots experimental measurements on ASDEX Upgrade with Neutral Particle Analyzer (NPA) in ICWC experiments. Hydrogen and deuterium were naturally released from the vessel walls during the Helium discharges. The NPA data shows the existence of energetic H and D ions ($\epsilon > 1\,\mathrm{keV}$) and suggest furthermore also a Kappa energy distribution function rather than a Maxwell energy distribution. Fig. 5.15(a) illustrates the NPA data for a discharge at $B_T = 2\,\mathrm{T}$, $f = 30\,\mathrm{MHz}$ and $P_G = 200\,\mathrm{kW}$. In this discharge, the fundamental H^+-ion reso-

nance is present in the vessel. The spectra for hydrogen and deuterium are fitted by a Kappa distribution with $T_\kappa^H = 6.8\,\mathrm{eV}$, $\kappa^H = 2.7$ for hydrogen and $T_\kappa^D = 4.9\,\mathrm{eV}$, $\kappa^D = 3.8$ for deuterium. The kappa parameter for hydrogen and deuterium has a ratio corresponding to the square root of their masses, $\frac{\kappa^H}{\kappa^D} = \sqrt{\frac{m_H}{m_D}}$. According to Eq. (5.42), these distributions have a high fraction of non-Maxwellian ions: 28% of hydrogen ions ($R_N = 0.28$) and 21% of deuterium ions ($R_N = 0.21$).

It is important to mention that the NPA data at ASDEX Upgrade were obtained from a viewing line nearly perpendicular to B_T. Our simulated ions have most of their energy in the parallel direction due to their acceleration solely in this direction by the electric field $E_z = E_z^{RF} + E_z^P$. For straight comparison between model and experimental measurements, ion temperature isotropization has to be fulfilled ($T_\perp = T_\parallel = T$). Temperature isotropization in ICWC discharges is achieved above $n_e > 10^{16}\,\mathrm{m}^{-3}$. The temperature isotropization is due to elastic ion-neutral collisions, and Coulomb collisions [11, 12]. Furthermore, the NPA data are measured at the well-developed phase of the RF discharge with densities $\sim 10^{16} - 10^{17}\,\mathrm{m}^{-3}$, while the validity limit of our model is in the density range $10^{15} - 10^{16}\,\mathrm{m}^{-3}$ (See Section 5.1.1). It remains to be verified that the physics responsible for the tails at lower $n_e < 10^{15}\,\mathrm{m}^{-3}$ continues to have a strong contribution to the tails observed at higher $n_e > 10^{16}\,\mathrm{m}^{-3}$.

It was previously considered that the presence of the fast ions depends solely on the efficiency of the resonant RF power absorption [13, 14, 20]. However, fast charge exchange neutrals are as well observed in discharges without the fundamental resonance when only inefficient higher harmonics are present in the vessel. Fig. 5.15(b) illustrates the NPA data for a discharge at $B_T = 0.2\,\mathrm{T}$, $f = 30\,\mathrm{MHz}$ and $P_G = 150\,\mathrm{kW}$. For this shot, the NPA signal is at the detection limit of the NPA diagnostic for high energy levels (above $7\,\mathrm{keV}$ for hydrogen and above $5\,\mathrm{keV}$ for deuterium). The spectra for hydrogen and deuterium are again fitted by a Kappa distribution with $T_\kappa^H = 42\,\mathrm{eV}$, $\kappa^H = 5.2$ for hydrogen and $T_\kappa^D = 110\,\mathrm{eV}$, $\kappa^D = 7.5$ for deuterium. The kappa parameters for this shot are higher than for the discharge at $B_T = 2\,\mathrm{T}$ which may be explained by higher loss rate of the energetic particles due to the low magnetic field. The kappa parameters for this shot indicates that around 15% of hydrogen ions ($R_N = 0.15$) and 11% of deuterium ions ($R_N = 0.11$) are non-Maxwellian. Again, the ratio of the kappa parameters for hydrogen and deuterium is equal to the square root of their masses ($\kappa^H/\kappa^D = \sqrt{m_H/m_D}$).

Numerical modelling [20] predicts that the high cyclotron harmonics (HCH) regime does have a weak absorption by ions via FW non-resonant collision damping. The waves damping at low magnetic field in a stellerator is also discussed in [21]. Nevertheless, our findings obtained with the PIC-MCC `RFdinity1d` model suggested that the energetic ions are created by another mechanism than only by resonant cyclotron absorption [1]. Our PIC model does not include the physics of typical resonant power absorption related to the perpendicular component of the antenna field. Nevertheless, we observe the acceleration of the ions by the parallel field $E_z = E_z^{RF} + E_z^P$. Therefore we have potentially identified a second mechanism responsible for the measured

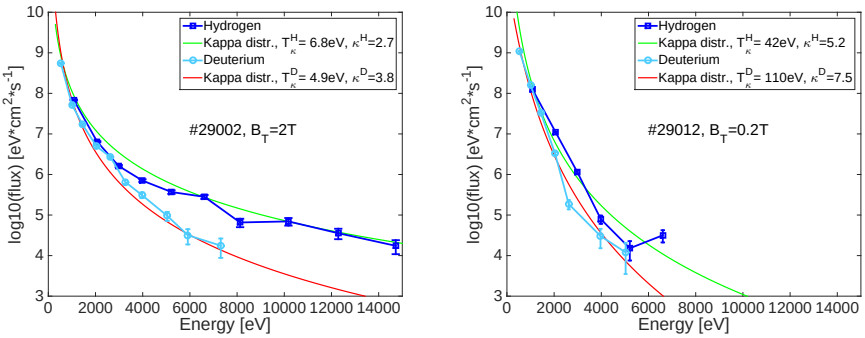

(a) (b)

Figure 5.15: Measurements of Neutral Particle Analyser (NPA) on ASDEX Upgrade in experiment with ICWC in Helium: (a) #29002, $B_T = 2\,\mathrm{T}$, $P_G = 200\,\mathrm{kW}$, $p_{He} = 4 \cdot 10^{-4}\,\mathrm{mbar}$, $f = 30\,\mathrm{MHz}$, (b) #29012, $B_T = 0.2\,\mathrm{T}$, $P_G = 150\,\mathrm{kW}$, $p_{He} = 3 \cdot 10^{-4}\,\mathrm{mbar}$, $f = 30\,\mathrm{MHz}$. Data are fitted by Kappa distributions with (a) $T_\kappa^H = 6.8\,\mathrm{eV}$, $\kappa^H = 2.7$ for hydrogen and $T_\kappa^D = 4.9\,\mathrm{eV}$ $\kappa^D = 3.8$ for deuterium, (b) $T_\kappa^H = 42\,\mathrm{eV}$ and $\kappa^H = 5.2$ for hydrogen and $T_\kappa^D = 110\,\mathrm{eV}$ and $\kappa^D = 7.5$ for deuterium.

fast ion populations in the ICWC experiments namely the action of the plasma waves via the parallel electric field $E_z = E_z^{RF} + E_z^P$.

Although the presented NPA measurements during the ICWC experiment on ASDEX Upgrade resembles Kappa rather than the Maxwell energy distributions, we have not detected Kappa energy distributions in NPA measurements during the ICWC experiment on JET [22]. These NPA measurements corresponded more closely to Maxwell distributions. However, all NPA measurements on tokamaks are designed to measure neutral particles at high energies during a normal operation of the tokamak, and not during ICWC experiments. We have to stress that all our ICWC discharges have low temperatures $\approx 3 - 5\,\mathrm{eV}$, while the NPA measurements on AUG suggest Maxwell distributions with temperatures $> 200\,\mathrm{eV}$ and NPA on JET $T_i > 1\,\mathrm{keV}$ [22]. At such high temperatures, we would have a full ionization of our plasma in ICWC experiments, whereas we have still neutral gas present in the vessel. This inconsistency can be explained that the NPA diagnostics measure only high energetic tail, while the majority of ions during ICWC experiments stay low energetic ($\approx 3 - 5\,\mathrm{eV}$) a feature that is captured by a Kappa distribution. This observation will be tested on TOMAS device [23, 24]. TOMAS device is specially constructed for wall conditioning experiments. It posses one strap ICRF antenna for ICWC, and it will also contain NPA diagnostic to detect low energy spectrum. This NPA diagnostic will be able to better study a formation of the energetic tails, type of the energy distribution (Kappa, Maxwell) and temperature of discharges.

5.4 Conclusion

In this chapter, we have presented the PIC-MCC model `RFdinity1d` for simulating discharge initiation by the ICRF antenna. The model follows the motion of both electrons and ions in a narrow bundle of magnetic field lines close to the antenna straps. The charged particles are accelerated in the parallel direction with respect to the magnetic field B_T by the Lorentz force. The force results from the sum of two electric fields: (i) the vacuum RF electric field in front of the ICRF antenna E_z^{RF} and (ii) the self-generated electrostatic field E_z^P obtained from Poisson's equation. The 1D approach in displacement is justified because the first plasma is a toroidally homogeneous narrow bundle in the antenna strap vicinity.

The simulation results of the PIC-MCC model suggest different stages of the electron density evolution in time. The last phase (phase IV) of the density evolution in the simulations is accompanied by a dramatic change in the EEDF and consequently a significant increase in the ionization rate. We observed similar behavior in ICWC experiments, in which the plasma resistance increases abruptly coinciding with the experimentally defined plasma breakdown moment. The rate of the plasma resistance increase has a same order of magnitude as the ionization rate in the simulations within phase IV, $\nu_{ion} \sim 10^5\,\mathrm{s}^{-1}$. We have used the single electron model to explain this increase in the ionization rate. The electrostatic field E_z^P was approximated in the single electron model by a shape observed during the PIC simulations. The single electron model demonstrated that the electrostatic field E_z^P significantly decreases the threshold energy for an electron to be accelerated by the RF field. When the electrostatic E_z^P and antenna E_z^{RF}-fields have comparable amplitudes, the decrease of the threshold energy is more significant. Next, we have illustrated that the electrostatic field E_z^P in phase IV has an identical shape in front of the strap as the antenna field E_z^{RF} with opposite sign. This electrostatic field E_z^P is then able to cancel out the antenna E_z^{RF}-field behaving as a disturbance of the charge distribution.

Furthermore, we found that the observed EEDF and IEDF in the simulations in phase IV ($n_e > 10^{12}\,\mathrm{m}^{-3}$) resembles a Kappa distribution. The NPA measurements on ASDEX Upgrade detect the formation of Kappa energy distributions for hydrogen and deuterium in the ICWC experiments. However, ions in our simulations have most of their energy in the parallel direction due to their acceleration solely in this direction, and our model is valid up to density range $10^{15} - 10^{16}\,\mathrm{m}^{-3}$. While the experimental NPA measurements are obtained in the perpendicular direction ($T_\perp$) and at the well-developed phase of the RF discharge ($\sim 10^{16} - 10^{17}\,\mathrm{m}^{-3}$). To qualitatively compare the distributions in the experiment and the simulations, one has to assume ion temperature isotropization ($T_\perp = T_\parallel = T$). This assumption is valid for discharges with densities $n_e > 10^{16}\,\mathrm{m}^{-3}$, corresponding to the moments when the NPA data are obtained. The observation of Kappa distributions in the simulations and the experiments is significant because it is considered that ICWC plasma is low temperature ($\approx 3 - 5\,\mathrm{eV}$). However, the NPA diagnostics measured fast charge exchange neutrals in the ICWC experiments with energies $\epsilon > 1\,\mathrm{keV}$. When these measured distributions are interpreted by a Maxwell energy distribution, it overestimated the plasma

temperature ($T > 200\,\mathrm{eV}$) in the ICWC experiments. Whereas by assuming a Kappa distribution for the experimental data, we obtain agreement with a majority of ions having a low energy ($3 - 5\,\mathrm{eV}$) and also having the energetic tails that we observe in the ICWC experiments with the high magnetic field ($B_T = 2\,\mathrm{T}$). The experimental measurements for the discharges with the low magnetic field ($B_T = 0.2\,\mathrm{T}$) are at the detection limit of the NPA diagnostic for the energies above $5\,\mathrm{keV}$. Therefore, the fit converges more into a Maxwell energy distribution and overestimates the temperature of the ions again.

Finally, the discharges with the high magnetic field show a significant ion population at high energies supposedly caused by an acceleration of the ions at the Ion Cyclotron Resonance or its harmonics. However, until now no proper explanation was given for the fast ion population observed in discharges with the low magnetic field. The present modeling of the ICRF discharge initiation with the PIC-MCC model suggests that these fast ions are already created at low electron density $n_e > 10^{13}\,\mathrm{m}^{-3}$ by the action of plasma waves, namely Langmuir waves. These waves are predicted to propagate in the toroidal direction for a case with the RF frequency ω close to the electron plasma frequency $\omega_{p,e}$ and the PIC-MCC model for the first time demonstrated their effect on discharge initiation by the ICRF antenna. Furthermore, these mechanisms are always present in the ICRF discharges regardless of the applied toroidal magnetic field B_T. These observations are new and they will be studied in future on TOMAS device in more details.

References

[1] M. Tripský et al. *A PIC-MCC code RFdinity1d for simulation of discharge initiation by ICRF antenna*. Nucl. Fusion, 57:126043, 2017.

[2] C. K. Birdsall and A. B. Langdon. *Plasma Physics Via Computer Simulation*. CRC Press, Boca Raton, USA-FL, 2004.

[3] G. Lapenta. *Chapter: Particle-based simulation of plasmas*, pages pp 4–1 – 4–37. Bristol: IOP Publishing, 2016.

[4] Y. Hu. *Particle In Cell (PIC) simulation*. Technical report, Institute of Plasma Physics, Chinese Academy of Sciences.

[5] Craig Stewart MacLachlan. *Numerical modelling of low temperature plasma*. PhD thesis, University of Glasgow, July 2009.

[6] V. Vahedi and M. Surendra. *A Monte Carlo collision model for particle-in-cell method: applications to argon and oxygen discharges*. Computer Physics Communications, 87:179–198, 1995.

[7] R. W. Hockney and J. W. Eastwood. *Computer Simulation Using Particles*. McGraw-Hill, New York, USA, 1981.

[8] D. Reiter. *Elementary Processes in Hydrogen-Helium Plasmas*. Springer, Forschungszentrum Jülich GmbH 52425 Jülich, Germany, 1987.

[9] D. Reiter. *The data file HYDHEL, Atomic and Molecular Data for EIRENE*. Technical report, Forschungszentrum Jülich GmbH, 52425 Jülich, Germany, 2002.

[10] R. Papoular et al. *The Genesis of Toroidal Discharges*. Nuclear Fusion, 16(1):37–45, 1976.

[11] M. Tripský et al. *Monte Carlo simulation of ICRF discharge initiation at* $\omega_{LHR} < \omega$. In European Conference Abstracts (ECA), volume 38.F. of *http://doi.org/10.1063/1.4864556*, Berlin, Germany, June 2014.

[12] M. Tripský et al. *Monte Carlo simulation of ICRF discharge initiation in ITER*. In AIP Conference Proceedings, volume 1689 of *http://doi.org/10.1063/1.4936507*, page 060009, California, USA, 2015.

[13] A. Lyssoivan et al. *Simulation of ITER full-field ICWC scenario in JET: RF physics aspects*. Plasma Phys. Control. Fusion, 54, 2012.

[14] A. Lyssoivan et al. *Wave aspect of neutral gas breakdown with ICRF antenna in ICWC operation mode*. In European Conference Abstracts. Vol. 38.F. European Conference Abstracts (ECA), Berlin, Germany, June 2014.

[15] F. F. Chen. *Introduction to plasma physics*. Plenum Press, 1974.

[16] V. Pierrard et al. Sol. Phys., 267(153), 2010.

[17] J. Dudik et al. Astrophysical Journal, 807(123), 2015.

[18] M. Hahn et al. Astrophysical Journal, 809(178), 2015.

[19] M. Oka et al. Astrophysical Journal, 764(6), 2013.

[20] A. Lyssoivan et al. In AIP Conf. Proc, volume 1580, 2013.

[21] A. V. Lozin et al. Plasma Phys. Rep., 39(624), 2013.

[22] D. Douai et al. J. Nucl. Mater., 415(S1021-8), 2011.

[23] A. Goriaev et al. *First results of W7-X - like GDC on the upgraded TOMAS device*. ECA, 41F(P1.117), 2017.

[24] T. Wauters et al. *Wall Conditioning by ECRH and GDC at the Wendelstein 7-X Stellarator*. ECA, 40A, 2016.

6 Discharge Initiation in Linear Device

Up to now, we were studying the discharge initiation in the toroidal devices in experiments and simulations with the Monte Carlo collision models with periodic boundary conditions. The important feature of the discharge initiation in a toroidal device is that electrons can re-enter the antenna region after they encircle around the torus. In Section 2.3.2.1, we presented the PDM-model [1] describing the discharge initiation by the ICRF antenna. One of the assumptions of their model was that the plasma is first initiated in the antenna region and electrons leaving the antenna region are neglected. Therefore, this model is not suitable for describing the discharge initiation in the tokamaks or stellarators. However, the model can be used to explain the discharge initiation by the ICRF antenna in linear devices with open ends or inside an antenna box. In this geometry, electrons leaving the antenna region are lost and will not contribute to the electron multiplication in front of the antenna strap. Only the electrons trapped in the potential well for sufficiently longer time than the typical time for the ionization collision will participate in the electron density increase. Thus, in this chapter, we study the discharge initiation in front of the antenna and inside the antenna box at the IShTAR device. The experimental results are validated by simulations with the `RFdinit1d` model, and by the PDMI theoretical predictions given by *Schüller* et al. [2].

6.1 Introduction

To simulate the discharge initiation in front of the antenna strap or inside the antenna box, we slightly modified the Monte Carlo collision model `RFdinity1d` presented in Chapter 3. The model simulates the motion of electrons along a parallel magnetic field line for two scenarios: (a) in front of the antenna and (b) in the antenna box.

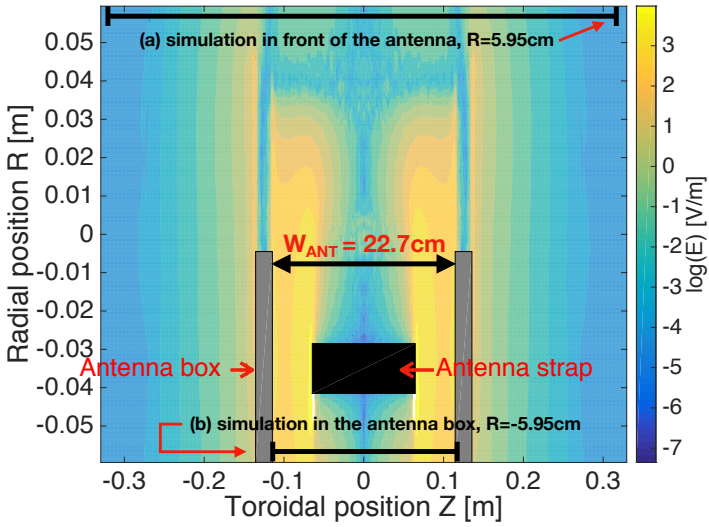

Figure 6.1: Top view geometry of the `RFdinity1d` model for the IShTAR experiment and simulation. Contour plot of the absolute value of the parallel E_z-field in (R-Z)-coordinates for one-strap IShTAR antenna obtained in the horizontal plane using the commercial electromagnetic software CST Microwave Studio®(MWS) for $f = 5\,\mathrm{MHz}$, $P = 1\,\mathrm{W}$. Two simulation domains are highlighted (black solid horizontal lines) at two radial distances: (a) in front of the antenna, $R = 5.95\,\mathrm{cm}$, (b) in the antenna box, $R = -5.95\,\mathrm{cm}$. The width of the antenna box is $W_{\mathrm{ANT}} = 22.7\,\mathrm{cm}$.

Fig. 6.1 illustrates the model geometry for these two scenarios for the IShTAR device at two radial positions $R = 5.95\,\mathrm{cm}$ (in front of the antenna) and $R = -5.95\,\mathrm{cm}$ (inside of the antenna box), where $R = 0.0\,\mathrm{cm}$ corresponds to the antenna box edge (See Fig. 6.1). The figure also shows the absolute value of the parallel E_z-field in (R-Z)-coordinates for one-strap IShTAR antenna obtained in the horizontal plane of the interest.

The horizontal black solid lines in Fig. 6.1 symbolize magnetic field lines along which the electrons move. The model boundary conditions are highlighted in the figure by short vertical lines at the edges of the horizontal black lines for the scenario in front of the antenna. An electron crossing one of the boundary conditions is deleted from the simulation because the electric field is already low at this position and the electron cannot reenter the antenna region anymore.

In the second scenario, the antenna box walls are the boundary conditions. For this reason, we had to take into account the secondary electron emission due to electrons hitting the antenna box wall. The IShTAR antenna box is made from aluminum. The secondary electron yield (SEY) depends strongly on the surface properties (roughness, cleanness, etc.), more than on the metal type [8]. It was reported that any insulating layers (e.g. oxides as well as adsorbed water) significantly increase the emissivity of surfaces [8]. The multiplication effect is an undesirable phenomenon among fusion RF devices and other applications using RF power [9–11]. It is documented that in

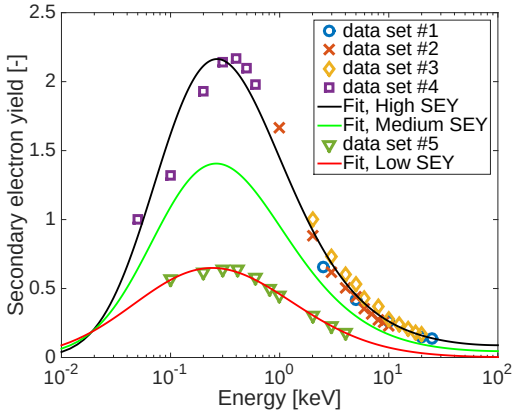

Figure 6.2: The secondary electron yield for aluminum. Experimental data sets #1-#5 are taken from [3–7] in the order. The data sets are grouped into 2 groups: data sets #1-#4 corresponding to High SEY and data set #5 for Low SEY. The analytic fits of the experimental data are used in the Monte Carlo model. The medium SEY is the average of the High and Low SEY.

some situations DC magnetic fields might affect the electron emission properties of the metallic surfaces of the RF components [9–12]. Therefore, we will study the contribution of the secondary electron emission to plasma production for different energy dependencies of the yield as it is challenging to know exactly the shape of the SEY function for our materials in the antenna box. We investigate the effect in our Monte Carlo model for three SEY dependencies on the incoming energy. These SEY dependencies have very similar shape, but they vary with their magnitude of the yield. It allows us to study the maximum SEY for which the plasma is not initiated inside the antenna box, and to propose a construction of the antenna box and straps using materials with a lower SEY and antenna conditioning to avoid the discharge initiation inside the box. Fig. 6.2 plots SEY dependencies for aluminum taken from [13]: (a) High SEY corresponds to the experimental data sets #1-#4 [3–6], (b) Low SEY is for the experimental data set #5 [7], and (c) Medium SEY is the average between the high and low SEY. The implementation of secondary electron emission in our model does not take into account the incoming angles of electrons. The number of the secondary electrons emitted from the material depends only on the yield (SEY) for the incoming energy of the electron (Fig. 6.2).

6.2 Experiment on IShTAR

The IShTAR (Ion cyclotron Sheath Test ARrangement) project, at the Max-Planck-Institut für Plasmaphysik in Garching (Germany), aims at studying antenna near-fields and RF sheath effects in the presence of a plasma and magnetic field [14]. It is a linear device consisting of a cylindrical main vessel of $1.1\,\mathrm{m}$ length and $1\,\mathrm{m}$ diameter, and a

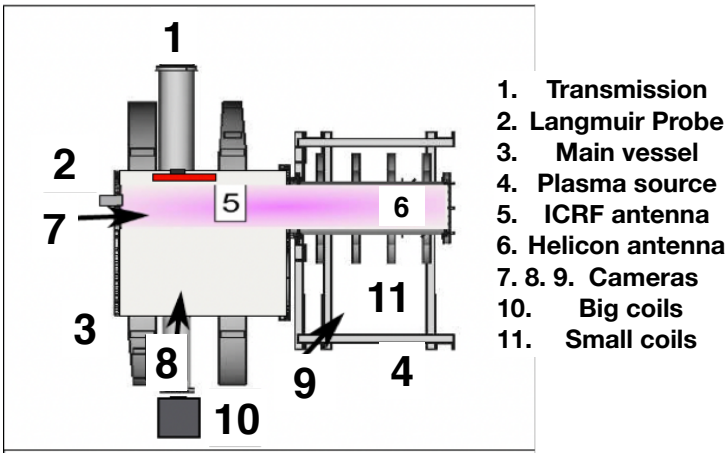

Figure 6.3: Overview of the IShTAR set-up with the different components [14].

separate chamber where the plasma is created by a helical antenna with $1.1\,\mathrm{m}$ length and $0.4\,\mathrm{m}$ diameter. A schematic of the device is shown in Fig. 6.3. For our experiment, the helical antenna was disabled to study the plasma initiation solely by the ICRF antenna. The magnetic field is created by two big coils around the main vessel. The maximal current in the big coils is $8\,\mathrm{kA}$ (for $10\,\mathrm{s}$), which corresponds to a magnetic field of $0.24\,\mathrm{T}$. The vacuum system is connected to the back flange and consists of a pre-vacuum pump to reach a pressure of $10^{-2}\,\mathrm{mbar}$, and a turbomolecular pump creates a vacuum ($10^{-6}\,\mathrm{mbar}$ level) [14]. The antenna consists of a single strap fed by transmission lines connected to a generator with a power up to $1\,\mathrm{kW}$ and with a frequency range $[0.1 - 100\,\mathrm{MHz}]$. The IShTAR device provides an excellent opportunity to focus on specific aspects of ICRF plasma production as it is a linear device. It can, therefore, be used to investigate the plasma formation in ponderomotive wells in front of the antenna box, or inside of the antenna.

We operated the IShTAR antenna at two frequencies, $f = 5.22\,\mathrm{MHz}$ and $f = 42.06\,\mathrm{MHz}$. The experiment was carried out in helium with a pressure up to $1\,\mathrm{Pa}$. On large and mid-size devices the operation pressure in ICRF discharge production is limited to $< 5 \cdot 10^{-2}\,\mathrm{Pa}$ for antenna system safety reasons. IShTAR provides the flexibility to study the events that occur at high pressure. During the experiment, we studied the parametric dependency for successful discharge initiation. It was observed that the location where the plasma is created depends on the antenna parameters. At $f = 5.22\,\mathrm{MHz}$, the plasma column is toroidally homogeneous and located in front of the antenna, and the plasma cannot be initiated below $p_{He} = 0.55\,\mathrm{Pa}$. While at $f = 42.06\,\mathrm{MHz}$, the plasma is always created in the antenna box near the feeding point for the pressure level above $p_{He} > 0.2\,\mathrm{Pa}$. This difference between the plasma column and its location is shown in Fig. 6.4. The figure illustrates two images from a

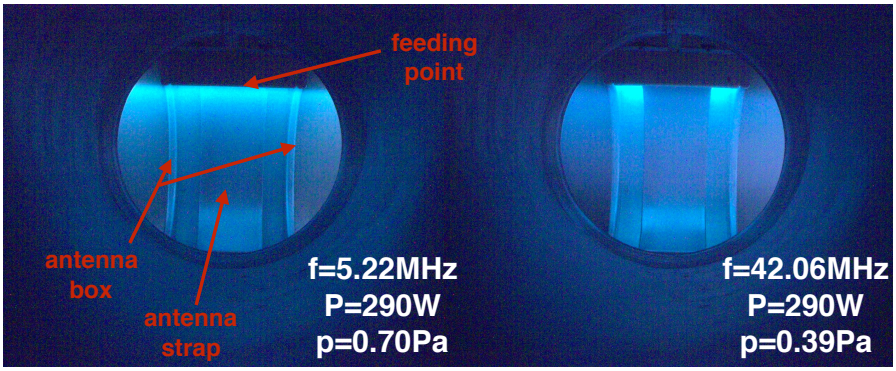

Figure 6.4: Camera views in IShTAR on the front side of the ICRF antenna for two frequencies at the generator power $P_G = 290\,\mathrm{W}$: (A) plasma is located in front of the strap for $f = 5.22\,\mathrm{MHz}$, $p_{He} = 0.7\,\mathrm{Pa}$, (B) plasma is created in antenna box for $f = 42.06\,\mathrm{MHz}$, $p_{He} = 0.39\,\mathrm{Pa}$.

camera on IShTAR facing the ICRF antenna for same generator power ($P_G = 290\,\mathrm{W}$) [15].

6.3 Simulations

The MCC model `RFdinity1d` described in Section 3 includes inelastic collisions (*excitation* and *ionization*) and elastic scattering between electrons and helium atoms. The collisions are summarized in Appendix A. Electrons interact with the vacuum parallel electric field E_z. Depending on the electric field and frequency, electrons can be trapped in the potential well in front of the antenna strap. If electrons remain trapped for a sufficient time compared to the ionization characteristic time, the electron density may increase. The trapped electrons must be accelerated by the electric field (the generator input power) above the ionization potential ($\Delta E^{\mathrm{ion}} \approx 24.6\,\mathrm{eV}$ for helium). Furthermore, for trapping the electrons, the electric field must have the shape (depending on the radial position) to minimize the electron losses. The performed simulations use the parallel electric field profiles as obtained by the commercial electromagnetic software CST Microwave Studio® [16]. Fig. 6.1 shows the absolute values of the E_z-field in the horizontal plane $0.5\,\mathrm{cm}$ below the antenna top for $f = 5\,\mathrm{MHz}$, $P = 1\,\mathrm{W}$. The figure demonstrates that not only the amplitude of the electric field changes radially but also the shape. We investigate plasma initiation at two radial locations: $R = -5.95\,\mathrm{cm}$ (inside the antenna box) and $R = 5.95\,\mathrm{cm}$ (in front of the antenna strap). The vacuum parallel electric field for these two radial positions are visualized in Fig. 6.5 for the forward power of $P = 1\,\mathrm{W}$ and frequency $f = 5\,\mathrm{MHz}$. Two arrows indicate locations of the antenna box walls marked by the abrupt change of the E_z-field profile for the electric field inside the antenna box ($R = -5.95\,\mathrm{cm}$) [15].

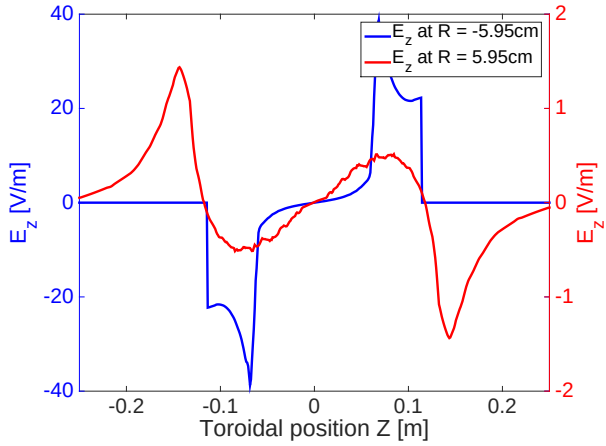

Figure 6.5: Vacuum E_z-field at $R = -5.95\,\mathrm{cm}$ (inside the antenna box) and $R = 5.95\,\mathrm{cm}$ (in front of the antenna strap) used by the model ($f = 5\,\mathrm{MHz}$, $P = 1\,\mathrm{W}$).

In chapters 2 and 4, we were investigating parametric dependency for an electron to enter antenna region and to be accelerated by the parallel antenna electric field [17]. In the case of IShTAR, we study the condition for which electrons might be trapped in front of the antenna by the potential well. This condition described by *Schüller* et al. [2] requires the residence time of the oscillating electrons in front of the antenna to be longer than the time needed for ionization $1/\nu_{\mathrm{ion}}^{RF}$. However, we have to stress that the conditions described by *Schüller* et al. (PDMI-model) rely on the description of the electron motion in the ponderomotive force given by the PDM-model. Unfortunately, the shape of the field in front of the antenna is such that the conditions for the Taylor expansion are not fulfilled in front of the antenna strap. Therefore, these theoretical conditions given by PDMI-model are only approximations because we do not have any better description at this moment. For the same reason, we cannot apply our theoretical description introduced in Section 4.5 to study the threshold energies for the IShTAR experiment.

The ionization frequency in front of the antenna is given by Eq. (2.50), and residence time $1/\nu^{\mathrm{res}}$ is expressed by the time electrons needs to travel $W_{\mathrm{ANT}} + L_z$ distance with the average velocity obtained from the ponderomotive force in front of the antenna v_{pdm}, where $L_z/2$, Eq. (2.47), is the e-folding length with which the field decays outside the toroidal antenna width W_{ANT} [2]. Thus,

$$\nu^{\mathrm{res}} < \nu_{\mathrm{ion}}^{\mathrm{RF}} \Leftrightarrow \frac{v_{\mathrm{pdm}}}{W_{\mathrm{ANT}} + L_z} < 1.78 \cdot 10^7 \left(\frac{E_z}{f}\right) n_{He} \left\langle \sigma_{\mathrm{ion}}^{\mathrm{RF}} \right\rangle, \tag{6.1}$$

where the ponderomotive velocity is equal to $\sqrt{\frac{2\cdot 1115 q_e}{m_e}} \frac{E_z}{f}$. Then, the condition for the minimum pressure [2] to initiate the plasma in front of the antenna can be ex-

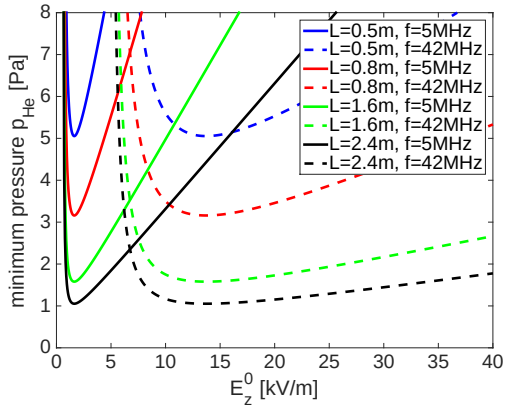

Figure 6.6: Theoretical predictions of the minimum pressure to initiate a discharge according to the PDMI theory for two frequencies $f = 5\,\mathrm{MHz}$ and $f = 42\,\mathrm{MHz}$ with different $L = (W_{\mathrm{ANT}} + L_z)$ distances ($[0.5,\ 0.8,\ 1.6,\ 2.4]\,\mathrm{m}$).

pressed as

$$n_{He} > \frac{1}{(W_{\mathrm{ANT}} + L_z)\left\langle \sigma_{\mathrm{ion}}^{\mathrm{RF}} \right\rangle}, \tag{6.2}$$

where n_{He} is the minimum neutral gas pressure, $\left\langle \sigma_{\mathrm{ion}}^{\mathrm{RF}} \right\rangle$ denotes the time-averaged ionization collision cross-section depending on the electric field strength and frequency.

Fig. 6.6 illustrates the condition for two frequencies, $f = 5$MHz, and $f = 42$MHz with the varying distances $W_{\mathrm{ANT}} + L_z$. The lowest value of the minimum pressure is independent of the frequency for the same distance $W_{\mathrm{ANT}} + L_z$. However, the lowest value decreases with the distance $W_{\mathrm{ANT}} + L_z$ for the same frequency. The experiment on IShTAR corresponds to the situation with $W_{\mathrm{ANT}} + L_z = 0.8\,\mathrm{m}$ for the case in front of the antenna and $W_{\mathrm{ANT}} + L_z = 0.5\,\mathrm{m}$ for the case inside the antenna box. In the figure, we can see that no plasma should be created in front of the antenna or inside the antenna box below $p_{He} < 3\,\mathrm{Pa}$ for both frequencies. However, in the experiment, we observe the plasma initiation above $0.55\,\mathrm{Pa}$ at $f = 5.22\,\mathrm{MHz}$, and above $0.2\,\mathrm{Pa}$ at $f = 42.06\,\mathrm{MHz}$. Therefore, a more detailed investigation is needed to explain the discrepancy between the experimental observations and theoretical predictions. It is important to highlight that the maximum allowed pressure for the ICRF plasma production is set around $5 \cdot 10^{-2}\,\mathrm{Pa}$ in tokamaks. This pressure level should be still safe considering the discrepancy between the experiment and PDMI condition is of the order of 10. Fig. 6.6 shows that for the rather long distance of $2.4\,\mathrm{m}$ (approximately size of the ITER ICRF antenna, See Fig. 4.11), the minimum pressure is around $1\,\mathrm{Pa}$, thus the safe pressure level in present ICRF systems should be below $0.1\,\mathrm{Pa}$. Although, we will show in the next section with simulations inside the antenna box that this minimum pressure strongly depends on the secondary electron emission. For an extremely

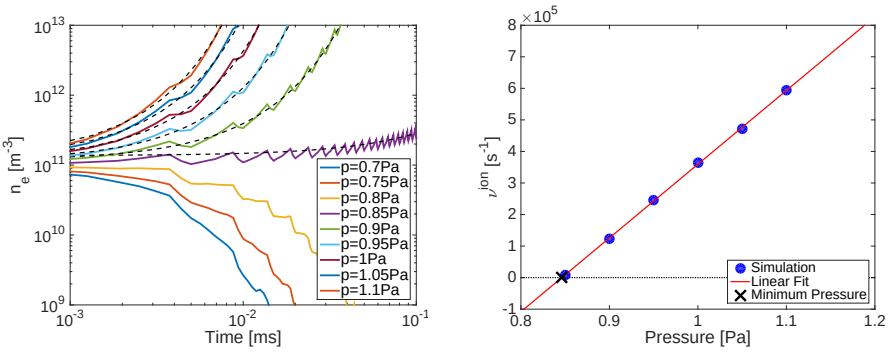

(a) (b)

Figure 6.7: (a) Electron density evolution in time for simulations for the forward power $P = 25\,\mathrm{kW}$, frequency $f = 5\,\mathrm{MHz}$ and varying neutral gas pressure. The evolution is fitted with the exponential function $n_e \sim \exp(\nu t)$, where ν corresponds to the ionization rate. (b) Dependence of the ionization frequency on the neutral gas pressure in simulations for the forward power $P = 25\,\mathrm{kW}$ and frequency $f = 5\,\mathrm{MHz}$. Linear fit of the simulations results denotes the minimum pressure with $\nu^{\mathrm{ion}} = 0$.

high secondary electron yield, the minimum pressure might be lower than $0.1\,\mathrm{Pa}$ as we will demonstrate in the next section.

6.3.1 Discharge initiation in front of the antenna strap

As we mentioned earlier, the plasma was created in front of the antenna strap only for $f = 5.22\,\mathrm{MHz}$. We launched simulations at this frequency with varying neutral gas pressure and forward power with the electric field at radial location $R = 5.95\,\mathrm{cm}$ (Fig. 6.5). Fig. 6.7(a) plots the simulation results of the electron density n_e evolution in time for the forward power $P = 25\,\mathrm{kW}$ and frequency $f = 5\,\mathrm{MHz}$ with varying initial neutral gas pressure. The electron density increase starts for the simulations with the neutral gas pressure above $p_{He} > 0.85\,\mathrm{Pa}$. The figure fits the density increase with an exponential function $n_e \sim \exp(\nu t)$. Thus, slopes of the density electron increase correspond to the ionization rate ν_{ion}^{RF}. The PDMI description predicts that the ionization frequency ν_{ion}^{RF} is changing linearly with the neutral gas pressure for the constant ratio of the electric field strength and frequency, $\nu_{\mathrm{ion}}^{RF} \sim n_{He}$ (Eq. (2.50)). The ionization rate dependency on the neutral gas pressure for the forward power $P = 25\,\mathrm{kW}$ and frequency $f = 5\,\mathrm{MHz}$ is plotted in Fig. 6.7(b). The figure demonstrates this linear dependence of the ionization rate on the neutral gas pressure obtained by the simulations. By fitting this linear dependence, we can identify the minimum pressure above which the ionization rate is higher than zero. This minimum pressure is visualized by a black cross point in Fig. 6.7(b).

Previously in Chapter 4 and Section 4.1, we have shown in Fig. 4.4(a) that the ionization rate in the simulations increases with the square root of the neutral gas pressure,

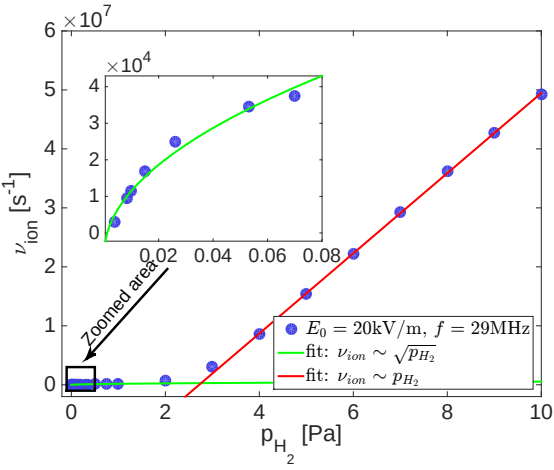

Figure 6.8: Ionization rate dependency on the neutral gas pressure. The zoomed area corresponds to values of the low pressures, $p_{H_2} < 0.5\,\mathrm{Pa}$.

$\nu_{\mathrm{ion}} \sim \sqrt{p_{H_2}}$. This square root dependency is in discrepancy with the linear dependency predicted by Eq. (6.1) and our simulations in this section (Fig. 6.7(b)). However, this square root dependency on the pressure is detected only for rather low values of the pressure relevant for the ICRF discharge initiation ($p_{H_2} < 0.2\,\mathrm{Pa}$). While in this section, we observed the linear dependency for the high neutral gas pressures, $p_{H_2} > 1\,\mathrm{Pa}$. These observations suggest a transition from the square root dependency for low pressure into the linear dependency. Therefore, we launched additional simulations for a toroidal geometry as in Section 4.1 for $E_0 = 20\,\mathrm{kV/m}$ and $f = 29\,\mathrm{MHz}$ (Fig. 4.4(a)) with the neutral gas pressure above $0.2\,\mathrm{Pa}$. The results of the ionization rate dependency on the neutral gas pressure, $p_{H_2} = 4 \cdot 10^{-3} - 10\,\mathrm{Pa}$, are shown in Fig. 6.8. The zoomed area plots the ionization rate dependency for low pressures. These results indeed confirm that for the high pressure, $p_{H_2} > 3\,\mathrm{Pa}$, the ionization rate increases linearly with the pressure, whereas for the low pressure, $p_{H_2} < 0.5\,\mathrm{Pa}$, the ionization rate follows the square root dependence. The transition from the square root to linear dependency is detected around $p_{H_2} \approx 2\,\mathrm{Pa}$.

In the experiment, the discharges at $f = 5.22\,\mathrm{MHz}$ were initiated in front of the strap and never in the antenna box. The minimum neutral gas pressure for plasma initiation decreases with the increasing generator power. Fig. 6.9(a) showing the experimental results (red line) indicates that the minimum pressure decreases steeply at lower generator power ($100 - 150\,\mathrm{W}$) where-after the minimum pressure decreases more slowly up to the maximum operation power on IShTAR ($P_G = 400\,\mathrm{W}$). In the figure, the forward power range used in the simulations is very different from the generator power range. The MWS E-field (in Fig. 6.5 and Fig. 6.1) are normalized to a forward power of $1\,\mathrm{W}$ arriving at the antenna feeding point. It was however difficult to determine the forward power on IShTAR due to complex matching system. No measurements of the voltages on the antenna strap were available. The minimum

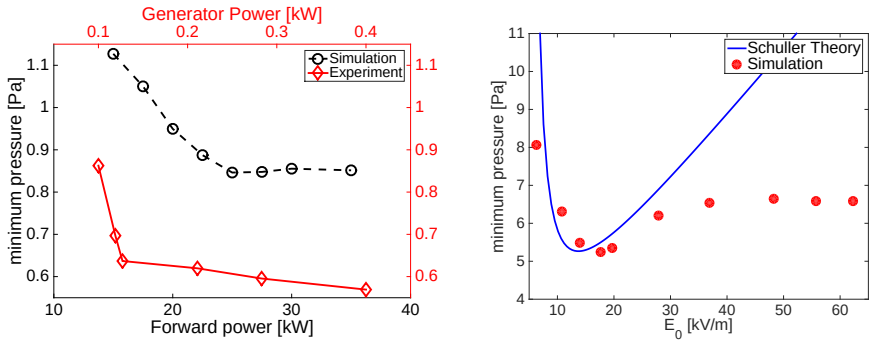

(a) (b)

Figure 6.9: (a) Dependence of the minimum pressure on the power in the experiment at $f = 5.22\,\mathrm{MHz}$ (red line) and the simulations at $f = 5\,\mathrm{MHz}$ (black line). (b) Comparison of the minimum pressure dependency on the electric field amplitude E_0 in the simulations and theoretical predictions (PDMI-theory) for $f = 42\,\mathrm{MHz}$, and $(W_{\mathrm{ANT}} + L_z) = 0.48\,\mathrm{m}$.

pressures in our simulations are slightly higher than the experimental ones. This shift towards the higher minimum pressures in the simulations may also be caused by the fact that our model contains only one neutral gas type, i.e. helium atom. However, the base pressure in IShTAR is rather high $p_{\mathrm{base}} = 10^{-4}\,\mathrm{Pa}$. It suggests that a high level of impurities can be present in the vessel (H_2O) with significantly lower ionization potentials than for the helium atom [15].

6.3.2 Discharge initiation in the antenna box

Unlike at $f = 5.22\,\mathrm{MHz}$, at $f = 42.06\,\mathrm{MHz}$ the plasma was initiated inside of the antenna box (Fig. 6.4). At both frequencies, the strongest electric field is located near the feeding point in the antenna box. Furthermore, at $f = 42.06\,\mathrm{MHz}$, the minimum pressure for the plasma initiation is lower than for the experiment at $f = 5.22\,\mathrm{MHz}$. The plasma in the antenna box was observed above $p_{He} > 0.2\,\mathrm{Pa}$ in the power range on IShTAR at $f = 42.06\,\mathrm{MHz}$. While the plasma in front of the antenna at $f = 5.22\,\mathrm{MHz}$ was initiated above $p_{He} > 0.55\,\mathrm{Pa}$ (Fig. 6.9(a)). According to the theoretical PDMI predictions (Fig. 6.6), the magnitude of the minimum pressure for discharge initiation should not vary with the frequency.

These discrepancies between the experimental and theoretical descriptions are, namely: (i) lower minimum pressure to initiate plasma for $f = 42.06\,\mathrm{MHz}$ than for $f = 5.22\,\mathrm{MHz}$, and (ii) plasma in the antenna box for $f = 42.06\,\mathrm{MHz}$, indicate insufficient assumptions in the theoretical description of the discharge initiation by the ICRF antenna. Here, we show that the Secondary Electron Emission (SEE) plays a vital role in the discharge initiation in the antenna box and neglecting the SEE is responsible for the discrepancies between the theory and experiments. To study the effect of the SE for the discharge initiation in the antenna box, we have first launched simula-

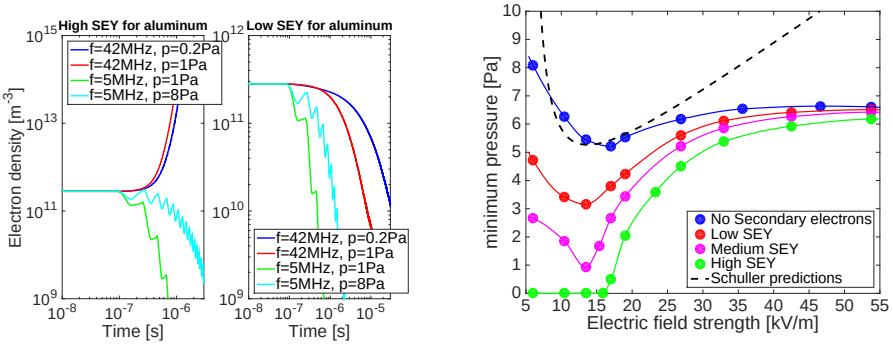

Figure 6.10: (a) Electron density evolution in time for simulations with the same electric field strength $E_0 \approx 10\,\mathrm{kV/m}$ at $f = 5\,\mathrm{MHz}$, $f = 42\,\mathrm{MHz}$, and various pressure levels for two scenarios with different SEY profiles: High SEY, and Low SEY for aluminum. (b) The minimum pressure dependence on the electric field amplitude in simulations with different SEY profiles at $f = 42\,\mathrm{MHz}$. The results of the minimum pressures are compared with the PDMI theoretical predictions and the simulations neglecting SE.

tions using the `RFdinit1d` model neglecting the SE. The results of this simulations are visualized in Fig. 6.9(b) for $f = 42\,\mathrm{MHz}$. The figure plots the minimum pressure above which we observe the density increase and its dependency on the forward power. The simulation results are in good agreement with the theoretical predictions. Both theoretical predictions and simulations results indicate that no plasma should be initiated in the antenna box below $5\,\mathrm{Pa}$ [15].

Then, we used the `RFdinity1d` model including the SE with three different Secondary Electron Yield (SEY) dependency on the incoming energy (Fig. 6.2). Fig. 6.10(a) shows an example of the simulations with different initial parameters, and their electron density evolution in time. The electric field strength and shape are for all eight simulations identical; we vary the frequency and neutral gas pressure for two SEY profiles: High SEY and Low SEY (Fig. 6.2). For the High SEY, the electron density increases only at $f = 42\,\mathrm{MHz}$ for both neutral gas pressure levels: $p_{He} = 0.2\,\mathrm{Pa}$ and $p_{He} = 1\,\mathrm{Pa}$, while at $f = 5\,\mathrm{MHz}$ we observe the electron density decrease even for the extremely high pressure of $p = 8\,\mathrm{Pa}$. For the electron density decrease, the ionization and secondary electron emission rates are too low to compensate for the electron losses. These simulations are in qualitative agreement with the experiments: plasma is formed in the antenna box only at $f = 42\,\mathrm{MHz}$. However, for the Low SEY, the electron density does not increase for both frequencies. The simulation results reveal a strong dependency on the antenna parameters (antenna power, frequency) and the SEY profiles. These dependencies are studied in more details in the next two subsections.

The effect of antenna frequency on the motion of electrons and secondary electron emission is visualized in Fig. 6.11. The figure visualizes a concentration of the

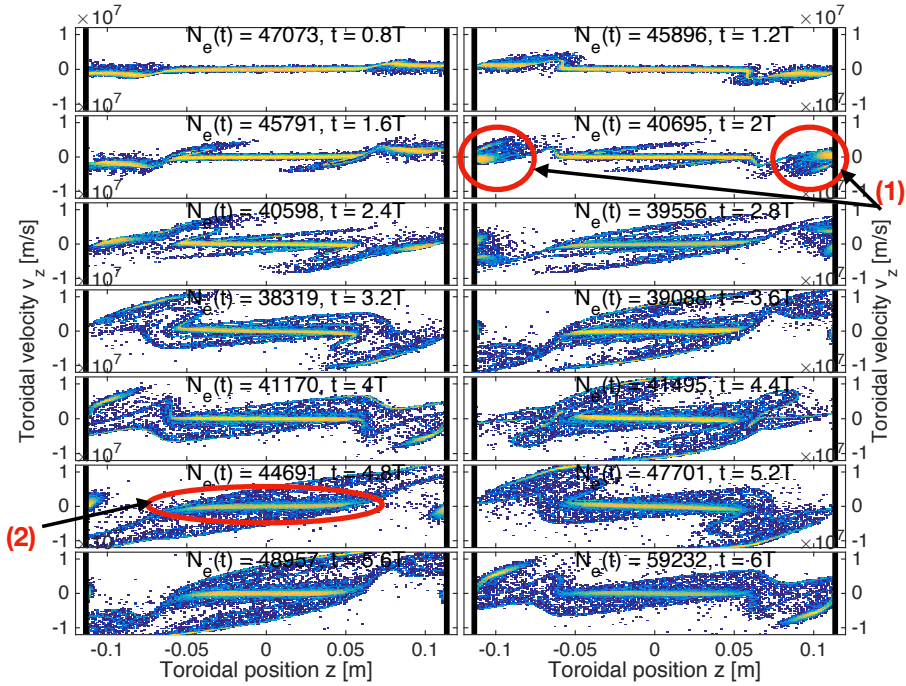

Figure 6.11: Evolution of the electron distribution for simulations with the IShTAR antenna electric field inside the antenna box at electric field amplitude of $E_0 = 13.4\,\mathrm{kV/m}$ for $f = 42\,\mathrm{MHz}$. The time instance for each plot is given as a function of the RF period. The antenna box walls highlighted by a black vertical solid lines are located at $z = \pm 0.1135\,\mathrm{m}$.

electrons at the toroidal position z with the toroidal velocity v_z (yellow color represents a higher concentration of the electrons) for the RF frequency $f = 42\,\mathrm{MHz}$ and electric field amplitude of $E_0 = 13.4\,\mathrm{kV/m}$ over six periods ($t_{\mathrm{sim}} \approx 1.4 \cdot 10^{-7}\,\mathrm{s}$) at $p_{He} = 1\,\mathrm{Pa}$ using High SEY. We can observe that there is a high concentration of the electrons trapped in front of the antenna for this simulation. The trapped electrons are highlighted by the red ellipse with nr. (2). It also shows that new electrons are created due to the secondary emission in the vicinity of the wall. These electrons are highlighted by two red circles with nr. (1). It is more likely that at this high frequency ($f = 42\,\mathrm{MHz}$) the electric field will change the sign such that it will accelerate the electrons towards the opposite side of the antenna box and re-enter the area in front of the strap. We can observe in the figure that these newly born electrons are indeed pushed back in front of the antenna strap and travel on opposite side of the antenna box. While at the low frequency ($f = 5\,\mathrm{MHz}$), the electric field does not change sign fast enough and newly born electrons are pushed back at the same wall where they were created, but this time with low energies and no newborn electrons are emitted. We will show later that our simulation results reproduce dependencies for the multipactor effect [18, 19]. Fig. 6.11 also illustrates the number of electrons in each time instance. First, the number of electrons decreases, but from a particular moment newly born electrons compensate the losses and the number of electrons starts to increase in time as the newly born electrons are in resonance with the RF field.

Dependency on the secondary electron yield

First, we study the dependence of the minimum pressure to initiate the plasma in the antenna box on the SEY. Fig. 6.10(b) illustrates the minimum neutral gas pressure dependency on the electric field (antenna power) at $f = 42\,\mathrm{MHz}$ for three different profiles of the SEY energy dependency (Fig. 6.2) and the situation neglecting the secondary electron emission. The simulation results behave as one would predict: the minimum pressures for a discharge initiation decrease with the increasing secondary electron yield. This decrease is mainly noticeable at the electric fields below $25\,\mathrm{kV/m}$. For the medium SEY, the plasma can be initiated in the antenna box slightly below $1\,\mathrm{Pa}$ around the electric field $E_0 \approx 13\,\mathrm{kV/m}$. The simulations with the High SEY show that below $E_0 < 16\,\mathrm{kV/m}$ the discharge initiation is independent of the pressure due to the secondary electron emission being the dominant process to create electrons. In this situation, the plasma is created even for $p_{He} = 0\,\mathrm{Pa}$ due to high secondary electron emission. Furthermore, the figure demonstrates that for $f = 42\,\mathrm{MHz}$ and high electric field strength the minimum pressure is similar for all the SEY profiles and even the model without SEY.

Dependency on the electric field strength and frequency

In the previous sections, we have seen that for specific parameters of the electric field strength and frequency, the electron density increases not only due to the ionization reactions but mainly because of the secondary electron emission on the antenna box

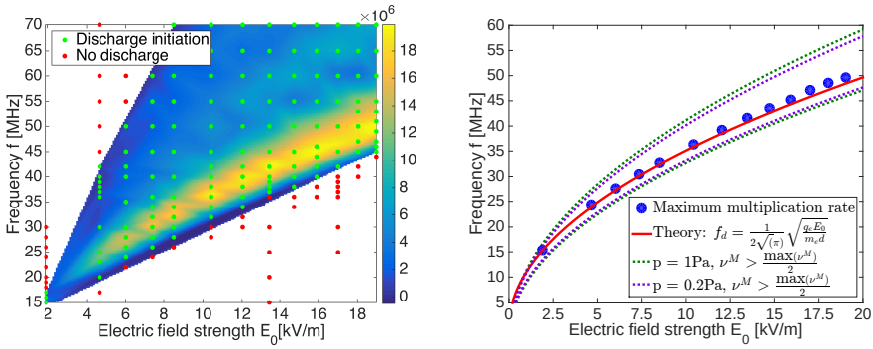

(a) (b)

Figure 6.12: (a) Contour plot of the electron multiplication rate ν^M in $(E_0 - f)$-coordinates. The contour plot is created by an interpolation of the simulation results highlighted by red and green points. Red points represent simulations with no increase in the electron density, and green points vice versa. (b) The frequency dependence on the electric field amplitude at which the maximum multiplication rate is observed corresponding to the frequency-gap product f_d. The boundary with the multiplication rates above half of the maximum value are highlighted for two pressure levels: $p = 0.2\,\mathrm{Pa}$ and $p = 1\,\mathrm{Pa}$.

walls. Furthermore, our simulations indicated that the secondary electron emission becomes the dominant mechanism for the discharge initiation in the antenna box. Therefore, we cannot refer to the electron density increase rate as the ionization rate, but we call it the electron multiplication rate ν^M.

In this subsection, we investigate the multiplication rate dependency on the electric field strength and frequency for the simulations using only the High SEY. Fig. 6.12(a) summarizes simulation results of multiplication rates for $p_{He} = 1\,\mathrm{Pa}$ using High SEY as a function of the electric field strengths and frequencies. Green points represent simulations with an electron density increase, and red points correspond to the simulations at the E_0 and f parameters with no discharge initiation. For each simulation with density increase, we measure the multiplication rates and plot it into the figure in the E_0-f plane. These values are interpolated to map the multiplication rate in the E_0-f plane. This map shows the limits for which the plasma is created in the antenna box. We can also see regions with the extremely high multiplication rates. This region depends on the ratio between the electric field strength and frequency. The antenna frequency dependence on the electric field amplitude E_0 with the maximum multiplication rate is plotted in Fig. 6.12(b). The phenomenon in radio frequency waveguides, where, under certain conditions, secondary electron emission is in resonance with the oscillating electric field is called the multipactor effect. This phenomenon leading to exponential electron multiplication was first observed by *Gutton* [18] and studied further by *Farnsworth* [19]. The formula describing the relationship between the electric field amplitude and frequency for maximal multiplication rate is called the frequency-

gap product:

$$f_d = \frac{1}{2\sqrt{\pi}} \sqrt{\frac{q_e E_0}{m_e d}}\,, \tag{6.3}$$

where d is distance between the surfaces. This equation is visualized in Fig. 6.12(b) (red curve) for $d = 0.1135\,\mathrm{m}$. This distance corresponds to the half width of the antenna box in our simulations. We observe a perfect agreement between the simulation results and theoretical predictions. The frequency-gap product f_d is a criterion for the maximum amount of the resonance, but the multipactor effect can be significant even for a different combination of the electric field amplitude and frequency. Therefore, we plot the boundary conditions (dashed lines) corresponding to the multiplication rates decrease by a factor of two from their peak value, $\nu^{\mathrm{ion}} > \frac{\max(\nu^{\mathrm{ion}})}{2}$. In the figure, we study the boundary conditions with the extremely high multiplication rate for two pressure levels: $p = 0.2\,\mathrm{Pa}$ and $p = 1\,\mathrm{Pa}$. The simulations show that the region of the high multiplication rates expands with increasing pressure. The multiplication rate is a sum of two rates: secondary electron emission rate and ionization rate. For a lower pressure, the ionization collisions are rare, and the electron multiplication is solely due to the secondary electron emission. While for a higher pressure, the region of the antenna parameters (E_0, f) expands due to increased ionization rate. It is expected that for extremely low pressure, the plasma will be created in the antenna box only for the parameters close to the red curve with the maximum multiplication rate given by the frequency-gap equation 6.3. It is necessary to avoid the combinations of the electric field and frequency close to this peak of the multiplication rate, as it has more than ten times higher value than for the rest of the ratio of the electric field amplitude and frequency at $p = 1\,\mathrm{Pa}$ (Fig. 6.12(a)). Also, we have to consider that, for a fixed RF frequency, the electric field magnitude E_0 decreases along the poloidal antenna strap from the maximum value at the feeding point to grounding. It means that for this fixed frequency, it is very likely to have a region with a ratio of E_0 and f to enhance a breakdown in the antenna box when the SEY is high.

Both figures 6.12(a) and 6.12(b) show that for the lower frequencies there is a limited range of the electric field amplitudes at which it is a potential to create the plasma in the antenna box at the IShTAR device. It poses possible risk of creating a discharge inside an antenna box for the ITER ICRF antenna operating in the frequency range $f = 40 - 55\,\mathrm{MHz}$. Therefore, a detailed investigation of the plasma discharge initiation in the ITER antenna box is needed with the antenna geometry. It is also important to know the approximated shapes of the SEY functions for the materials of the ITER antenna box and straps, and ways how to reduce it. For example by the *Antenna conditioning*, we can remove oxidation layers or other impurities from the antenna box walls that can potentially increase the SEY [8, 12]. It was shown in Fig. 6.10(b) that the secondary electron emission becomes the dominant process to initiate an electron density increase for the High yield. It also demonstrates that for a such high secondary electron yield the plasma initiation in the simulations is independent of the neutral gas pressure.

6.4 Conclusion

In this chapter, we have studied discharge initiation in front of the ICRF antenna, and inside the antenna box by the vacuum parallel electric field in a linear device. We showed the first experimental study of discharge initiation in Helium in IShTAR linear device with the one strap ICRF antenna operating at two frequencies. The experimental observations were compared with our modeling and theoretical predictions given by the PDMI-model.

In the experiment, the homogeneous plasma column in front of the antenna was formed at $f = 5.22\,\mathrm{MHz}$. The minimum pressures above which the plasma was created depend on the generator power and are in qualitative agreement with the modeling predictions. However, the experimental values of the minimum pressures are slightly shifted towards lower pressures. This shift may be caused by insufficient vacuum conditions. Impurities present in the vessel with lower ionization potential than for the helium could increase the ionization rate. The MCC-model `RFdinity1d` in the current version is not able to simulate a gas mixture.

For the experiment at $f = 42.06\,\mathrm{MHz}$, the plasma is always also created in the antenna box. The plasma was observed in the antenna box starting from pressures above $0.2\,\mathrm{Pa}$ for the generator power $P_G = 290\,\mathrm{W}$. This experimental observation is in discrepancy with the theoretical description given by the PDMI-model. This model predicts that no plasma should be created inside the antenna box below $5\,\mathrm{Pa}$ for the IShTAR configuration. The modeling predictions meet the experiment only after including the secondary electron emission into the MCC-model. The effect of the secondary electron emission on the discharge initiation was studied with the model for three dependencies of the secondary electron yield on the incoming electron energy, and for varying ratios between the electric field amplitude E_0 and frequency f. The results demonstrated that with increasing secondary yield, the minimum pressure to create the plasma in the antenna box decreases. Secondly, the simulation results show a strong dependency on the ratio between the electric field strength and frequency to initiate the discharge in the antenna box.

The simulations further indicated that for rather high but realistic SEY for aluminum, the secondary electron emission becomes the dominant process for the electron multiplication and density build-up. The density increase in simulations with the high SEY is independent of the neutral gas pressure, and it poses a potential danger of the plasma creation in the antenna box. Therefore, it is necessary to construct the antenna box using materials with already low SEY or apply antenna conditioning methods. It was reported that the presence of an oxide layer and of adsorbed water increases the SEY, but it can be decreased by antenna conditioning that partly or totally removes these layers.

References

[1] M. D. Carter et al. *Plasma production using radiofrequency fields near or below the ion cyclotron range of frequencies*. Nuclear Fusion, 30(723), 1990.

[2] F. Schuller et al. *Report on Applications of ICWC on ITER*. Technical Report IO/2009/ADM-014 report version 3, ITER - IO, 13115, St. Paul-lez-Durance, France, November 2009.

[3] D. A. Moncrieff and P. R. Barker. *Scanning 1*. Technical Report 195, 1976.

[4] R. Shimizu et al. J. appl. Phys, 45(2107), 1974.

[5] M. Kanter et al. Phys. Rev., 121(1677), 1961.

[6] H. Bruining et al. Physica, V(17), 1938.

[7] I.M. Bronstein and B.S. Fraiman. *Vtorichnaya Elektronnaya Emissiya*, page p340. Nauka: Moskva, 1959.

[8] V. Baglin. *The secondary electron yield of technical materials and its variation with surface treatments*. In C. Petit-Jean-Genaz, editor, Proceedings of EPAC, Vienna, Austria, 2000. CERN.

[9] G. Rumolo, F. Ruggiero, and F. Zimmermann. Phys. Rev. Spec. Top. - Accel. Beams, 4(1):25–36, 2001.

[10] J. de Lara et al. IEEE Trans. Plasma Sci., 34(2):476–484, 2006.

[11] M. Goniche et al. Nucl. Fusion, 54(1):13003, 2014.

[12] N. Fil et al. *Studies of electron emission properties under magnetic field for copper samples used for LH antenna waveguides*. In Proc. 22nd topical conference, number A-26, Aix-en-Provence, France, 2017.

[13] D.C. Joy. *A database of electron-solid interactions*. EM Facility, University of Tennessee, and Oak Ridge National Laboratory, 2008.

[14] K. Crombé et al. *Studies of RF sheaths and diagnostics on IShTAR*. In AIP Conference Proceedings, volume 1689 of *http://doi.org/10.1063/1.4936471*, page 030006, California, USA, 2015.

[15] M. Tripský et al. *Discharge initiation by ICRF antenna in IShTAR*. EPJ Web of Conferences, 157:03056, May 30 - June 2 2017.

[16] CST STUDIO SUITE (R), http://www.cst.com. *CST AG*, 2015.

[17] T. Wauters and M. Tripský et al. *Advanced ponderomotive description of electron acceleration in ICRF discharge initiation*. EPJ Web of Conferences, 157:03064, May 30 - June 2 2017.

[18] C. Gutton et al. *Sur la décharge électrique a fréquence trés élevée*. Comptes-Rendus Hebdomadaires des Séances de l'Académie des Sciences, 178:467, 1924.

[19] P. T. Farnsworth et al. *Television by Electron Image Scanning*. Journal of the Franklin Institute, 2:411, 1934.

7 Conclusion

This manuscript focused on the study of the discharge initiation by the ICRF antenna in tokamaks, stellarators, linear device and antenna box. Discharges created by the ICRF antenna are applied for wall conditioning in fusion devices. The Ion-Cyclotron-Wall-Conditioning (ICWC) technique intends to be employed during ITER operation and on future fusion devices due to its significant advantage over the standard Glow-Discharge-Conditioning (GDC) to operate in the presence of the toroidal magnetic field. The GDC technique is not efficient when the toroidal magnetic field is present in the vessel. ITER and future fusion devices are designed to operate with the superconducting toroidal field coils. These coils cannot be turned off in-between pulses or overnight for wall conditioning. Therefore, the wall conditioning technique efficiently operating in the presence of the toroidal magnetic field is needed in ITER and future fusion devices.

The ICWC method is currently used on tokamaks with ICRF antenna, i.e., JET, ASDEX Upgrade, WEST and starting from 2018 campaign also on W7-X. However, using ICRF antennas for the plasma production brings some problems and operation limitations during ICWC experiments. The ICRF antenna system is designed to operate when the plasma is already present in the vessel for the plasma heating and current drive by exciting fast waves. The antenna system is not intended to couple into the vacuum to initiate the discharge. During the density build-up, high voltages are present on the antenna strap and in the transmission lines as both forward and reflected waves exist between the matching system and antenna straps. Only after the plasma breakdown, does this high voltage drop as a result of the improved coupling into the plasma. Therefore, when setting the antenna parameters (power, frequency, and phasing) and neutral gas pressure during ICWC experiments, it is essential to assure swift density build-up (short plasma breakdown). Otherwise, when high voltages are kept a long

time in the transmission lines, there is a risk of creating spurious plasma inside the antenna box or transmission lines leading potentially even in destruction of the ICRF system. Here, in this manuscript, we study the discharge initiation by ICRF antennas to better understand the process and to set the safety parameters limits for the ICWC operation on the present fusion devices and ITER.

The goal of this manuscript is to investigate the dependencies of the discharge initiation by the ICRF antennas on the antenna parameters (generator power, frequency, and phasing) and neutral gas pressure. I have developed Monte Carlo models to study these dependencies and provide better understanding of the ICRF discharge initiation. Knowing these dependencies, I could propose new safety margins of the antenna parameters and pressure to minimize the presence of the high voltages and possibility of a dangerous parasitic sparking in the transmission lines. These safety guidelines will be especially crucial for the ITER ICRF antennas which are designed to couple up to $20\,\mathrm{MW}$.

My MCC-model `RFdinity1d` follows the motion of electrons in a narrow bundle of magnetic field lines close to the antenna straps. These electrons are accelerated in the antenna vicinity by the toroidal component of the electric field E_z (or $E_\parallel$), which is generated by the ICRF antenna. I have implemented collisions between the electrons and neutral atoms (hydrogen or helium) using the Monte Carlo Collision Scheme. This model for the first time considered that electrons could reenter the antenna region and be re-accelerated by the antenna field. Previously developed models (PDM- and PDMI-models) before my Ph.D. research describing the discharge initiation by ICRF antennas considered: (i) creation of the plasma only in front of the ICRF antenna and (ii) electrons leaving the antenna region do not contribute anymore in discharge initiation. Therefore, it is believed that my MCC-model has more accurate results and a better description of discharge initiation dependencies on the antenna parameters (generator power, frequency, and phasing) and neutral gas pressure.

From my simulations using the MCC-model `RFdinity1d`, I measure the electron density evolution over time. This increase in time corresponds to the ionization rate, and it is an indirect measurement of the breakdown time. A higher ionization rate means a shorter breakdown time due to a faster electron density increase in time. My simulations indicated that the ionization rate:

- increases with a square root of the neutral gas pressure, $\nu_{\text{ion}} \sim \sqrt{p}$, for the pressures below $p \leq 5 \cdot 10^{-2}\,\mathrm{Pa}$
- decreases with the circumference length (or toroidal distance between ICRF antennas) as $\nu_{\text{ion}} \sim C^{-1}$
- decreases with increasing RF frequency
- quickly increases with the applied electric field strength (generator power) reaching the maximum value and then saturates when further increasing the electric field strength

According to the PDM-model, the ionization rate should be dependent on the ratio between the electric field amplitude and frequency. However, I showed with the MCC-model `RFdinity1d` that simulations with the same ratio but different values of the electric field amplitude and frequency have very different ionization rates. Also, my simulation results indicating the square root dependence on the pressure are in discrepancy with the PDMI-model predicting a linear dependency. Additionally, we obtained almost ten times smaller ionization rates in our simulations than predicted by the PDMI-model. These discrepancies demonstrate that the PDM and PDMI-models are crude approximations of the discharge initiation by the ICRF antennas. My parameter dependencies on the electric field amplitude and neutral gas pressure in simulations with the MCC-model `RFdinity1d` were confirmed by experimental observations during ICWC experiments on ASDEX Upgrade and TEXTOR.

I have improved and modified my MCC-model `RFdinity1d` into Particle-In-Cell Monte Carlo Collision model `RFdinity1d`. This model includes the motion of ions and generation of an electrostatic field due to the charge inhomogeneity. The profile of this electrostatic field is estimated by solving Poisson's equation. This time electrons and ions are accelerated by a sum of two electric fields: (i) the vacuum RF electric field in front of the ICRF antenna E_z^{RF} and (ii) the self-generated electrostatic field E_z^P obtained from Poisson's equation.

This PIC-MCC model `RFdinity1d` detected a transition in the Electron and Ion energy distribution functions due to the Langmuir waves excitation. These energy distributions resemble a Kappa energy distribution, which is similar to a Maxwell distribution at low energy but falls off as a power law at higher energies. By assuming a Kappa energy distribution, I disproved conclusion of the NPA measurements on ASDEX Upgrade suggesting the ICWC plasma having the plasma temperatures $T > 200\,\mathrm{eV}$. These NPA measurements were in disagreement with the fact that we have a partially ionized low-temperature plasma during ICWC experiments ($T = 3 - 5\,\mathrm{eV}$). My modeling of ICRF discharge initiation with the PIC model suggests that these fast ions are already created at low electron density $n_e > 10^{13}\,\mathrm{m}^{-3}$ by the action of the Langmuir waves via the parallel electric field $E_z = E_z^{RF} + E_z^P$. Furthermore, these mechanisms are always present in the ICRF discharges regardless of the applied toroidal magnetic field B_T.

In addition to the investigation of the discharge initiation by the ICRF antennas in toroidal devices, the MCC model `RFdinity1d` was modified to simulate and study for the first time the discharge initiation in front of the antenna in a linear device or inside the antenna box. The simulation results were compared with my experimental observations on the IShTAR linear device equipped with one strap antenna. I demonstrated a strong relationship between the place of the discharge formation and applied antenna frequency:

- For $f = 5.22\,\mathrm{MHz}$ a homogeneous plasma column in front of the antenna was formed. The minimum pressures above which the plasma was created depend on the generator power and are in qualitative agreement with the modeling predictions.

- For $f = 42.06\,\mathrm{MHz}$, the plasma was always first created inside the antenna box near the feeding point.

I could reproduce these results in our simulations only after including the secondary electron emission into our model. I had studied the effect of the secondary electron emission on the discharge initiation with the model for different yields of the secondary electron emission, and for varying ratios between the electric field amplitude and frequency. My simulation results indeed confirmed that for the high frequency ($f = 42.06\,\mathrm{MHz}$) it is very likely that the plasma is initiated inside the antenna box. Whereas for the low frequency ($f = 5.22\,\mathrm{MHz}$), it is very unlikely that the plasma is created inside the antenna box. In fact, we did not observe the plasma inside the antenna box at this low frequency in our experiment neither in simulations. The simulations further indicate that for rather high but realistic SEY, the secondary electron emission becomes the dominant process for the electron multiplication and density build-up. The density increase in simulations with the high SEY is independent of the neutral gas pressure, which poses a concern for the plasma creation in the antenna box. Therefore, it is necessary to construct the antenna box using materials with already low SEY, perform antenna conditioning, or to operate the antenna at a lower frequency. My findings are first evidence that operating with high frequencies during the ICWC experiments increase the risk of creating the plasma inside the antenna box.

ICRF discharge initiation on ITER

The ITER ICRF antenna will operate in the range of $40 - 55\,\mathrm{MHz}$. This frequency range is slightly higher than the frequencies ranges currently used in ICRF systems on tokamaks and stellarators. Based on my simulations this frequency range presents several potential disadvantages during the discharge initiation using ICRF antennas. First, my simulations indicated that the ionization rate decreases with increasing antenna frequency. Thus, it may be preferred to operate with $f = 40\,\mathrm{MHz}$ during ICWC experiments on ITER. Secondly, simulations inside the antenna box imply that at higher frequencies it is more probable to create the plasma inside the antenna box independently on the pressure if the secondary electron emission is high. We will not know precisely the secondary electron emission yield in the ITER antenna box, but we can reduce the risk of creating the plasma inside the antenna box by operating at the lowest possible frequency with the ITER antenna ($f = 40\,\mathrm{MHz}$). Therefore, I conclude and propose to operate during the ICWC experiments on ITER with the lower frequency of $f = 40\,\mathrm{MHz}$.

Due to the square root dependence of the ionization rate on the pressure, it will not be beneficial to operate at the present maximum pressure during the ICWC experiments of $p = 5 \cdot 10^{-2}\,\mathrm{Pa}$. My simulations with the ITER antenna field indicated that already for the pressure $p = 0.01\,\mathrm{Pa}$, the breakdown time is around $\approx 2\,\mathrm{ms}$. Therefore, I propose that it will be sufficient to initiate ICWC experiments with pressure below $p \leq 10^{-2}\,\mathrm{Pa}$. Additionally, this lower pressure level will also decrease the probability of creating the plasma inside the antenna box or in the transmission lines.

Concerning the optimal power level on the ITER ICRF antennas for plasma production, I found in our simulations that above a specific magnitude of the generator power the breakdown time saturates. The breakdown time does not further decrease upon increasing power. My simulations indicated that already relatively moderate generator power of $P = 0.5\,\mathrm{MW}$ creates the plasma within $2\,\mathrm{ms}$. Operating the ICWC on ITER with higher antenna power than $0.5\,\mathrm{MW}$ will only increase the voltage between the antenna straps and matching system and potentially increase a chance of arcing in the transmission lines. After breakdown, when a plasma load appears, the power may be increased to enhance wall conditioning efficiency.

Finally, I observed in my simulations that the ionization rate decreases with the increasing circumference length, $\nu_{\mathrm{ion}} \sim C^{-1}$. Therefore, it would be optimal to have the ITER ICRF antennas located at the toroidal location opposite to that of each other. In the present design, the ITER ICRF antennas are located next to each other separated only by one port. However, my simulations for ITER were launched with only one ICRF antenna, and the long ITER circumference length was not a hurdle to initiate the plasma by the ICRF antenna. This circumference length dependence will be of use to optimize the toroidal locations of ICRF antennas in future machines.

Suggestions for future work

In this manuscript, I studied the ICRF discharge initiation using mostly numerical modeling. From my simulations, we observed a lot of new phenomena during the density build-up. For example, the observation of the Langmuir waves in the plasma production process, or the formation of a Kappa energy distribution. Although this Kappa energy distribution was measured by NPA diagnostics on ASDEX Upgrade, it is necessary to study a Kappa distribution and its formation during ICWC experiments in more details. It will be tested and examined on TOMAS device, which is specially constructed for wall conditioning experiments. It posses one strap ICRF antenna, and it will also contain NPA diagnostic to detect low energy spectrum. This NPA diagnostic will be able to better study the formation of the energetic tails, the type of the energy distribution (Kappa, Maxwell) and the temperature of discharges.

Furthermore, my simulations reproduced our experimental observations on IShTAR device in which plasma was created inside the antenna box. This phenomenon was observed only when the ISHTAR ICRF antenna was operating at high frequency ($f = 42\,\mathrm{MHz}$). I have discovered in my simulations that the plasma is formed inside the antenna box due to the Secondary Electron Emission. Therefore, it is essential to study this plasma formation inside the antenna box in more details, because we want to avoid such phenomenon during the ICWC operation in ITER. It will be necessary to find a scenario for which we can operate with high RF frequency (ITER: $f = 40 - 55\,\mathrm{MHz}$) without the plasma inside the antenna box. This study can be performed in IShTAR or TOMAS devices where we can operate beyond safety parameters and with a more extensive variety of antenna parameters to find a relevant scenario for ITER without plasma inside the antenna box.

A

Inelastic collision reactions in Hydrogen and Helium

Inelastic collisions in Hydrogen

Ionization reaction of H_2:

$$e + H_2\left(X^1\Sigma_g^+\right) \longrightarrow e + H_2^+(v) + e \quad \Delta E = 15.43\,\mathrm{eV}$$

We distinguish two types of excitation:
Vibration excitation reactions of H_2 (Excitation 1):

$$e + H_2\,(v=0) \longrightarrow e + H_2^*(v=1) \quad \Delta E = 0.5\,\mathrm{eV}$$
$$e + H_2\,(v=0) \longrightarrow e + H_2^*(v=2) \quad \Delta E = 1\,\mathrm{eV}$$

Electronic excitation reactions with H_2 (Excitation 2):

$$e + H_2\left(X^1\Sigma_g^+\right) \longrightarrow e + H_2^*\left(B^1\Sigma_u^+ 2p\sigma\right) \quad \Delta E = 12.1\,\mathrm{eV}$$
$$e + H_2\left(X^1\Sigma_g^+\right) \longrightarrow e + H_2^*\left(C^1\Pi_u 2p\pi\right) \quad \Delta E = 12.4\,\mathrm{eV}$$
$$e + H_2\left(X^1\Sigma_g^+\right) \longrightarrow e + H_2^*\left(E, F^1\Sigma_g^+\right) \quad \Delta E = 12.7\,\mathrm{eV}$$

Dissociation reactions of H_2:
for all dissociation reactions in our model: $\Delta E = 10.5\,\mathrm{eV}$

$$e + H_2\left(X^1\Sigma_g^+\right) \longrightarrow e + H_2^*\left(b^3\Sigma_u^+, a^3\Sigma_g^+ \text{ and } c^3\Pi_u\right) \longrightarrow e + H(1s) + H(1s)$$
$$e + H_2\left(X^1\Sigma_g^+\right) \longrightarrow e + H_2^*\left(1s\sigma_g, nl\lambda|^1\Lambda\right) \longrightarrow e + H(1s) + H^*(2s)$$
$$e + H_2\left(X^1\Sigma_g^+\right) \longrightarrow e + H_2^*\left(2p\sigma_u, nl\lambda|Q_2^1\Pi_u\right) \longrightarrow e + H^*(2p) + H^*(2s)$$
$$e + H_2\left(X^1\Sigma_g^+\right) \longrightarrow e + H_2^*\left(2p\sigma_u; n=3\right) \longrightarrow e + H(1s) + H^*(n=3)$$

Dissociative ionization reaction of H_2:

$$e+H_2\left(X^1\Sigma_g^+\right) \longrightarrow e+[H_2\left(\Sigma_g \text{ and } \Sigma_u\right)+e] \longrightarrow e+H^+ +H(1s)+e\Delta E = 21.1\,\text{eV}$$

Recombination reaction of H_2^+:

$$e + H_2^+(v) \longrightarrow H(1s) + H^*(n)\,, (v = 0 \ldots 9, n \geq 2)\,.$$

Dissociative ionization reaction of H_2^+:

$$e + H_2^+(v) \longrightarrow e + H^+ + H^+ + e, \;\; (v = 0 \ldots 9) \;\; \Delta E = 17.9\,\text{eV}$$

Dissociation of H_2^+:

$$e + H_2^+(v) \longleftrightarrow e + H_2^{+*}(2p\sigma_u) \longleftrightarrow e + H^+ + H(1s), \;\; (v = 0 \ldots 9) \;\; \Delta E = 2.9\,\text{eV}$$
$$e + H_2^+(v) \longleftrightarrow e + H_2^{+*}(2p\pi_u) \longleftrightarrow e + H^+ + H^*(n = 2), \;\; (v = 0 \ldots 9) \;\; \Delta E = 14.4\,\text{eV}$$

Recombination reaction of H^+:

$$e + H^+(v) \longleftrightarrow H + h\nu, \;\; (v = 3)$$

Inelastic collisions in Helium

Ionization reaction of He:

$$e + He\left(1s^2 1S\right) \longrightarrow e + He^+(1s) + e \;\; \Delta E = 24.5\,\text{eV}$$

We distinguish three types of excitation:
Electronic excitation reactions with He (Excitation 1):

$$\begin{aligned} e + He\left(1s^2 1S\right) &\longrightarrow e + He^*\left(1s^1 2p^1 1P\right) \;\; \Delta E = 21.217\,\text{eV} \\ e + He\left(1s^2 1S\right) &\longrightarrow e + He^*\left(1s^1 3p^1 1P\right) \;\; \Delta E = 23.086\,\text{eV} \end{aligned} \tag{A.1}$$

Electronic excitation reactions with He (Excitation 2):

$$e + He\left(1s^2 1S\right) \longrightarrow e + He^*\left(1s^1 2s^1 1S\right) \;\; \Delta E = 20.614\,\text{eV}$$

Electronic excitation reactions with He (Excitation 3):

$$\begin{aligned} e + He\left(1s^2 1S\right) &\longrightarrow e + He^*\left(1s^1 2s^1 3S\right) \;\; \Delta E = 19.818\,\text{eV} \\ e + He\left(1s^2 1S\right) &\longrightarrow e + He^*\left(1s^1 2p^1 3P\right) \;\; \Delta E = 20.936\,\text{eV} \\ e + He\left(1s^2 1S\right) &\longrightarrow e + He^*\left(1s^1 3s^1 3S\right) \;\; \Delta E = 22.717\,\text{eV} \\ e + He\left(1s^2 1S\right) &\longrightarrow e + He^*\left(1s^1 3p^1 3P\right) \;\; \Delta E = 23.006\,\text{eV} \end{aligned}$$

Ionization reaction of He^+:

$$e + He^+(1s) \longrightarrow e + He^{++} + e \quad \Delta E = 54.4\,\mathrm{eV}$$

Electronic excitation reactions of He^+:

$$e + He^+(1s) \longrightarrow e + He^+(2p) \quad \Delta E = 40.8\,\mathrm{eV}$$
$$e + He^+(1s) \longrightarrow e + He^+(2s) \quad \Delta E = 40.8\,\mathrm{eV}$$

Recombination reaction of He:

$$e + He^+ \longleftrightarrow He + h\nu,$$